

ERDC/CHL TR-04-12

Coastal and Hydraulics Laboratory

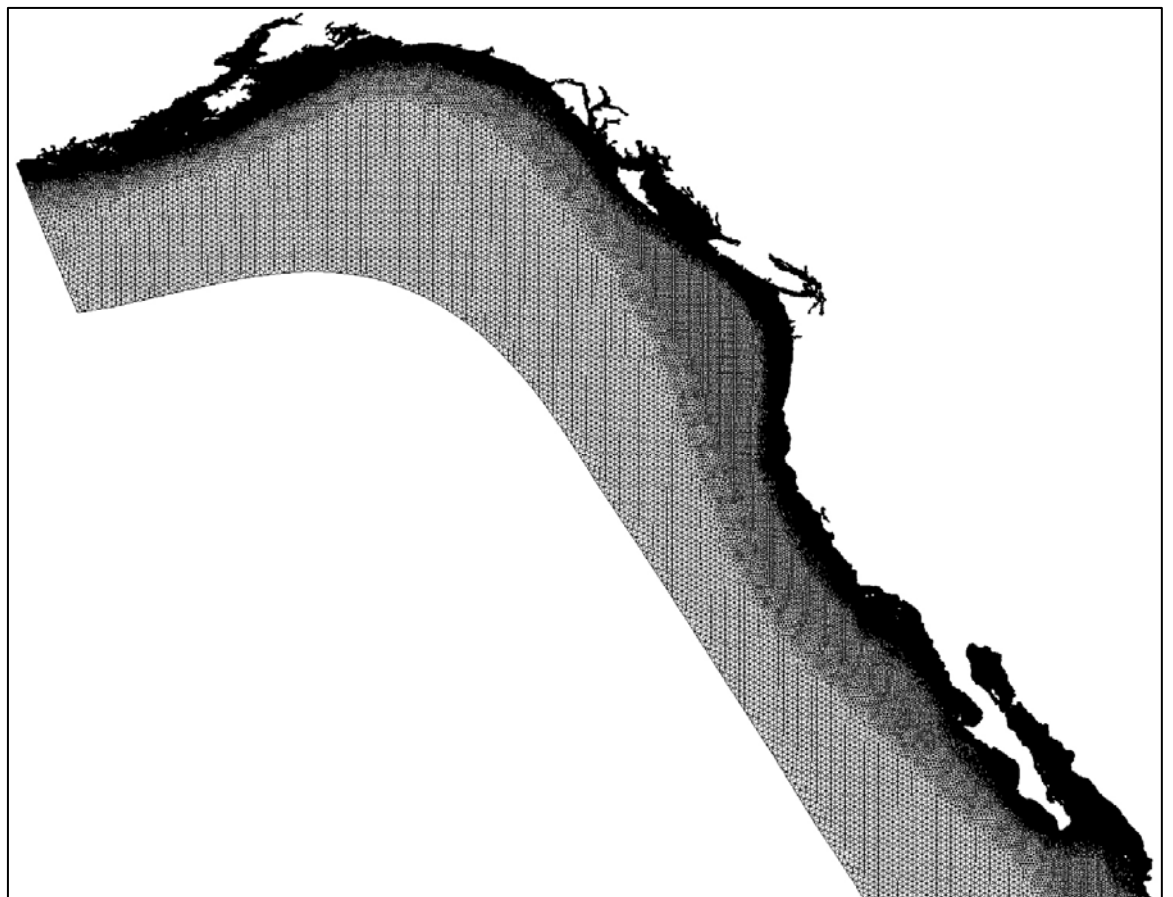


**US Army Corps
of Engineers®**
Engineer Research and
Development Center

ENPAC 2003: A Tidal Constituent Database for Eastern North Pacific Ocean

Emily A. Spargo, Joannes J. Westerink, Richard A.
Luettich, Jr., and David J. Mark

September 2004



ENPAC 2003: A Tidal Constituent Database for Eastern North Pacific Ocean

David J. Mark

*Coastal and Hydraulics Laboratory
U.S. Army Engineer Research and Development Center
3909 Halls Ferry Road
Vicksburg, MS 39180-6199*

Emily A. Spargo and Joannes J. Westerink

*Department of Civil Engineering and Geological Sciences
University of Notre Dame
Notre Dame, IN 46556*

Richard A. Luettich, Jr.

*University of North Carolina at Chapel Hill
Institute of Marine Sciences
Morehead City, NC 28557*

Final report

Approved for public release; distribution is unlimited

Prepared for U.S. Army Corps of Engineers
Washington, DC 20314-1000
Under Work Unit No. DACW 42-00-C-0006

ABSTRACT:

This report describes the development of the Eastern North Pacific (ENPAC) 2003 tidal database of elevations and velocity components for eight major tidal constituents. This database was developed using the two-dimensional, depth-integrated form of the coastal hydrodynamic model, ADCIRC, which solves the shallow-water equations in the generalized wave continuity equation form. The final ENPAC 2003 incorporates the most accurate bathymetric data available. The resolution of the unstructured finite element mesh was designed to provide a high level of resolution along the continental slope and throughout the coastal waters to resolve the nonlinear hydrodynamics that dominate this area.

DISCLAIMER: The contents of this report are not to be used for advertising, publication, or promotional purposes. Citation of trade names does not constitute an official endorsement or approval of the use of such commercial products. All product names and trademarks cited are the property of their respective owners. The findings of this report are not to be construed as an official Department of the Army position unless so designated by other authorized documents.

Contents

Preface	iv
Summary	vi
1—Introduction and Objectives	1
2—Governing Equations and 2-D Modeling	4
3—Field Data: Description, Error Analysis, and Model Validation	
Techniques	7
Field Data Description	7
Field Data Error Analysis	7
Model Validation by Field Data	9
4—ENPAC 2002 Model Development	10
Background	10
Domain, Bathymetry, and Grid	11
Model Input Parameters	14
Model Results	16
5—ENPAC 2003 Model Development	19
Domain Definition	19
Model Results	20
6—Discussion and Conclusions	22
References	25
Figures 1-187	
Tables 1-6	
SF 298	

Preface

This research was conducted as part of activities of the Coastal Inlets Research Program (CIRP), Inlet Modeling System (IMS) Work Unit. CIRP is administered at the U.S. Army Engineer Research and Development Center (ERDC), Coastal and Hydraulics Laboratory (CHL), under the Navigation Systems Program for Headquarters, U.S. Army Corps of Engineers (HQUSACE). Mr. Barry W. Holliday is HQUSACE lead technical monitor for CIRP. Dr. Sandra K. Knight, CHL, is Technical Director for the Navigation Systems Program. Dr. Nicholas C. Kraus, Senior Scientists Group, CHL, is CIRP Program Manager, and Ms. Mary A. Cialone, Coastal Processes Branch, CHL, is IMS Work Unit Principal Investigator. The computations were performed on IBM Power3 SMP and Cray T3E computers at ERDC's Major Shared Resource Center (MSRC), Information Technology Laboratory (ITL) in Vicksburg, MS. Professors Mary Wheeler and Clint Dawson and Dr. Victor Parr of the University of Texas at Austin developed the domain decomposition-based parallel version of ADCIRC.

The mission of CIRP is to conduct applied research to improve USACE capability to manage federally maintained inlets, which exist on all coasts of the United States (including the Atlantic Ocean, Gulf of Mexico, Pacific Ocean, and Great Lakes regions). CIRP objectives are to (a) make management of channels – the design, maintenance, and operation – more effective to reduce the cost of dredging, and (b) preserve the adjacent beaches in a systems approach that treats the inlet and beach together. To achieve these objectives, CIRP is organized in work units conducting research and development in hydrodynamic, sediment transport, and morphology change modeling; navigation channels and adjacent beaches; inlet scour and jetties; laboratory and field investigations; and technology transfer.

This report was prepared by Drs. Emily Spargo and Joannes Westerink, University of Notre Dame, Dr. Richard Luetlich, University of North Carolina at Chapel Hill, and Mr. David Mark, ERDC. Dr. Westerink was Principal Investigator for ADCIRC model development. Mr. Mitchell Brown, ERDC, contributed to model testing. Final word processing and report formatting were completed by Ms. J. Holley Messing, Coastal Evaluation and Design Branch, CHL and editing was performed by Mr. Bill Mullen, Information Technology Laboratory, ERDC. Work was performed under the general administrative supervision of Mr. Thomas W. Richardson, Director, CHL, and Dr. William D. Martin, Deputy Director, CHL.

Dr. James R. Houston was Director of ERDC. COL James Rowan, EN, was
Commander and Executive Director.

Summary

This report describes the development of the Eastern North Pacific (ENPAC) 2003 tidal database of elevations and velocity components of eight major tidal constituents. This database was developed using the two-dimensional, depth integrated form of the coastal hydrodynamic model, ADCIRC, which solves the shallow-water equations in the generalized wave continuity equation form. The final ENPAC 2003 model incorporates the most accurate bathymetric data available. The resolution of the unstructured finite element mesh was designed to provide high levels of resolution along the continental slope and throughout the coastal waters to resolve the nonlinear hydrodynamics that dominate this area. The domain of this model extends beyond the continental shelf, into deep ocean waters but does not include any amphidromes located in the Pacific Ocean. At the open boundary, the forcing conditions are extracted from global ocean models, in the area where these models are most accurate. The results of the ENPAC 2003 model approach the error levels found in the station data that were used for model validation.

1 Introduction and Objectives

Providing accurate prediction of the ocean tides is necessary for many coastal engineering applications including defining water depths for navigation, calculating the energy potential from tides, and determining pollutant and sediment movement. The shallow-water equations that govern tidal processes cannot be solved analytically without making many unphysical assumptions and therefore, these equations must be solved numerically. Over the past 25 years, finite element methods have been successfully employed to obtain highly accurate solutions to these equations (Lynch 1983; Westerink and Gray 1991; Kolar and Westerink 2000; Mukai et al. 2001).

Engineers and scientists have the greatest need for tidal information in coastal waters, but creating small, regional models to describe these nearshore areas must be done with caution. The boundary conditions for these models are often selected from global ocean models. These models are highly accurate in the deep ocean, but traditionally do not provide the necessary resolution over the continental shelf and through coastal waters to correctly resolve both astronomical and the associated nonlinear tides that exist in nearshore waters. If the regional models extract their boundary conditions from these models, they may be forcing the model with inaccurate information. To provide accurate boundary conditions for regional models, a larger scale model can be employed. This model will be able to place the open boundary in the deep ocean where boundary conditions can be extracted from the global ocean model where the global model has the highest level of accuracy. Using unstructured grids, a larger scale model can provide a high level of resolution over the shelf break and along the coasts in order to capture the complicated physics that dominate these regions. This technique has been successfully employed to provide accurate information for many coastal regions (Lynch and Gray 1979; Foreman 1986; Blain et al. 1994; Westerink et al. 1994, 1996; Luetlich et al. 1992; Kolar et al. 1996; Mukai et al. 2001).

The objective of this particular study is to produce a tidal model of the coastal waters along the United States west coast and lower Alaska. A so-called larger scale domain was employed for this model. The resulting domain extends into the more stable waters of the Eastern North Pacific Ocean, and this model is aptly named the Eastern North Pacific (ENPAC) 2003 tidal model. This model was developed using the two-dimensional (2-D) depth integrated finite element code, ADCIRC (Luetlich et al. 1992; Luetlich and Westerink 2003).

The original work on this project began in 1994 with the production of the ENPAC 1994 tidal model. The model domain for this project extended from Unimak Island, AK, to Punta Parada, Peru, covering an area of approximately 2.1×10^7 km and is shown in Figure 1. With resolution ranging from 70-km elements in the deep ocean to 5-km elements along the U.S. west coast, this grid took advantage of the flexibility of the finite element method by providing the most resolution along the continental slope, shelf, break, and coastal waters. To validate the performance of this model, the ENPAC 1994 output was compared to field records throughout the domain. Unfortunately, the model results, for both the amplitude and the phase components, compared poorly to the field data. In some places, the ENPAC 1994 results were worse than the global ocean models used to provide the open boundary forcing.

Extensive improvements were made to produce the ENPAC 2002 tidal model. These changes began by redefining the domain. The new domain began at the same location, Unimak Island, AK, but extended only to Acapulco, Mexico, stopping short of including Central and South America. The reason behind this domain change was the location of a cluster of amphidromes located off the west coast of Peru. The location of these amphidromes is shown with the ENPAC 1994 and ENPAC 2002 domain boundaries in Figure 2. It was assumed that these amphidromes were being incorrectly predicted by the global ocean model and that information was being propagated into the ENPAC 1994 model through the boundary conditions. Improvements in the bathymetry were made by including two more up-to-date databases. Extensive grid refinement was undertaken to produce a grid that contained over 10 times the number nodes as the ENPAC 1994 finite element mesh and area only 64 percent of the size of the original domain. The element sizes ranged from, on average, 25 km in the deep ocean to 1 km along the U.S. west coast. The results showed vast improvements over the initial ENPAC 1994 results, but major problems were evident, especially in the semidiurnal constituents along the U.S. west coast. This systematic error appeared to correlate with the location of a cluster of semidiurnal amphidromic points off the U.S. west coast.

To correct these errors, a new domain, ENPAC 2003, was created. The ENPAC 2002 and ENPAC 2003 domain boundaries and the approximate location of the semidiurnal amphidromes within the ENPAC 2002 domain are shown in Figure 3. This domain extends from Unimak Island, AK, to Chamela, Mexico, approximately 650 km north of Acapulco, Mexico, along the coastline. Nearly the entire ENPAC 2002 coastline remains intact, but 68 percent of the domain was removed. The eliminated area consists mainly of deep ocean waters, particularly in the vicinity of the amphidromes. The final grid is a band that parallels the coastline. The grid extends far enough into the deep waters to, again, take advantage of extracting boundary conditions from the global ocean models where they are most accurate. Although a large portion of the grid area was removed, 94 percent of the nodes remained because the areas of fine resolution, namely the coastal waters and shelf area, were retained in the ENPAC 2003 domain. This final version of the ENPAC model compared favorably with field data records.

The remainder of this report will expand on the themes introduced in this first chapter. In Chapter 2, the governing equations and parameters used in the

ADCIRC model will be defined. Validating the model was done by comparison to field data. This process will be discussed in Chapter 3 and will include error analysis of the model compared to the field data as well as give estimates of the error of the field data itself. Chapters 4 and 5 will show the development of the ENPAC 2002 and ENPAC 2003 models. Finally, this report will conclude with the results from these models.

2 Governing Equations and 2-D Modeling

The 2-D, depth-integrated (2DDI) form of the ADCIRC (Advanced Circulation) model was used to perform the hydrodynamic computations (Luettich et al. 1992; Luettich and Westerink 2003). This model uses the depth-integrated mass and momentum equations with incompressibility, Boussinesq, and hydrostatic pressure approximations. For this application, a hybrid form of the standard quadratic parameterization for bottom stress was used that provides a friction factor that increases as the depth decreases in shallow water similar to a Manning relationship. Baroclinic processes were neglected, including any expansion and contraction due to radiational heating. The primitive continuity and momentum equations, expressed in a spherical coordinate system (Flather 1988; Kolar et al. 1994b) are shown as follows:

Equation 1 is the primitive continuity equation, and Equations 2 and 3 are the λ (degrees longitude) and ϕ (degrees latitude) direction primitive momentum equations in nonconservative form.

$$\frac{\partial \xi}{\partial t} + \frac{1}{R \cos \phi} \left[\frac{\partial UH}{\partial \lambda} + \frac{\partial (VH \cos \phi)}{\partial \phi} \right] = 0 \quad (1)$$

$$\begin{aligned} \frac{\partial U}{\partial t} + \frac{1}{R \cos \phi} U \frac{\partial U}{\partial \lambda} + \frac{V}{R} \frac{\partial U}{\partial \phi} - \left(\frac{\tan \phi}{R} U + f \right) V = \\ - \frac{1}{R \cos \phi} \frac{\partial}{\partial \lambda} \left\{ \frac{p_s}{\rho_0} + g [\xi - (\eta + \Gamma)] \right\} + \frac{\tau_{s\lambda}}{\rho_0 H} - \tau_* U \end{aligned} \quad (2)$$

$$\begin{aligned} \frac{\partial V}{\partial t} + \frac{1}{R \cos \phi} U \frac{\partial V}{\partial \lambda} + \frac{V}{R} \frac{\partial V}{\partial \phi} + \left(\frac{\tan \phi}{R} U + f \right) U = \\ - \frac{1}{R} \frac{\partial}{\partial \phi} \left\{ \frac{p_s}{\rho_0} + g [\xi - (\eta + \Gamma)] \right\} + \frac{\tau_{s\phi}}{\rho_0 H} - \tau_* V \end{aligned} \quad (3)$$

where

ξ = free surface elevation relative to the geoid

U, V = depth-averaged horizontal velocities
 $H = \xi + h$ = total water column
 h = bathymetric depth relative to the geoid
 $f = 2\Omega \sin \phi$ = Coriolis parameter
 Ω = angular speed of the Earth
 p_s = atmospheric pressure at the free surface
 g = acceleration due to gravity
 η = Newtonian equilibrium tidal potential and earth tide
 Γ = self-attraction and load tide
 ρ_0 = reference density of water
 $\tau_{s\lambda}, \tau_{s\phi}$ = applied free surface stress
 $\tau_* = C_f(U^2 + V^2)^{1/2}/H$
 C_f = bottom friction coefficient

The Newtonian equilibrium tide potential is expressed by Reid (1990) in the following equation:

$$\eta(\lambda, \phi, t) = \sum_{j,n} \alpha_{jn} C_{jn} f_{jn}(t_o) L_j(\phi) \cos \left[\frac{2\pi(t - t_o)}{T_{jn} + j\lambda + u_{jn}(t_o)} \right] \quad (4)$$

where

α_{jn} = reduction in the field of gravity due to earth tides
 C_{jn} = Newtonian equilibrium tidal potential amplitude
 $f_{jn}(t_o)$ = nodal factor accounting for the influence of the 18.6-year tidal cycle on shorter period tides
 j = tidal species (i.e., 1 for diurnal and 2 for semidiurnal constituents)
 n = constituent name
 $L_1(\phi) = \sin(2\phi)$
 $L_2(\phi) = \cos^2(\phi)$
 λ = degrees longitude
 ϕ = degrees latitude
 t = time
 t_o = reference time
 T_{jn} = tidal period

For the earth tide reduction factor, α_{jn} , Hendershott (1981) introduced a standard of 0.690 to be used for all constituents, but the values shown in Table 1

reflect those proposed by Wahr (1981). This table lists the pertinent information needed to obtain the Newtonian equilibrium tide (as in Equation 4), for the main four diurnal, K_1 , O_1 , P_1 , Q_1 , and four semidiurnal, M_2 , S_2 , N_2 and K_2 , constituents.

Solving the shallow-water equations in the primitive form, Equations 1-3, results in spatial oscillations in the solution on the order of $2\Delta x$ (Lynch and Gray 1979; Kolar et al. 1994a, 1994b; Kolar and Westerink 2000). These oscillations can be eliminated by the addition of nonphysical damping by viscous terms. To avoid the addition of nonphysical characteristics to the solution, a reformulation of these equations was proposed by Lynch and Gray (1979) and modified by Kinmark (1986). This reformulation is the Generalized Wave Continuity Equation (GWCE). The spatially differentiated form of the conservative momentum equation is substituted into the time derivative of the primitive continuity equation. Then, the primitive continuity equation multiplied by the numerical weighting parameter, G is added to create the GWCE. The numerical parameter, G , sets the balance between a pure wave equation, where G equals zero, and the primitive continuity equation, where G is much greater than zero. The GWCE was solved in conjunction with the primitive momentum equations.

The finite element method was then applied to discretize these equations in space. Triangular elements were used for elevation, velocity and depth. The temporal discretization of the GWCE was solved using a finite difference, weighted three-time level implicit scheme except for the nonlinear, Coriolis, atmospheric pressure forcing and tidal potential terms. These latter terms were treated explicitly. In the momentum equations, a two-time level Crank-Nicolson scheme was applied to all terms except a portion of the bottom friction and convective terms which were treated explicitly. This time-stepping scheme does require the time-steps to be Courant-limited for the nonlinear terms to remain stable. The decoupling of the time and space discrete forms of the equations, the time independent and/or tridiagonal system matrices, and the full vectorization of all major loops leads to a highly efficient code.

The parallel version of this code applies domain decomposition, a conjugate gradient solver and MPI (message passing interface). Benchmark tests have been performed to show linear and even super-linear performance rates on up to 128 processors for grids of approximately 300,000 nodes.

3 Field Data: Description, Error Analysis, and Model Validation Techniques

Elevation recording stations and pelagic pressure gauges were used to validate the ENPAC 2003 model. Since more than one set of recorded data was collected at some stations, an error estimate on the field data could be determined. The analysis techniques for the field data error and the model error are also discussed in this section.

Field Data Description

The ENPAC 2003 model was validated using 91 pelagic pressure and coastal tide gauges located throughout the domain. The model results, at these 91 locations, were compared to the amplitude and phase results available from the station data records. The station data were available from several sources, specifically the International Hydrography Organization (IHO), National Ocean Service (NOS) and the Pacific Marine Environmental Laboratory (PMEL) (Eble and Gonzalez 1991). The locations of all 91 stations are shown in Figure 4. Figures 5-8 show the station numbers in four regions: Mexico, U.S. west coast, Canada, and Alaska.

To examine the errors on a regional basis, the location of the gauges was divided into five regions: (a) Mexico, (b) U.S. west coast, (c) Canada, (d) Alaska, and (e) deep ocean. Table 2 lists the station number, name, location, name of the subdomain, and the source. Some stations have two or three different sources indicating more than one set of constituent values was obtained for one location.

Field Data Error Analysis

At the stations where more than one source of data could be found, the amplitude and phase values for different tidal constituents were used to perform an estimation of the station data error. For the amplitude values, a standard proportional deviation was calculated according to Equation 5.

$$E_{j-amp}^{obs1-obs2} = \left\{ \frac{\sum_{l=1}^L [\eta_j^{obs1}(x_l, y_l) - \eta_j^{obs2}(x_l, y_l)]^2}{\sum_{l=1}^L [\eta_j^{obs2}(x_l, y_l)]^2} \right\}^{1/2} \quad (5)$$

In Equation 5, η_j^{obs1} = the observed amplitude at a given (x_1, y_1) location for constituent j from the first data source, η_j^{obs2} = the observed amplitude at a given (x_1, y_1) location for constituent j from the second data source, and L = number of elevation recording stations in the domain (or subregion) with more than one data set. When IHO and NOS data were available, IHO data were considered the first data source (*obs1*) and the NOS data were considered the second data source (*obs2*). When IHO and PMEL data were available, IHO data were considered the first data source and PMEL data were considered the second data source. When NOS and PMEL data were available, NOS data were considered the first data source and PMEL data were considered the second data source. When all three data sources were available, IHO data were considered the first data source and PMEL data were considered the second data source.

For the phase data, an absolute average was calculated according to Equation 6.

$$E_{j-pha}^{obs1-obs2} = \frac{1}{L} \sum_{l=1}^L |\varphi_j^{obs1}(x_l, y_l) - \varphi_j^{obs2}(x_l, y_l)| \quad (6)$$

In Equation 6, φ_j^{obs1} = the observed phase at a given (x_1, y_1) location for constituent j from the first data source, φ_j^{obs2} = the observed phase at a given (x_1, y_1) location for constituent j from the second data source, and L = number of elevation recording stations in the domain (or subregion) with more than one data set.

The standard proportional deviation amplitude errors and absolute average phase errors for eight tidal constituents are reported in Table 3 for the entire domain, as well as the U.S. west coast, Canada, Alaska, and deep ocean subdomains. Since no duplicate station records were found in the Mexico stations subdomain, no errors were reported.

In general, this analysis shows lower error levels in the diurnal than semidiurnal constituents. In particular, the highest error levels were seen in the S_2 and N_2 constituents for the U.S. west coast and Alaska stations. Later it will be noted that similar high error levels were found in the computed values of these constituents in these locations. This may correspond to shifting of the semidiurnal amphidromes off the U.S. west coast by such phenomena as shifting currents or changes in the Pacific Ocean environment due to the El Niño Southern Oscillation.

Model Validation by Field Data

The amplitude error is defined as the proportional standard deviation error between the model output and the station data. Equation 7 defines this error where η_j^{calc} = the calculated ENPAC model amplitude at a given (x_1, y_1) location for constituent j , η_j^{obs} = the observed amplitude at a given (x_1, y_1) location for constituent j , and L = number of elevation recording stations in the domain (or subregion). There are 91 stations in the entire domain, consisting of five stations in the Mexico subregion, 17 stations in the U.S. west coast subregion, 31 stations in the Canada subregion, seven stations in the Alaska subregion, and 31 stations in the deep ocean subregion.

$$E_{j-amp}^{calc-obs} = \left\{ \frac{\sum_{l=1}^L [\eta_j^{calc}(x_l, y_l) - \eta_j^{obs}(x_l, y_l)]^2}{\sum_{l=1}^L [\eta_j^{obs}(x_l, y_l)]^2} \right\}^{1/2} \quad (7)$$

Equation 8 defines the phase error calculated as an absolute average where φ_j^{calc} = the calculated ENPAC model phase at a given (x_1, y_1) location for constituent j , φ_j^{obs} = the observed station data phase at a given (x_1, y_1) location for constituent j , and L = number of elevation recording stations in the domain (or subregion).

$$E_{j-pha}^{calc-obs} = \frac{1}{L} \sum_{l=1}^L |\varphi_j^{calc}(x_l, y_l) - \varphi_j^{obs}(x_l, y_l)| \quad (8)$$

The proportional standard deviation error used to define the amplitude error in the station data and the computed model results can be interpreted as an estimate of the mean percent deviation from the measured error. The advantage of the proportional standard deviation error measure over a standard percentage error is that the proportional standard deviation incorporates the uncertainty in the data. The phase error is similar, but does not normalize the results.

4 ENPAC 2002 Model Development

The ENPAC 2002 model development began with a change in domain to eliminate amphidromic points off the coast of Central and South America. Updated bathymetry was added. Extensive grid refinement was completed. The results showed a great improvement over the original ENPAC 1994 model.

Background

The first ADCIRC Eastern North Pacific (ENPAC) tidal database was completed in 1994. The western edge of the ENPAC 1994 domain (shown in Figure 1) extends through the open ocean from Seal Cape on Unimak Island, AK, in the north to Punta Parada, Peru, in the south. The eastern land boundary includes the Pacific coastlines of Alaska, Canada, United States, Mexico, Guatemala, El Salvador, Nicaragua, Costa Rica, Panama, Columbia, and northern Peru. The domain does not extend to the Hawaiian Islands. The entire domain is 2.81×10^7 sq km.

Bathymetric information was incorporated into the ENPAC 1994 domain using the Earth Topography 5-arc-min grid (ETOPO-5). This database, published in 1988 (National Geophysical Data Center 1988), was created by the U.S. Naval Oceanographic Office from hand-drawn contour charts.

The finite element mesh developed for the ENPAC 1994 domain is shown in Figure 9. It contains 27,494 nodes and 52,444 elements with resolution ranging from 70 km in the open ocean to 5 km along the coast. Figure 10 shows the grid size in kilometers. This grid takes advantage of the flexibility inherent in the finite element method, which allows nodes and elements to be concentrated in areas where increased resolution is necessary. In this study, the important features along the continental shelf and U.S. west coast and Alaskan waters were highlighted with increased resolution.

The results from the ENPAC 1994 model showed a poor correlation between the model output and the data at the 91 validation stations discussed in Chapter 3. The proportional standard deviation amplitude error and absolute average phase error results are shown for five constituents, K_1 , O_1 , M_2 , S_2 , and N_2 , in Table 4.

The table shows a much higher error in the semidiurnal constituents compared to the diurnal constituents with markedly higher errors in the S_2 constituent for both the amplitude and phase error analysis. As noted in the previous chapter, the error in the model results corresponds to errors in the observed data; the highest station data errors were seen in the semidiurnal constituents off the U.S. west coast and Alaska. The error in the model, though, is much greater than that of the station data. Although the source of these errors could be from a variety of sources, the first step was to examine the location of the amphidromic points as determined from Geosat altimetry data (Cartwright and Ray 1991). Two distinct amphidromic clusters were identified within the ENPAC 1994 domain. As discussed in Chapter 1, the abundance of amphidromes and their close proximity to the open boundary off the coast of South America led to decision to limit the domain size.

Domain, Bathymetry, and Grid

The cluster of both diurnal and semidiurnal amphidromes centered on the point lat. -105° , long. 0° , off the coast of South America, were believed to be located too close to the open ocean boundary and were, therefore, causing disturbances in the boundary conditions that were being propagated throughout the domain. With the main focus of the ENPAC tidal constituent database on the U.S. west coast and Alaskan coastal waters, it was determined that the Central and South American portions of the domain could be eliminated. The revised ENPAC 1994 domain, henceforth called the ENPAC 2002 domain as shown in Figure 11, extends from Seal Cape on Unimak Island, AK, in the north to Acapulco, Mexico, in the south. The eastern land boundary includes the Pacific coastlines of Alaska, Canada, United States west coast, and Mexico. The area of the entire domain is 1.79×10^7 sq km. Although 64 percent of the original domain was removed, the U.S. west coast and Alaska coastlines remain intact.

In addition to the domain change, other improvements were incorporated into the ENPAC 2002 domain. The bathymetry was updated from the original ETOPO-5 data, used for the development of the ENPAC 1994 tidal database. Analysis of the ETOPO-5 data found that large overall errors existed due to the reliance on contour charts instead of the more exact bathymetric sounding data. A biased distribution of bathymetric contours and less variation in the data than what should be seen in the physical world are documented problems with this bathymetric database (Smith 1993). Improvements in the ETOPO-5 database were made by including a wider variety of international sounding data. ERS-1 and Geosat satellite surveys of gravity fields over most of the world's ocean areas were incorporated using a regional calibration method (Smith and Sandwell 1997). The new database was configured on a 2-arc-min grid and, therefore, called ETOPO-2 (National Geophysical Data Center 1998). The improved ETOPO-2 bathymetry was used for the ENPAC 2002 model and is shown in Figure 12.

The National Ocean Service (NOS) compiled a database of dense bathymetric soundings that were too detailed to be included in usual nautical charts and worldwide databases, such as ETOPO-2. These surveys were

considered more reliable than the global ETOPO-2 bathymetric data, but were only available in a small area of the waters covered by the ENPAC 2002 domain. The dense NOS bathymetry was incorporated into the grid using a cluster averaging approach. In this method, the cluster area includes one node and all of the elements surrounding it. All of the bathymetric sounding points in this larger cluster area are averaged together to define the bathymetry at the node. This procedure automatically filters the available bathymetric data to the existing grid scale. The extent of the NOS bathymetry soundings is shown in Figure 13. The bathymetric depths of the NOS survey data are shown superimposed on the ENPAC 2002 domain.

To demonstrate the difference between the NOS bathymetric data and the ETOPO-2 data, the fractional difference was calculated. Figure 14 shows these differences. The general differences between the two databases can be seen in this figure; the databases align closely in the deeper waters, but tend to have considerable differences near the shorelines. Because the NOS bathymetric sounding data exists on a denser scale than the ETOPO-2 bathymetric data, it was decided that the NOS bathymetry would be the primary source used in developing the ENPAC 2002 database. Where there was no available NOS bathymetric soundings data, the ETOPO-2 data was used. The composite bathymetry is shown in Figure 15.

An extensive effort was put forth to refine the ENPAC 1994 finite element grid. The initial step was to extract the coastal outline from the National Imagery and Mapping Agency (NIMA, formerly the Defense Mapping Agency (DMA)) using the Coastline Extractor program available on the World Wide Web at <http://www.ngdc.noaa.gov/mgg/shorelines/shorelines.html> (National Geophysical Data Center 2002). This agency provides the World Vector Shoreline (WVS) digital data files that contain shorelines at a nominal scale of 1:250000. At this scale, shoreline features can be determined within 500 m of their true geographic positions with respect to the World Geodetic System (WGS 84) horizontal datum (Solaria and Woodson 1990). The finite element grid developed for the ENCPAC 2002 domain was constructed to correspond to this WVS coastline.

The flexibility inherent in the finite element method makes it possible to provide increased levels of grid resolution where necessary. To ensure that all key hydrodynamic features were resolved, it was important to consider several mesh development techniques. In this report, the first criterion examined will be the wavelength to grid size ratio, which is based on linear, frictionless constant-depth wave theory (Kashiyama and Okada 1992). For a constant acceleration of gravity, g , and a given wave period, T , to maintain a constant wavelength to grid size, $\lambda/\Delta x$, ratio, Equation 9 shows that as the water depth, h , decreases, the grid size must also decrease.

$$\frac{\lambda}{\Delta x} = \frac{\sqrt{gh}}{\Delta x} T \quad (9)$$

Based on this criterion, the resulting grid will need increasing resolution over decreasing depths. Studies have demonstrated that a wavelength to grid size ratio

of at least 25 should be maintained for accurate results. However, this criterion alone is not sufficient to achieve the desired accuracy. In fact, areas of sharp bathymetric gradients, such as the continental shelf break, are under-resolved if grid development is based exclusively on the wavelength to grid size criterion (Westerink et al. 1994; Hannah and Wright 1995; Luettich and Westerink 1995; Hagen 2001; Hagen et al. 2001). To address this problem the introduction of a topographic length scale (TLS) criteria, as in Equation 10, is necessary.

$$\Delta x \leq \frac{\alpha h}{h_{,x}} \quad (10)$$

The grid size, Δx , is now determined by the water depth, h , in addition to the bathymetric gradient, $h_{,x}$. The mesh generation criterion α is designed so that α does not exceed a maximum value within the domain. The problem with the TLS criteria is that where there was little or no bathymetric change (i.e., when $h_{,x} \rightarrow 0$), the grid size is allowed to increase to infinity. To create a grid on which convergent results will be produced, both the wavelength to grid size ratio and the TLS criterion need to be considered. Grids that incorporate both of these criteria are similar to grids that are designed per the more complex local truncation error analysis (LTEA). LTEA examines the truncation error in the governing equations. Grids are designed by this process by setting a limit to the maximum allowable localized truncation error (Hagen 2001; Hagen et al. 2001).

The ENPAC 2002 model did not involve LTEA, but this level of resolution was simulated by incorporating both the wavelength to grid size and the TLS criterion. Figure 16 shows the final finite element grid. The grid consists of 290,715 nodes and 567,145 elements. Approximately 85 percent of the total number of elements lies between the toe of the continental slope and the coastal shoreline boundary demonstrating the high level of resolution needed to adequately resolve these areas of steep bathymetric gradients and shallow waters.

Figure 17 shows that the element size in kilometers ranges from 25 to 40 km in the deep ocean to less than 1 km in select coastal areas. Since the U.S. west coast was one of the focuses of this study, the highest level of resolution exists in this area with element sizes in the 1- to 2-km range.

Figure 18 shows the wavelength to grid size ratio over the domain for an M_2 tide (with a tidal period of 12.42 hr). For a depth greater than 1.0 m, the wavelength to grid size ratio ranges from 27 to 1939 above the lowest recommended wavelength to grid size ratio of 25.

The TLS criterion for the ENPAC 2002 model is shown in Figure 19. This figure shows the α -value from Equation 10 given the grid size, bathymetric depth and bathymetric gradient for each element. Throughout most of the domain, the α -values are very low. Especially in deep ocean waters, the values are well below 0.5. A band of higher α -values (from 1.0 to 1.5) can be seen along the continental slope. This indicates that more refinement would be needed over the continental slope to produce the same α -values associated with areas of small bathymetric gradient, namely the deep ocean and coastal waters. Another way to maintain a

constant α -value would be to decrease the resolution in the deep ocean and coastal waters. Although it may be possible to decrease the resolution in the deep ocean and still achieve an accurate solution, decreasing the resolution in the coastal waters was not appropriate. As previously discussed, the wavelength to grid size criterion calls for a high level of resolution in these shallow waters in order to capture the physics that are unique to this area due to nonlinearities trapped in the coastal waters by the continental shelf break. This demonstrates both the impossibility of maintaining a constant α -value over the entire domain, and the need to incorporate both the TLS and wavelength to grid size criterion when developing a finite element mesh.

Model Input Parameters

Sixty-day tidal simulations were run with the time-history computed at every node in the domain. For the last 30 days of the simulation, data were recorded every 12 min and used for the harmonic analysis. Thirty-seven frequencies and steady state were used in this process, including the main diurnal, K_1 , O_1 , P_1 , and Q_1 , and semidiurnal, M_2 , S_2 , N_2 , and K_2 . To account for nonlinear interactions between these constituents, overtones, M_4 , N_4 , M_6 and M_8 , and compound tides, MN , SO_1 , SM , MNS_2 , $2MS_2$, $2MN_2$, MSN_2 , $2SM_2$, MO_3 , SO_3/MK_3 , SK_3 , $3MS_4$, MN_4 , $3MN_4$, MS_4 , $2MSN_4$, $2NM_6$, $2MN_6$, MSN_6 , $2MS_6$, $2SM_6$, $2(MN)_8$, $3MN_8$, $2MSN_8$, and $3MS_8$ were included in the harmonic decomposition. This was necessary to ensure the accuracy of the least squares based analysis.

The time weighting factors in the GWCE at time levels $k+1$, k , and $k-1$ were 0.35, 0.3, and 0.35, respectively. In the final runs, a 6-sec time-step was used to insure stability by keeping the Courant number below 1.0 for the entire domain. Due to the large area of the domain, a spatially variable Coriolis parameter was used.

A fully nonlinear hybrid bottom friction law was incorporated. This formulation of bottom friction was similar to a Manning-type friction law where friction increases as the depth decreases. Above a given break depth (i.e., in deep ocean), the friction coefficient was constant and a quadratic bottom friction law results. Below the break depth, the friction coefficient was determined according to Equation 11:

$$C_f = C_{fmin} \left[1 + \left(\frac{H_{break}}{H} \right)^\theta \right]^{\gamma/\theta} \quad (11)$$

where C_{fmin} = minimum deepwater friction coefficient (dimensionless), H_{break} = break depth (in meters), H = the total water column depth, γ = parameter to determine how the friction factor increases as the water depth decreases (dimensionless), and θ = parameter to determine how rapidly the hybrid bottom friction relationship approaches its deepwater limits when the water depth was greater than or less than H_{break} . For the runs described in this report, $C_{fmin} = 0.003$, $H_{break} = 2.0$ m, $\gamma = 1.33333$, and $\theta = 10.0$. The lateral eddy viscosity coefficient

was set at 20 m/sec. Since tests have shown that the ideal G value is two to 10 times τ_{*s} , the bottom friction parameter, a variable G was chosen that reflects the changes in the importance of the bottom friction over the domain (Kolar et al. 1994b). When H was greater than 10 m, $G = 0.005$, and when H was less than 10 m, $G = 0.02$.

The finite amplitude terms were enabled and wetting and drying was allowed to occur. If the water level at a node dropped below the nominal water depth of 0.25 m, the element was considered dry. A minimum of 75 time-steps needed to pass before the element was allowed to wet again. The minimum velocity for wetting was 0.05 m/sec. The nonlinear advective terms were not included in the computations.

The elevation specified boundary conditions were applied using a hyperbolic tangent ramp function for the first 15 days of the model run. This ramp function increased the boundary forcings from zero to almost their full value at day 15. The hyperbolic tangent ramp function was used to alleviate the problems that occur when a model was shocked from the zero η elevation and the u and v velocity response initial conditions.

The model was forced with the amplitude and phase of four diurnal (K_1 , O_1 , P_1 , and Q_1) and four semidiurnal (M_2 , S_2 , N_2 and K_2) constituents. The amplitude and phase data for these constituents were extracted from Oregon State University's TPXO.2, TPXO.5 and TPXO.6 global ocean tidal models (Egbert et al. 1994; Egbert 1997; Egbert and Erofeeva 2002). The TPXO models use a generalized inversion (GI) method, which is basically a large linear least-squares analysis to assimilate TOPEX/Poseidon satellite data. This approach tries to minimize a quadratic penalty function that is developed from trying to find the best fit between the hydrodynamic equations and the satellite (or other) data. All of the models use an Arakawa "C" grid with elevations specified for the open boundary forcing at the lat. 80°N line. These elevations were supplied from the Schwiderski (1980) global ocean model. The TPXO.2 model used a coarse 512×256 grid (which is 78×65 km at the equator). The TPXO.5 and TPXO.6 models used a dense $1,440 \times 721$ grid. The TPXO models solved the linearized shallow-water equations by time-stepping forward from homogeneous initial conditions. The TPXO.5 and TPXO.6 models switched to solving the equations in the frequency domain, saving the time required to run the TPXO.2 model with small time-steps for a long period of time. The simpler, TPXO.2 model used linear bottom friction while the TPXO.5 and TPXO.6 models incorporated quadratic bottom friction by solving an initial problem with the nonlinear shallow-water equations. This prior solution was then used to produce a spatially varying linear bottom friction field, which was incorporated into the model for the generalized inversion. Improvements in the efficiency of the computations come with the inclusion of conjugate gradient solvers (Egbert et. al. 1994; Egbert 1997; Egbert and Erofeeva 2002).

Figure 20 shows the approximate distance, in kilometers, along the open boundary of the ENPAC 2002 grid. For reference, the shelf break begins about 75 km off the Alaskan shoreline along the open boundary. The bottom of the Aleutian trench is about 195 km off the shoreline along the open boundary.

Figures 21-28 show the amplitude and phase data, from the three different TPXO models, used to force the ENPAC 2002 model along the open boundary.

In general, the TPXO.5 and TPXO.6 models match each other closely while the TPXO.2 model shows a difference in many of the tidal constituent amplitudes. The phase output from all three models was similar. The major differences between all three of the TPXO models were apparent along the coastal waters, continental shelf break, and continental slope leading into the Aleutian trench. Some discrepancies were also seen on the narrow slope and coastal waters off the coast of Mexico. Not only do the models disagree with each other, but also the semidiurnal constituents can appear physically unrealistic in shallow coastal waters. Although the hydrodynamics incorporated in the global ocean models should be similar to those in the ADCIRC model, the ADCIRC model output to the east of the Alaskan open boundary, showed a smooth increase in the constituent amplitudes instead of the unrealistic constituent amplitudes shown in Figures 21-28. This suggests that the boundary conditions do not satisfy the governing equations. At the open boundary in the Alaskan cross shelf area, unrealistic circulation cells developed in the initial ADCIRC model runs. As the model run progressed, these cells would advect into the domain and cause the model to become unstable. To compensate for the unrealistic open boundary forcings and to eliminate the model instability, the ADCIRC model had to be run with the advective terms turned off.

The interior domain was forced with four diurnal, K_1 , O_1 , P_1 , and Q_1 , and four semidiurnal, M_2 , S_2 , N_2 , and K_2 , constituents. The Newtonian tidal potential and earth tide reduction factors were included, but the self-attraction/load tide forcings were not.

Model Results

Improvements in the amplitude and phase results were seen with the ENPAC 2002 tidal database when compared to the ENPAC 1994 tidal database. Figures 29-34 show the proportional standard deviation amplitude and absolute average phase results for the ENPAC 1994 model compared to the ENPAC 2002 model with three different open boundary forcings: TPXO.2, TPXO.5 and TPXO.6, and the field data error.

In general, significant improvements can be seen between the ENPAC 1994 and the ENPAC 2002 models, particularly in the semidiurnal constituents. It was likely that the improvements between the ENPAC 1994 and ENPAC 2002 databases were due mainly to increased grid resolution and the incorporation of more reliable bathymetric data. Additionally, the decision to remove the Central and South American part of the domain, which contained a cluster of amphidromic points, likely aided this improvement. Error levels in the semidiurnal constituents remain high in all of the ENPAC models, though.

To determine which of the ENPAC models was the best, a weighted average based on the Newtonian equilibrium tidal potential amplitude (listed in Table 1),

was computed for the overall amplitude and phase errors per Equation 12. The results from this analysis are shown in Table 5.

$$E_{weighted} = [(0.1912 * K_{1-error}) + (0.1357 * O_{1-error}) + (0.0633 * P_{1-error}) + (0.0260 * Q_{1-error}) + (0.3273 * M_{2-error}) + (0.1524 * S_{2-error}) + (0.0627 * N_{2-error}) + (0.0415 * K_{2-error})] \quad (12)$$

Table 5 shows that the lowest error is with the TPXO.5 open boundary forcing. Due to the dominance of the M_2 equilibrium tidal potential amplitude, the weighted average error was dominated by the error in that constituent. To see if the error in other constituents dominates the overall error measures, a straight average was calculated using Equation 13. The results of this analysis are also shown in Table 5.

$$E_{straight} = \left(\frac{K_{1-error} + O_{1-error} + P_{1-error} + Q_{1-error} + M_{2-error} + S_{2-error} + N_{2-error} + K_{2-error}}{8} \right) \quad (13)$$

The results from the straight average are similar; again producing not only comparable values to the weighted average analysis, but also showing the best results with the TPXO.5 open boundary forcing.

The amplitude errors (as a percent) and phase errors (in degrees) for the ENPAC 2002 model with TPXO.5 open boundary forcing are shown projected onto the ENPAC 2002 domain in Figures 35-50. The errors are represented by symbols showing the error range. Blue symbols represent underprediction by the ENPAC 2002 model and red symbols represent overprediction by the ENPAC 2002 model. A yellow star indicates that no corresponding station data, for the given constituent, was available at that station.

Examining these plots of the amplitude and phase error over the domain, it can be seen that the diurnal constituents were well predicted over the entire domain. The semidiurnal constituents, though, have consistently high levels of error along the U.S. west coast. It is likely that these errors correspond to the semidiurnal amphidromic cluster to the west of this region.

Further investigation into the source of this error led to a comparison of the ENPAC 2002 (with the TPXO.5 open boundary forcing) amplitude and phase results and OSU's TPXO.5 model results over the entire domain. The amplitude and phase results for the K_1 diurnal and M_2 and S_2 semidiurnal constituents were extracted from OSU's TPXO.5 global tidal databases onto the ENPAC 2002 finite element mesh. The fractional difference between the ENPAC 2002 and OSU's TPXO.5 results are shown in Figures 51-56.

These plots show little difference between the ENPAC 2002 and TPXO.5 global ocean model K_1 amplitude and phase results. As expected, there was some difference along the shelf region and coastal waters where global ocean models, typically, do not perform as well as they do in the deep ocean. There was a large difference between the placement of the M_2 and S_2 amphidromes by the global

models versus the placement of these amphidromes by the ENPAC 2002 model. Although the exact source of this difference is not known it should be noted that the largest error in the data is also in the semidiurnal constituents. This suggests that the amphidromes may be shifting position due to large-scale dynamic forces such as current systems or even the El Niño Southern Oscillation, which causes many changes in the Pacific Ocean over seasons, years, and decades. Although the OSU global ocean models assimilate data, which can compensate for missing physics not included in the model, this does not eliminate all sources of error. There are several reasons why both models may lack the physics to correctly model this ocean system. Neither the OSU models nor the ADCIRC model incorporate baroclinic effects, or other 3-D effects. Additionally, the ADCIRC model does not include the load and self-attraction tide. None of the models, but particularly the global ocean models, have the high level of resolution needed to include the vast number of bays, estuaries, and rivers (especially in the southern Alaskan and Canadian waters) which are a major dissipative mechanism for this domain given the narrow shelf. Finally, none of the processes believed to be causing the shift in the amphidromes' locations, are included in any of the models.

To see if the placement (or possibly misplacement) of the semidiurnal amphidromic points in the ENPAC 2002 domain was the major source of the remaining tidal constituent database errors, additional restrictions in the domain were made.

5 ENPAC 2003 Model Development

The ENPAC 2003 model development began with a change in domain to eliminate the semidiurnal amphidromic points off the U.S. west coast. The bathymetry and grid resolution remained the same as that in the ENPAC 2002 model. The final results showed a great improvement over the original ENPAC 1994 model and the ENPAC 2002 model.

Domain Definition

The ADCIRC model physics with open boundary conditions extracted from the OSU TPXO global ocean models was not placing the semidiurnal amphidromes in the correct locations. To eliminate this problem, changes were made in the ENPAC 2002 domain in order to avoid this cluster of amphidromes off the west coast of the United States. This new domain will henceforth be called the ENPAC 2003 domain. This smaller domain extends from Seal Cape on Unimak Island, AK, in the north to Chamela, Mexico, in the south. The eastern land boundary includes the Pacific coastlines of Alaska, Canada, United States west coast, and some of Mexico. The area of the entire domain is 7.57×10^6 sq km. Although 42 percent of the ENPAC 2002 domain was removed, the U.S. west coast and Alaska coastlines remained intact. The bathymetry remained the same as that of the ENPAC 2002 model domain, as a combination of NOS and ETOPO-2 bathymetric data. Figure 57 shows this bathymetry and demonstrates how the open boundary of this new domain remains in the deep ocean off the continental shelf break where accurate boundary conditions can be extracted from global ocean models.

Although a sizeable portion of the ENPAC 2002 model area was removed to create the ENPAC 2003 model domain, nearly 94 percent of the elements were retained in the finite element grid. This is due to the fact that the highest concentration of elements exists along the coastal areas - the areas that were retained in the finite element grid of the ENPAC 2003 model domain. Figure 58 shows the finite element grid representing the ENPAC 2003 model domain. This finite element mesh contains 531,680 elements and 272,913 nodes.

Model Results

Figures 59-64 show the proportional standard deviation amplitude and absolute average phase results for the ENPAC 2003 model with three different open boundary forcings, TPXO.2, TPXO.5 and TPXO.6, and the field data error. Significant improvements in the semidiurnal constituents, as compared to the previous ENPAC 2002 version, are noticeable.

To determine which open boundary forcing produced the best ENPAC 2003 model, a weighted average, based on the Newtonian equilibrium tidal potential amplitude (listed in Table 1), was computed for the overall amplitude and phase errors. The results from this analysis are shown in Table 6. This table shows that the lowest error is found with the TPXO.5 open boundary forcing. Due to the dominance of the M2 equilibrium tidal potential amplitude, the weighted average error was dominated by the error in that constituent. To see if the error in other constituents dominates the overall error measures, a straight average was calculated and the results are also shown in Table 6. The results from the straight average were similar, again producing not only comparable values to the weighted average analysis, but also showing the TPXO.5 open boundary forcing to produce the best results.

The amplitude errors as percent and phase errors in degrees for the ENPAC 2003 model with TPXO.5 open boundary forcing are shown projected onto the ENPAC 2003 domain in Figures 65-80. The errors are represented by symbols showing the error range. Blue symbols represent underprediction by the ENPAC 2003 model and red symbols represent overprediction by the ENPAC 2003 model. A yellow star indicates that no corresponding station data, for the given constituent, was available at that station.

The ENPAC 2003 model accurately predicts the tidal constituent amplitude and phase components throughout the domain. The largest improvements over the ENPAC 2002 model can be seen along the U.S. west coast in the semidiurnal constituents. This clearly demonstrates the advantage of eliminating the semidiurnal amphidromes from the ENPAC 2003 domain. Still, the exact physics behind this observation are obscure. It is interesting to note that the ADCIRC models of the Western North Atlantic Tidal (WNAT) did not have as much trouble correctly placing the amphidromes as did the ADCIRC model for the ENPAC 2002 domain (Mukai et al. 2001). One of the differences between these domains is the width of the continental shelf. The eastern North Pacific physical domain has a narrow shelf and many complex bays, estuaries and rivers, particularly in the Canadian and lower Alaskan waters, while the western North Atlantic physical domain has a much wider shelf with fewer bays and estuaries. The wide continental shelf, which was sufficiently resolved in the WNAT models, provides much more natural dissipation than the narrow shelf in the ENPAC 2002 model. The bays and estuaries, where much of the natural dissipation will occur, are under-resolved in the ENAPC 2002 model; but whatever the physical reason behind the problems in the ENPAC domain, eliminating the sensitive amphidromes from the model domain and forcing the open boundary with reasonably accurate deepwater values, has eliminated much of the error seen in the ENPAC 2002 results.

The harmonically analyzed amplitude and phase results from the ENPAC 2003 model with the TPXO.5 open boundary forcing were compared to 91 pelagic pressure and coastal tidal station gauges. Figures 81-171 show the amplitude and phase results from the model run compared to the station data. The results for the K_1 , O_1 , P_1 , Q_1 , M_2 , S_2 , N_2 , and K_2 constituents are shown when the corresponding station data are available. The legend indicates which shapes represent which constituents. The solid line, at a 45-deg angle, indicates a one-to-one correspondence between the model results and the station data. Ideally, all of the tidal constituents would fall on this line. Overprediction by the ENPAC 2003 model is seen when the results are shown in the triangular region above the solid line. Underprediction is noted when the results are shown in the triangular region below the solid line. Error bands are also shown. In the amplitude error plots, the dashed lines indicate a 5 percent difference between the model results and the station data. The dashed-dot lines indicate a 10 percent difference between the model results and the station data. In the phase error plots, the dashed lines indicate a 10-deg difference and the dashed-dot lines indicate a 20-deg difference between the model results and the station data.

Cotidal and cophase plots for the four diurnal (K_1 , O_1 , P_1 , and Q_1 ,) and four semidiurnal (M_2 , S_2 , N_2 , and K_2) constituents based on the ENPAC 2003 model with the TPXO.5 open boundary forcing are shown in Figures 172-187. The diurnal cotidal plots show a smooth gradation of increasing amplitude from the south-west to north-east with extreme values in the Vancouver Island and Cook Inlet areas. The semidiurnal cotidal charts demonstrate similar amplitude properties, with increasing amplitude along the same direction. The semidiurnal constituents show the nearness of amphidromic points along the open boundary off the west coast of the United States with areas of extremely low amplitude and converging phase lines. Additionally, a degenerate amphidrome appears in the northern portion of the Gulf of California. The diurnal cophase charts show an increase in the phase values from the southeast to the northwest. The semidiurnal cophase charts show a similar increase with a concentrated area of phase lines converging at an assumed amphidromic point near the boundary off the U.S. west coast. This is particularly evident in the K_2 and S_2 constituents, which show some unphysical anomalies near the amphidrome locations.

6 Discussion and Conclusions

The ENPAC 2003 model with the TPXO.5 open boundary forcing provides accurate tidal amplitude and phase data for the ENPAC 2003 domain. The overall proportional standard deviation amplitude errors for the tidal constituents, as compared to pelagic pressure and coastal tide gauge data, ranges from 0.0546 in the O_1 constituent (or approximately 5 percent) to 0.1098 in the K_2 constituent (or approximately 10 percent). The overall absolute average phase error, as compared to the station data, ranges from 3.19 deg in the K_1 constituent to 7.60 deg in the K_2 constituent. In comparison, the overall proportional standard deviation amplitude error for the recorded station data ranges from 0.0231 in the O_1 constituent (or approximately 2 percent) to 0.1205 in the N_2 constituent (or approximately 12 percent). The overall absolute average phase error for the recorded station data ranges from 2.27 deg in the O_1 constituent to 6.40 deg in the N_2 constituent.

The high level of accuracy of this model, as compared to early ENPAC 1994 and ENPAC 2002 versions, is due to several factors including improved bathymetry, increased grid resolution, and appropriate domain definition.

Improvements in the bathymetry began with updates from the ETOPO-5 to the more refined ETOPO-2 database. Then, dense bathymetric sounding data from NOS was used in areas along the U.S. west coast and Alaska, where that data was available. The grid resolution was increased as the element sizes decreased, from the original 70 km in the deep ocean and 5 km along the U.S. west coast in the ENPAC 1994 model to approximately 25 km in the deep ocean down to a 1- to 2-km element size along the U.S. west coast in the ENPAC 2002 and ENPAC 2003 models.

Vast areas of the original ENPAC 1994 domain were eliminated to avoid amphidromic clusters off the coast of Central America and produce the ENPAC 2002 model domain. Additional areas of the ENPAC 2002 domain were eliminated to avoid the amphidromic clusters off the U.S. west coast. The final ENPAC 2003 domain is a band that parallels the coastline from Unimak Island, AK, to Chamela, Mexico, eliminating the remaining amphidromes in the ENPAC 2002 domain.

Although the errors in the ENPAC 2003 model results are low, they are still, in some cases, greater than the data error, thus indicating that additional

improvements may be possible. Future work on this project could incorporate improvements in three categories: bathymetry, grid resolution, and physics.

The comparison between the NOS and ETOPO-2 data showed a significant difference between these two sources of data, especially in the shallow coastal waters. Since the ETOPO-2 data are not as dense as the NOS sounding data, it is not possible for the ETOPO-2 to capture the small-scale bathymetric differences in these shallow waters. Future work should incorporate high-density bathymetric data, like the NOS data, in more areas of the domain. The final ENPAC 2003 domain particularly lacks this level of bathymetric resolution along the Mexican and Canadian coasts.

Another important issue is the grid resolution. Little dissipation is inherent in the deepwater areas, and due to the narrow continental shelf in this domain, little dissipation is inherent on the shelf. Instead, much of the dissipation may occur in the bays, estuaries, and rivers that exist all along the coast, but in a particularly high density in the Canadian and lower Alaskan waters. Adding the shallow channels and estuaries into the domain and continuing to further refine those that exist, is key to providing the appropriate physical dissipation. This, in turn, should lead to even more accurate results throughout the domain, but particularly in the Canada and Alaska subregions.

Better understanding the physics that govern this system is important to further improvement in this model. As seen in the ENPAC 1994 and ENPAC 2002 models, the ADCIRC model had many difficulties placing the amphidromes in the appropriate places. Part of this problem could be from inaccurate open boundary forcing conditions. Although global models that assimilate satellite altimetry data are, in some ways, compensating for the missing physics, this does not produce an error-free solution. No model can incorporate all of the physics, which govern ocean hydrodynamics. Specifically, neither the ADCIRC nor the global models incorporate major current systems, baroclinic effects or any 3-D effects. The global ocean models have a relatively coarse resolution along the coasts (especially when compared to the ENPAC 2003 model) and do not include the bays, estuaries, and rivers that are important in providing dissipation for this domain. The propagation of errors into the ENPAC 2002 domain from the boundary (when this model was run with the advective terms turned on) is a testimony to this. While the boundary conditions may be propagating inaccurate information into the domain, the ADCIRC model itself, is lacking the physics previously mentioned as well as the load and self-attraction tide. It was shown that the ADCIRC model did not project the amphidromes into the same location as the OSU TPXO.5 model, but lack of the load and self-attraction tide may not be the only reason behind this error. While it was assumed that the global ocean models placed the amphidromes in their correct locations, the complications of changing current patterns or events as the El Niño Southern Oscillation, which causes many changes in many Pacific Ocean parameters such as surface-water level and water temperature, allow the possibility that the global ocean models may also be wrong. The possibility of shifting amphidromes can be supported by the examination of the station data errors. The station data showed particularly high errors in the semidiurnal constituents off the U.S. west coast indicating possible changes in the location of these troublesome amphidromes. The questions of domain definition, amphidrome locations, and the physics

incorporated into the ADCIRC and global ocean models is a complicated issue which will require more in-depth study.

Although improvements can be made in the ENPAC 2003 model, the results produced were in the desired output range of less than 10 percent amplitude error and less than 10-deg phase error. The error levels in the field data were highest in the U.S. west coast and Alaska regions, approaching (and in the case of the N_2 and S_2 amplitude errors off the U.S. west coast, exceeding) the error of the ENPAC 2003 model. This high level of field data error seems to indicate the advent of shifting amphidrome locations and demonstrates the need for up-to-date station records to be used in the validation process. While the field data error was much lower than the ENPAC 2003 model error in the Canadian and deep-ocean stations, overall, the field data errors were similar to the error levels in the ENPAC 2003 model. This indicates that this model is approaching a point, and in some constituents is at the point, where validating the accuracy of the model is constrained by the error in the field data. While further improvements could be achieved in the ENPAC 2003 model by incorporating more accurate bathymetry, increasing grid resolution and incorporating the complicated physics that govern such complex processes as shifting amphidromes, the ENPAC 2003 model has produced results with an acceptable error level. The final results of this model will be provided as the ENPAC 2003 tidal constituent database for users to extract elevation and velocity information for the eight major tidal constituents (K_1 , O_1 , P_1 , Q_1 , M_2 , S_2 , N_2 , and K_2) at any location within the domain.

References

- Blain, C. A., Westerink, J. J., and Luetlich, R. A. (1994). "The influence of domain size on the response characteristics of a hurricane storm surge model," *Journal of Geophysical Research* 99(C9), 18,467-18,479.
- Cartwright, D. E., and Ray, R. D. (1991). "Energetics of global ocean tides from geosataltimetry," *Journal of Geophysical Research* 96(C9), 16,897-16-912.
- Eble, M. C., and Gonzalez, F. I. (1991). "Deep-ocean bottom pressure measurements in the northeast Pacific Ocean," *Journal of Atmospheric and Oceanic Technology* 8(2), 221-33.
- Egbert, G. A., Bennett, M. Foreman, M. G. G. (1994). "TOPEX/Poseidon tides estimated using a global inverse model," *Journal of Geophysical Research* 99(C12), 24,821-24,852.
- Egbert, G. A. (1997). "Tidal data inversion: Interpolation and inference," *Progress in Oceanography* 40, 53-80.
- Egbert, G. A., and Erofeeva, S. Y. (2002). "Efficient inverse modeling of barotropic ocean tides," *Journal of Atmospheric and Ocean Technology* 19, 183-204.
- Flather, R. A. (1988). "A numerical model investigation of tides and diurnal-period continental shelf waves along Vancouver Island," *Journal of Physical Oceanography* 18, 115-139.
- Foreman, M. G. G. (1986). "An accurate analysis of boundary conditions for the forced shallow water equations," *Journal of Computational Physics* 64, 334-367.
- Hagen, S. C. (2001). "Estimation of the truncation error for the linearized, shallow water momentum equations," *Engineering with Computers* 17, 354-362.
- Hagen, S.C., Westerink, J. J., Kolar, R. L., and Horstmann, O. (2001). "Two-dimensional, unstructured mesh generation for tidal models," *International Journal of Numerical Methods Fluids* 35, 669-86.

- Hannah, C.G., and Wright, D. G. (1995). "Depth dependent analytical and numerical solutions for wind-driven flow in the coastal ocean," *Quantitative skill assessment for coastal ocean models*. D. R. Lynch and A. M. Davies (ed.), *American Geophysical Union* 47, 125-152.
- Hendershott, M. C. (1981). "Long waves and ocean tides," *Evolution of physical oceanography*. B. A. Warren and C. Wunsch (ed.), MIT Press, Cambridge, MA.
- Kashiyama, K., and Okada, T. (1992). "Automatic mesh generation method for shallow water flow analysis," *International Journal of Numerical Methods Fluids* 15, 1037-57.
- Kinmark, I. (1986). *The shallow water wave equations: Formulation, analysis and application*. Springer-Verlag Berlin, Heidelberg.
- Kolar, R. L., Westerink, J. J., Cantekin, M. E., and Blain, C. A. (1994a). "Aspects of nonlinear simulations using shallow water models based on the wave continuity equation," *Computers and Fluids* 23(3), 523-38.
- Kolar, R. L., Gray, W. G., Westerink, J. J., and Luettich, R.A. (1994b). "Shallow water modeling in spherical coordinates: Equations formulation, numerical implementation and application," *Journal of Hydraulic Research* 32(1), 3-24.
- Kolar, R. L., Gray, W. G., and Westerink, J. J. (1996). "Boundary conditions in shallow water models – an alternative implementation for finite element codes," *International Journal of Numerical Methods Fluids* 22, 603-18.
- Kolar, R. L., and Westerink, J. J. (2000). "A look back at 20 years of GWC-based shallow water models," *Computational methods in water resources* XIII, L. R. Bently et al. (ed.), Balkema, Rotterdam, 899-906.
- Luettich, R. A., Westerink, J. J., and Scheffner, N.W. (1992). "ADCIRC: An advanced three-dimensional circulation model of shelves, coasts, and estuaries, Report 1: Theory and methodology of ADCIRC-2DDI and ADCIRC-3DL," Dredging Research Program Technical Report DRP-92-6, U.S. Army Engineer Research and Development Center, Vicksburg, MS.
- Luettich, R. A., and Westerink, J. J. (1995). "Continental shelf scale convergence studies with a barotropic tidal model," *Coastal and Estuarine Studies* 47, 349-71.
- Luettich, R.A., and Westerink, J. J. (2003). "Theory report: Formulation and numerical implementation of the 2D/3D ADCIRC finite element model version 43.XX," http://www.marine.unc.edu/C_CATS/adcirc/adcirc.htm (3 March 2003).
- Lynch, D. R., and Gray, W. G. (1979) "A wave equation model for finite element tidal computations," *Computers and Fluids* 7, 207-28.

- Lynch, D. R. (1983). "Progress in hydrodynamic modeling, review of U.S. contributions," *Reviews of Geophysics and Space Physics* 21(3), 741-54.
- Mukai, A. M., Westerink, J. J., and Luettich, R. A. (2001). "Guidelines for using the Eastcoast 2001 database of tidal constituents within the Western North Atlantic Ocean, Gulf of Mexico and Caribbean Sea," Coastal and Hydraulics Technical Note CERD/CHL CHTEN-IV-40, U.S. Army Engineer Research and Development Center, Vicksburg, MS.
- National Geophysical Data Center. (1988). "ETOPO-5 bathymetry/topography data," Data Announcement 88-MGG-02, National Oceanic and Atmospheric Administration, U.S. Department of Commerce, Boulder, CO.
- National Geophysical Data Center. (1998). "GEODAS CD-ROM hydrographic survey data, Data Announcement 98-MGG-03, National Oceanic and Atmospheric Administration, U.S. Department of Commerce, Boulder, CO.
- National Geophysical Data Center. (2002). "Coastline extractor," <http://www.ngdc.noaa.gov/mgg/shorelines/shorelines.html> (25 January 2002).
- Reid, R. O. (1990). "Water level changes," *Handbook of coastal and ocean engineering*. J. Herbich, (ed.), Gulf Publishing, Houston TX.
- Schwiderski, E. W. (1980). "Ocean tides II. A hydrodynamic interpolation model," *Marine Geodesy* 3, 219-55.
- Smith, W. H. F. (1993). "On the accuracy of digital bathymetric data," *Journal Geophysical Research* 98(B6), 9591-603.
- Smith, W. H. F., and Sandwell, D.T. (1997). "Global sea floor topography from satellite altimetry and ship depth soundings," *Science* 277, 1956-1962.
- Solaria, E. A., and Woodson, V. A. (1990). "World vector shoreline," *International Hydrographic Review* LCVII(1).
- Wahr, J. M. (1981). "Body tides on an elliptical rotation, elastic and oceanless earth," *Geophys. J. R. Astr. Soc.* 64, 677-703.
- Westerink, J. J., and Gray, W. G. (1991). "Progress in surface water modeling," *Reviews of Geophysics Supplement*, 210-217.
- Westerink, J. J., Luettich, R. A., Muccino, J. C. (1994). "Modeling tides in the western North Atlantic using unstructured graded grids," *Tellus* 46A, 178-199.
- Westerink, J. J., Luettich, R. A., and Kolar, R. L. (1996). "Advances in finite element modeling of coastal ocean hydrodynamics," *Computational methods in water research* XI. A. A. Aldama et al. (ed.), 2,313-2,322.

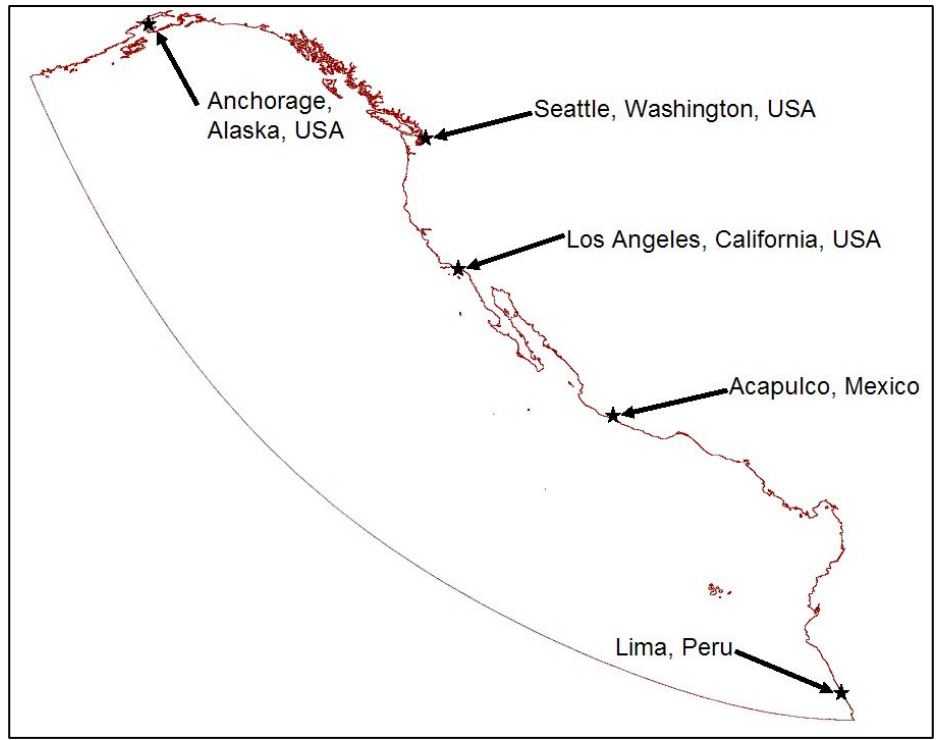


Figure 1. ENPAC 1994 domain

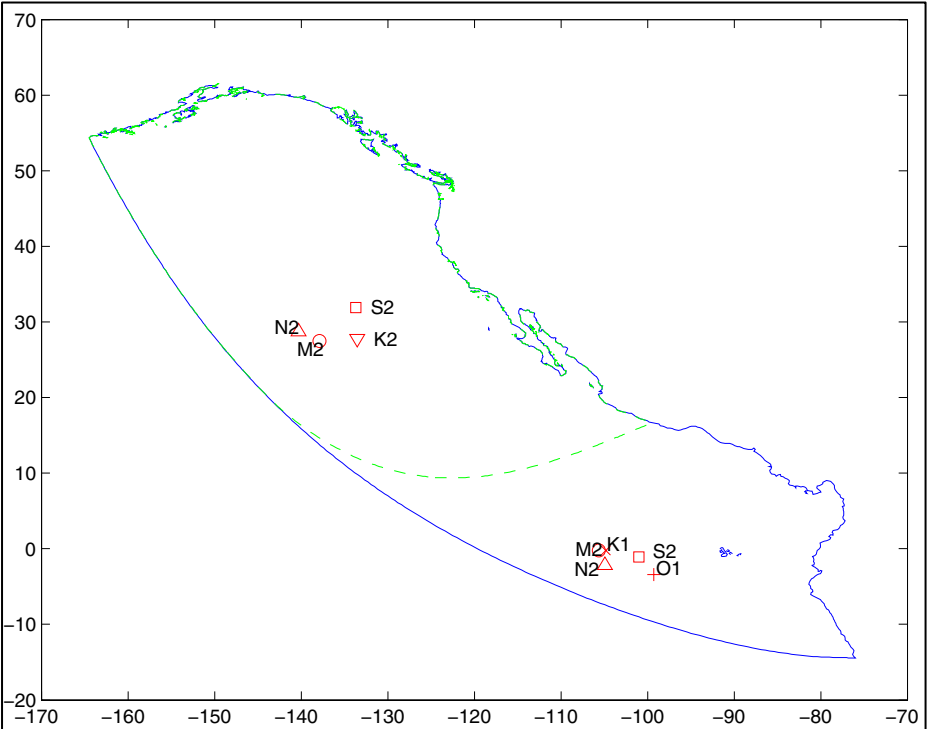


Figure 2. Approximate location of amphidromes within ENPAC 1994 (solid line) boundary and ENPAC 2022 (dashed line) boundary

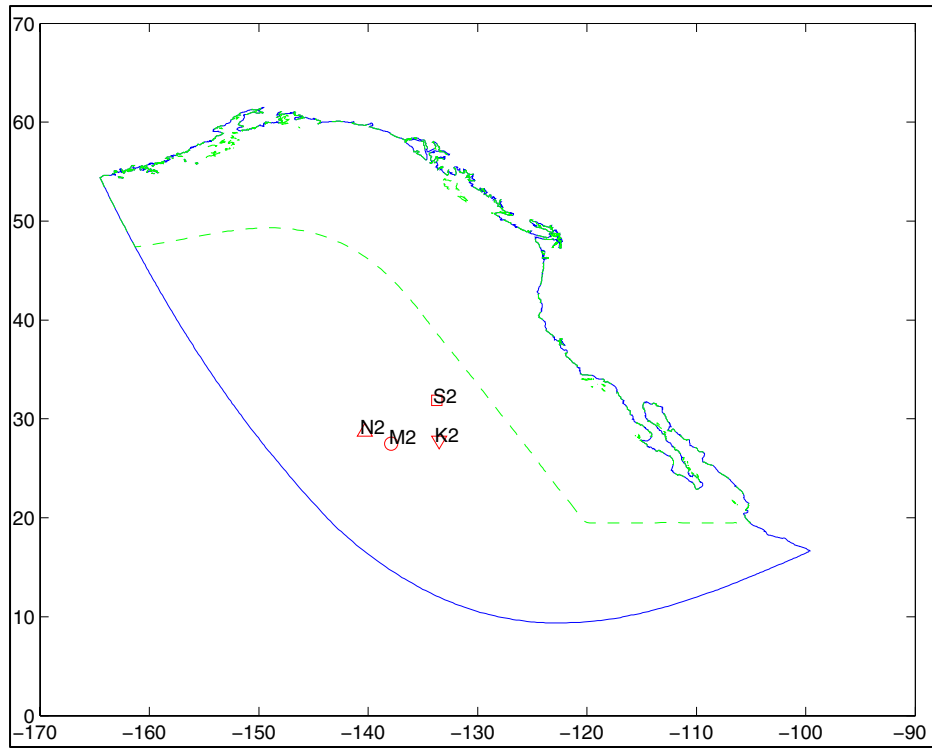


Figure 3. Approximate location of amphidromes within ENPAC 2002 (solid blue line) domain and ENPAC 2003 (dashed line) domain

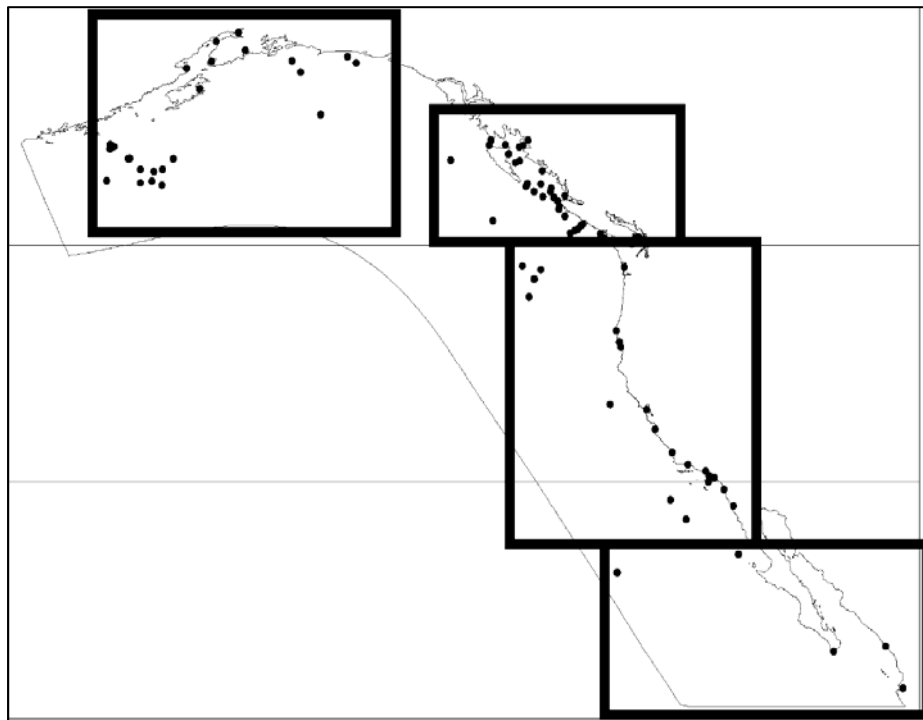


Figure 4. Location of 91 pelagic pressure and coastal tide gauge stations used for model validation

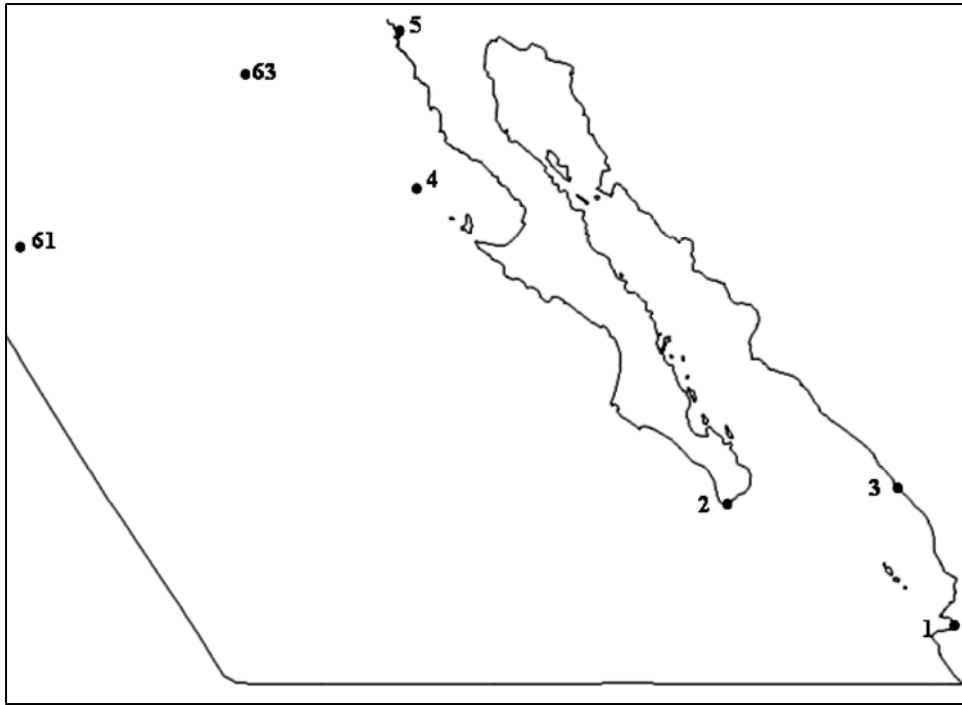


Figure 5. Location of stations in Mexico region of ENPAC 2003 domain

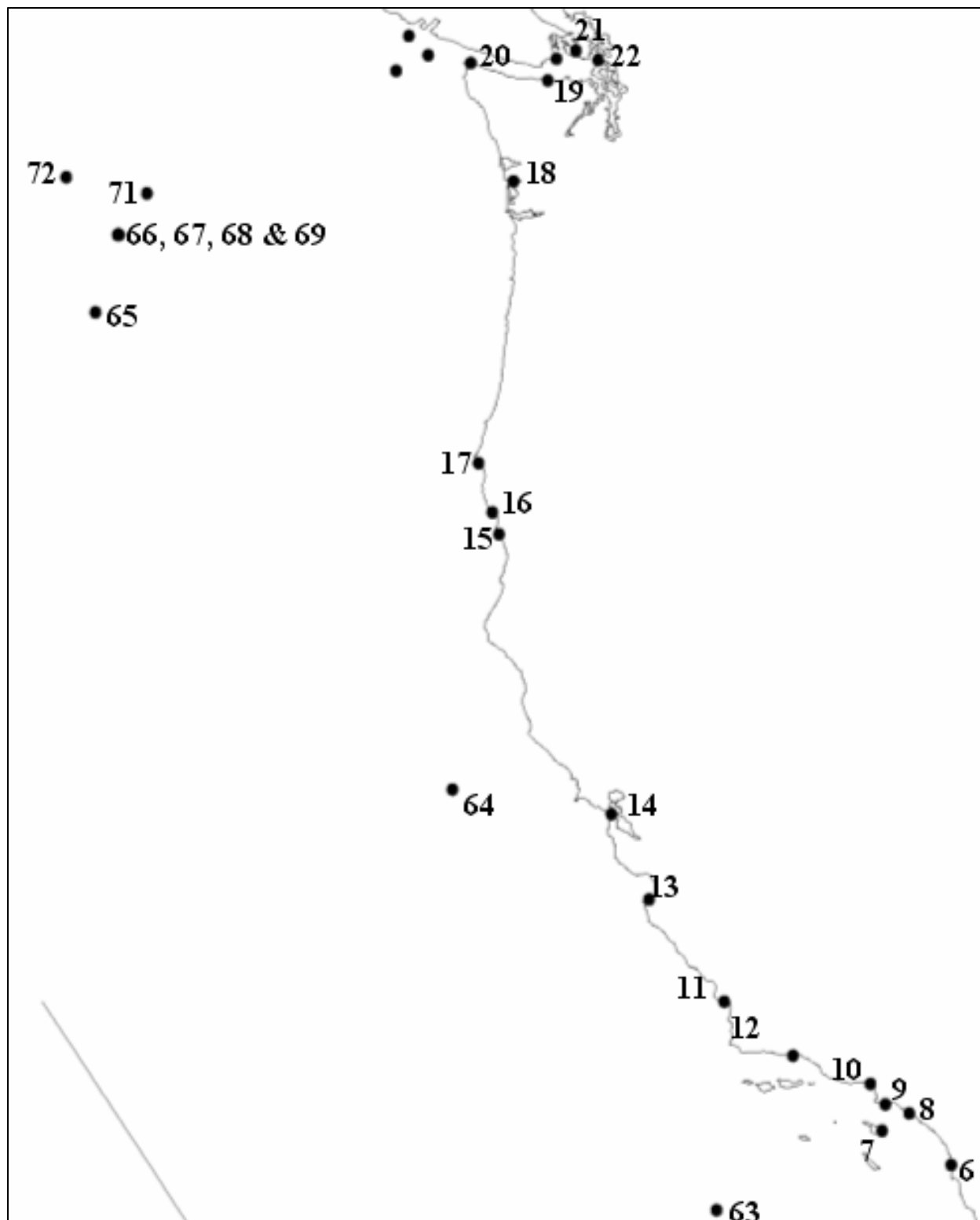


Figure 6. Location of stations in U.S. west coast of ENPAC 2003 domain

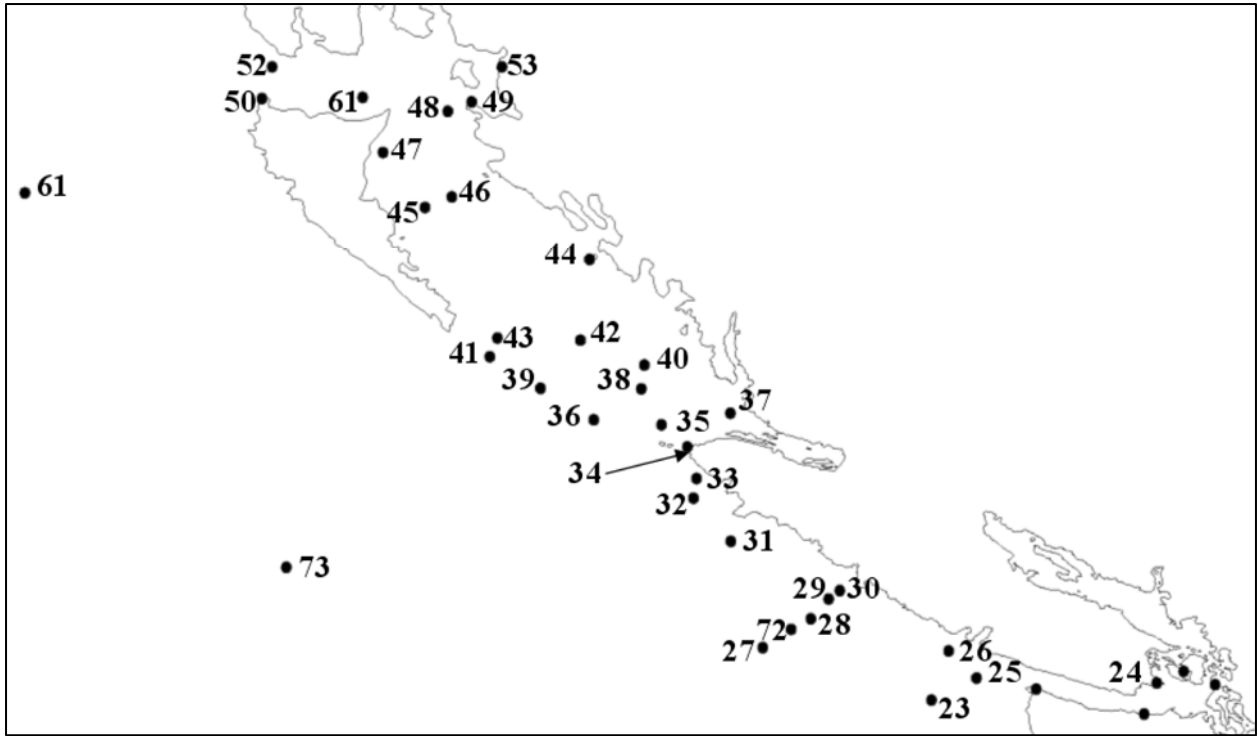


Figure 7. Location of stations in Canada region of ENPAC 2003 domain

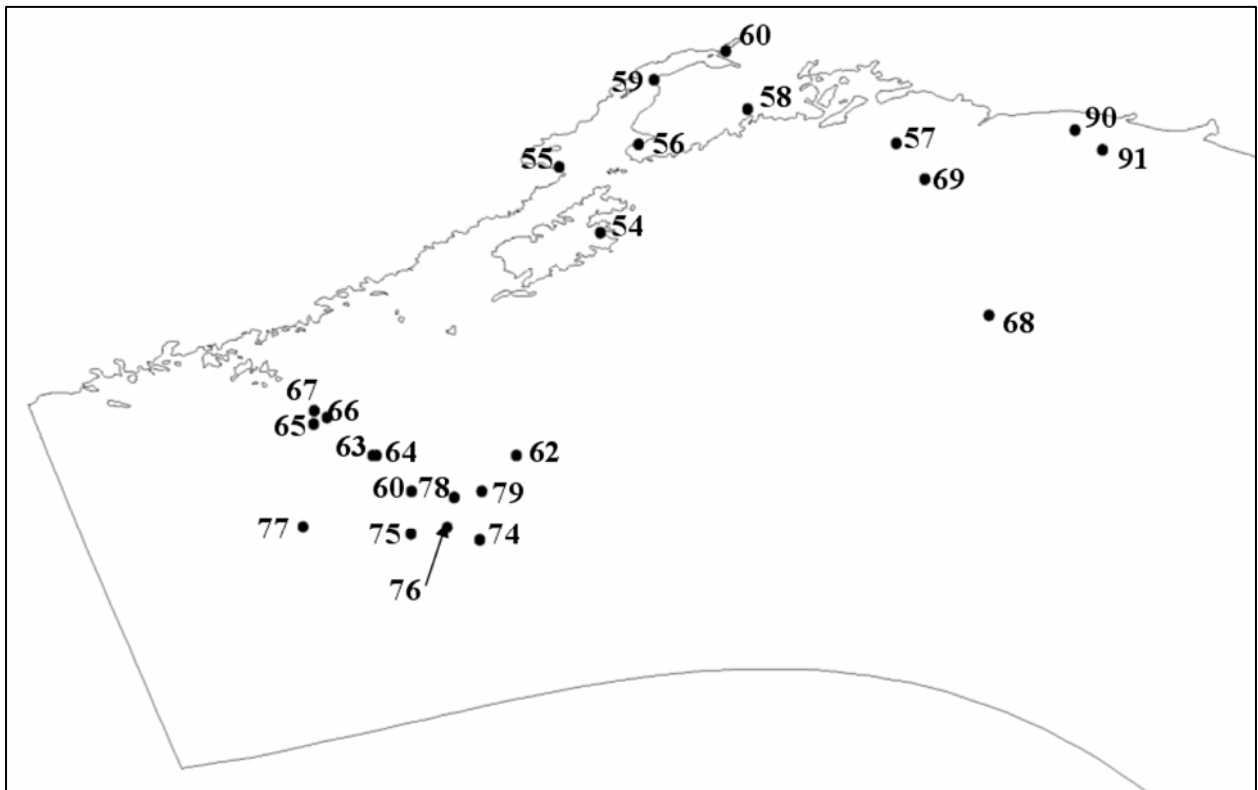


Figure 8. Location of stations in Alaska region of ENPAC 2003 domain

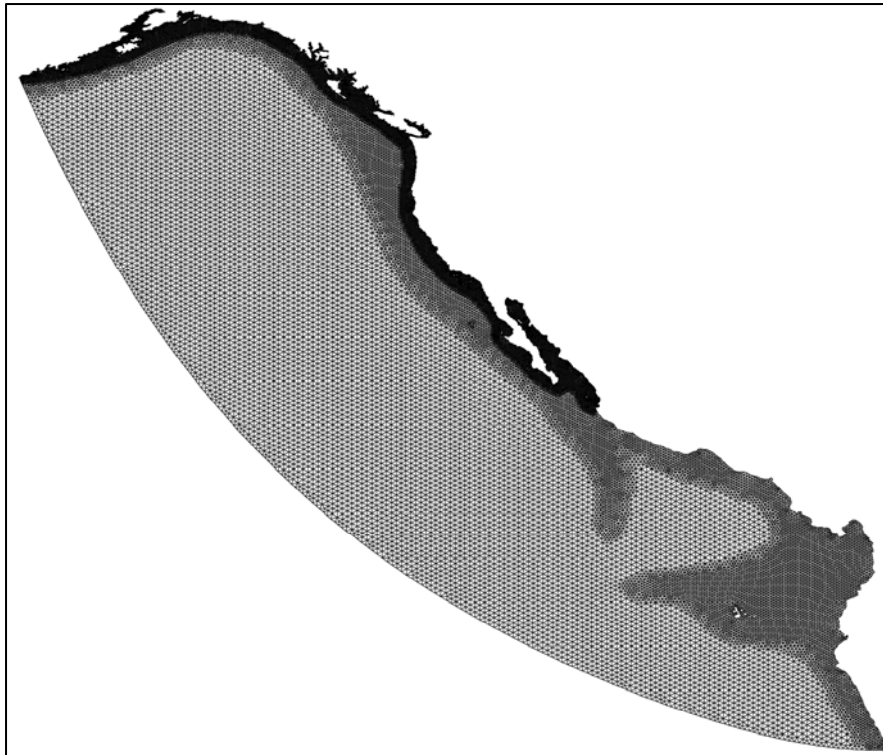


Figure 9. ENPAC 1994 finite element grid

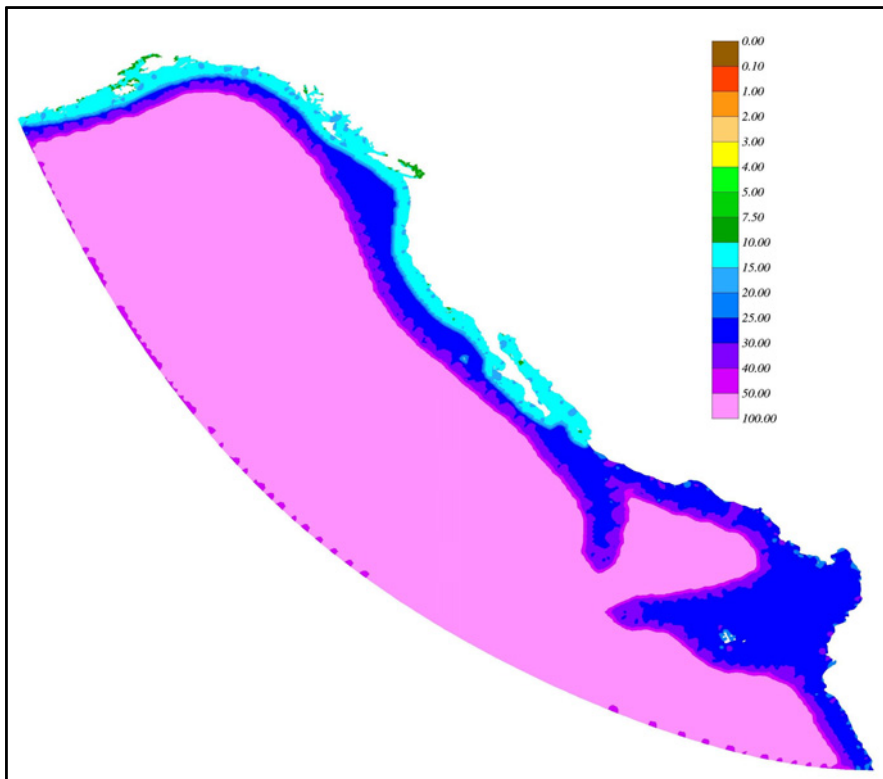


Figure 10. ENPAC 1994 grid size (kilometers)

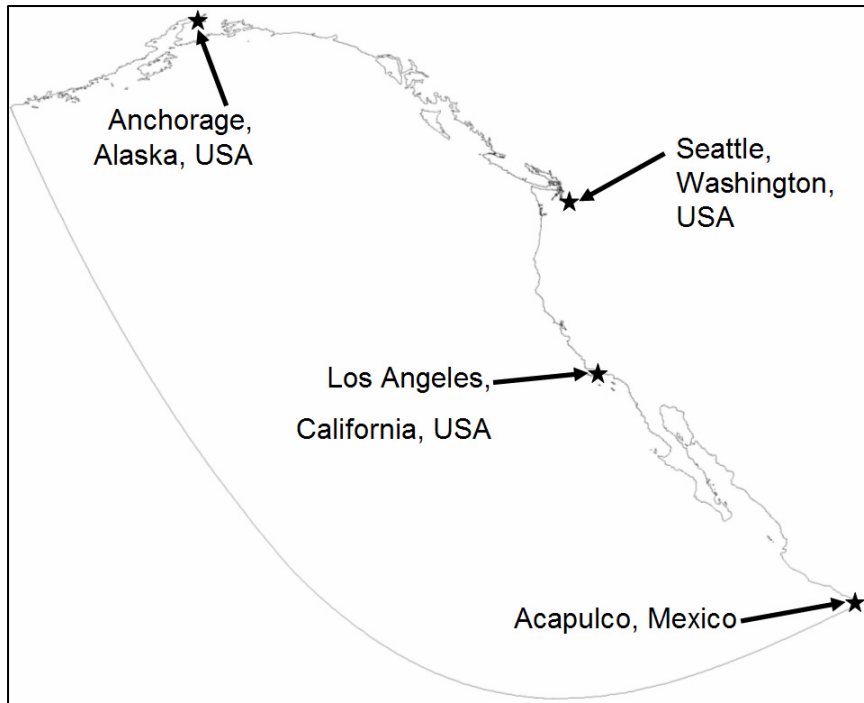


Figure 11. ENPAC 2002 domain

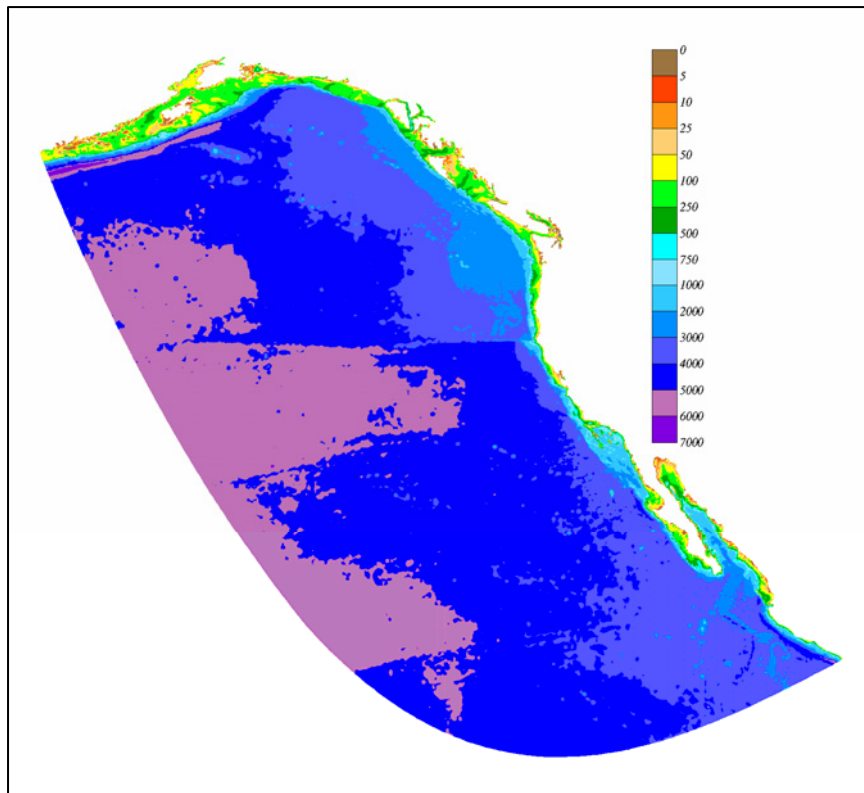


Figure 12. ENPAC 2002 ETOPO-2 bathymetric data values (meters)

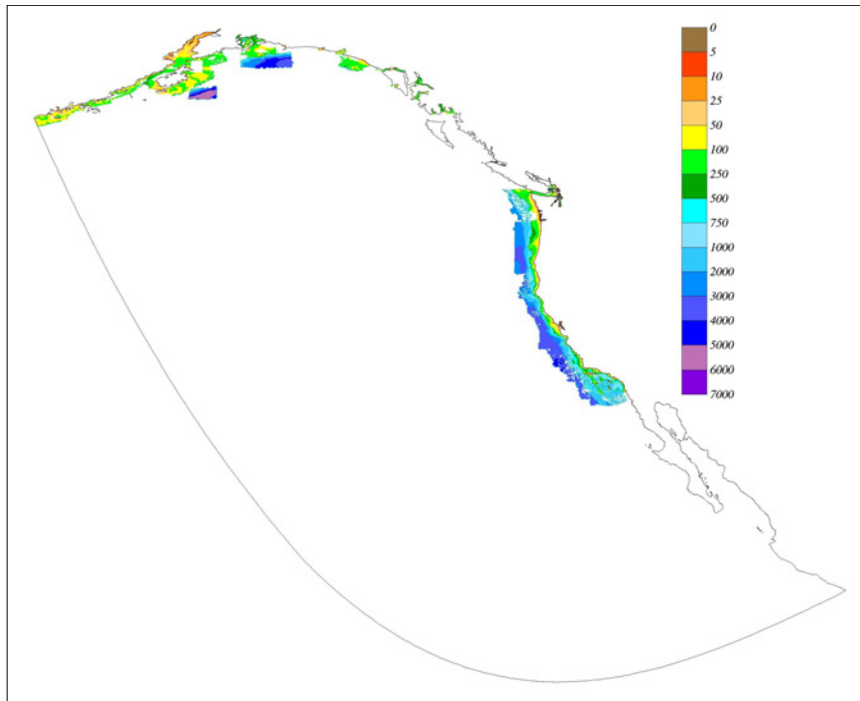


Figure 13. NOS bathymetric data values (meters) superimposed on ENAPC 2002 domain

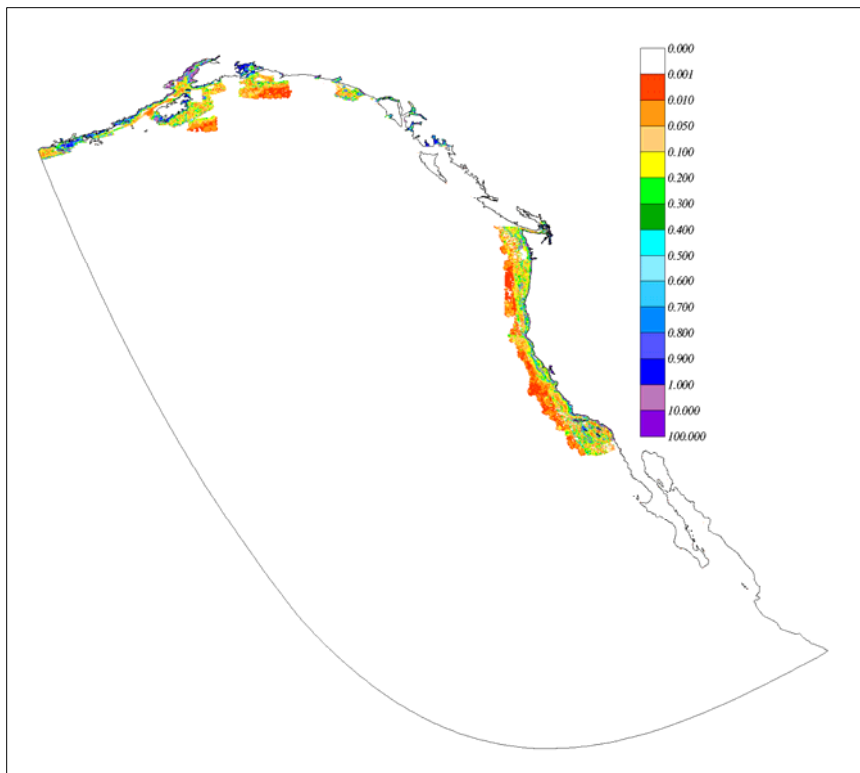


Figure 14. Fraction difference between ETOPO-2 and NOS bathymetric data superimposed on ENAPC 2002 domain (for percent, multiply by 100)

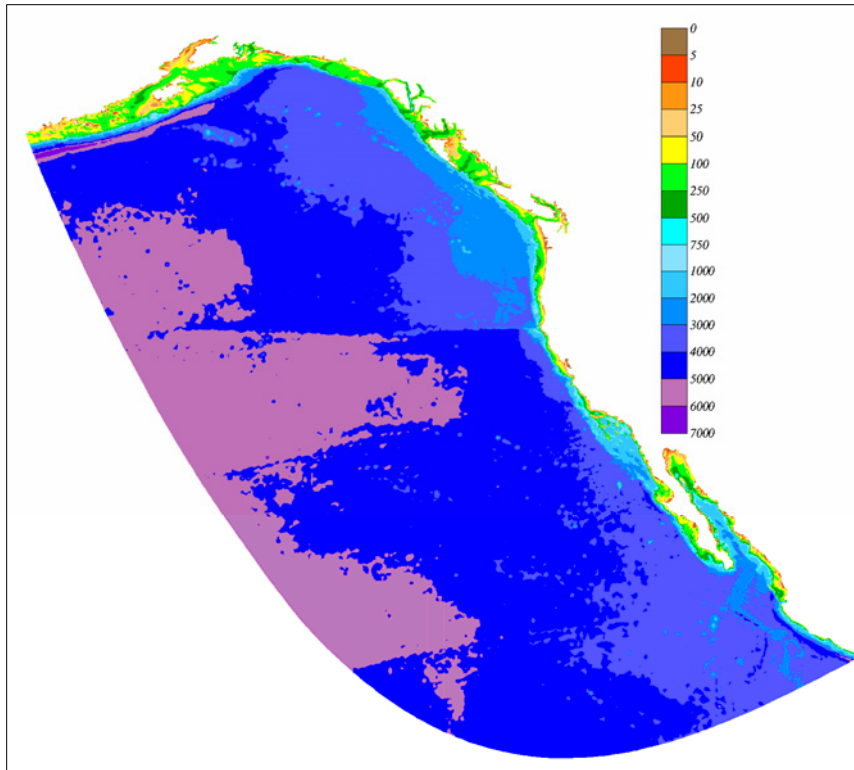


Figure 15. ENPAC 2002 composite bathymetry (meters)

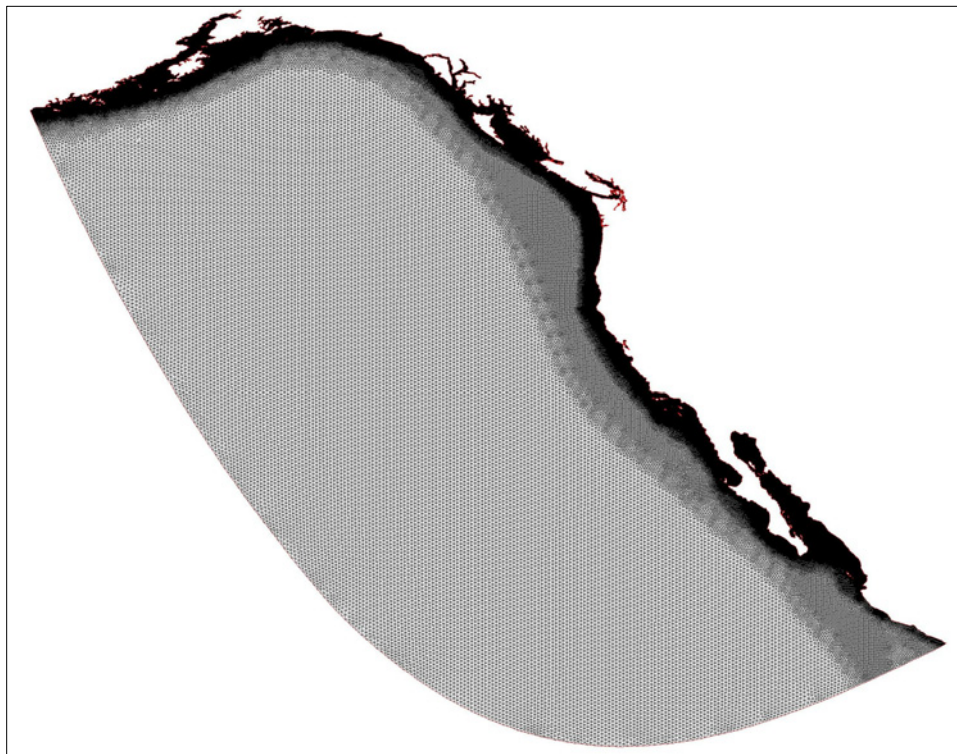


Figure 16. ENPAC 2002 finite element grid

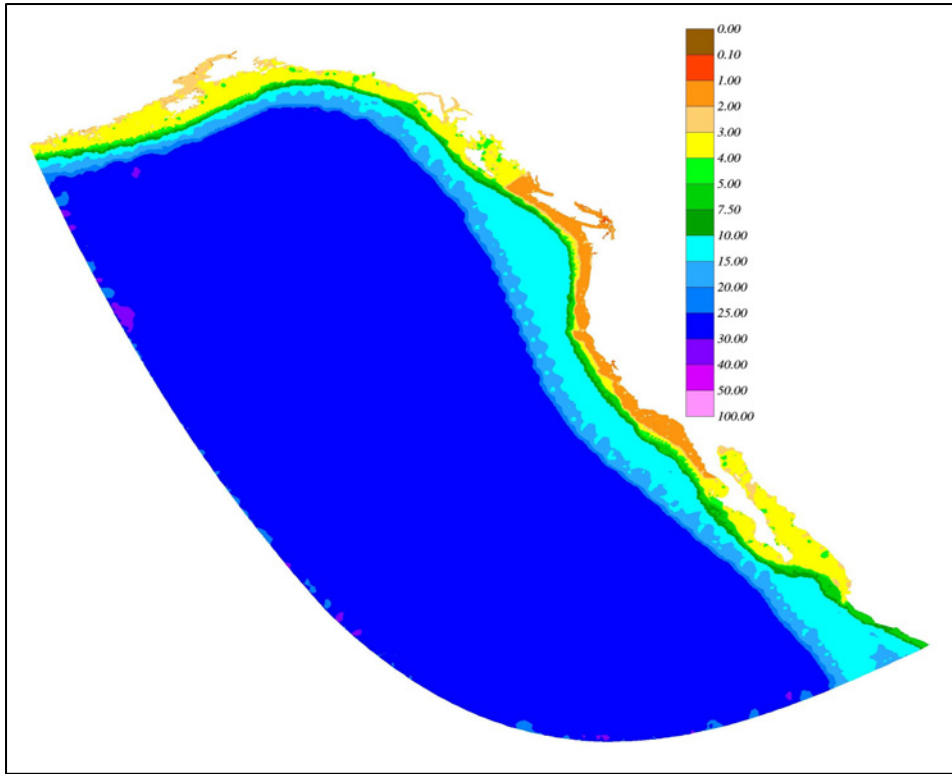


Figure 17. ENPAC 2002 grid size (kilometers)

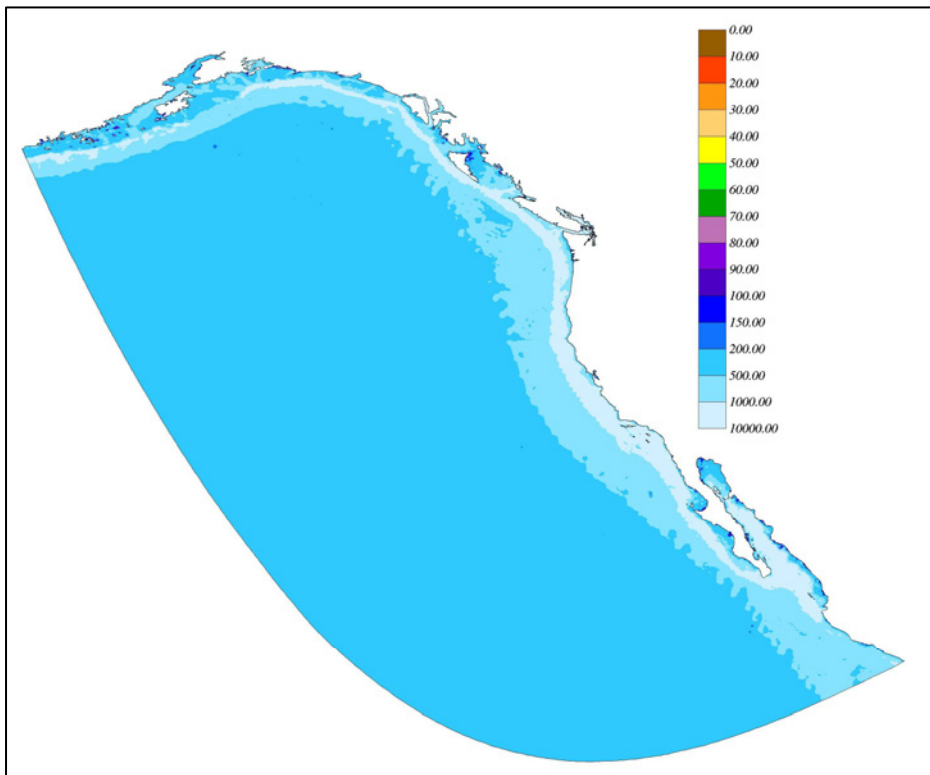


Figure 18. ENPAC 2002 wavelength to grid size ratio based on an M_2 tidal period

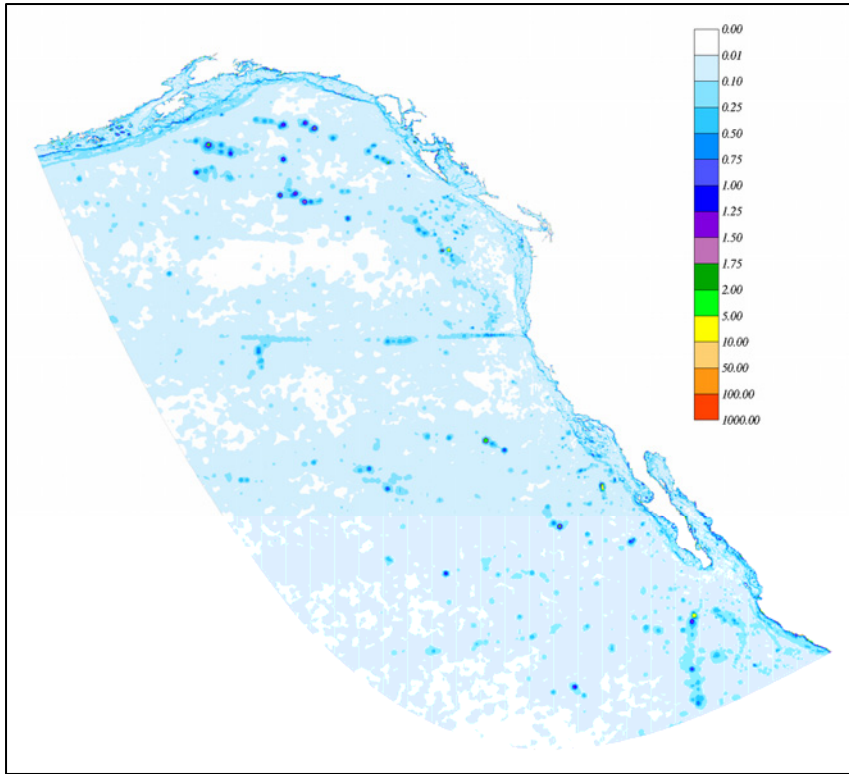


Figure 19. ENPAC 2002 grid topographic length scale (TLS) criterion

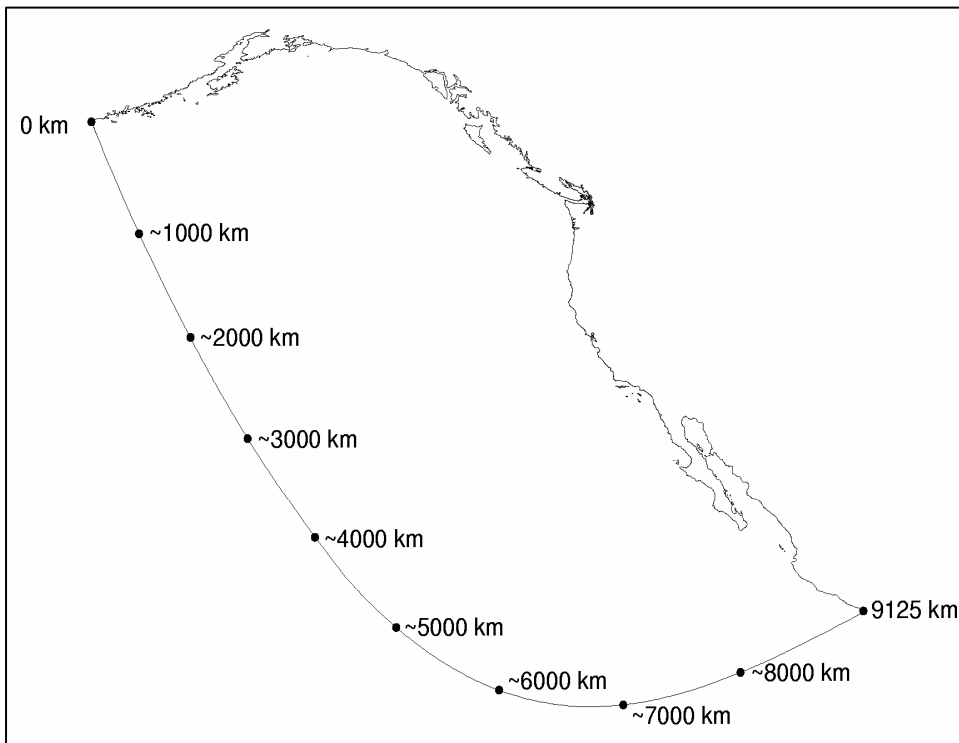


Figure 20. Distance along open boundary of ENPAC 2002 domain

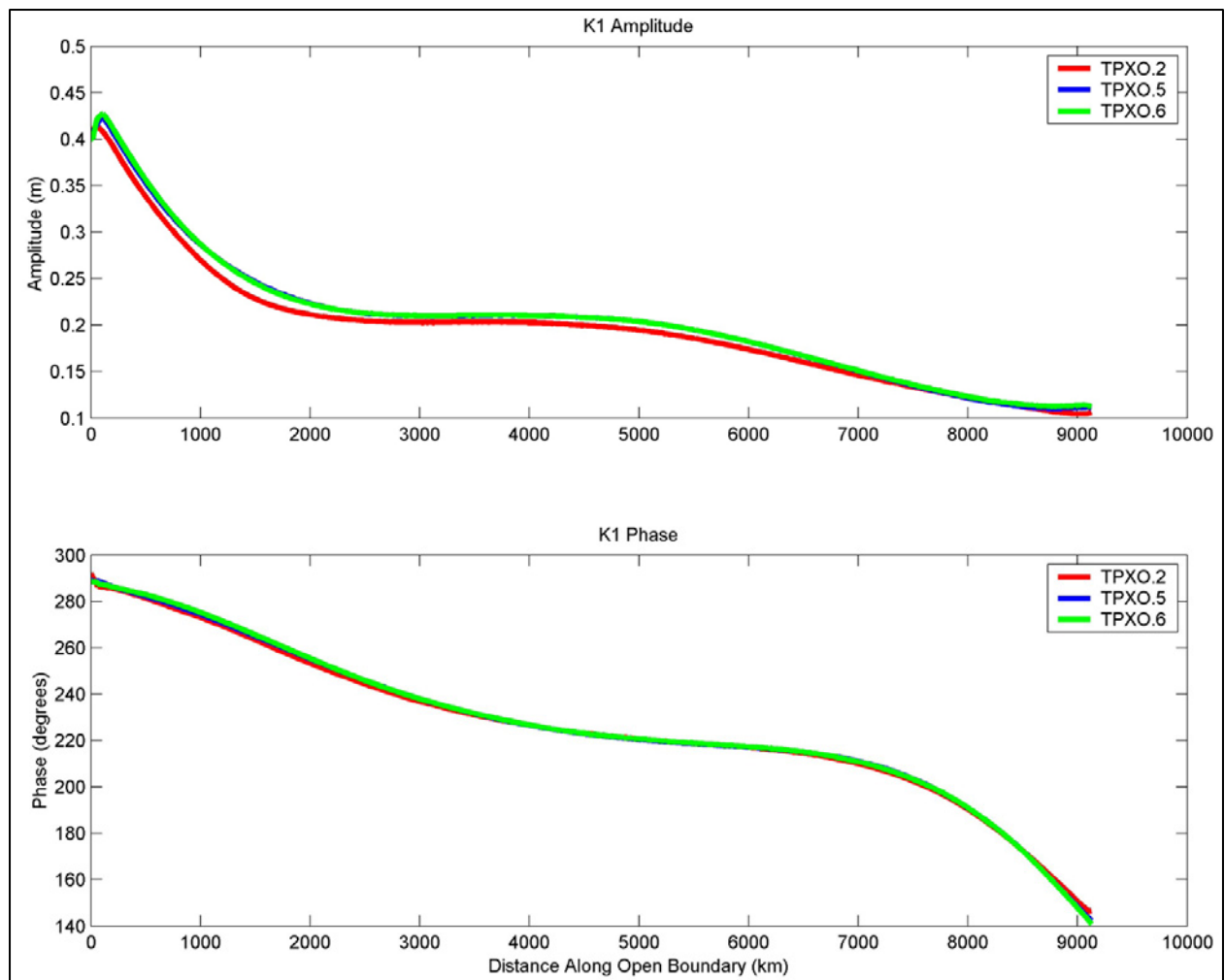


Figure 21. TPXO.2, TPXO.5, and TPXO.6 amplitude and phase versus distance (m) along ENPAC 2002 open boundary for K_1 tidal constituent

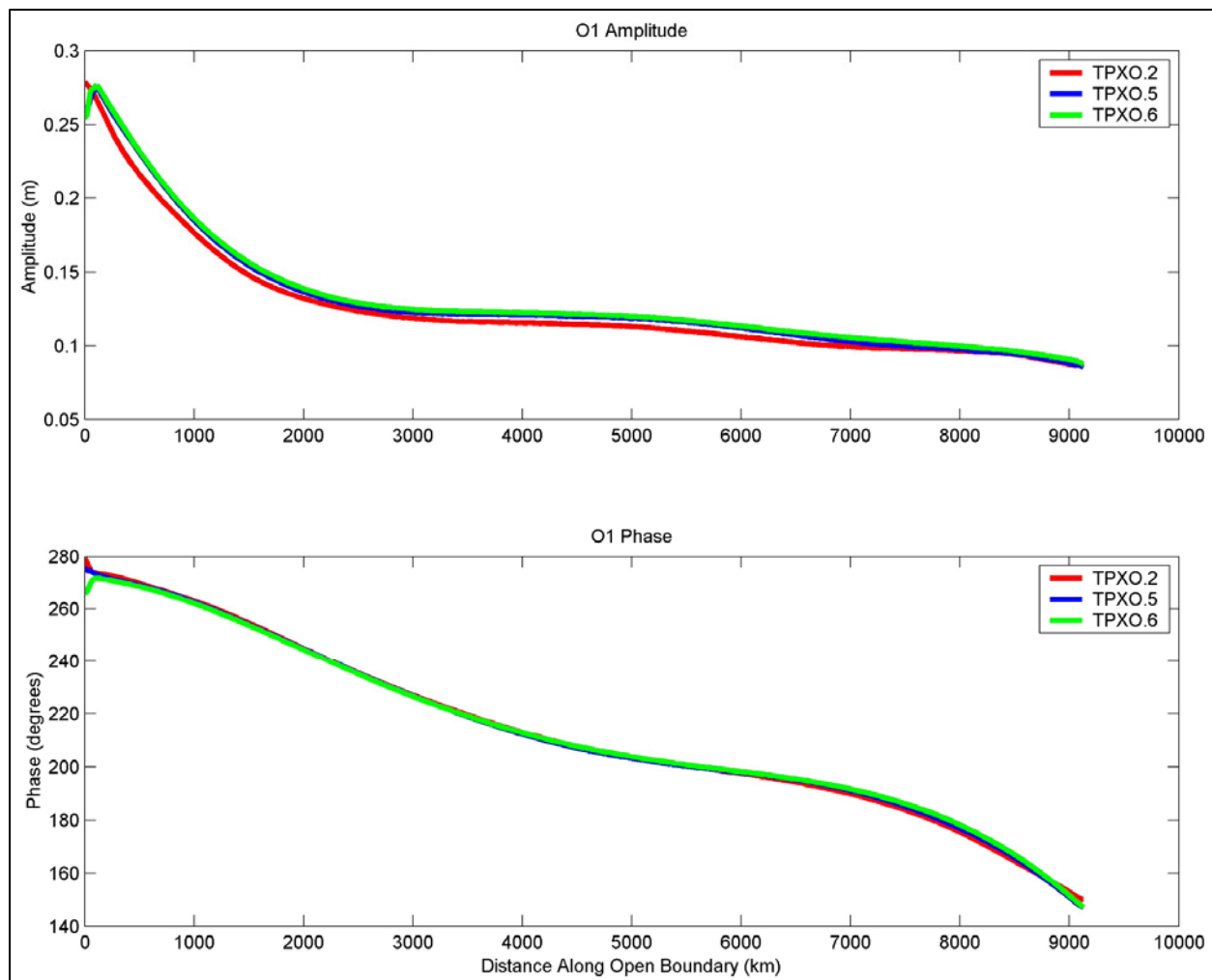


Figure 22. TPXO.2, TPXO.5, and TPXO.6 amplitude and phase versus distance (m) along ENPAC 2002 open boundary for O_1 tidal constituent

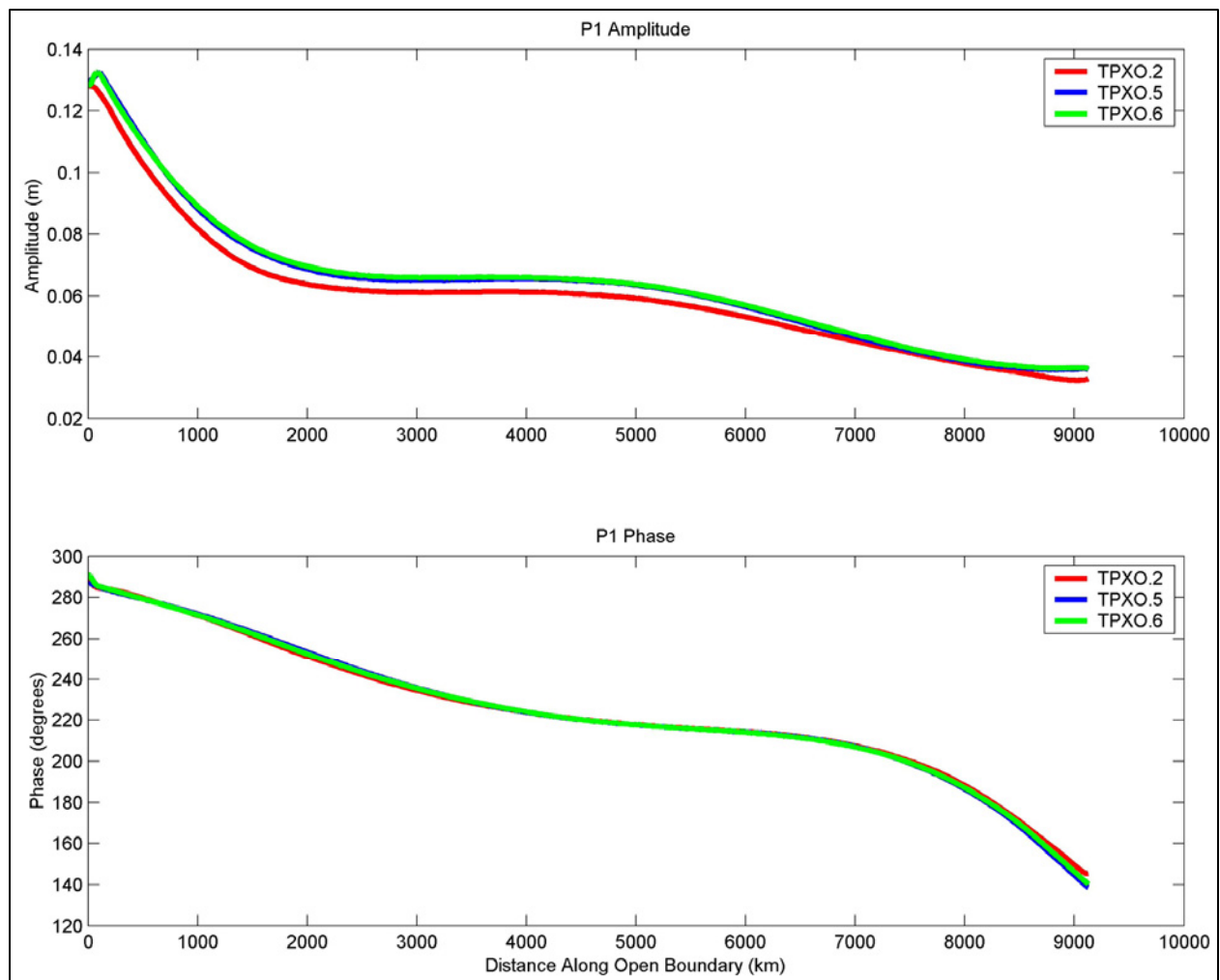


Figure 23. TPXO.2, TPXO.5, and TPXO.6 amplitude and phase versus distance (m) along ENPAC 2002 open boundary for P_1 tidal constituent

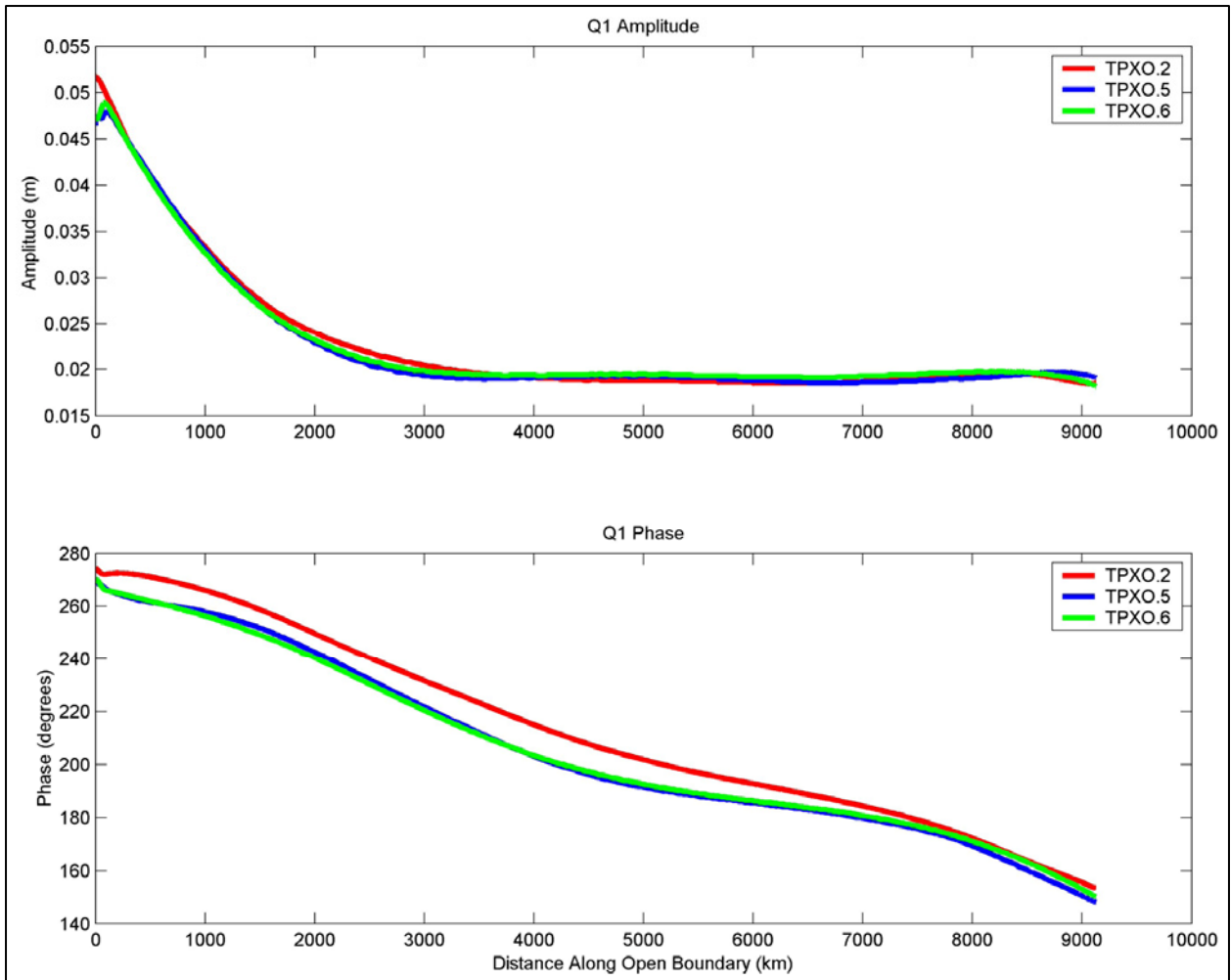


Figure 24. TPXO.2, TPXO.5, and TPXO.6 amplitude and phase versus distance (m) along ENPAC 2002 open boundary for Q_1 tidal constituent

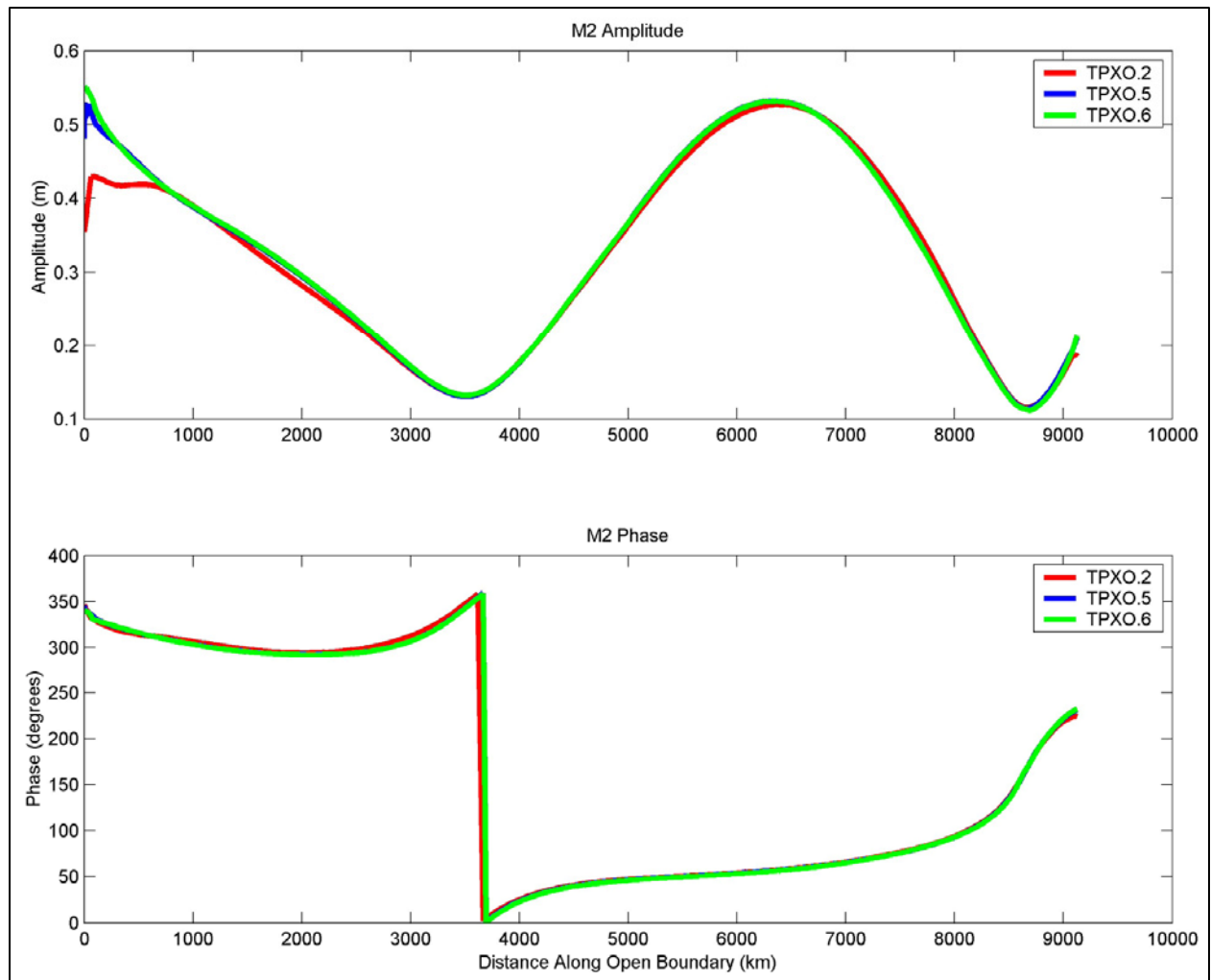


Figure 25. TPXO.2, TPXO.5, and TPXO.6 amplitude and phase versus distance (m) along ENPAC 2002 open boundary for M_2 tidal constituent

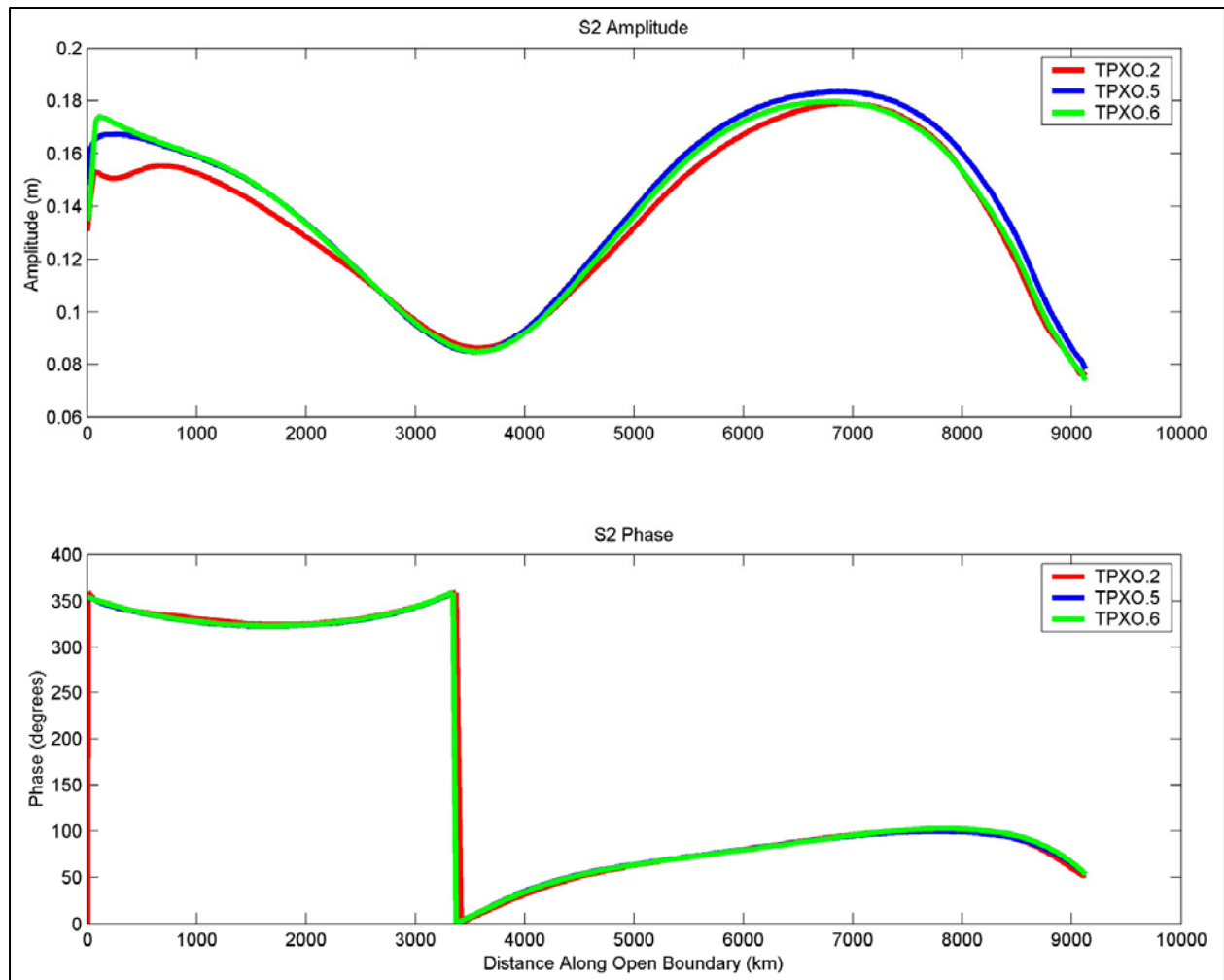


Figure 26. TPXO.2, TPXO.5, and TPXO.6 amplitude and phase versus distance (m) along ENPAC 2002 open boundary for S_2 tidal constituent

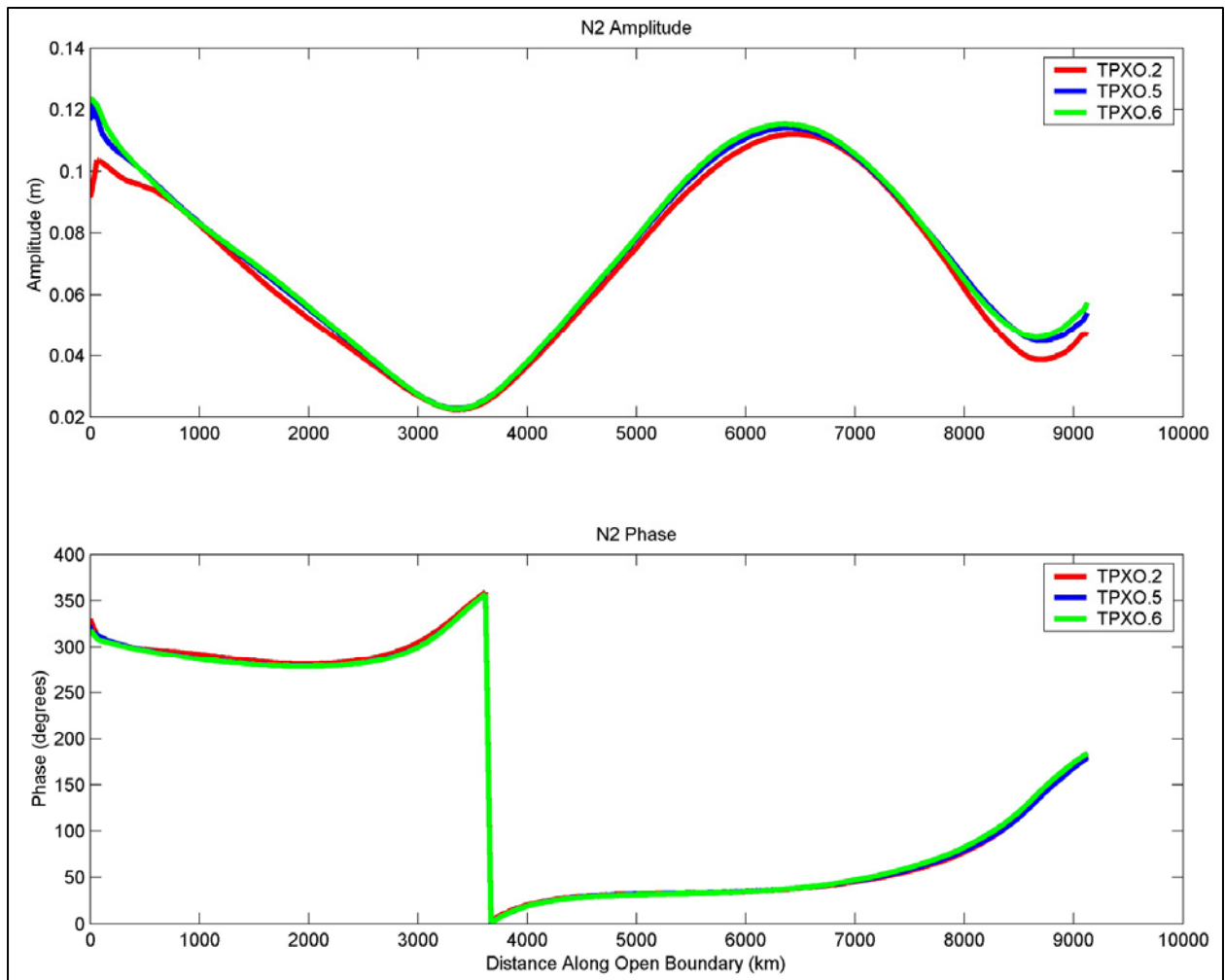


Figure 27. TPXO.2, TPXO.5, and TPXO.6 amplitude and phase versus distance (m) along ENPAC 2002 open boundary for N_2 tidal constituent

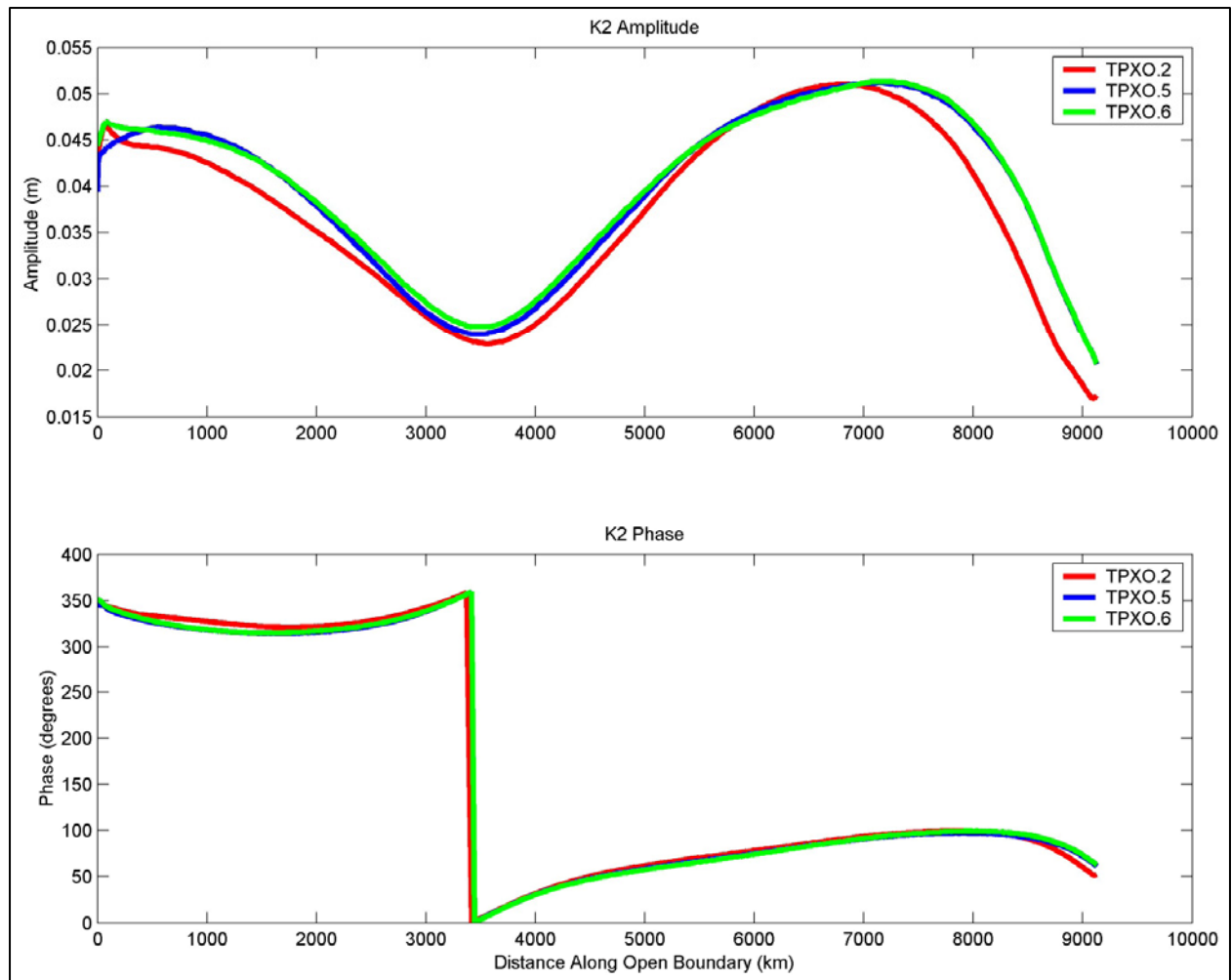


Figure 28. TPXO.2, TPXO.5, and TPXO.6 amplitude and phase versus distance (m) along ENPAC 2002 open boundary for K_2 tidal constituent

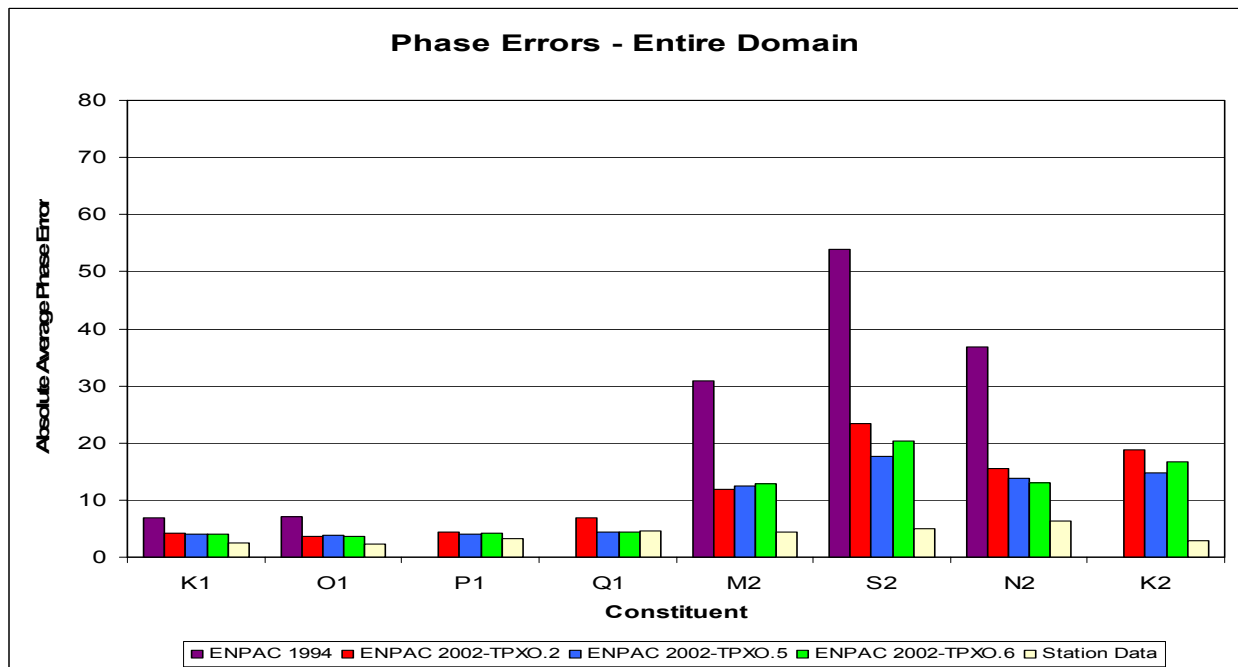
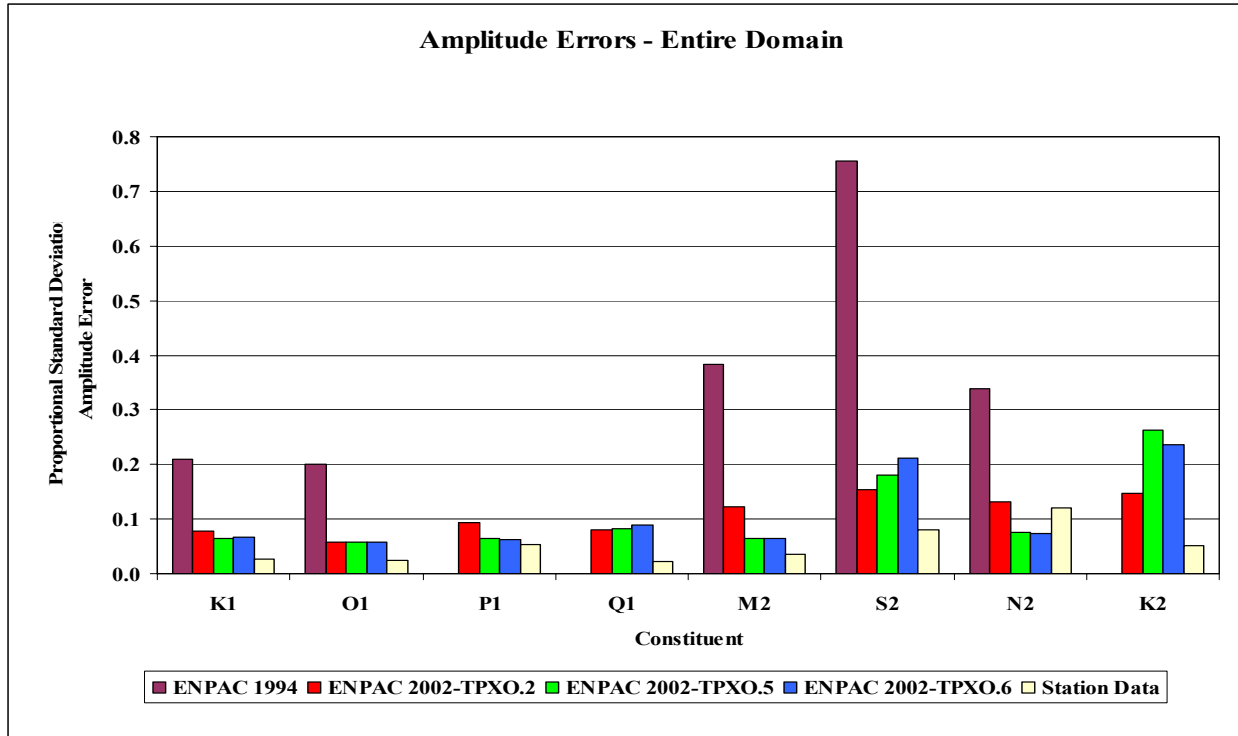


Figure 29. Proportional standard deviation amplitude errors and absolute average phase errors for 91 stations for ENPAC 1994 model, ENPAC 2002 model with TPXO.2, TPXO.5, and TPXO.6 open boundary forcing and station data

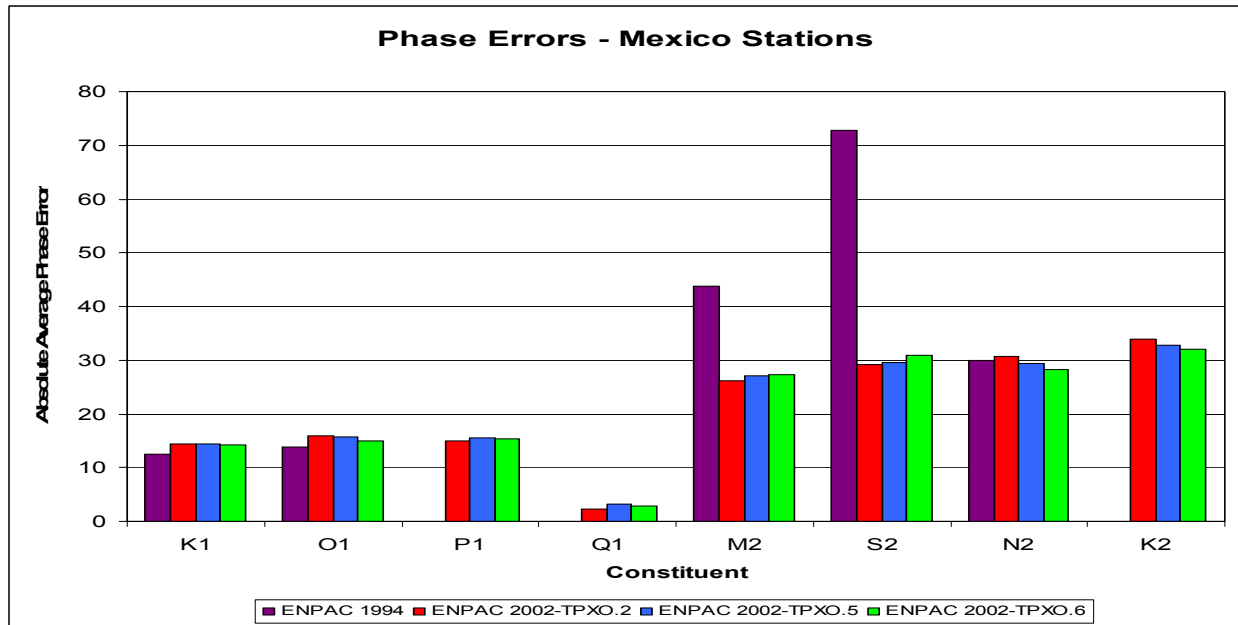
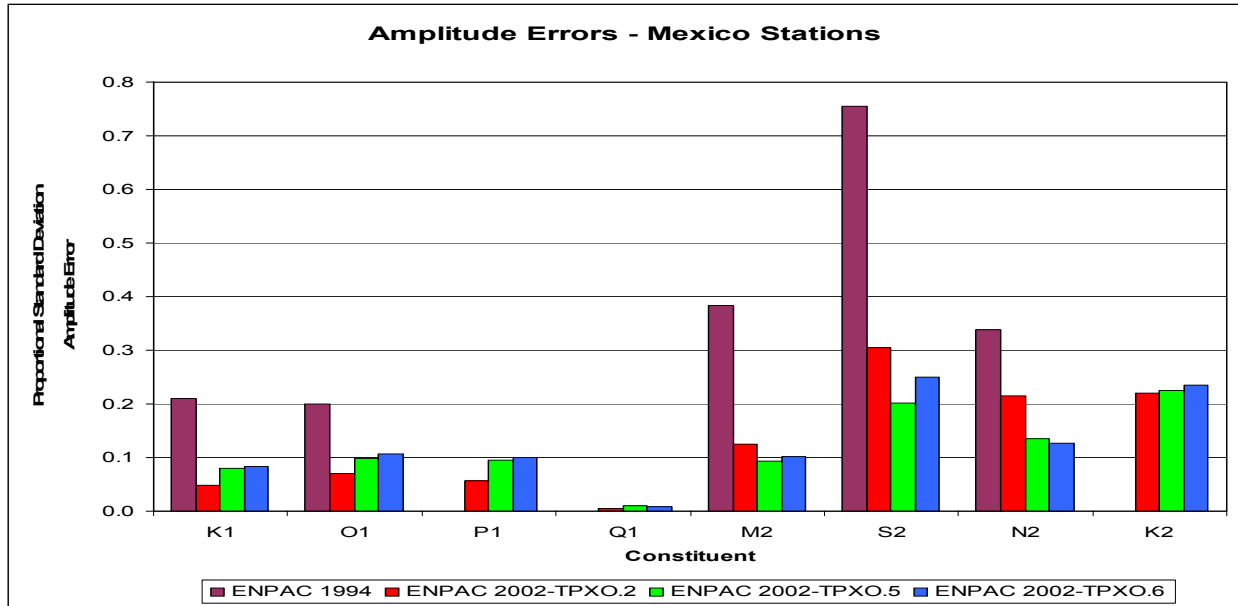


Figure 30. Proportional standard deviation amplitude errors and absolute average phase errors for five stations in Mexico subdomain for ENPAC 1994 model, ENPAC 2002 model with TPXO.2, TPXO.5, and TPXO.6 open boundary forcing and station data

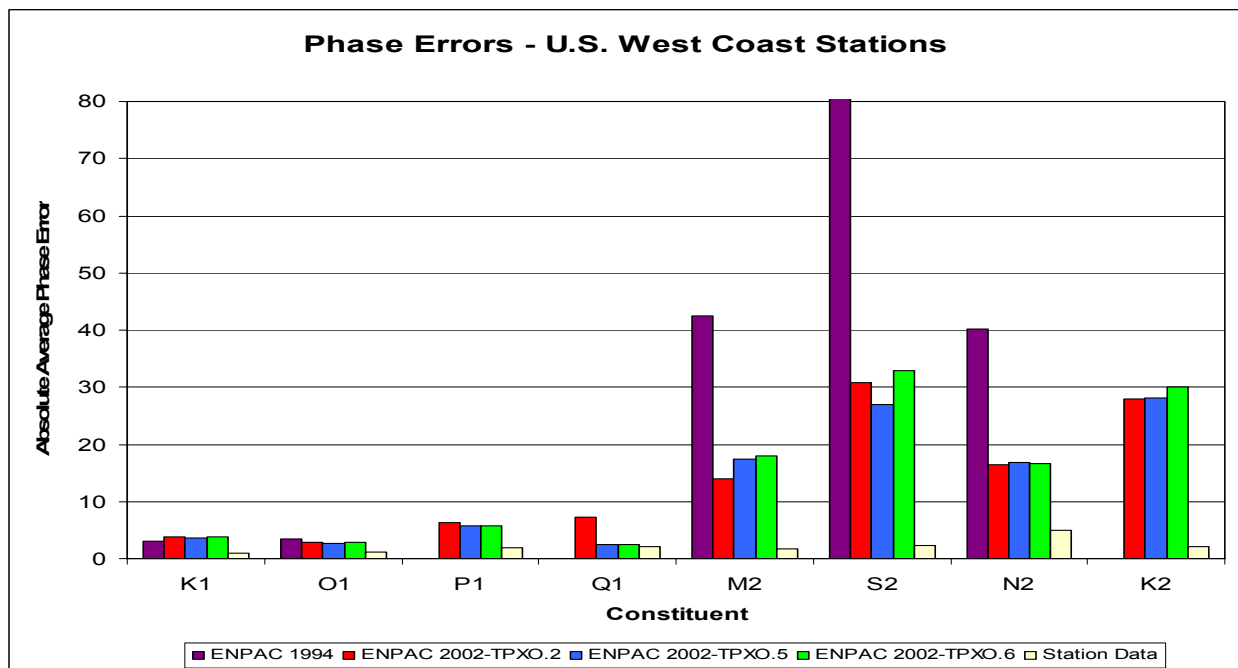
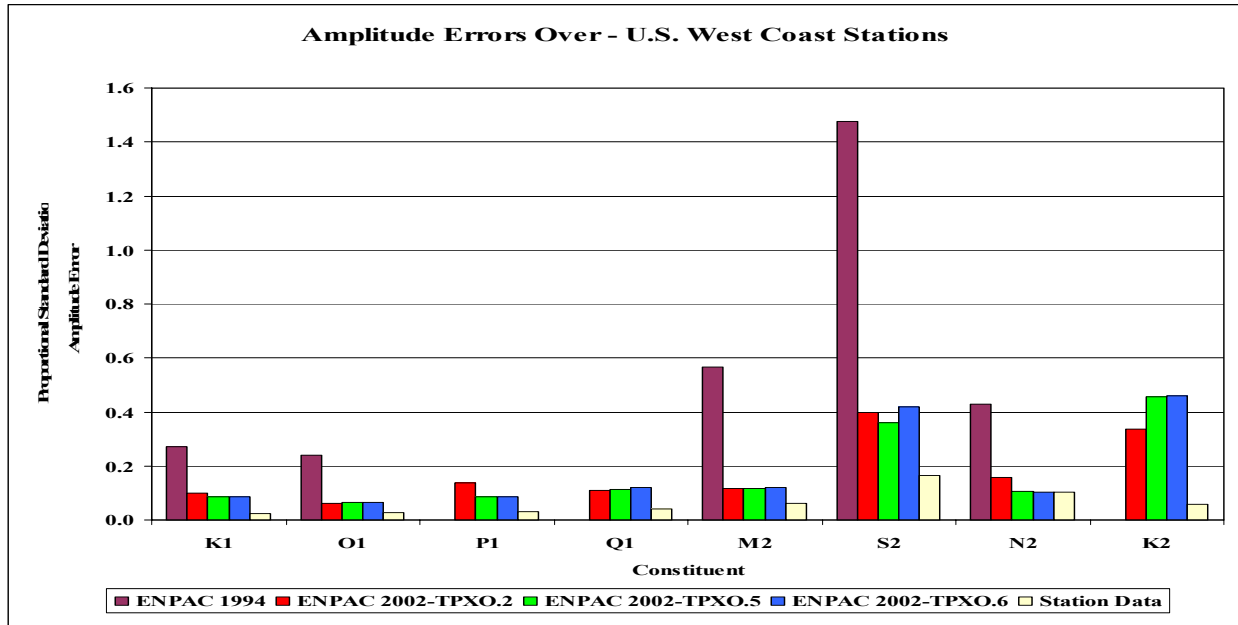


Figure 31. Proportional standard deviation amplitude errors and absolute average phase errors for 17 stations in U.S. west coast subdomain for ENPAC 1994 model, ENPAC 2002 model with TPXO.2, TPXO.5, and TPXO.6 open boundary forcing and station data

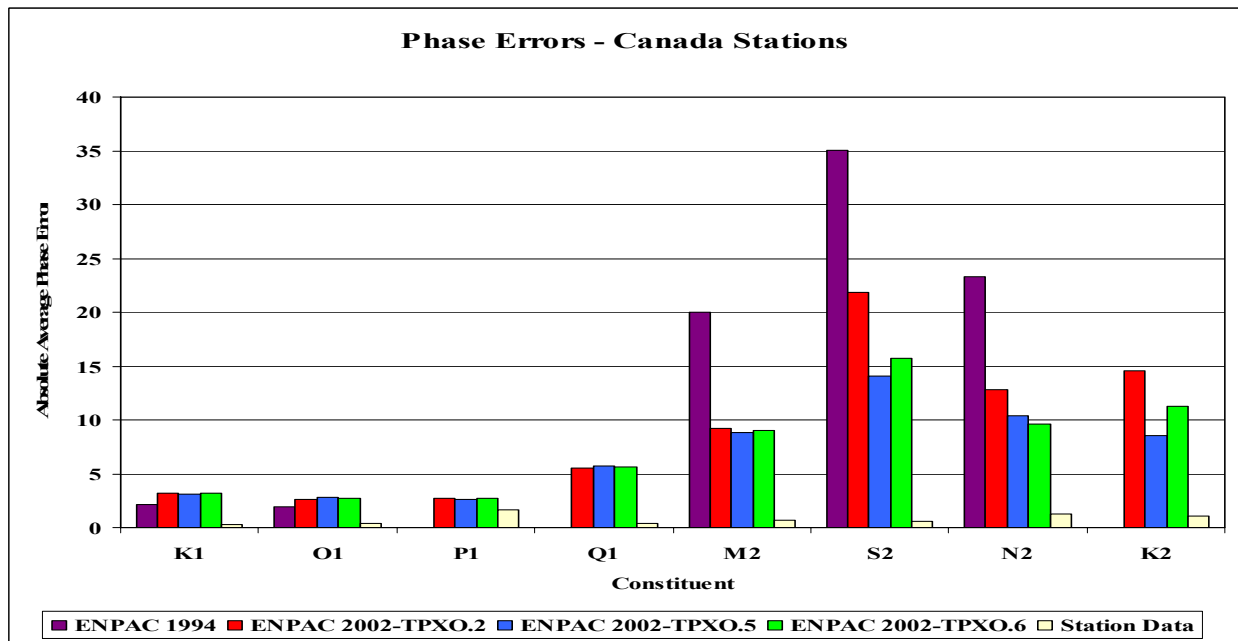
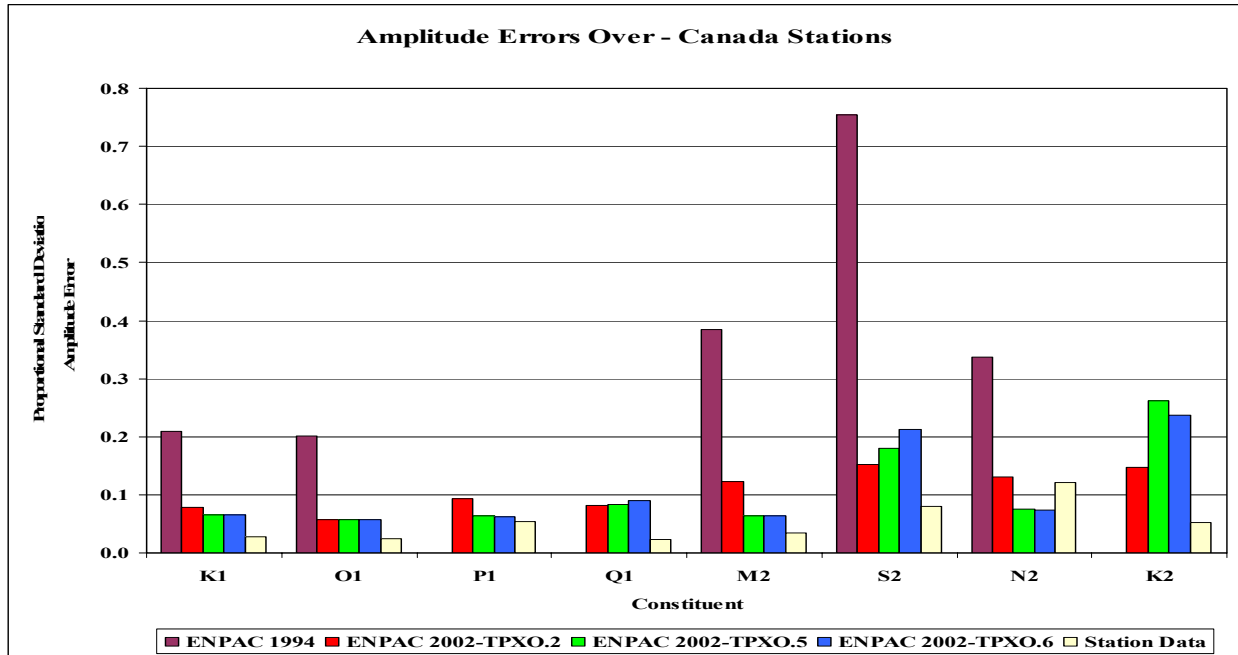


Figure 32. Proportional standard deviation amplitude errors and absolute average phase errors for 37 stations in Canada subdomain for ENPAC 1994 model, ENPAC 2002 model with TPXO.2, TPXO.5, and TPXO.6 open boundary forcing and station data

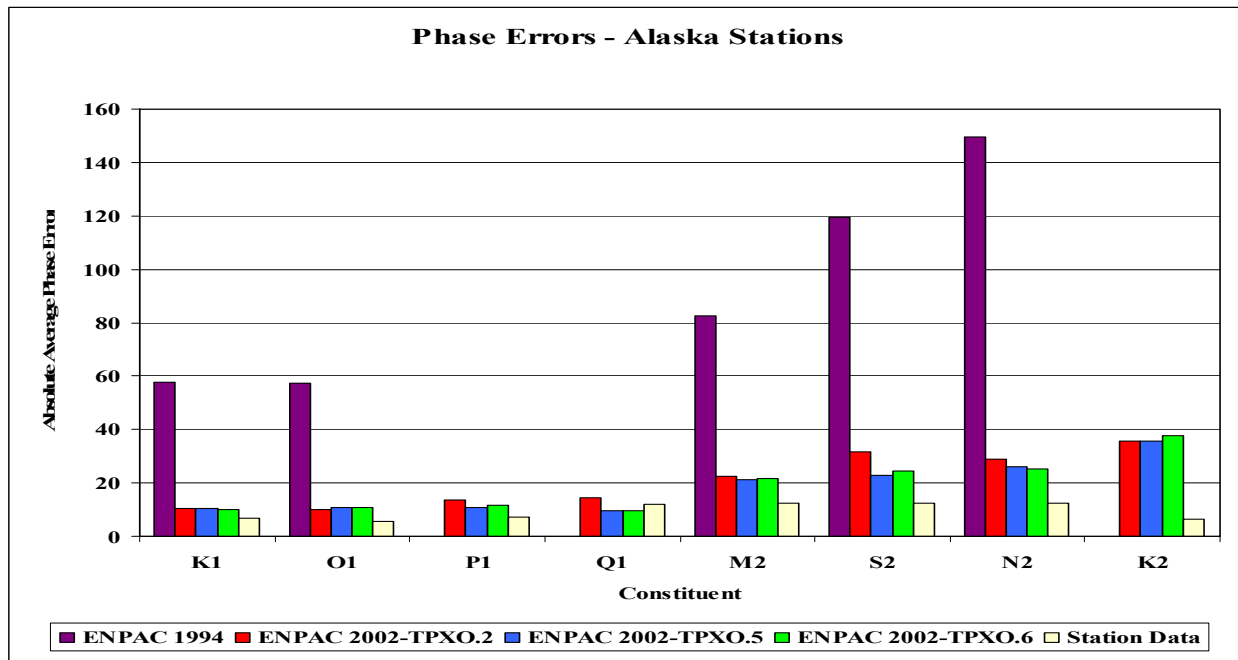
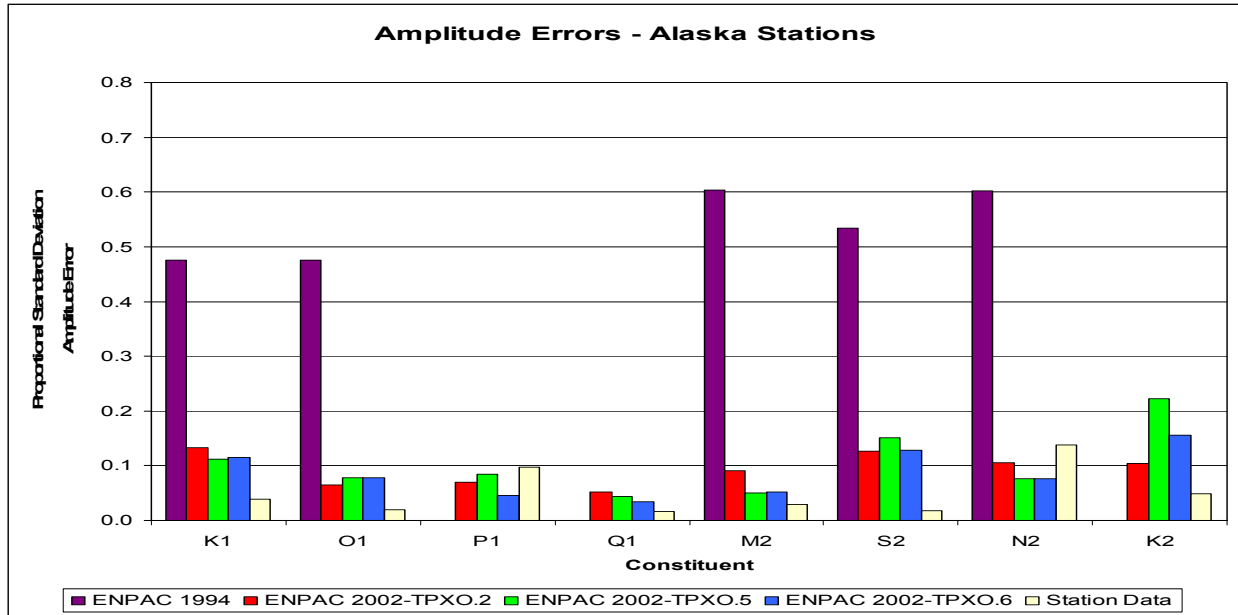


Figure 33. Proportional standard deviation amplitude errors and absolute average phase errors for five stations in Alaska subdomain for ENPAC 1994 model, ENPAC 2002 model with TPXO.2, TPXO.5, and TPXO.6 open boundary forcing and station data

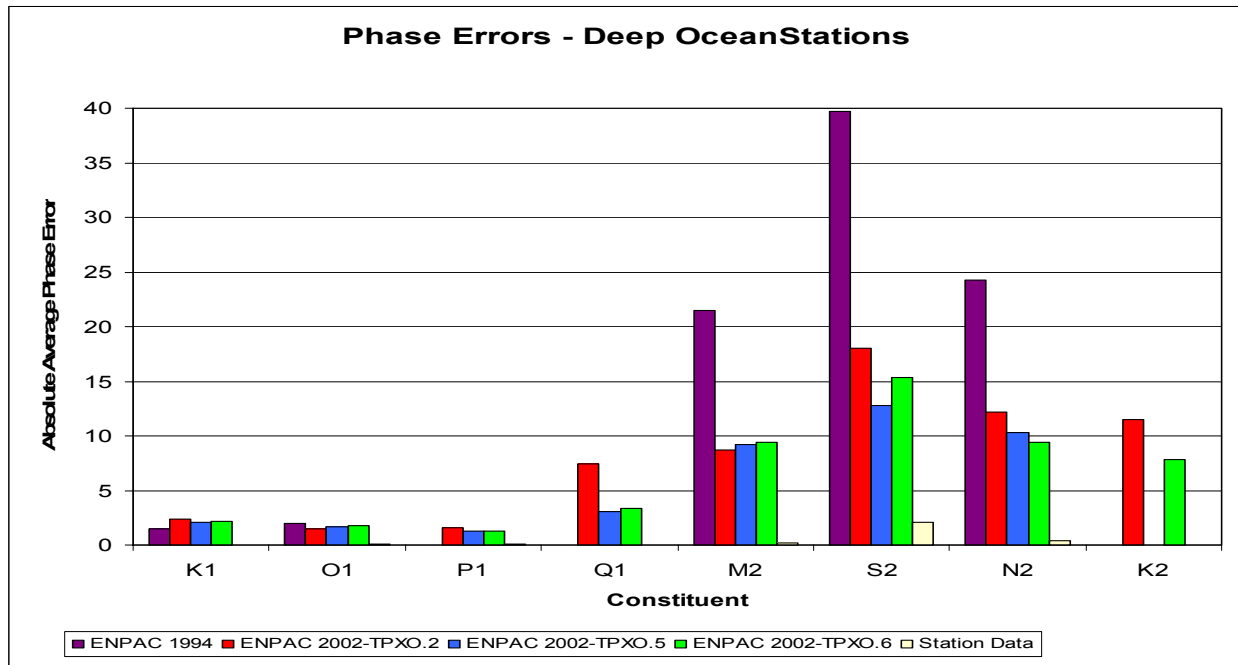
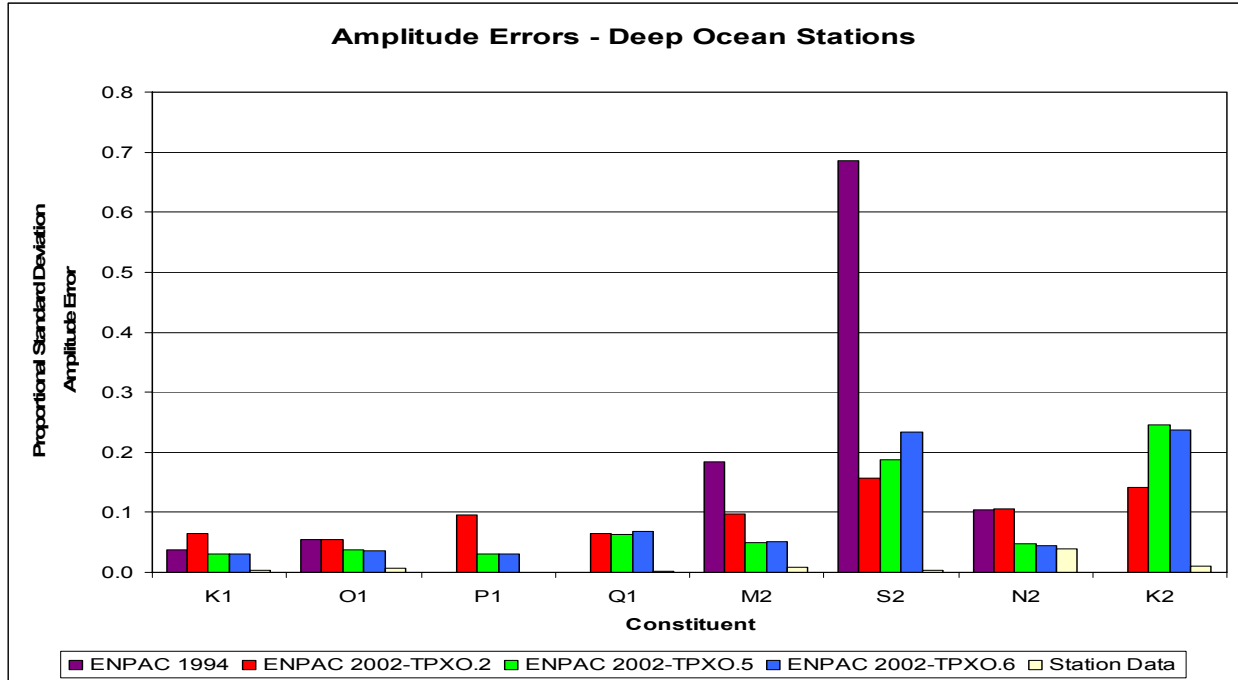


Figure 34. Proportional standard deviation amplitude errors and absolute average phase errors for 31 stations in deep ocean subdomain for ENPAC 1994 model, ENPAC 2002 model with TPXO.2, TPXO.5, and TPXO.6 open boundary forcing and station data

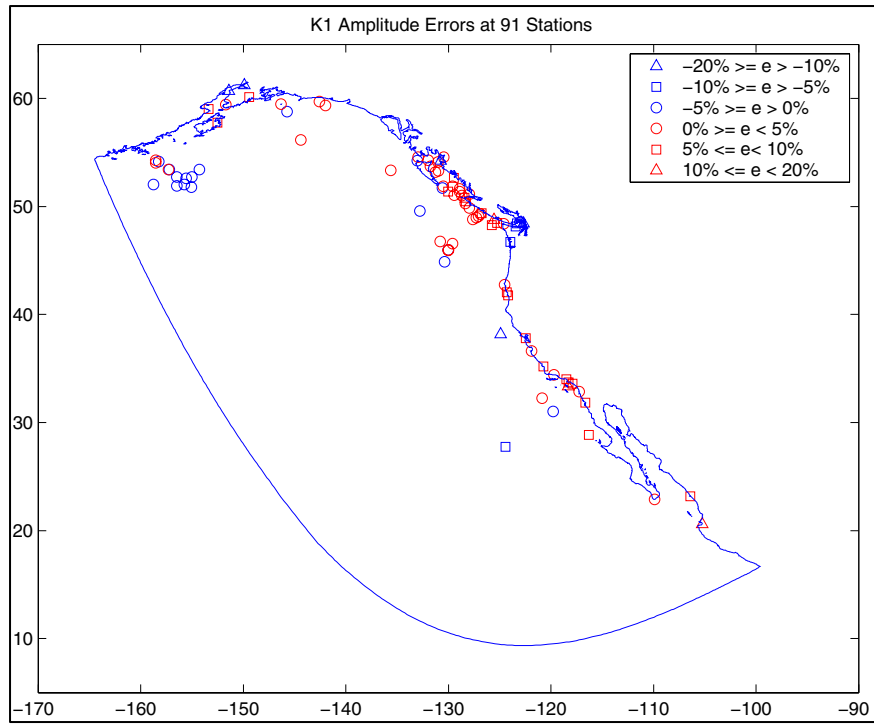


Figure 35. K_1 amplitude errors (percent) for ENPAC 2002 model with TPXO.5 open boundary forcing

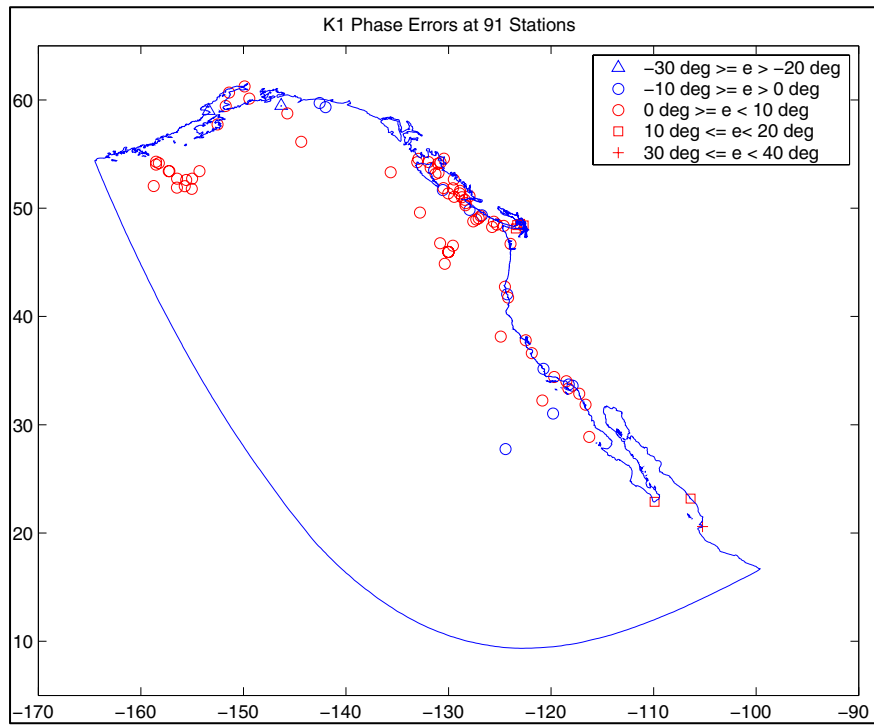


Figure 36. K_1 phase errors (degree) for ENPAC 2002 model with TPXO.5 open boundary forcing

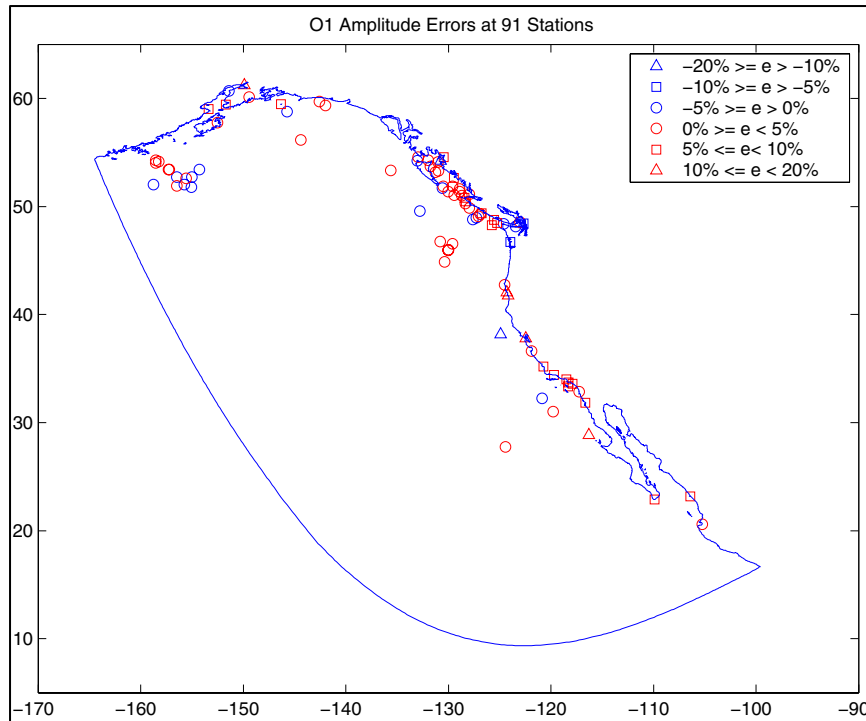


Figure 37. O_1 amplitude errors (percent) for ENPAC 2002 model with TPXO.5 open boundary forcing

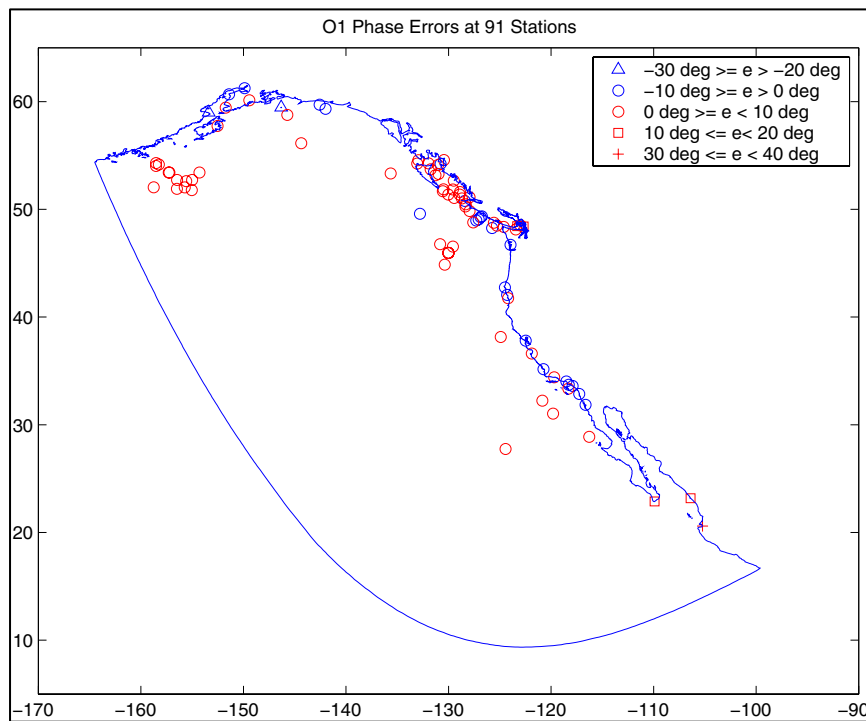


Figure 38. O_1 phase errors (degree) for ENPAC 2002 model with TPXO.5 open boundary forcing

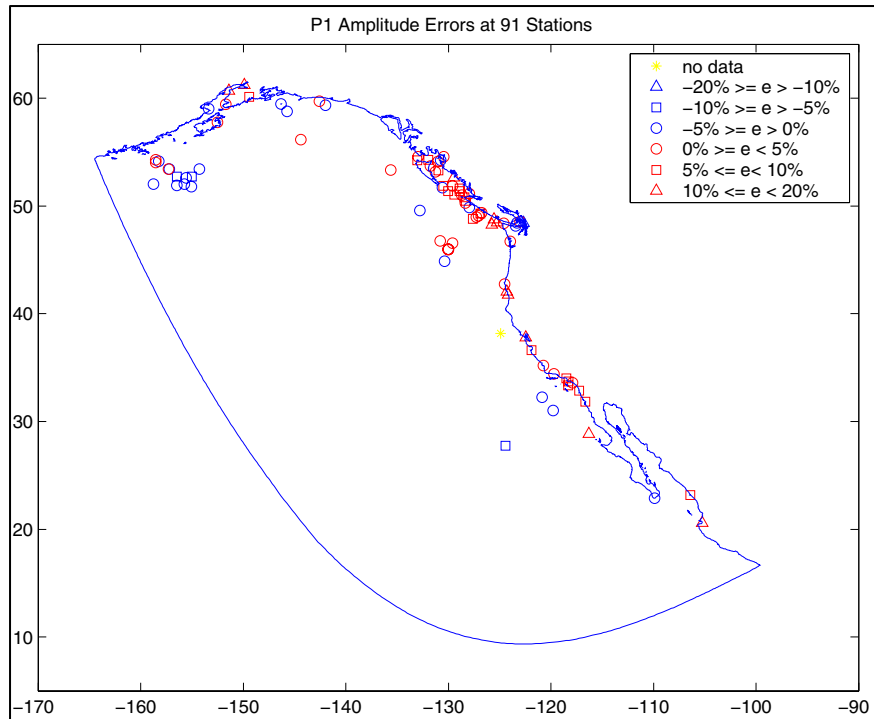


Figure 39. P_1 amplitude errors (percent) for ENPAC 2002 model with TPXO.5 open boundary forcing

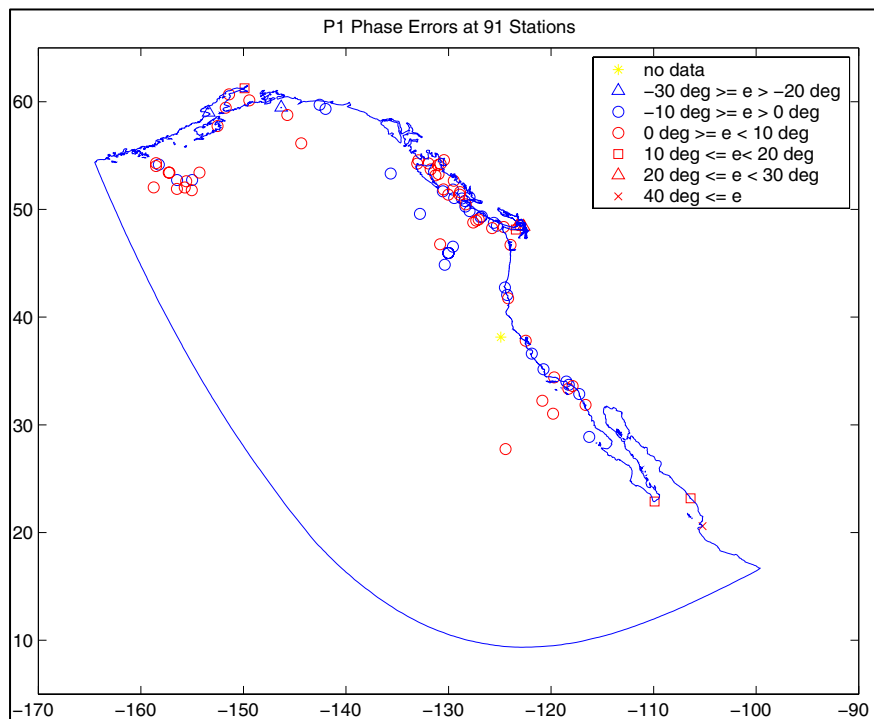


Figure 40. P_1 phase errors (degree) for ENPAC 2002 model with TPXO.5 open boundary forcing

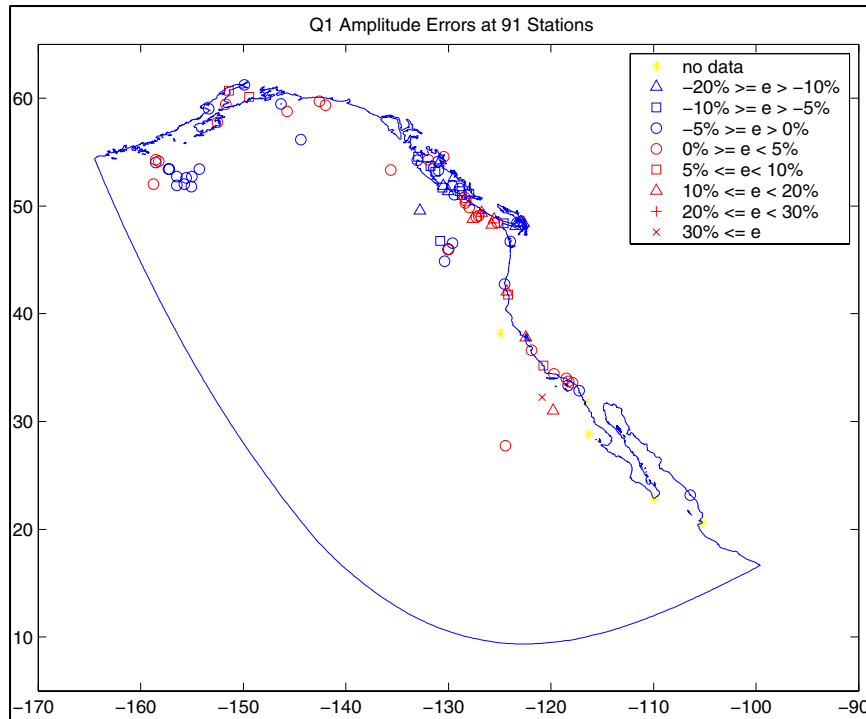


Figure 41. Q_1 amplitude errors (percent) for ENPAC 2002 model with TPXO.5 open boundary forcing

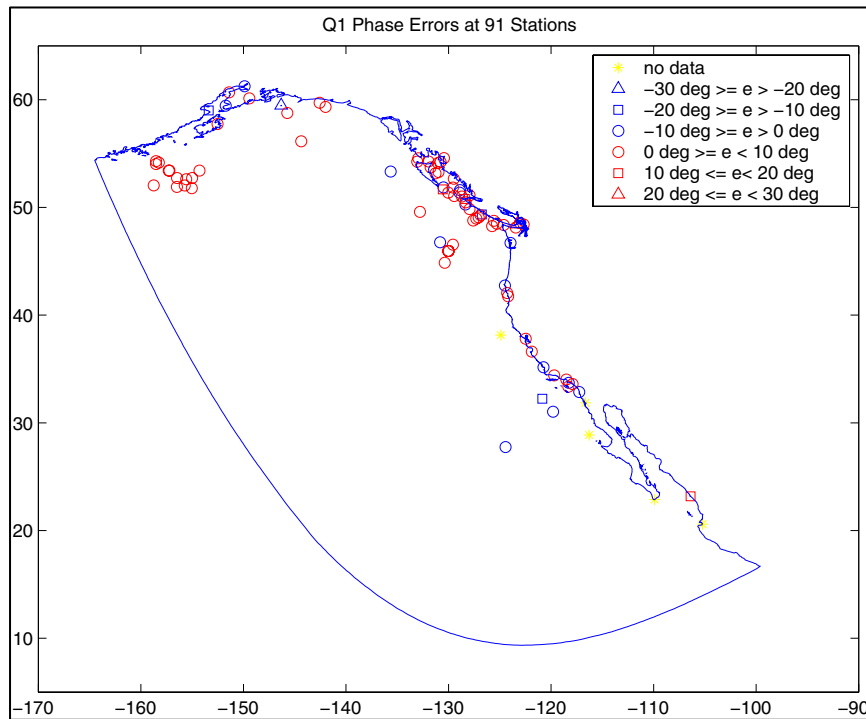


Figure 42. Q_1 phase errors (degree) for ENPAC 2002 model with TPXO.5 open boundary forcing

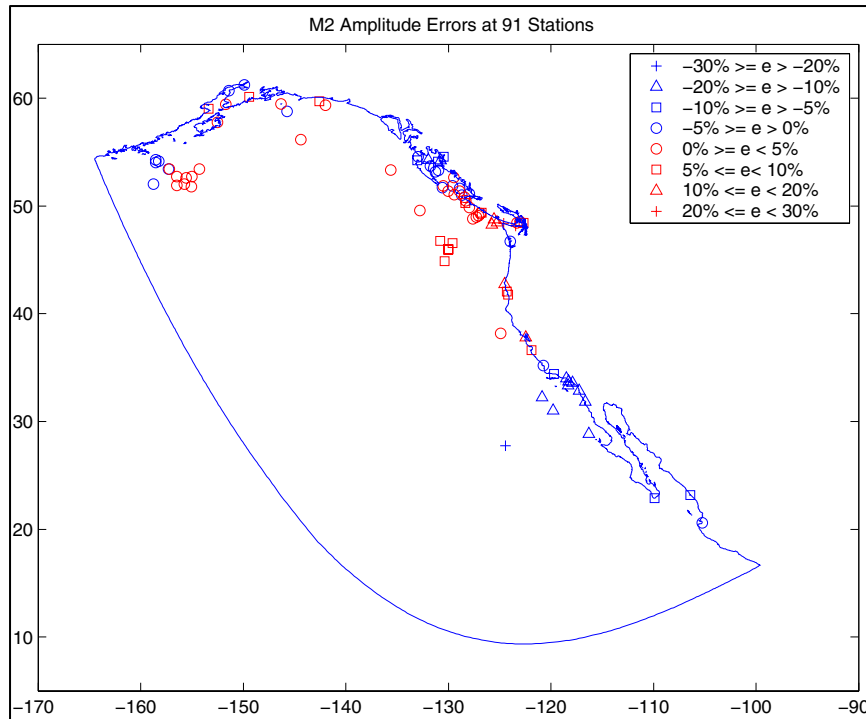


Figure 43. M_2 amplitude errors (percent) for ENPAC 2002 model with TPXO.5 open boundary forcing

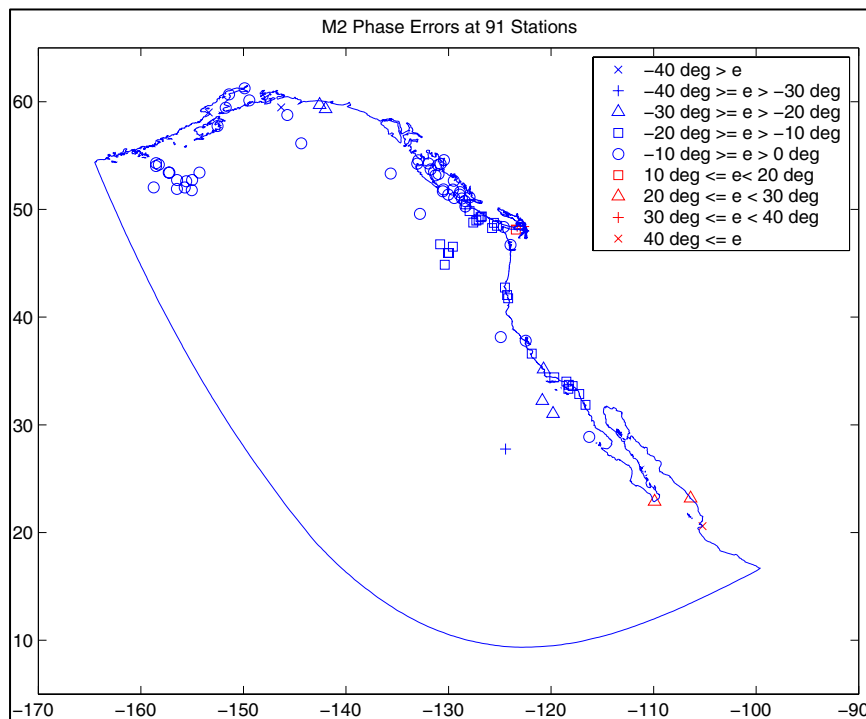


Figure 44. M_2 phase errors (degrees) for ENPAC 2002 model with TPXO.5 open boundary forcing

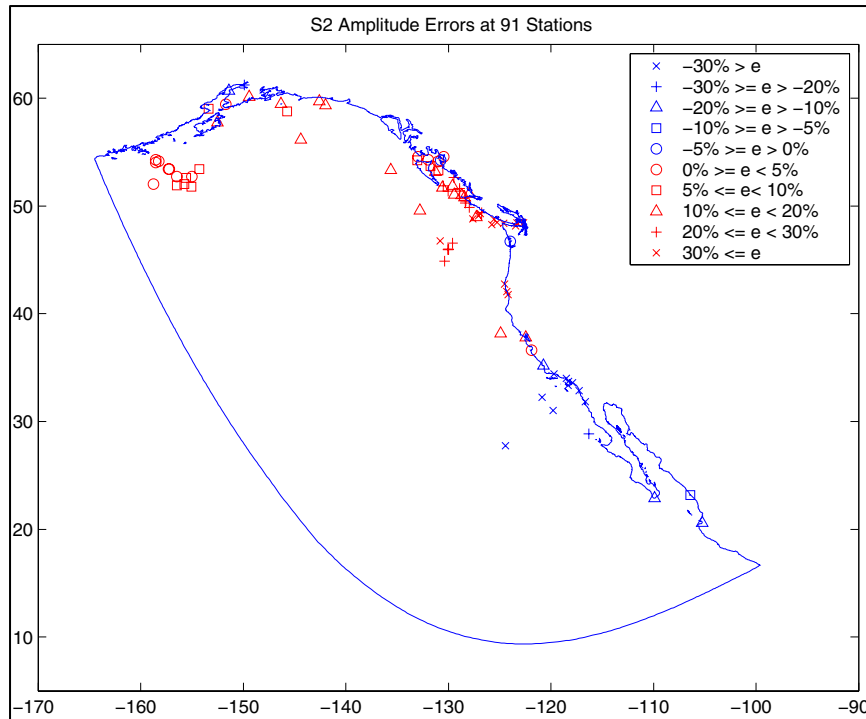


Figure 45. S_2 amplitude errors (percent) for ENPAC 2022 model with TPXO.5 open boundary forcing

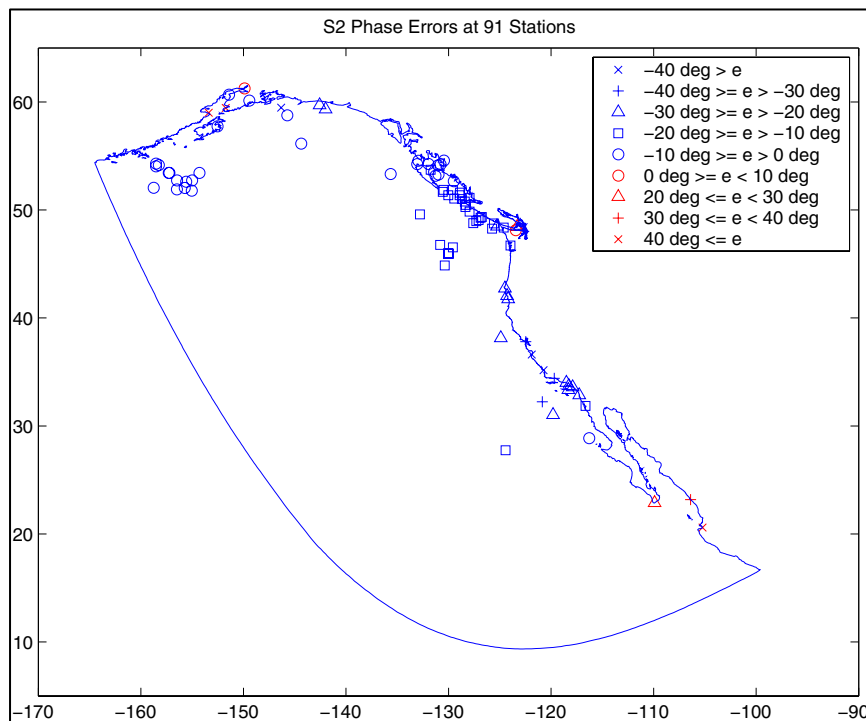


Figure 46. S_2 phase errors (degrees) for ENPAC 2022 model with TPXO.5 open boundary forcing

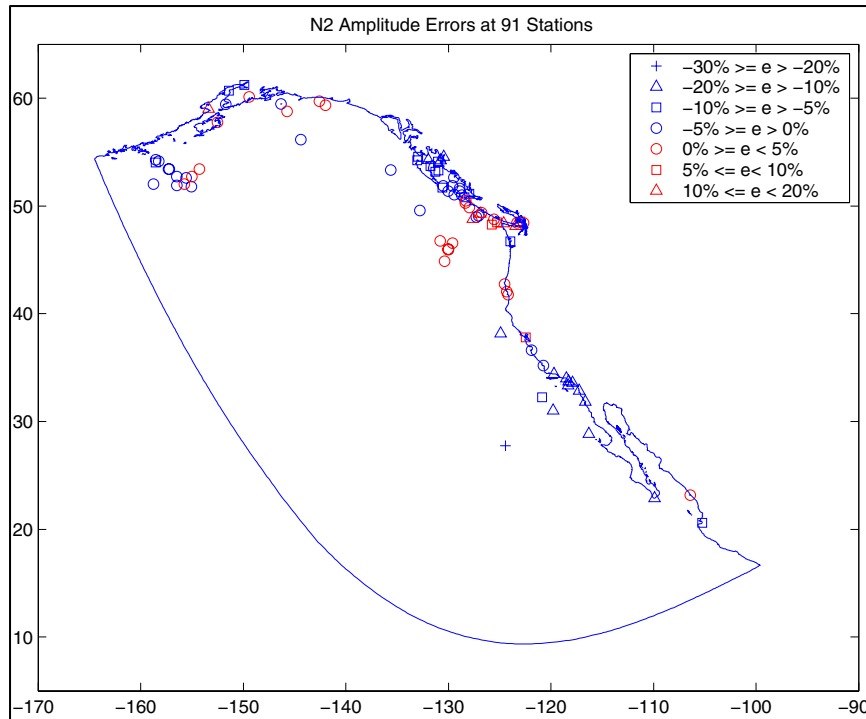


Figure 47. N₂ amplitude errors (percent) for ENPAC 2002 model with TPXO.5 open boundary forcing

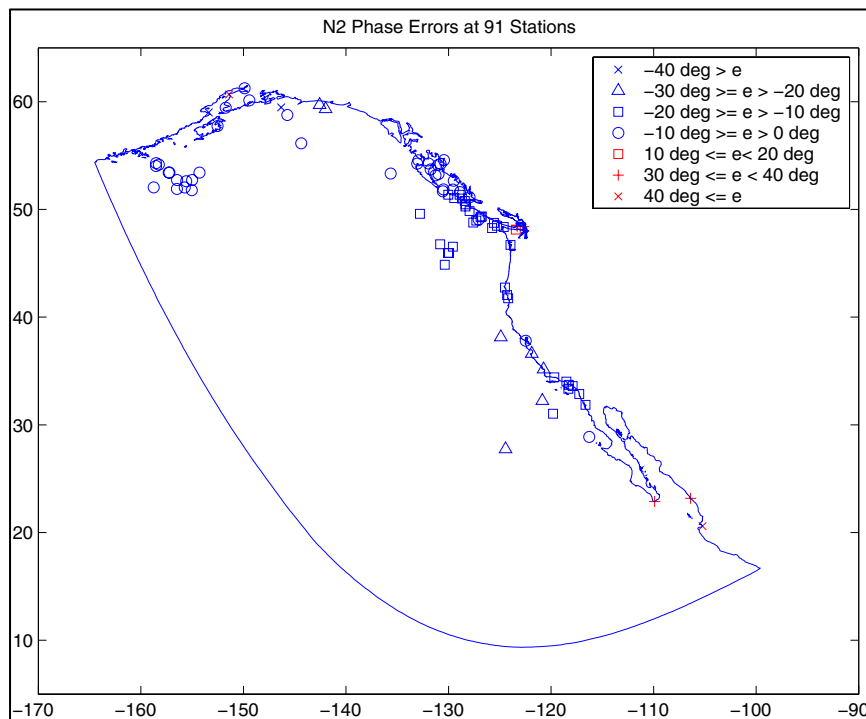


Figure 48. N₂ phase errors (degrees) for ENPAC 2002 model with TPXO.5 open boundary forcing

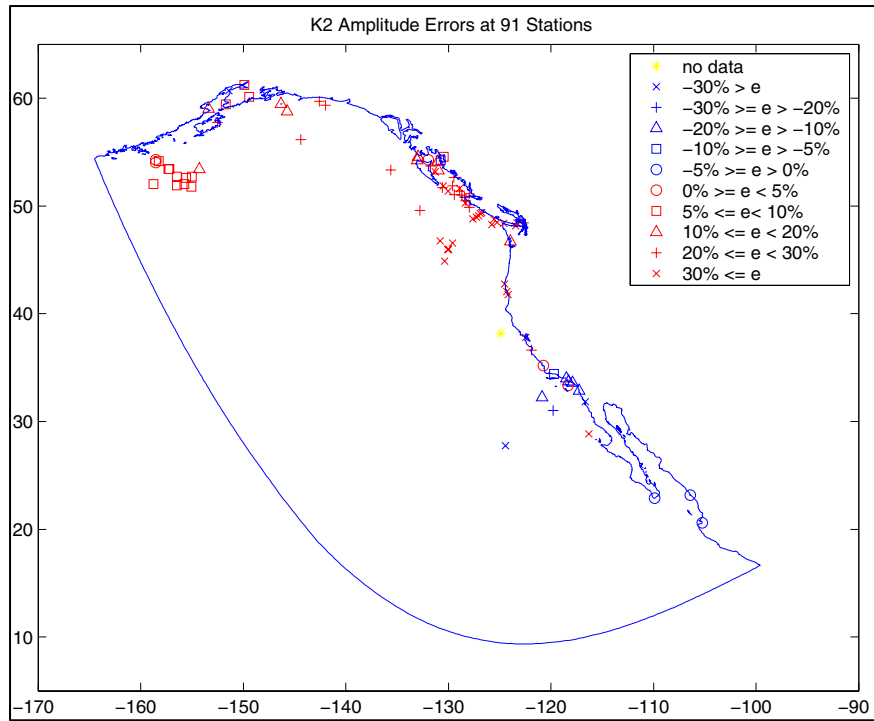


Figure 49. K_2 amplitude errors (percent) for ENPAC 2022 model with TPXO.5 open boundary forcing

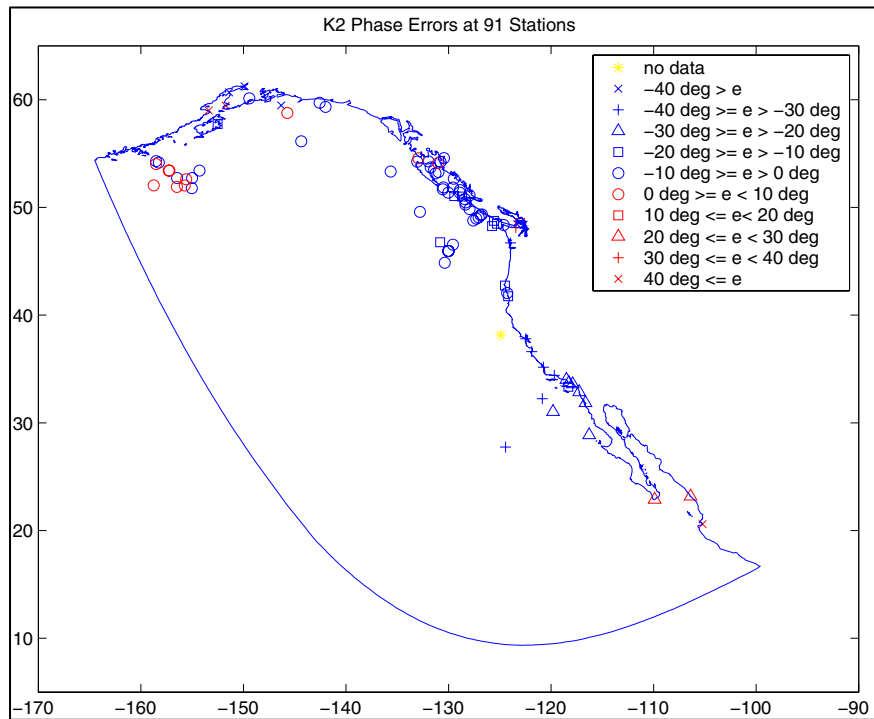


Figure 50. K_2 phase errors (degrees) for ENPAC 2022 model with TPXO.5 open boundary forcing

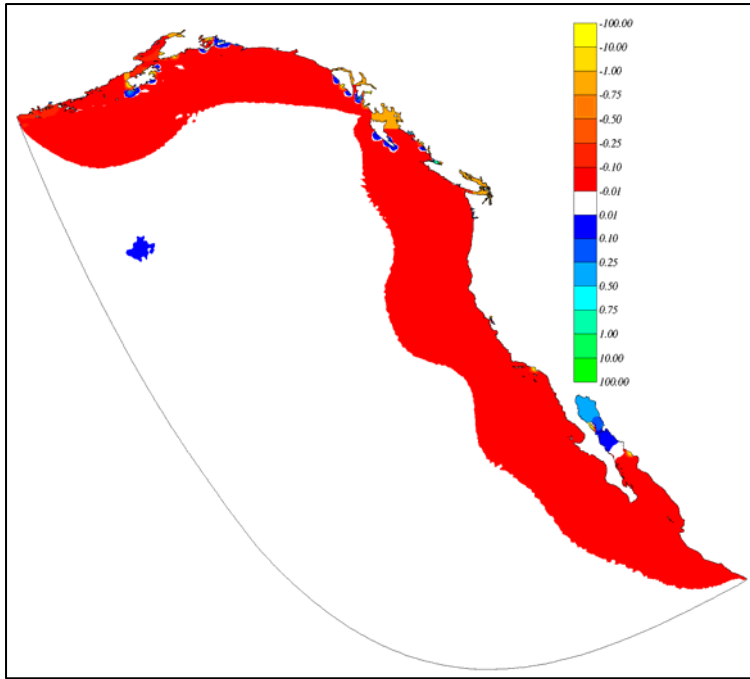


Figure 51. Fractional difference between K_1 amplitude results from TPXO.5 global ocean model and NEPAC 2002 model (with TPXO.5 open boundary forcing)

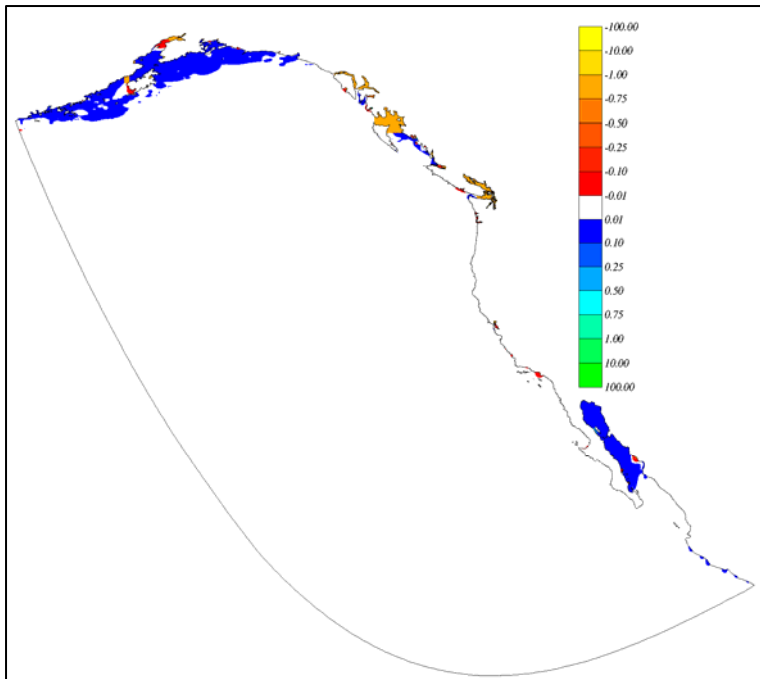


Figure 52. Fractional difference between K_1 phase results from TPXO.5 global ocean model and NEPAC 2002 model (with TPXO.5 open boundary forcing)

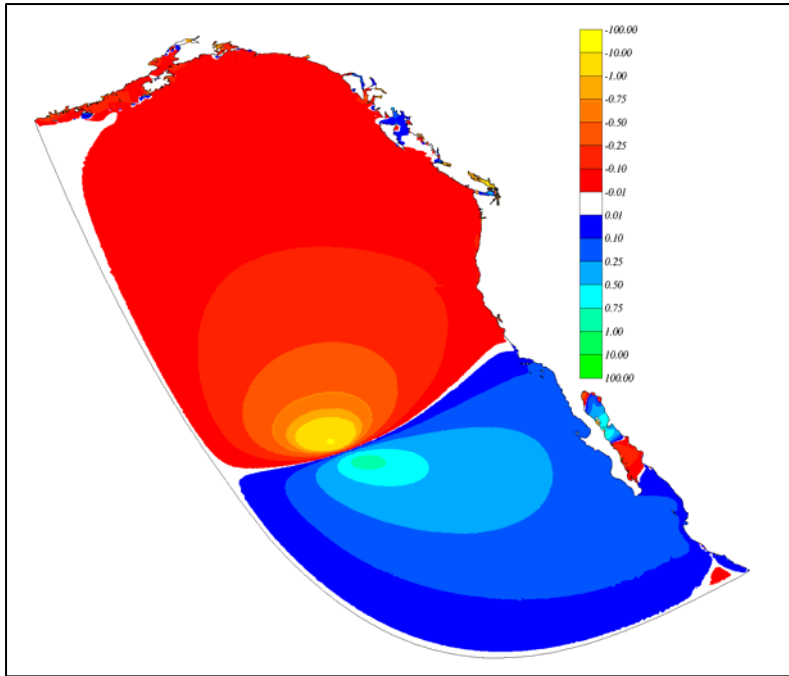


Figure 53. Fractional difference between M_2 amplitude results from TPXO.5 global ocean model and NEPAC 2002 model (with TPXO.5 open boundary forcing)

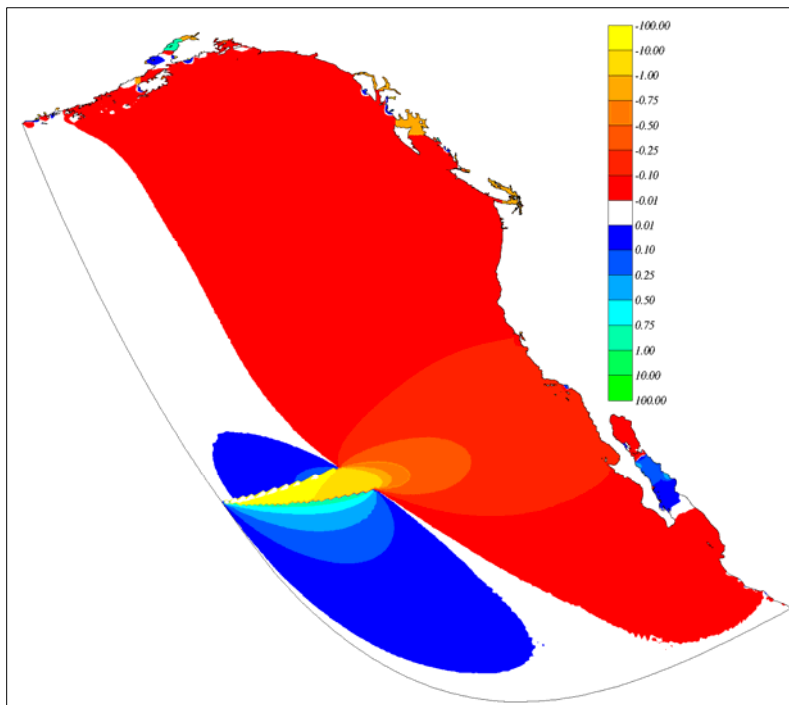


Figure 54. Fractional difference between M_2 phase results from TPXO.5 global ocean model and NEPAC 2002 model (with TPXO.5 open boundary forcing)

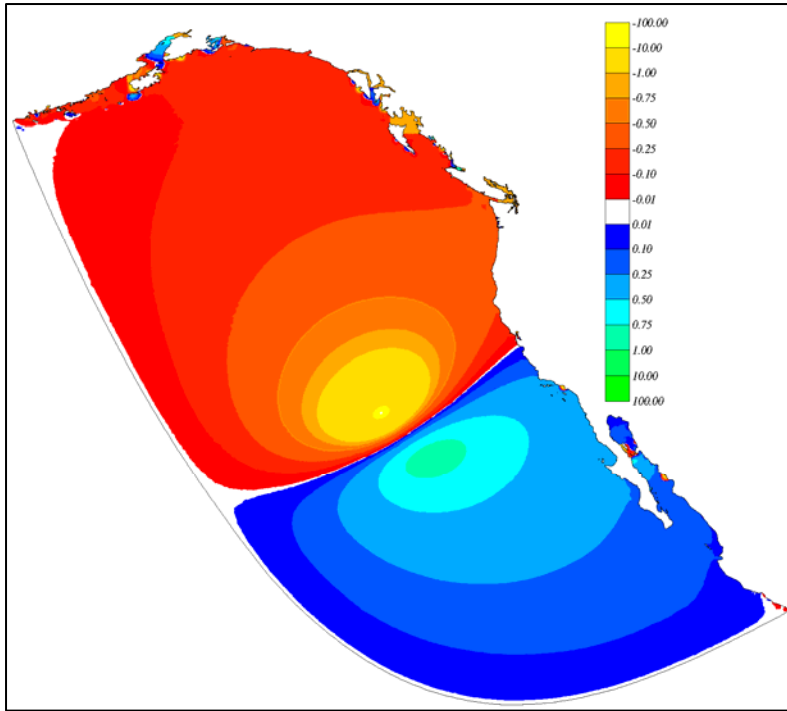


Figure 55. Fractional difference between S_2 amplitude results from TPXO.5 global ocean model and NEPAC 2002 model (with TPXO.5 open boundary forcing)

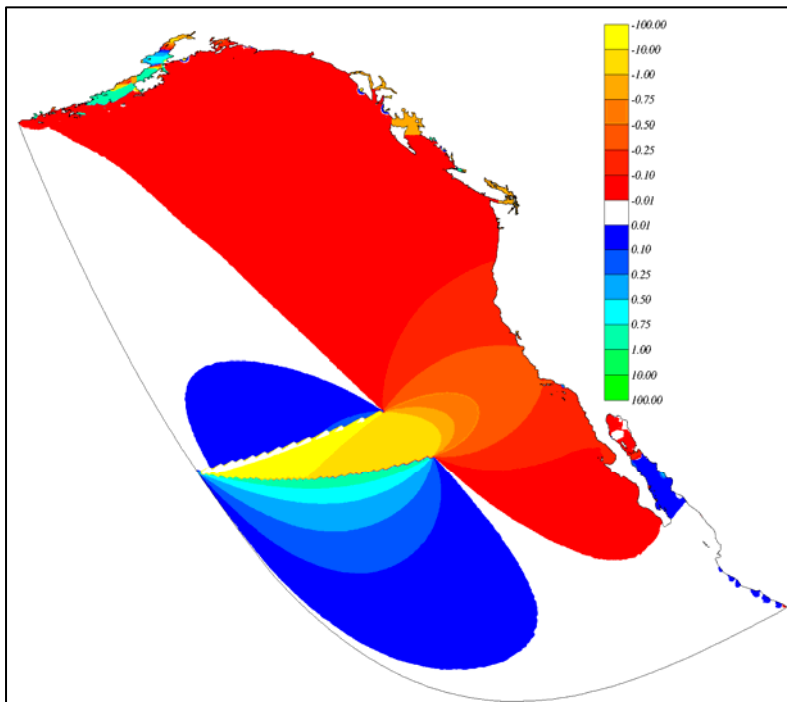


Figure 56. Fractional difference between S_2 phase results from TPXO.5 global ocean model and NEPAC 2002 model (with TPXO.5 open boundary forcing)

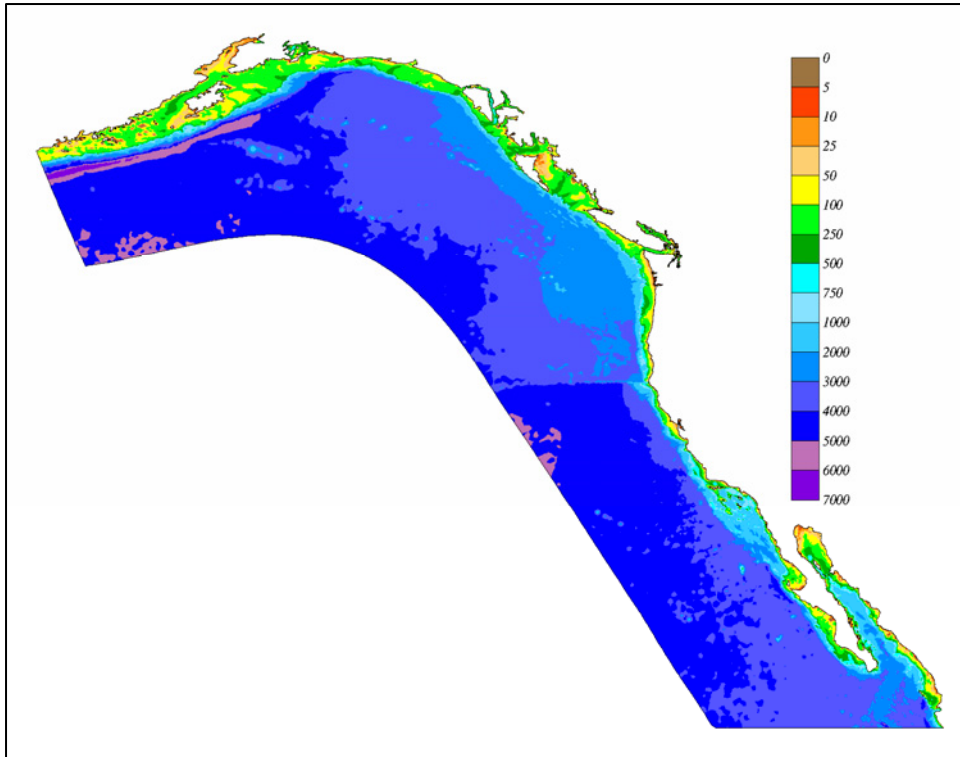


Figure 57. ENPAC 2003 bathymetry (meters)

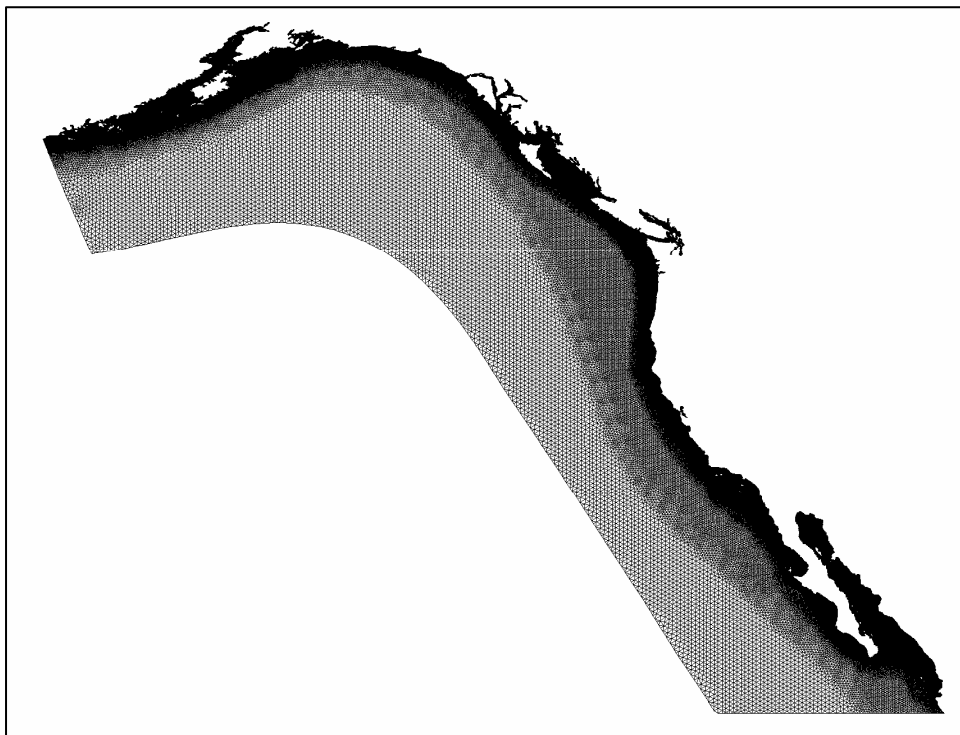


Figure 58. ENPAC 2003 finite element grid

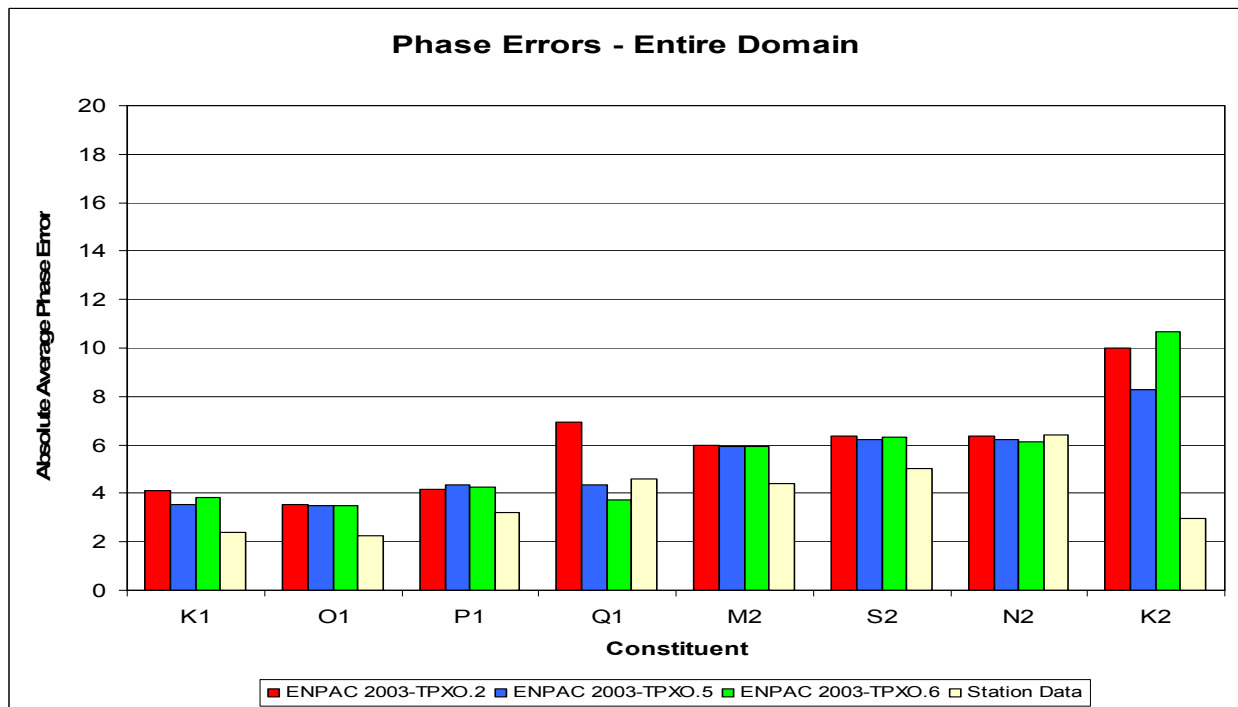
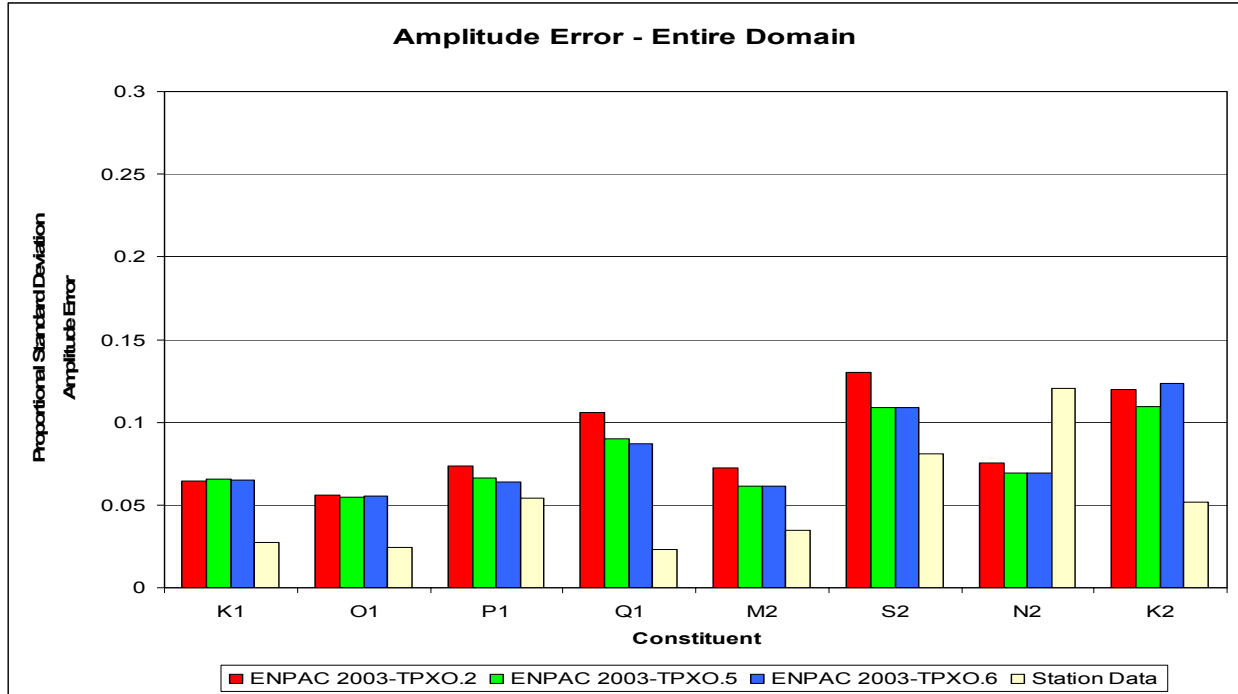


Figure 59. Proportional standard deviation amplitude errors and absolute average phase errors for 91 stations over entire domain for ENPAC 2003 model with TPXO.2, TPXO.5, and TPXO.6 open boundary forcing

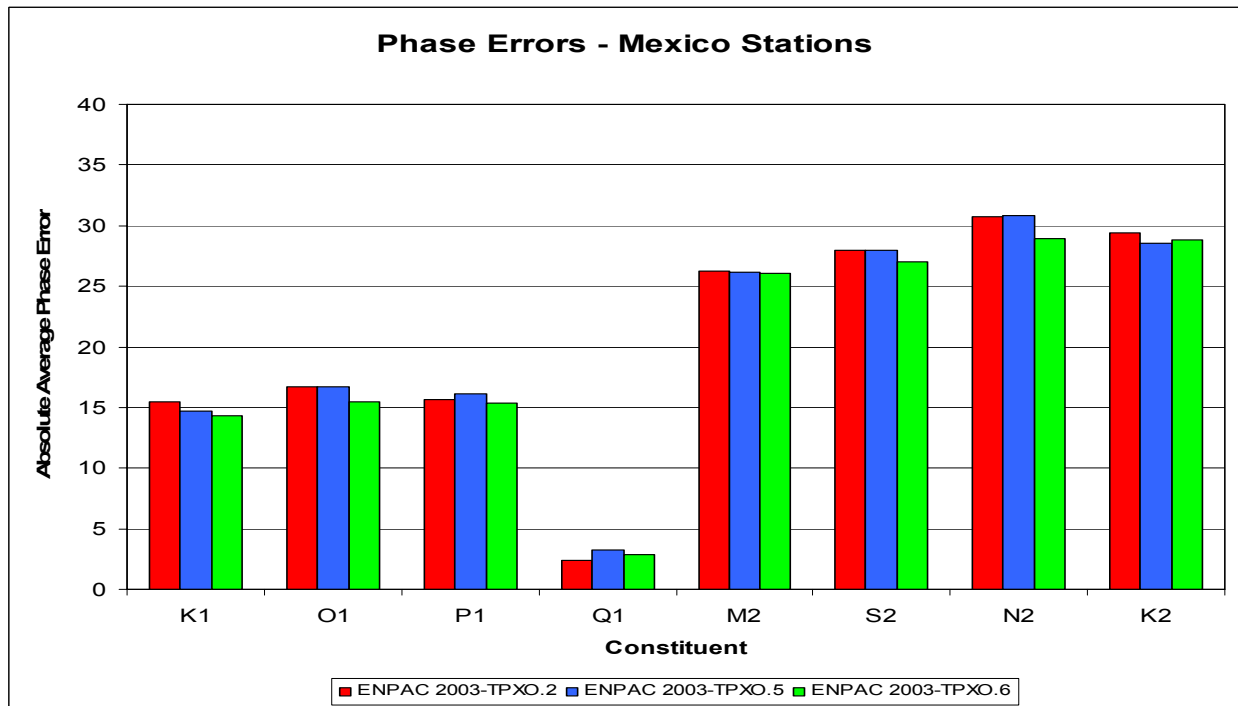
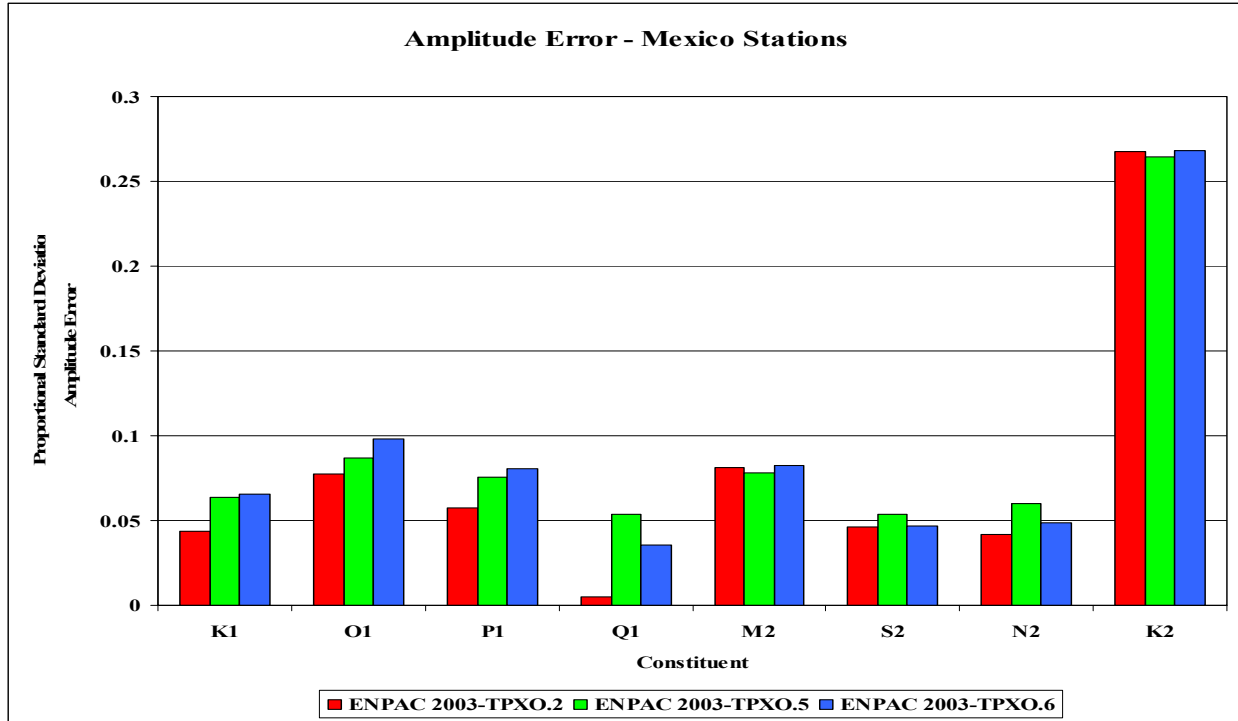


Figure 60. Proportional standard deviation amplitude errors and absolute average phase errors for five stations in Mexico subdomain for ENPAC 2003 model with TPXO.2, TPXO.5, and TPXO.6 open boundary forcing

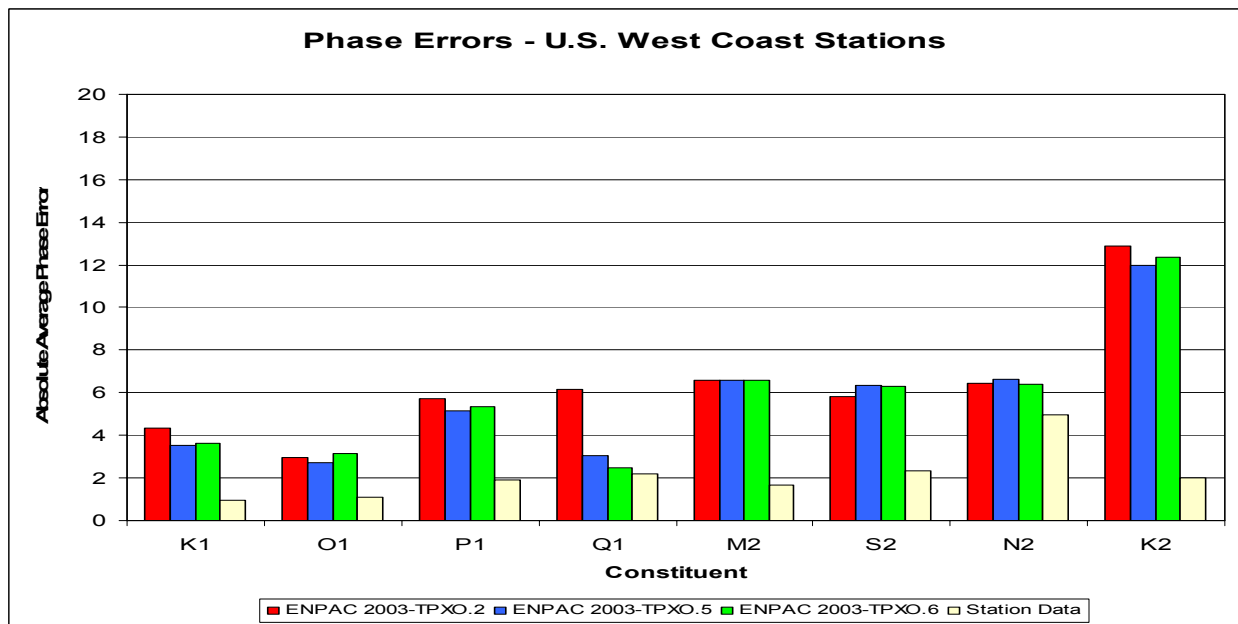
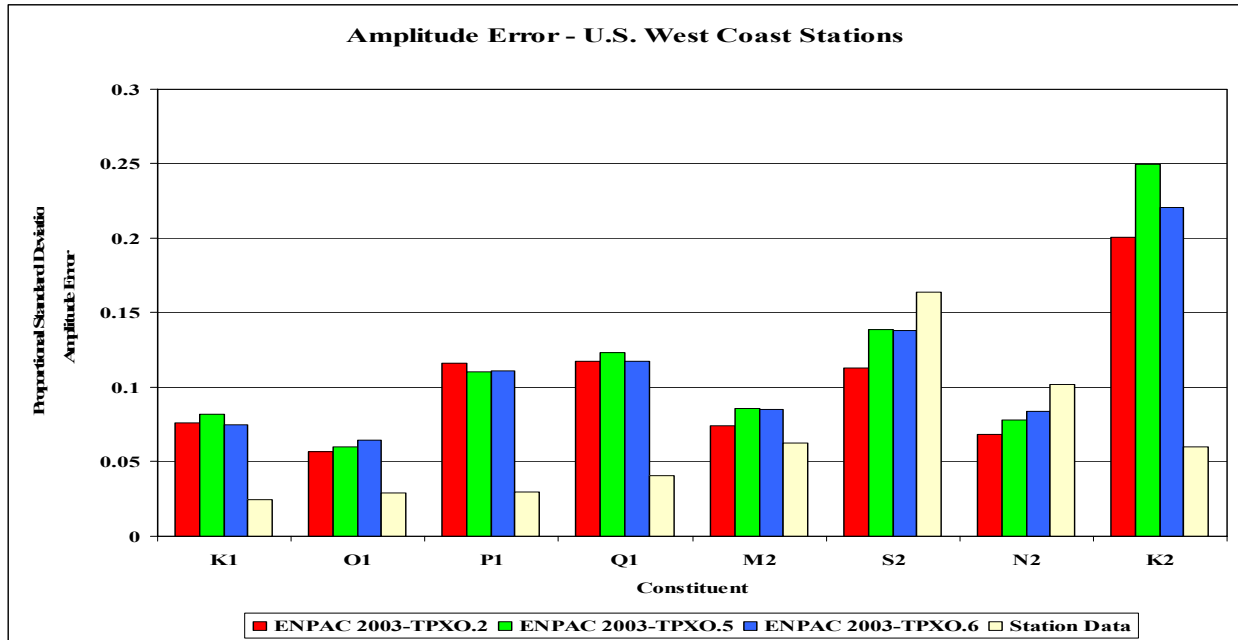


Figure 61. Proportional standard deviation amplitude errors and absolute average phase errors for 17 stations in U.S. west coast subdomain for ENPAC 2003 model with TPXO.2, TPXO.5, and TPXO.6 open boundary forcing

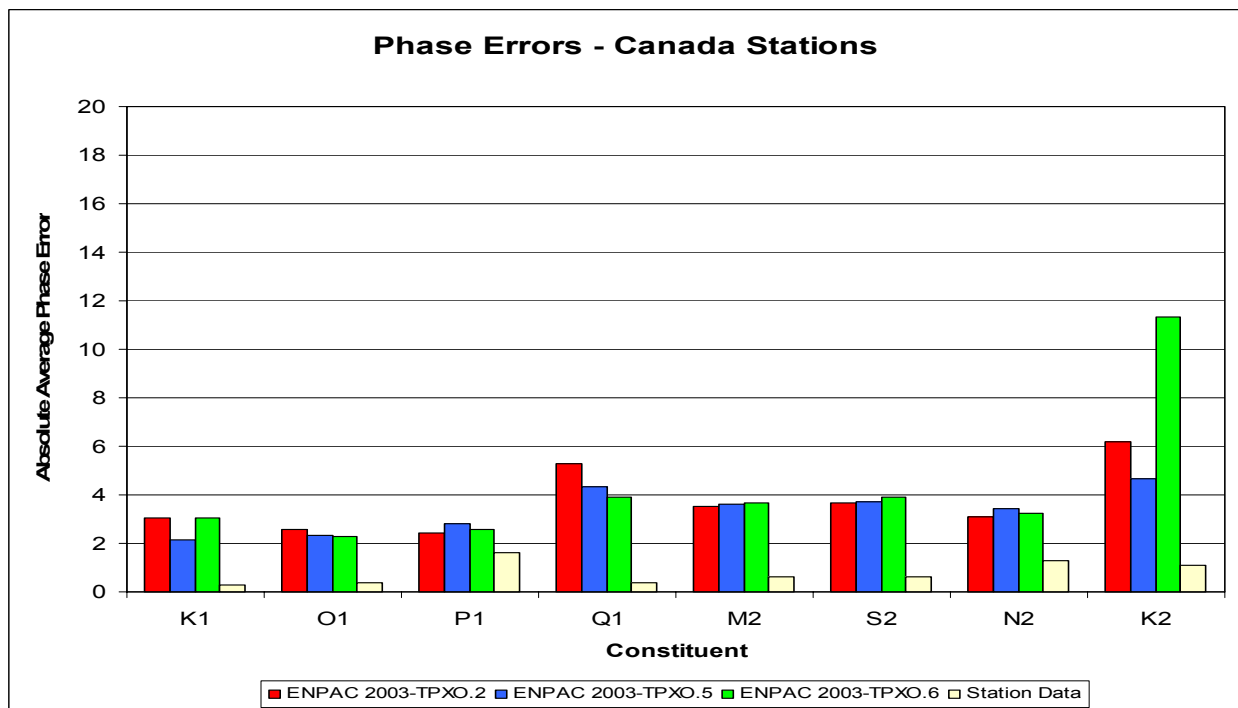
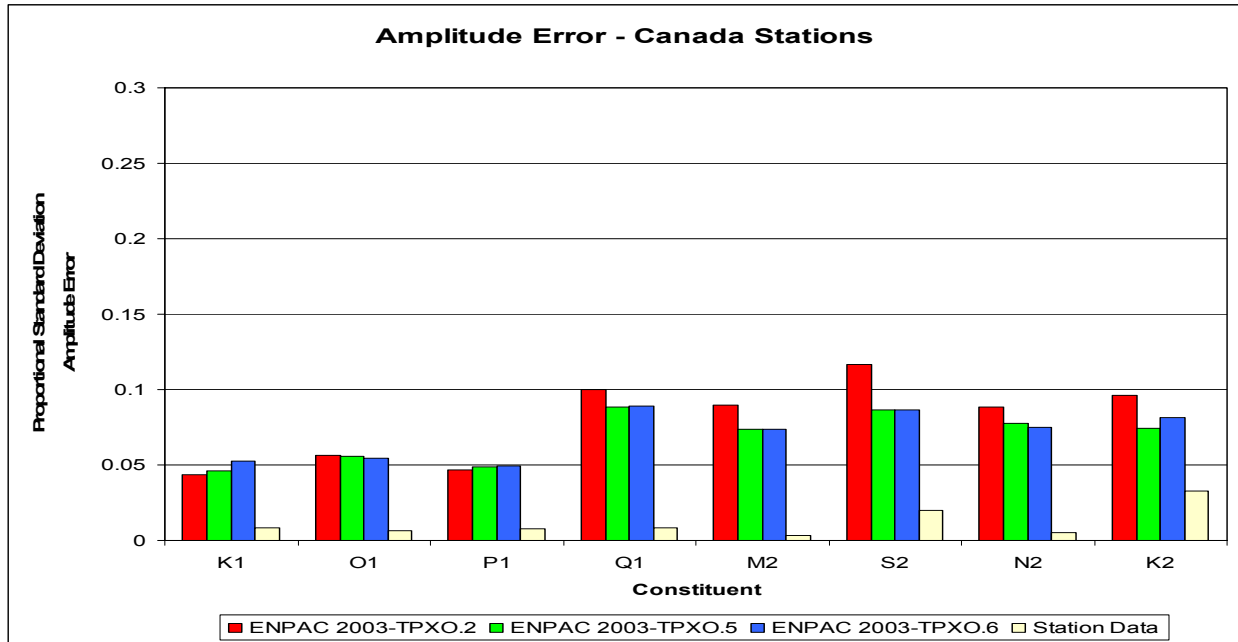


Figure 62. Proportional standard deviation amplitude errors and absolute average phase errors for 31 stations in Canada subdomain for ENPAC 2003 model with TPXO.2, TPXO.5, and TPXO.6 open boundary forcing

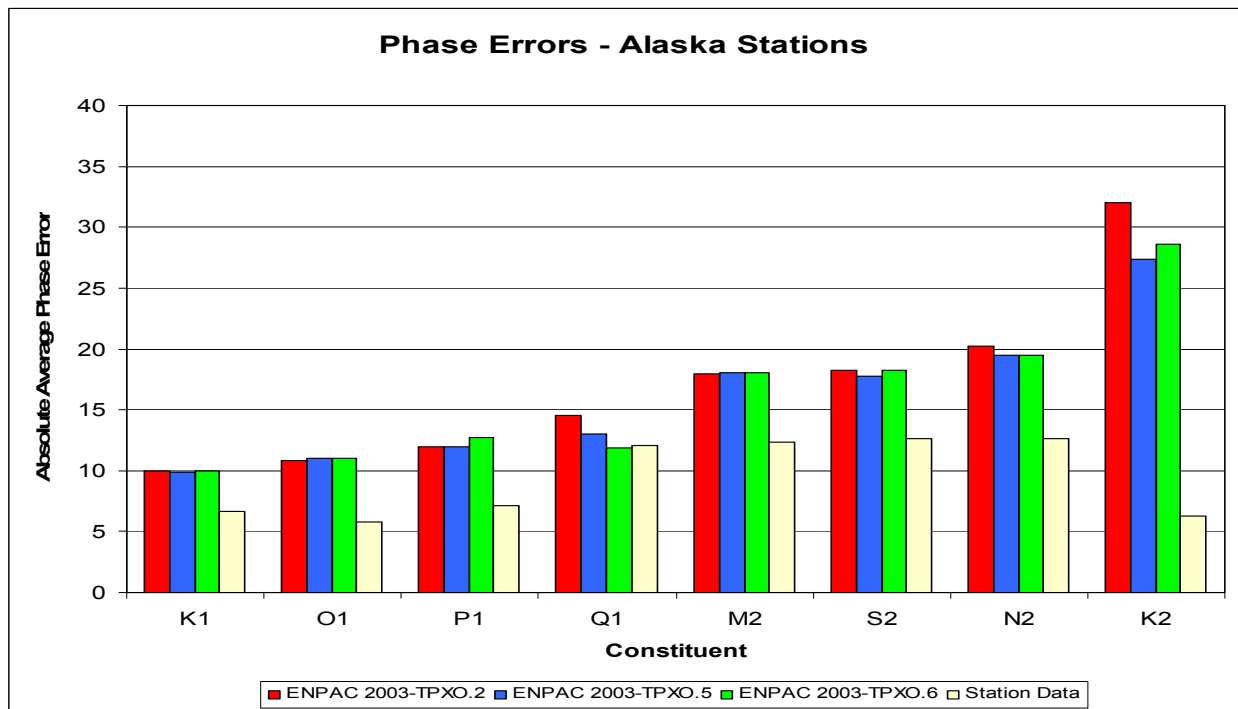
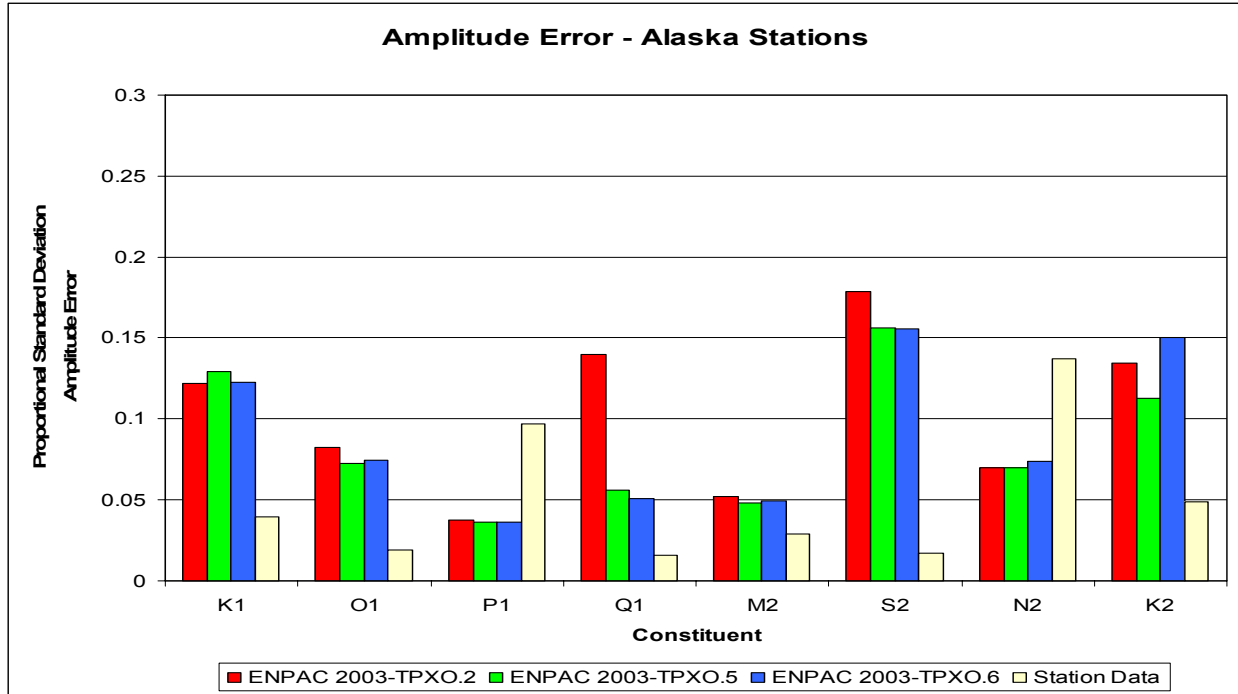


Figure 63. Proportional standard deviation amplitude errors and absolute average phase errors for 37 stations in Alaska subdomain for ENPAC 2003 model with TPXO.2, TPXO.5, and TPXO.6 open boundary

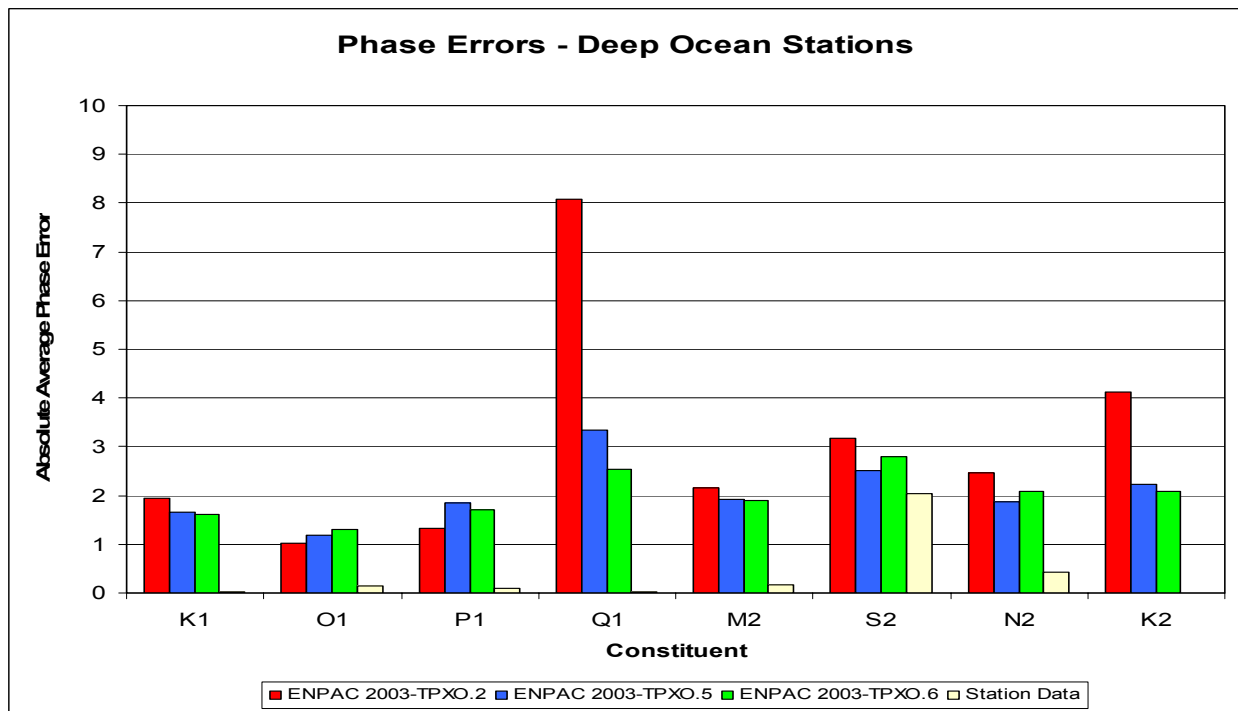
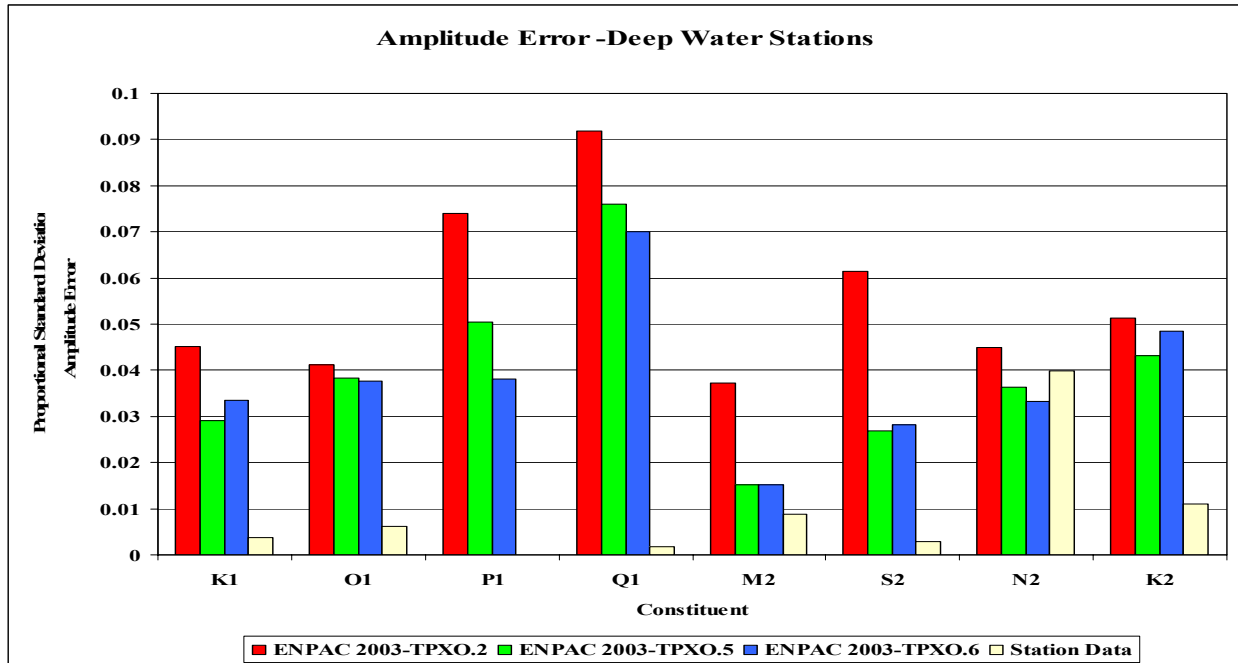


Figure 64. Proportional standard deviation amplitude errors and absolute average phase errors for 31 stations in deep ocean subdomain for ENPAC 2003 model with TPXO.2, TPXO.5, and TPXO.6 open boundary forcing

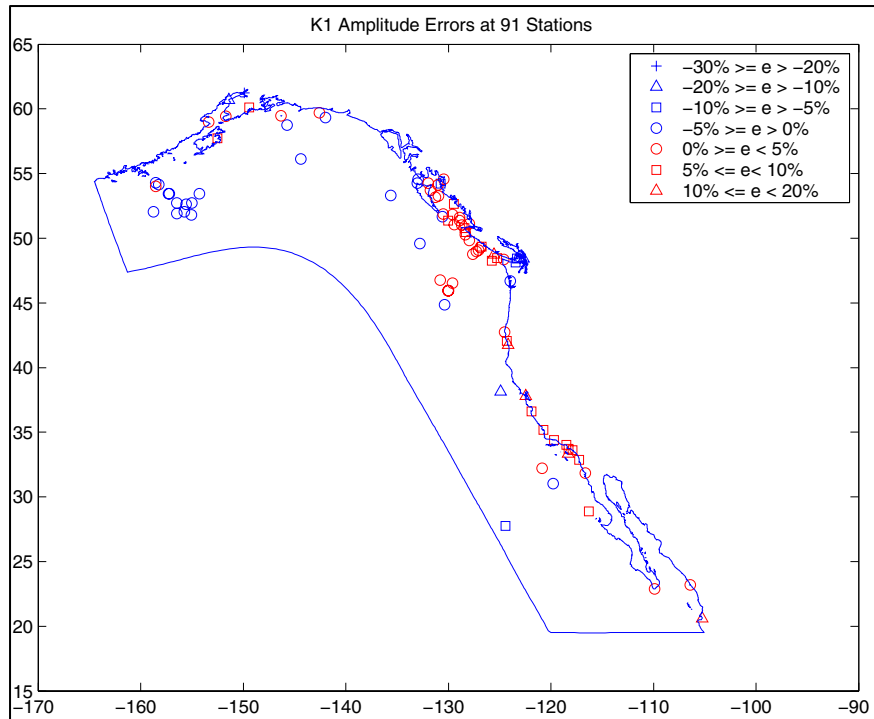


Figure 65. K_1 amplitude errors (percent) for ENPAC 2003 model with TPXO.5 open boundary forcing

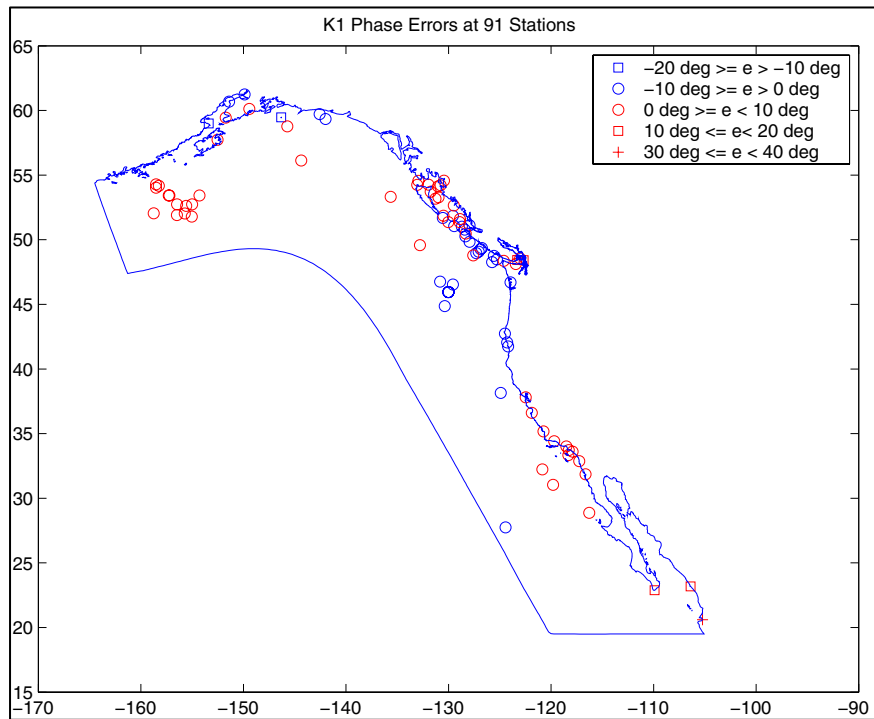


Figure 66. K_1 phase errors (degree) for ENPAC 2003 model with TPXO.5 open boundary forcing

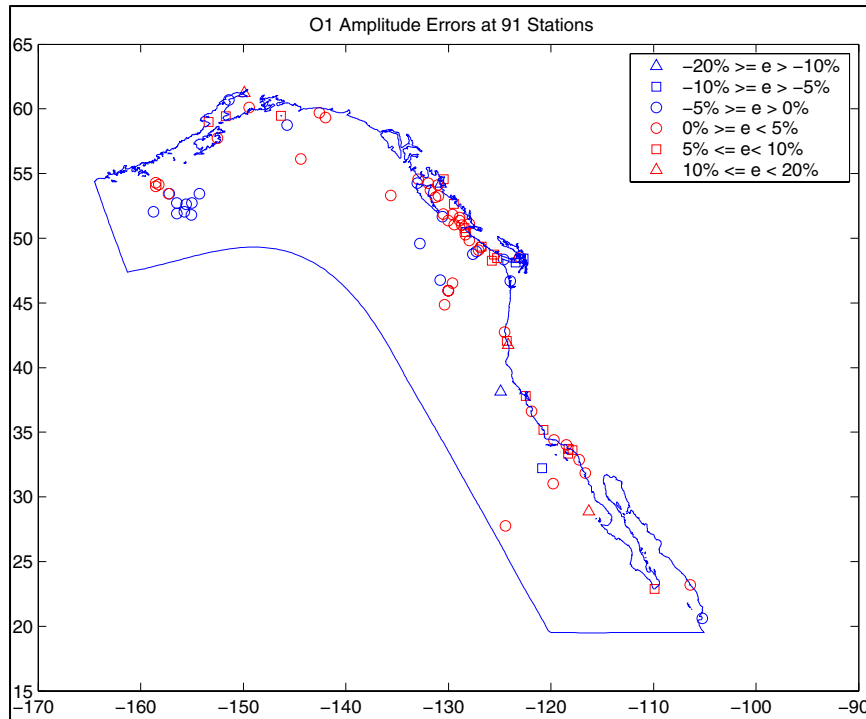


Figure 67. O₁ amplitude errors (percent) for ENPAC 2003 model with TPXO.5 open boundary forcing

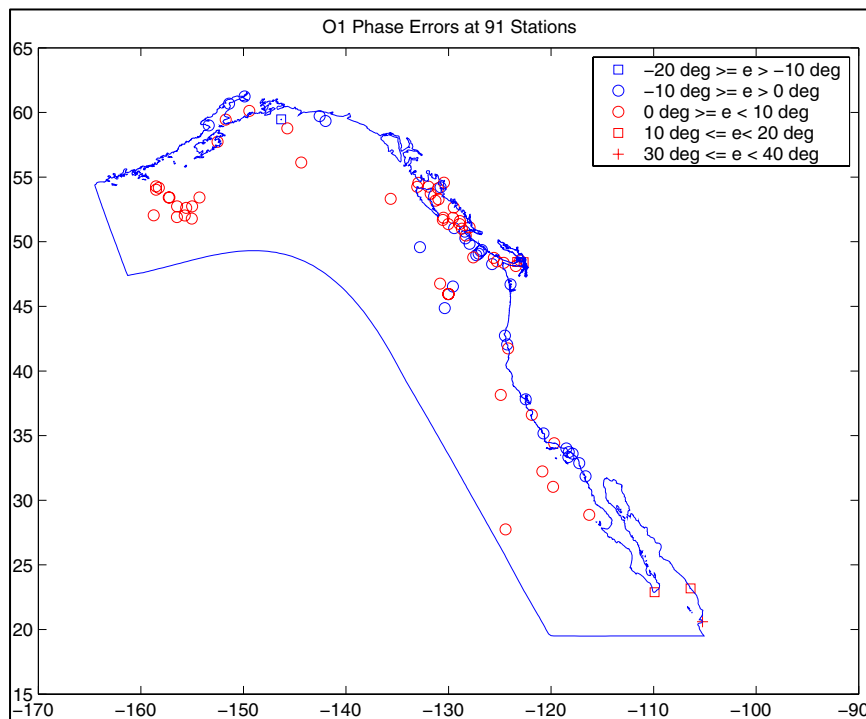


Figure 68. O₁ phase errors (degree) for ENPAC 2003 model with TPXO.5 open boundary forcing

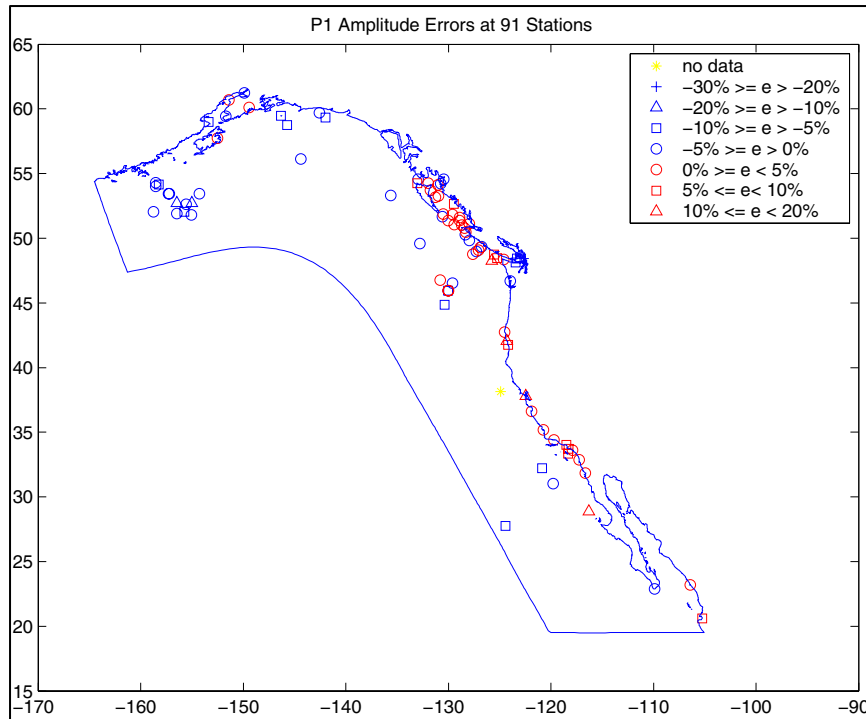


Figure 69. P_1 amplitude errors (percent) for ENPAC 2003 model with TPXO.5 open boundary forcing

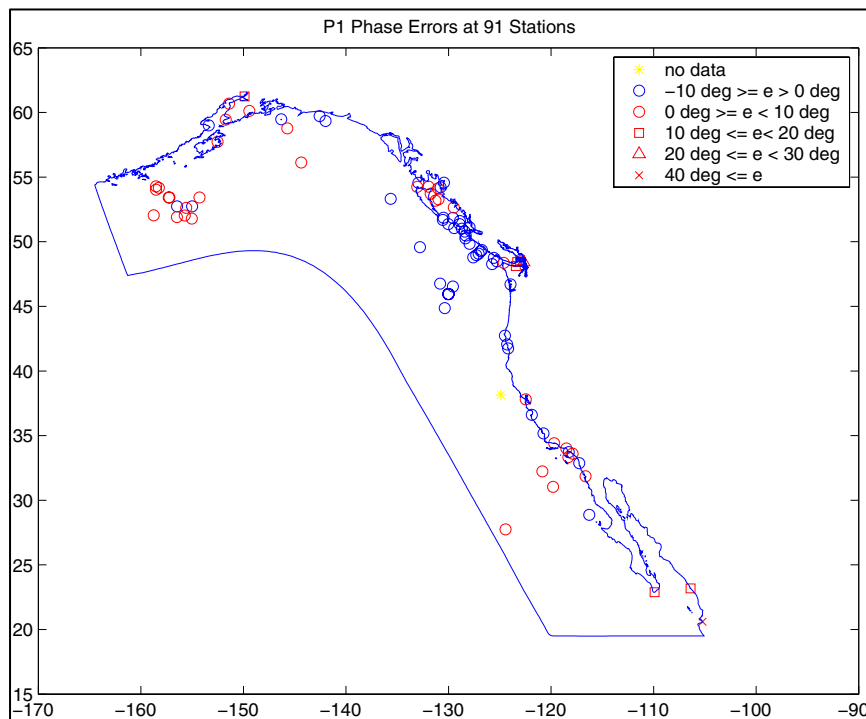


Figure 70. P_1 phase errors (degree) for ENPAC 2003 model with TPXO.5 open boundary forcing

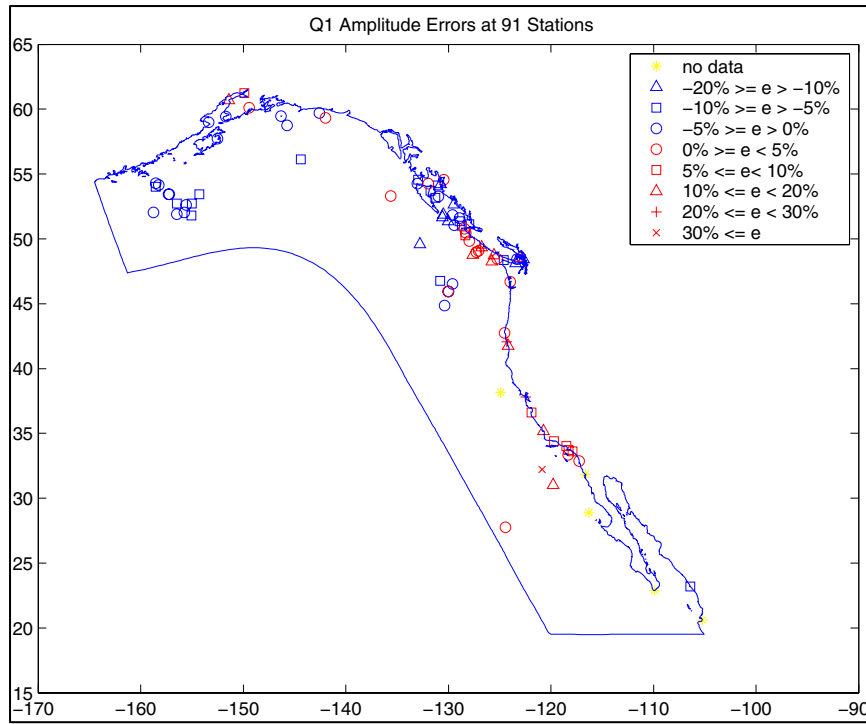


Figure 71. Q_1 amplitude errors (percent) for ENPAC 2003 model with TPXO.5 open boundary forcing

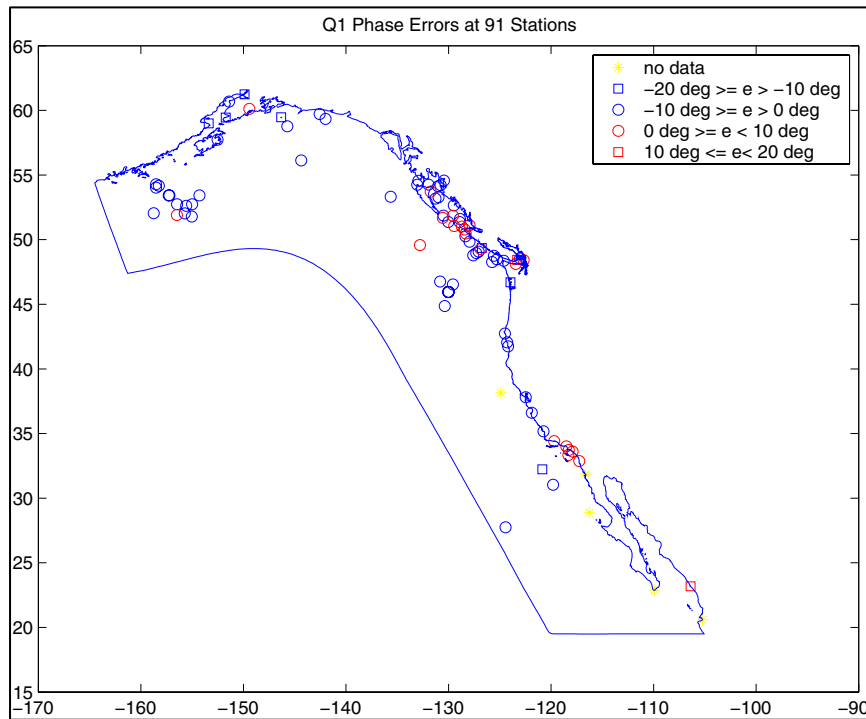


Figure 72. Q_1 phase errors (degree) for ENPAC 2003 model with TPXO.5 open boundary forcing

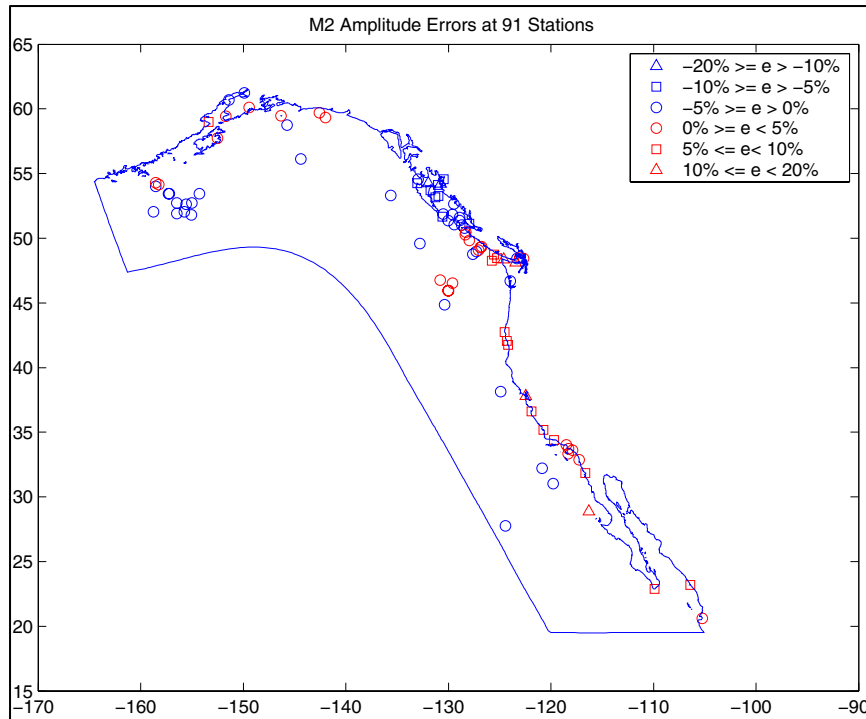


Figure 73. M_2 amplitude errors (percent) for ENPAC 2003 model with TPXO.5 open boundary forcing

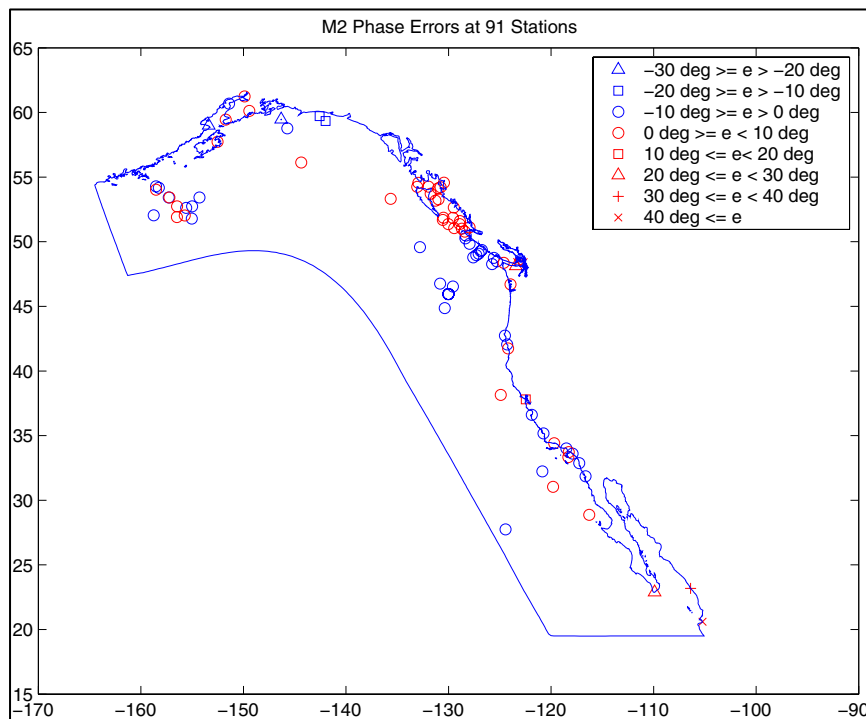


Figure 74. M_2 phase errors (degrees) for ENPAC 2003 model with TPXO.5 open boundary forcing

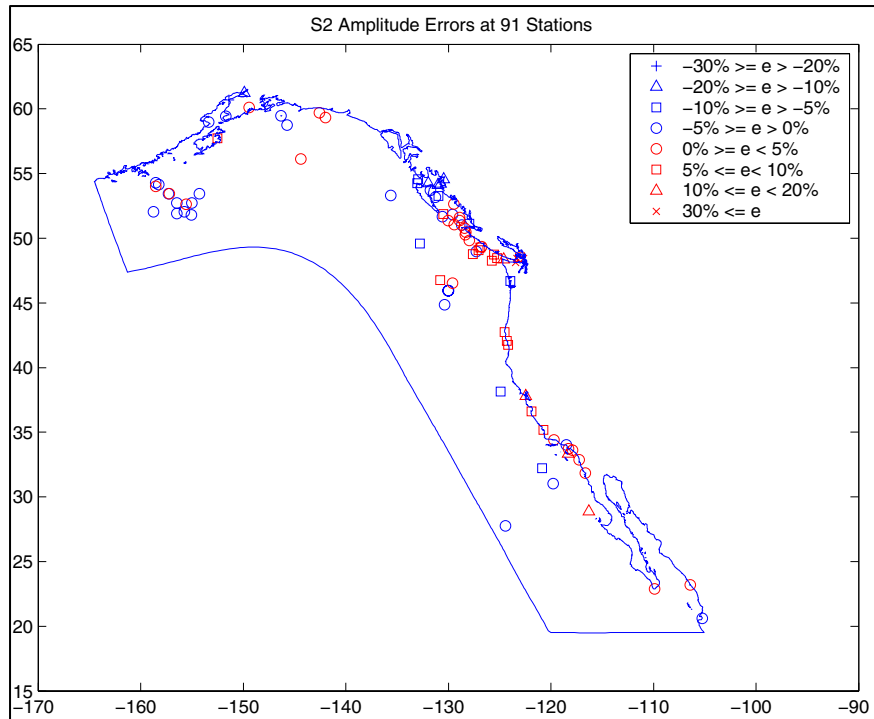


Figure 75. S_2 amplitude errors (percent) for ENPAC 2003 model with TPXO.5 open boundary forcing

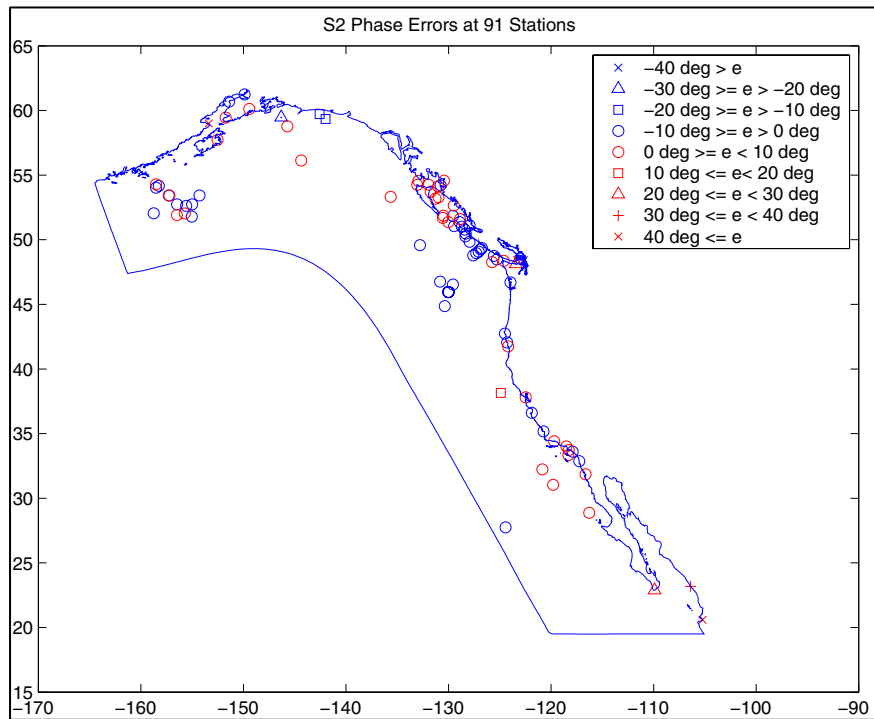


Figure 76. S_2 phase errors (degrees) for ENPAC 2003 model with TPXO.5 open boundary forcing

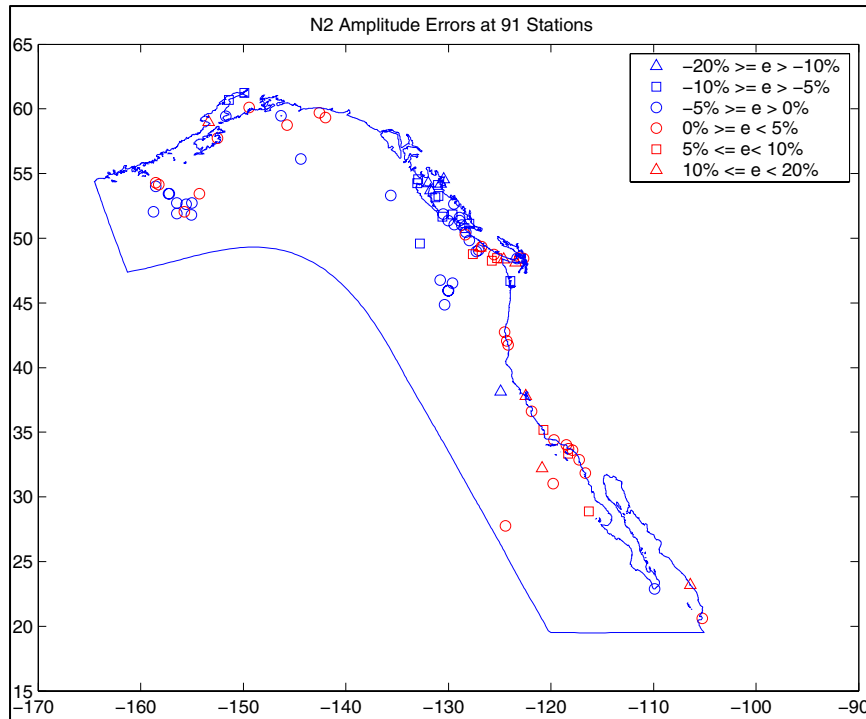


Figure 77. N₂ amplitude errors (percent) for ENPAC 2003 model with TPXO.5 open boundary forcing

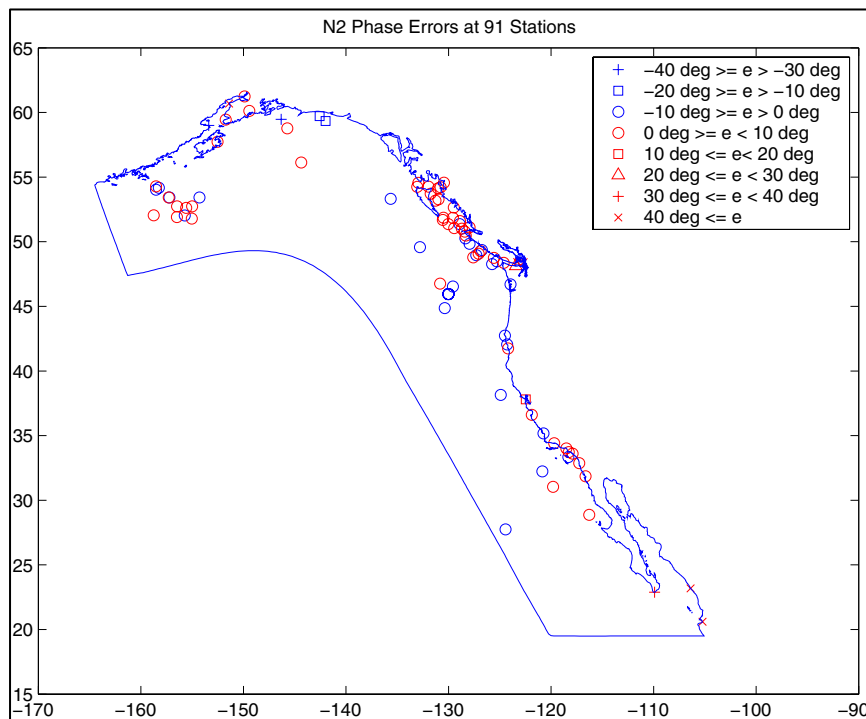


Figure 78. N₂ phase errors (degrees) for ENPAC 2003 model with TPXO.5 open boundary forcing

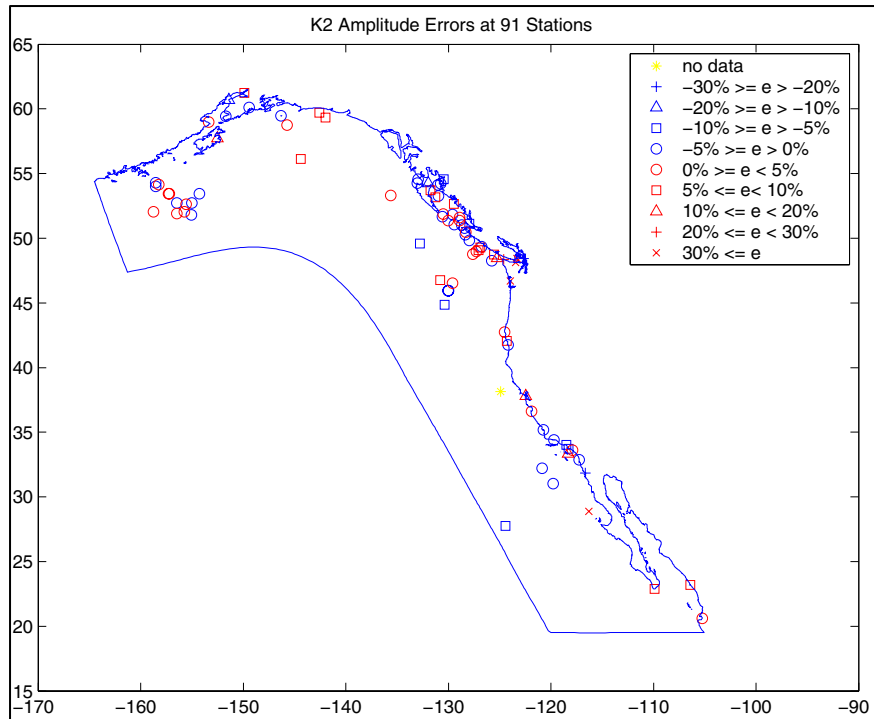


Figure 79. K_2 amplitude errors (percent) for ENPAC 2003 model with TPXO.5 open boundary forcing

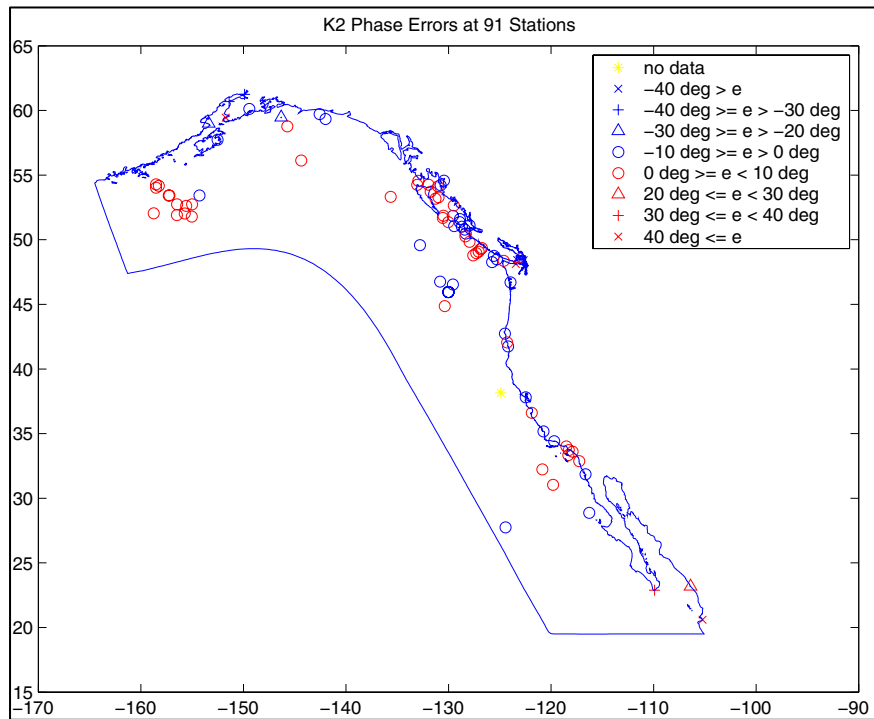


Figure 80. K_2 phase errors (degrees) for ENPAC 2003 model with TPXO.5 open boundary forcing

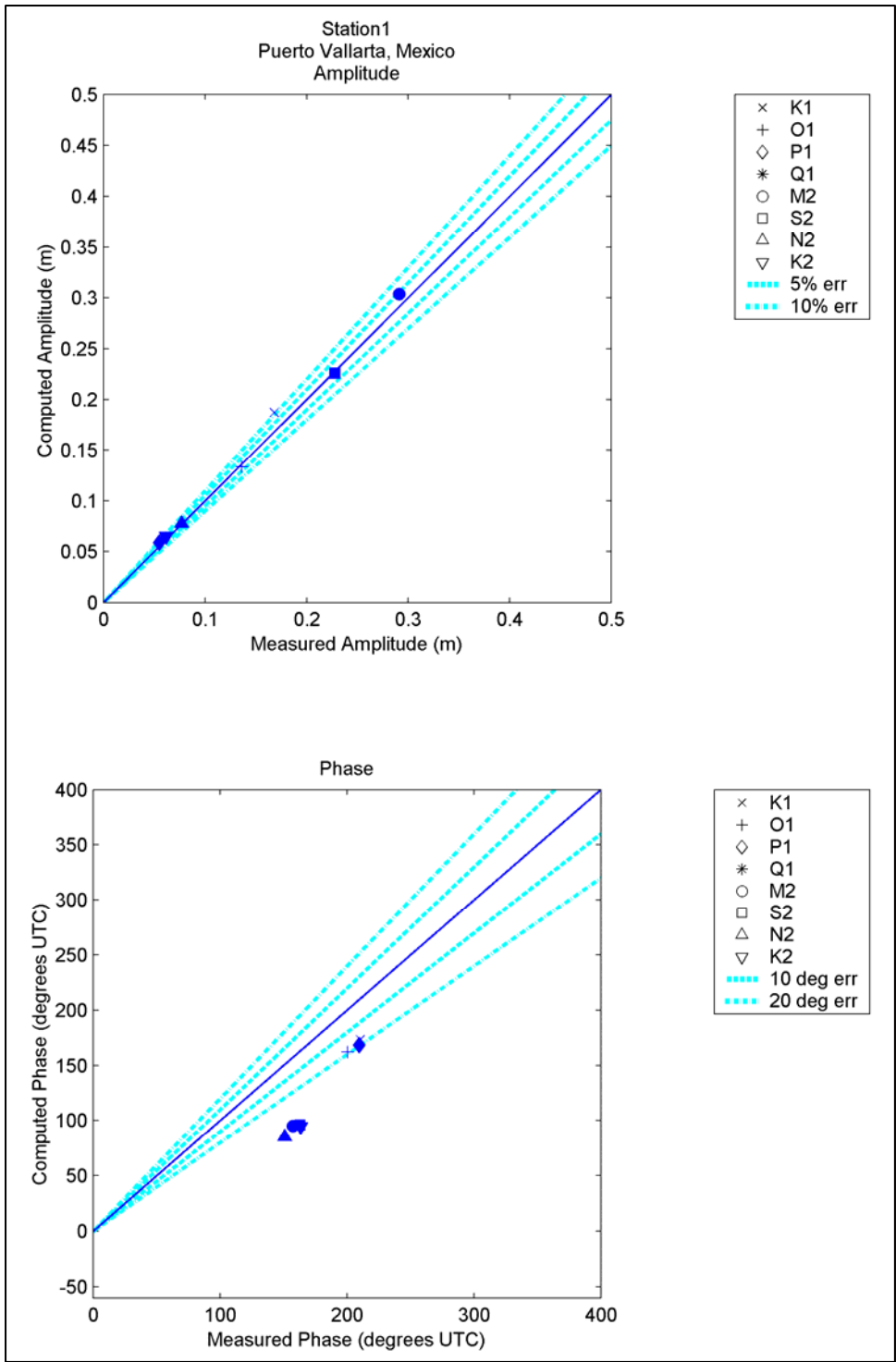


Figure 81. Computed vs. measured harmonic constituents at sta 1

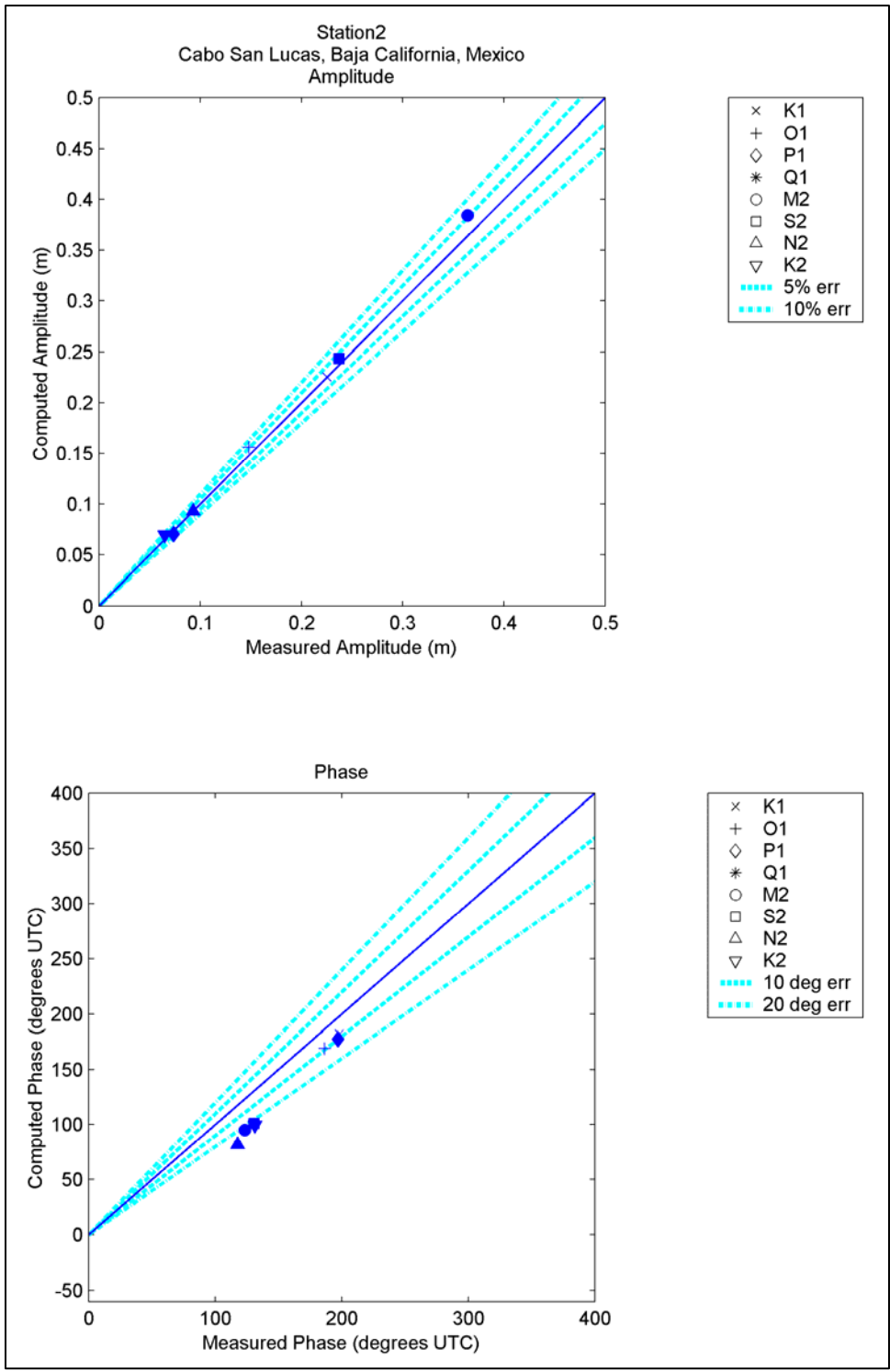


Figure 82. Computed vs. measured harmonic constituents at sta 2

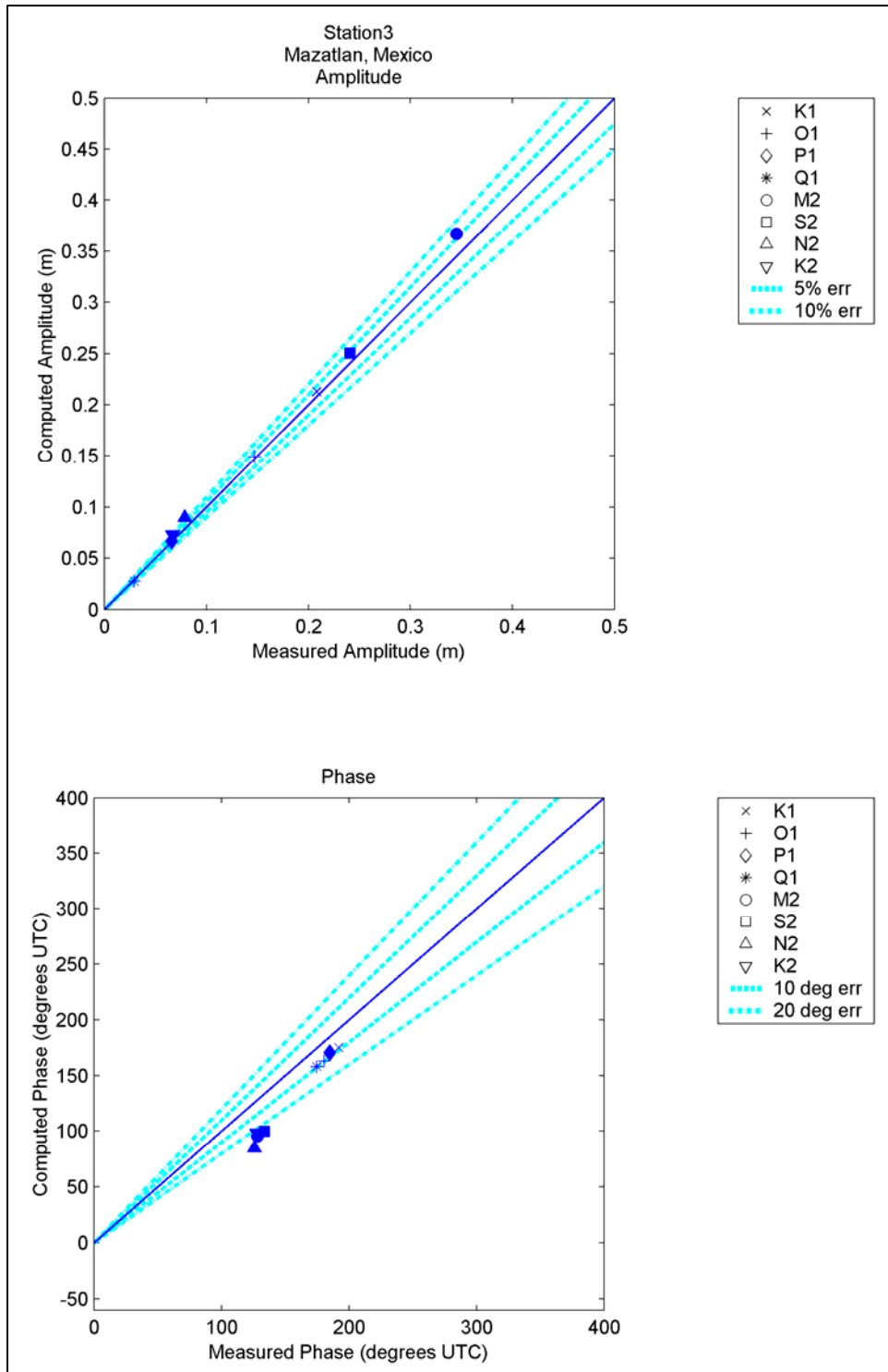


Figure 83. Computed vs. measured harmonic constituents at sta 3

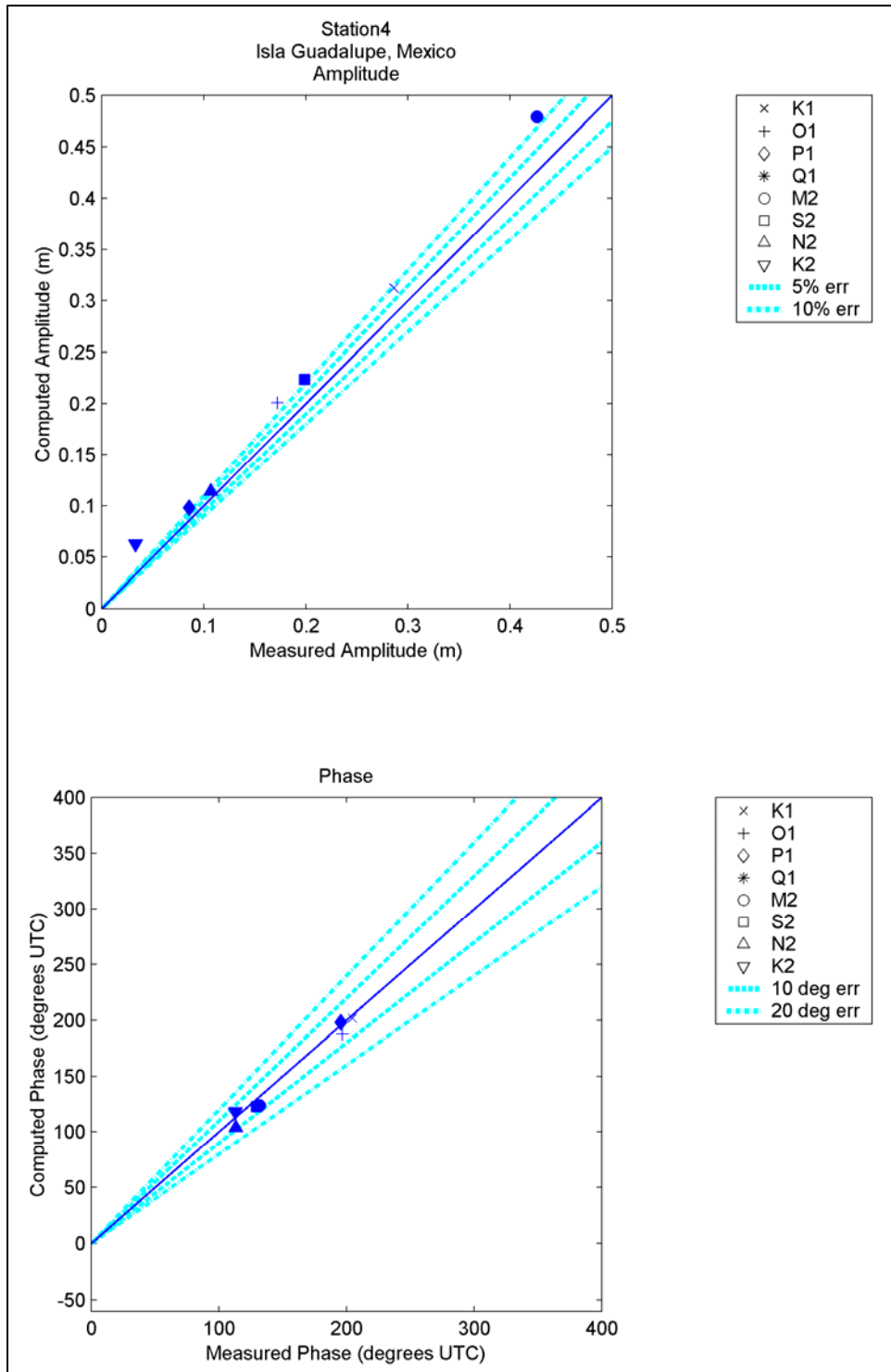


Figure 84. Computed vs. measured harmonic constituents at sta 4

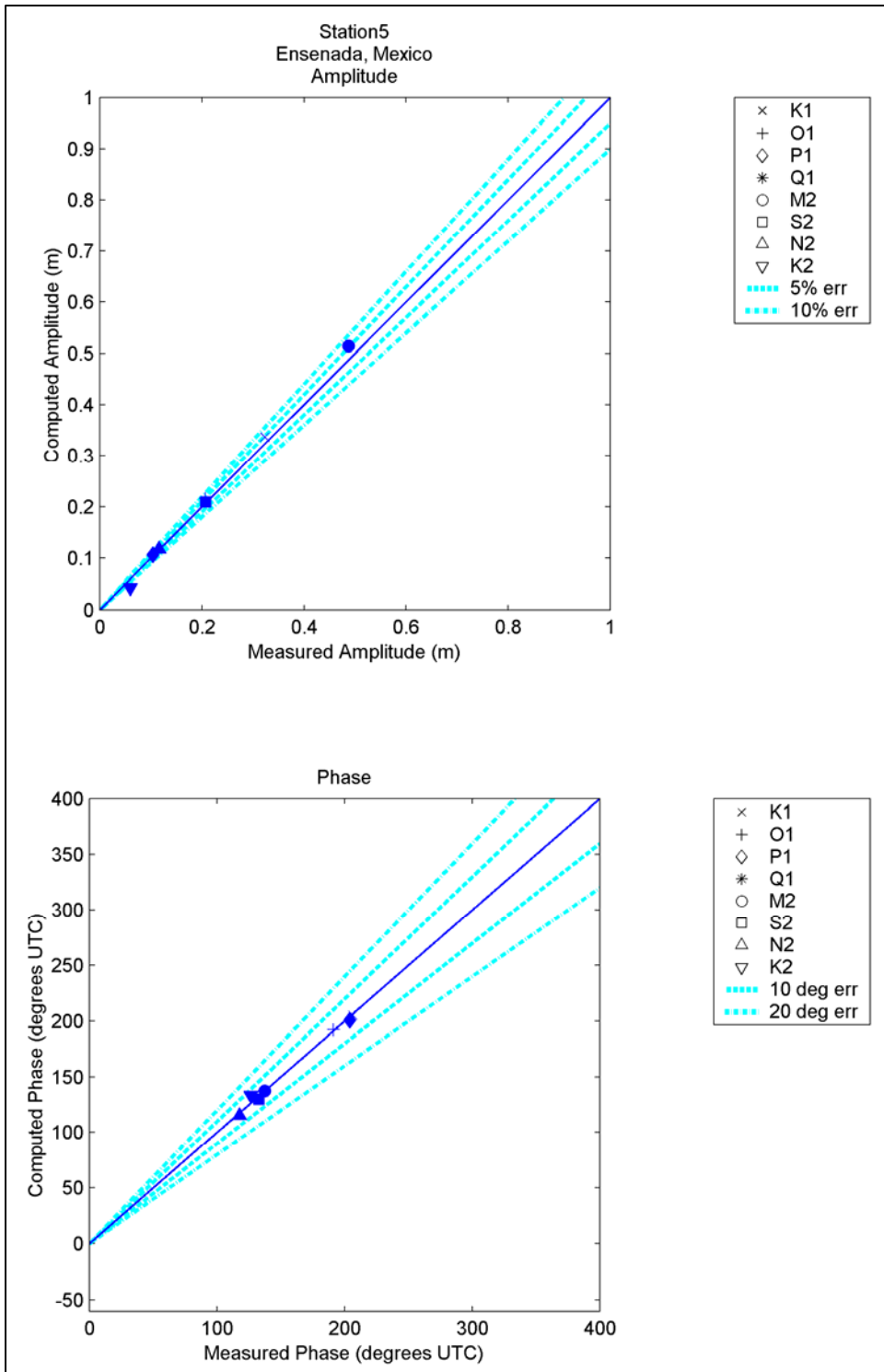


Figure 85. Computed vs. measured harmonic constituents at sta 5

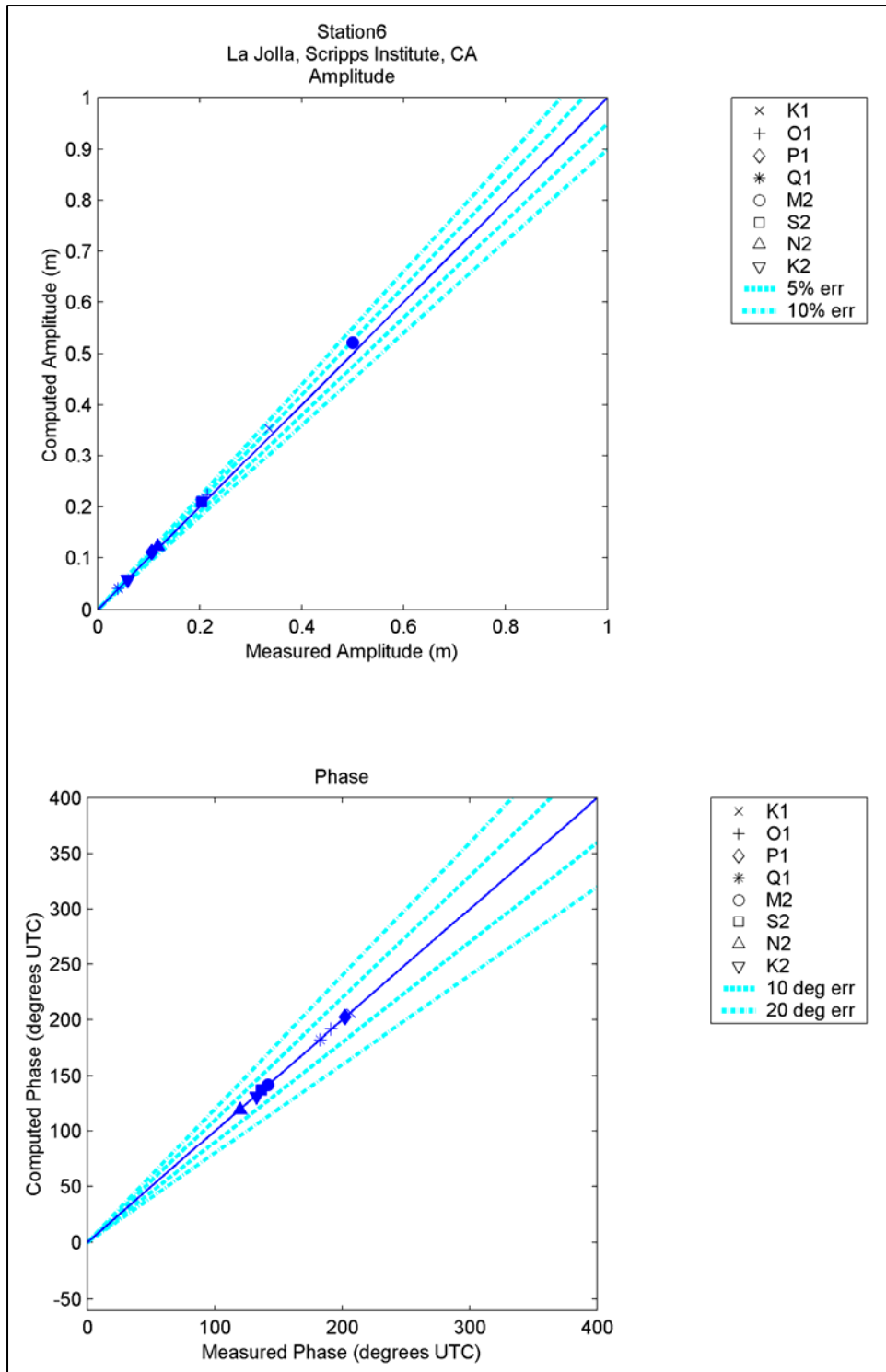


Figure 86. Computed vs. measured harmonic constituents at sta 6

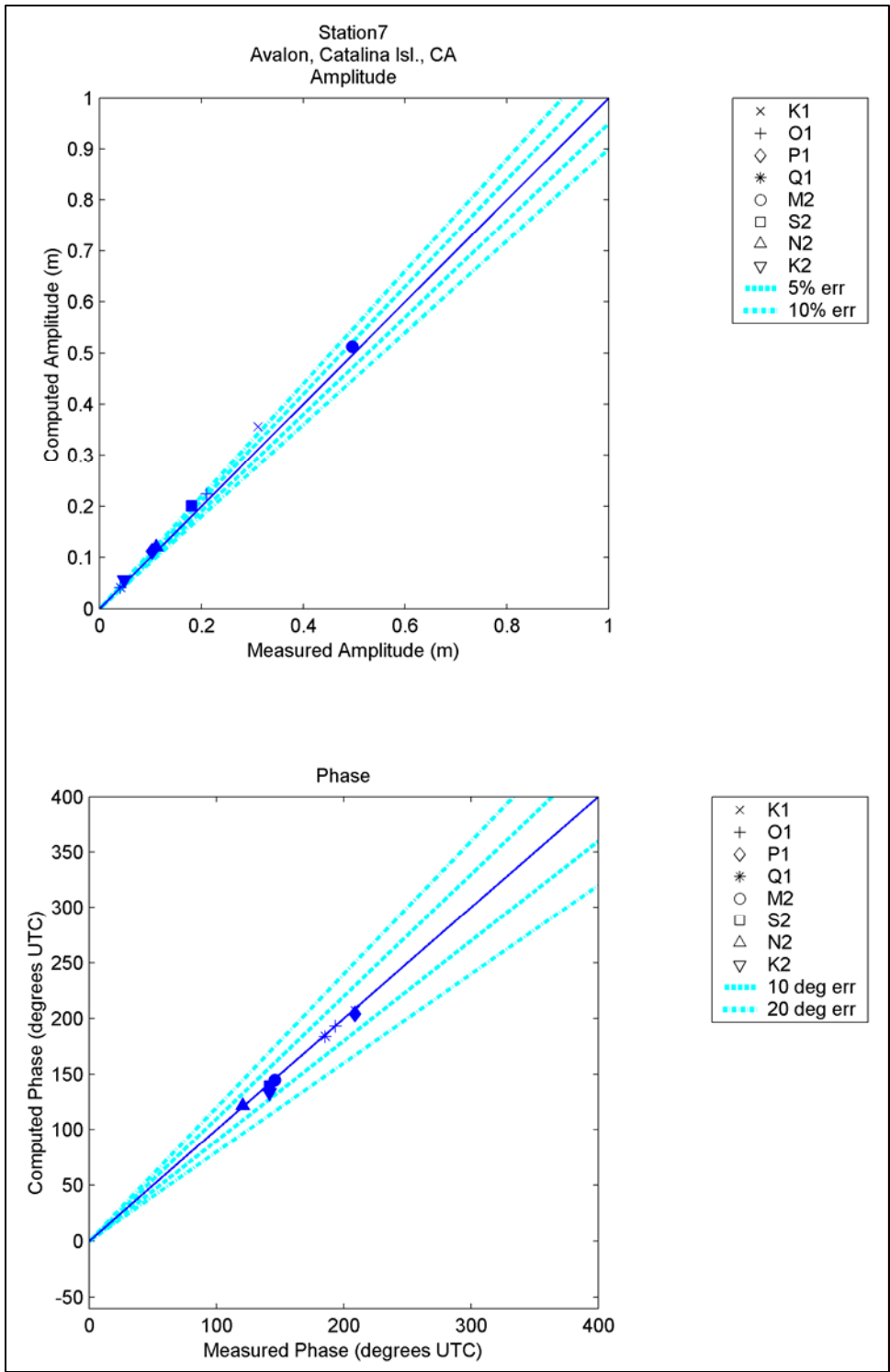


Figure 87. Computed vs. measured harmonic constituents at sta 7

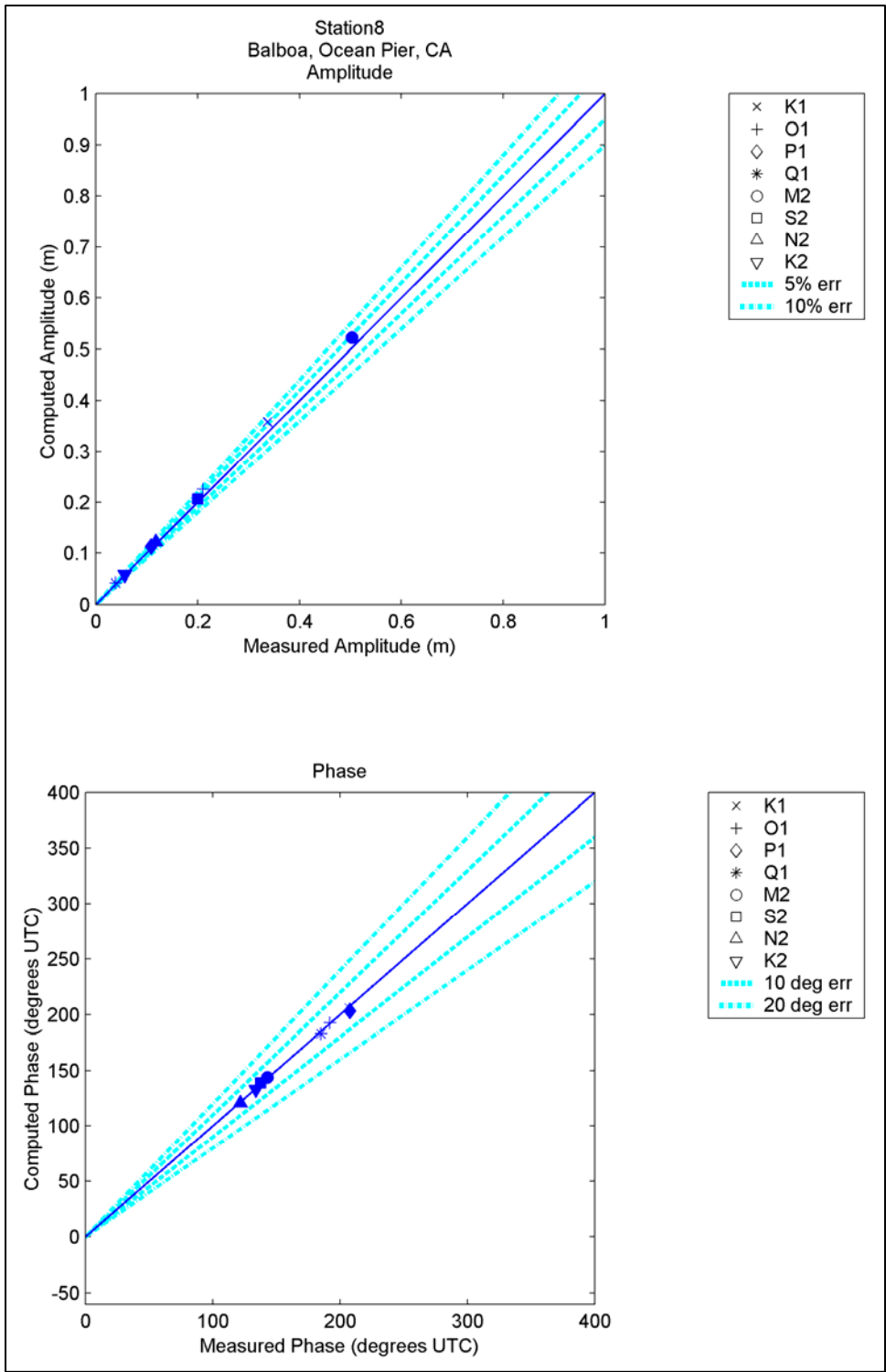


Figure 88. Computed vs. measured harmonic constituents at sta 8

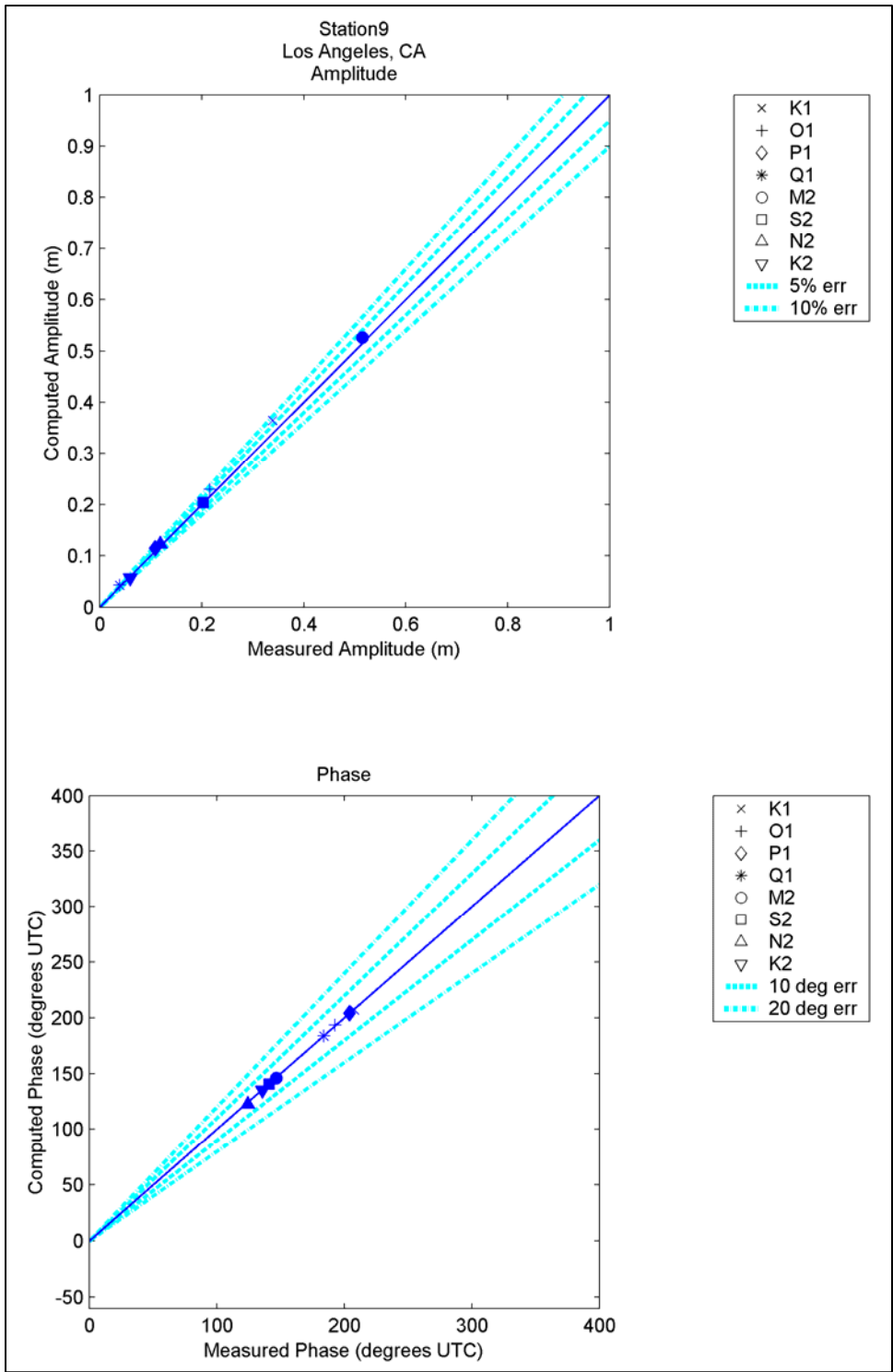


Figure 89. Computed vs. measured harmonic constituents at sta 9

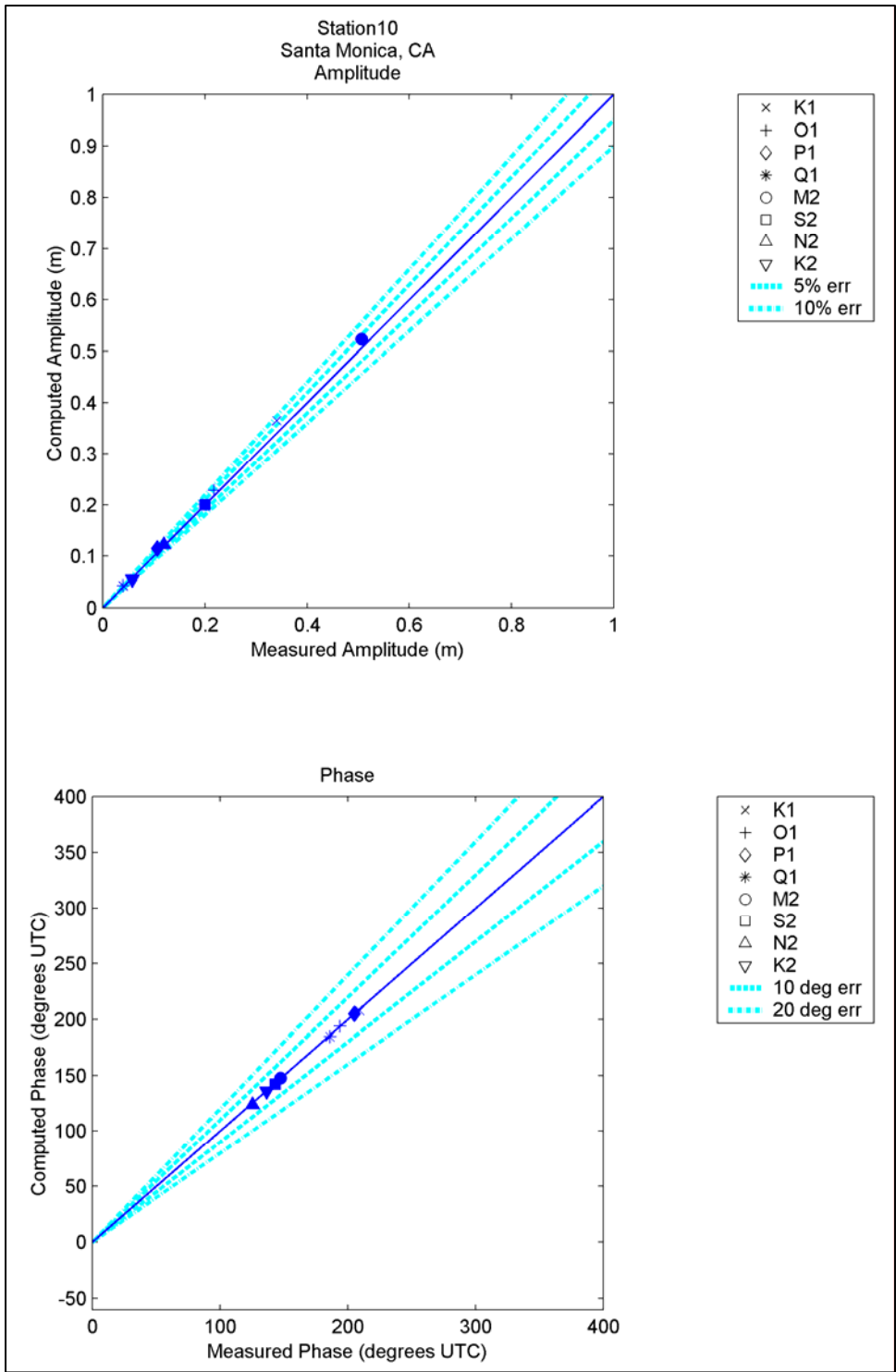


Figure 90. Computed vs. measured harmonic constituents at sta 10

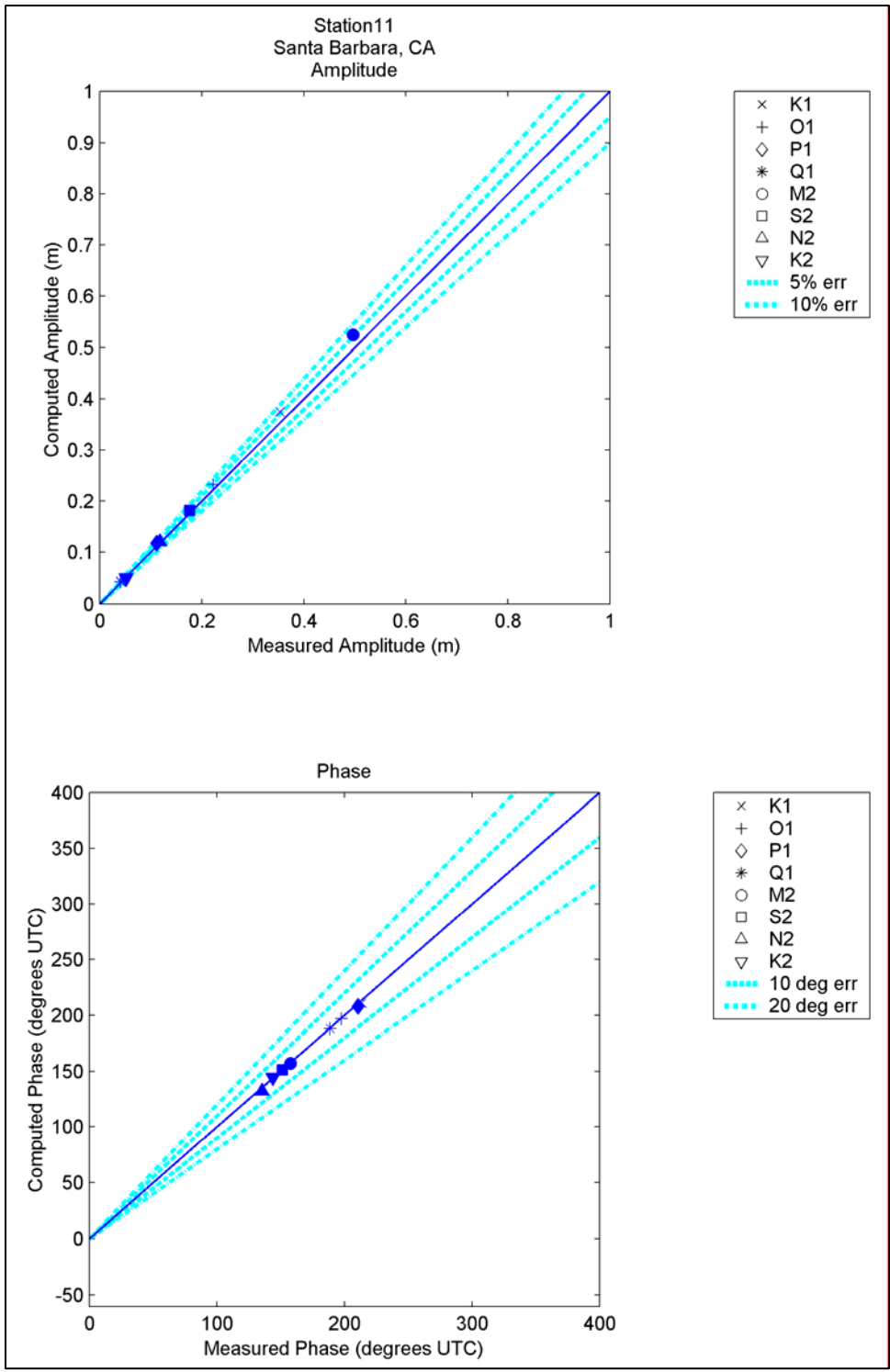


Figure 91. Computed vs. measured harmonic constituents at sta 11

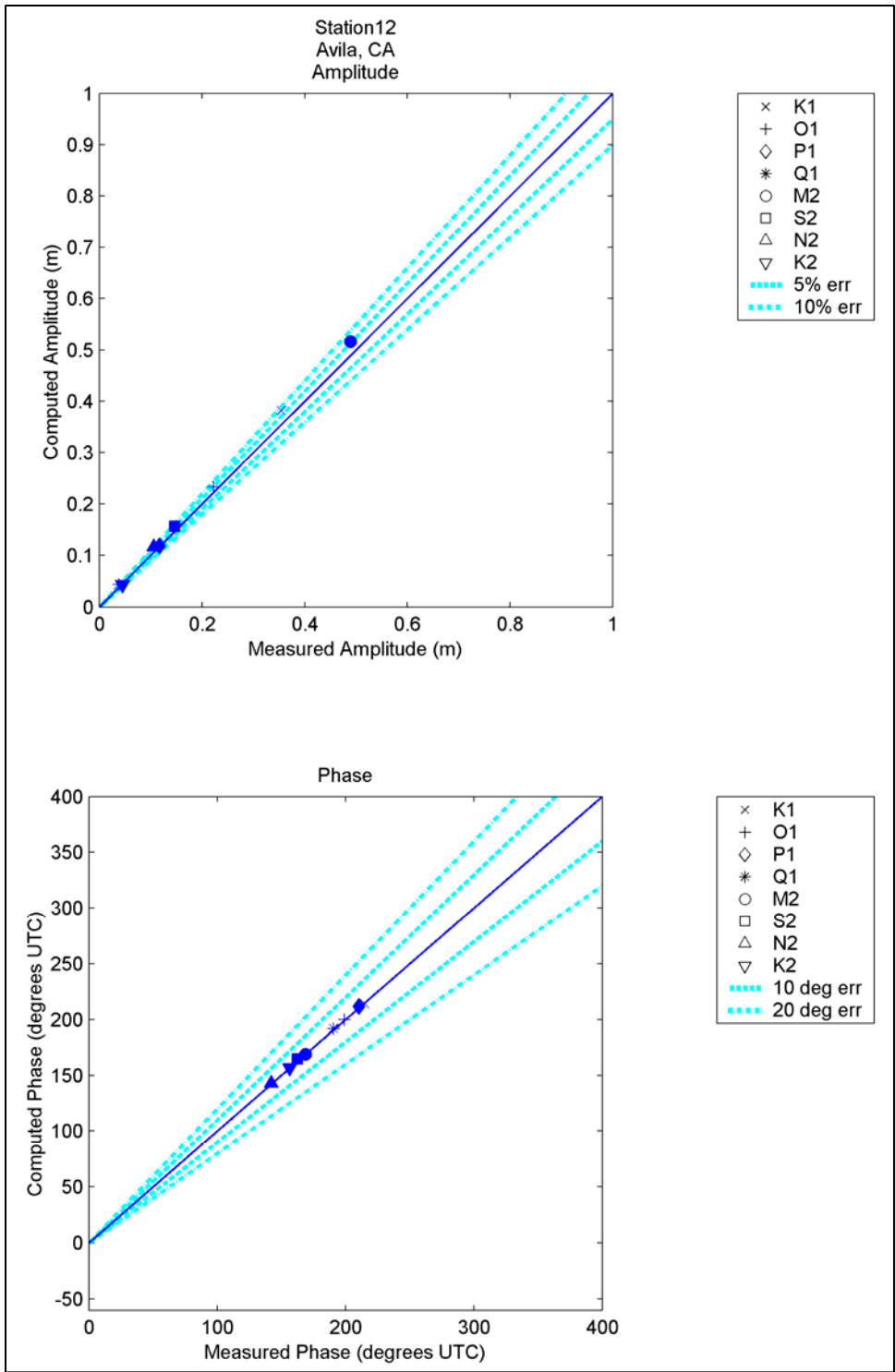


Figure 92. Computed vs. measured harmonic constituents at sta 12

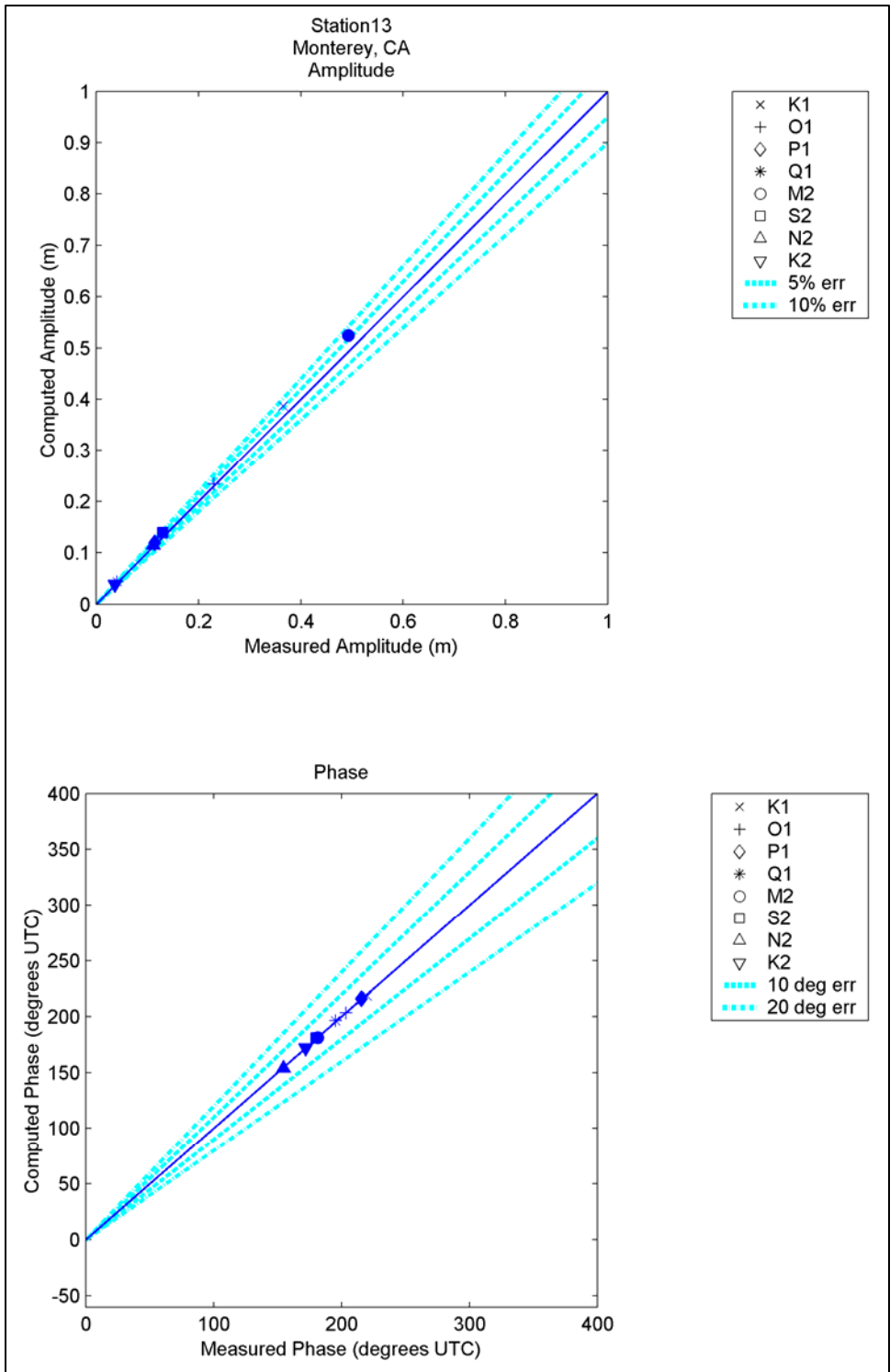


Figure 93. Computed vs. measured harmonic constituents at sta 13

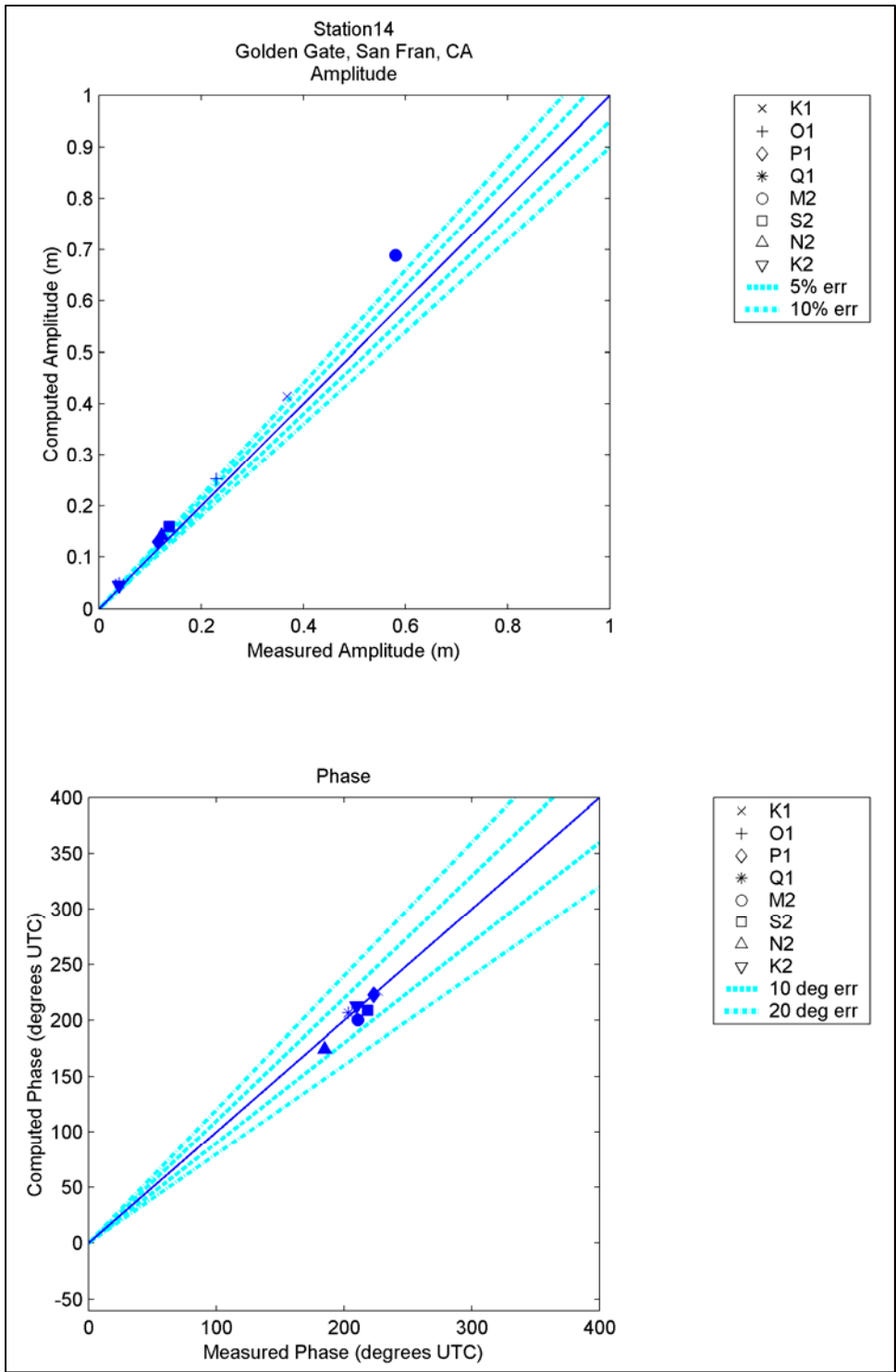


Figure 94. Computed vs. measured harmonic constituents at sta 14

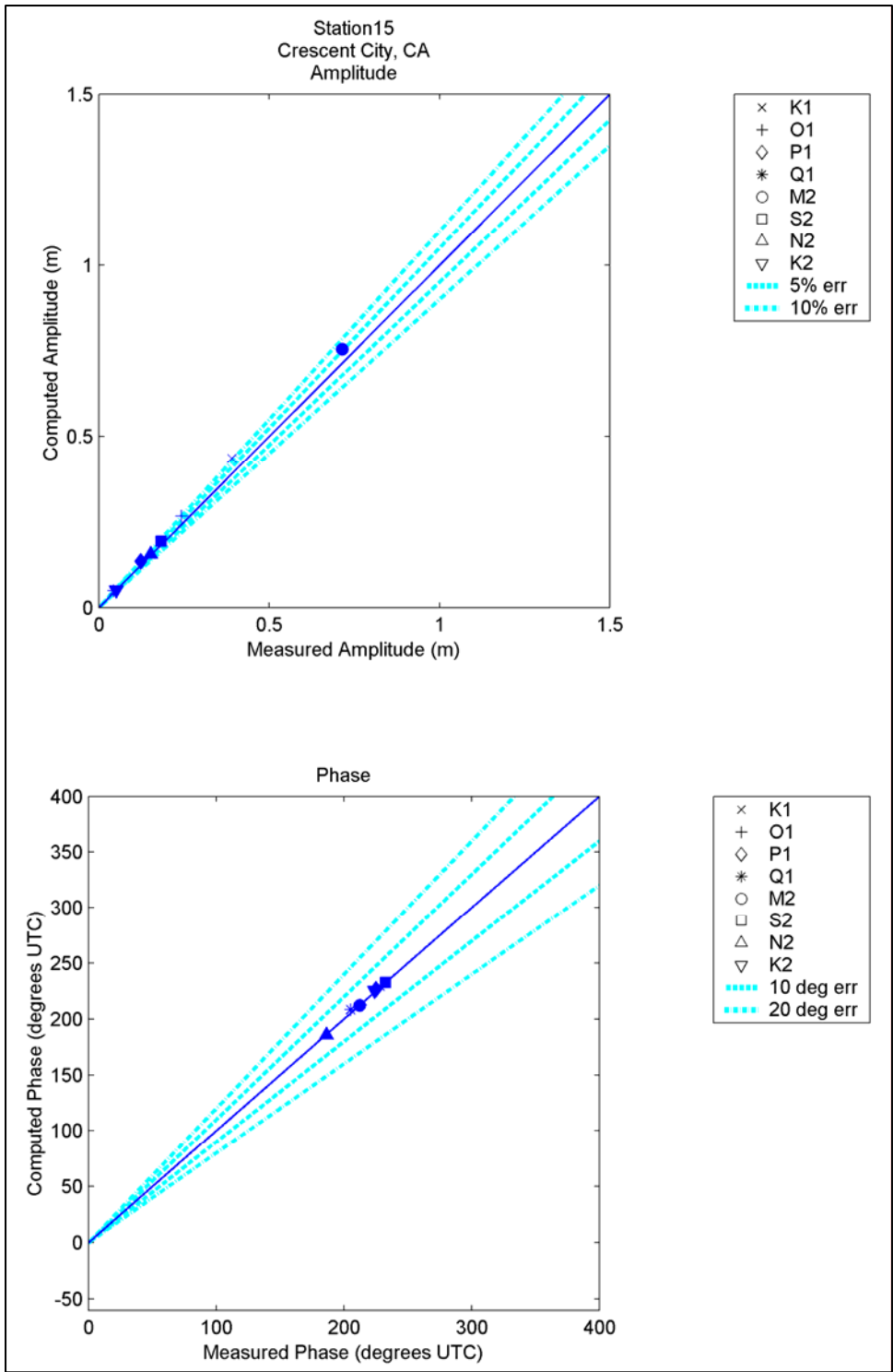


Figure 95. Computed vs. measured harmonic constituents at sta 15

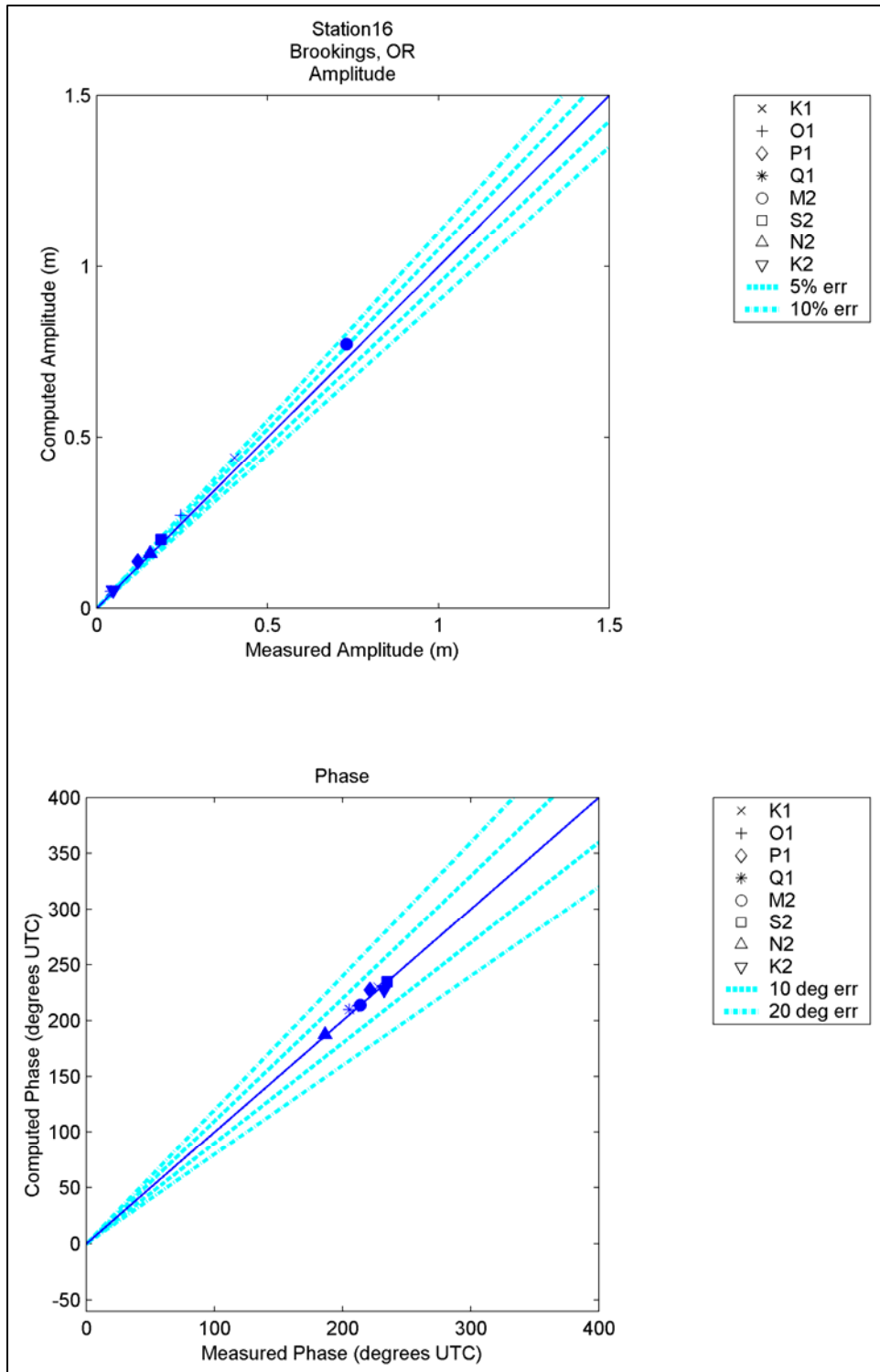


Figure 96. Computed vs. measured harmonic constituents at sta 16

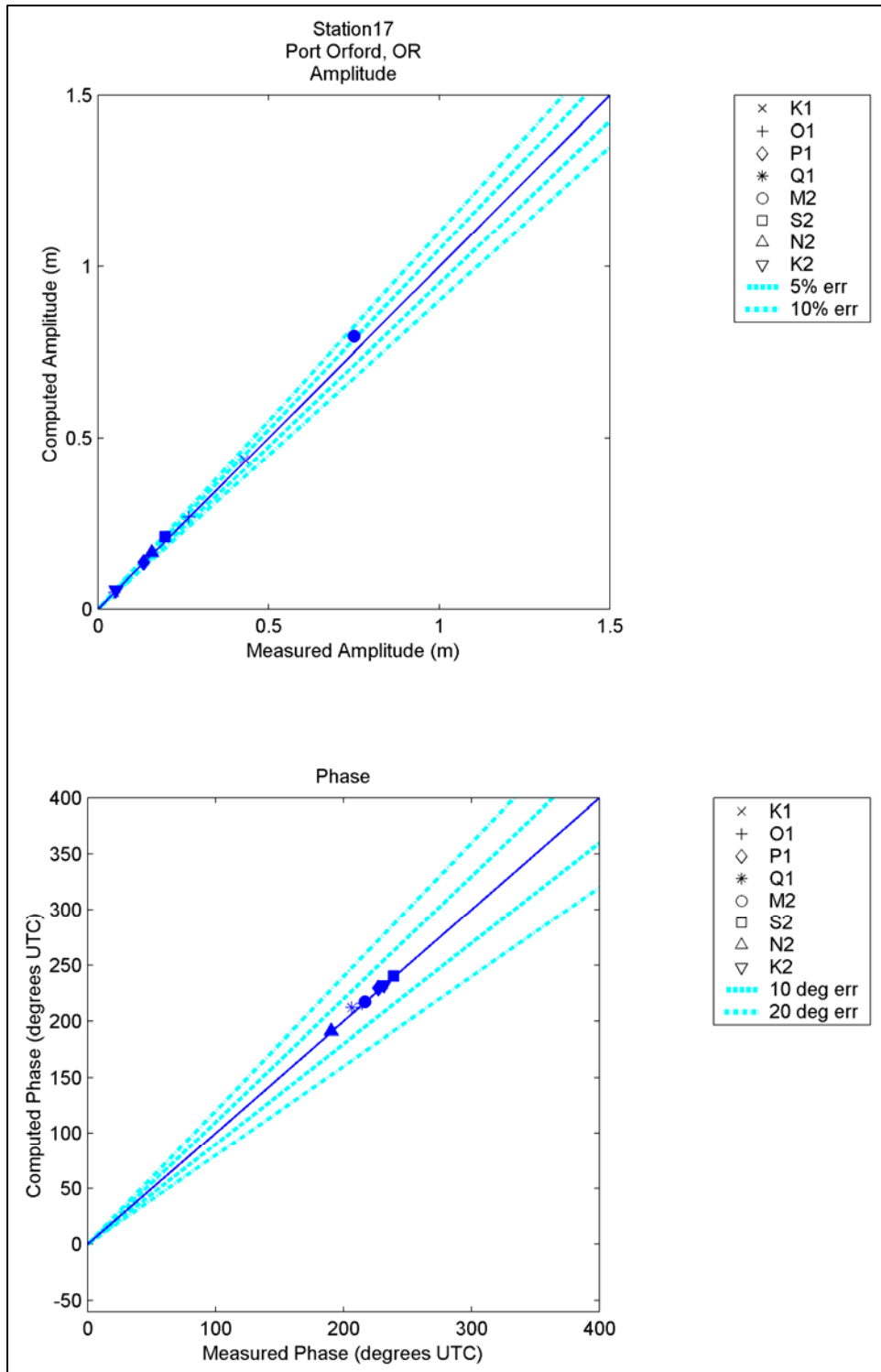


Figure 97. Computed vs. measured harmonic constituents at sta 17

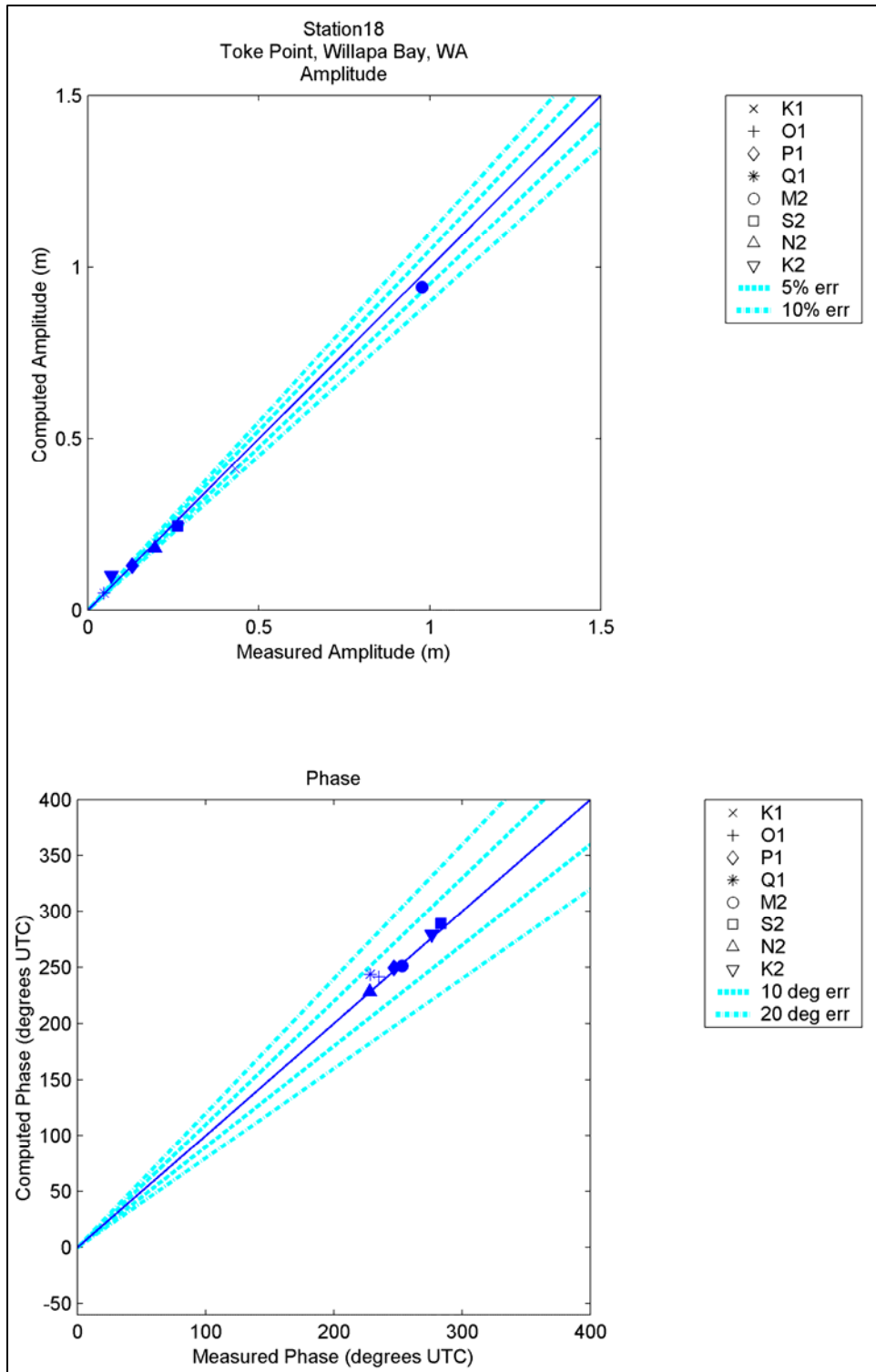


Figure 98. Computed vs. measured harmonic constituents at sta 18

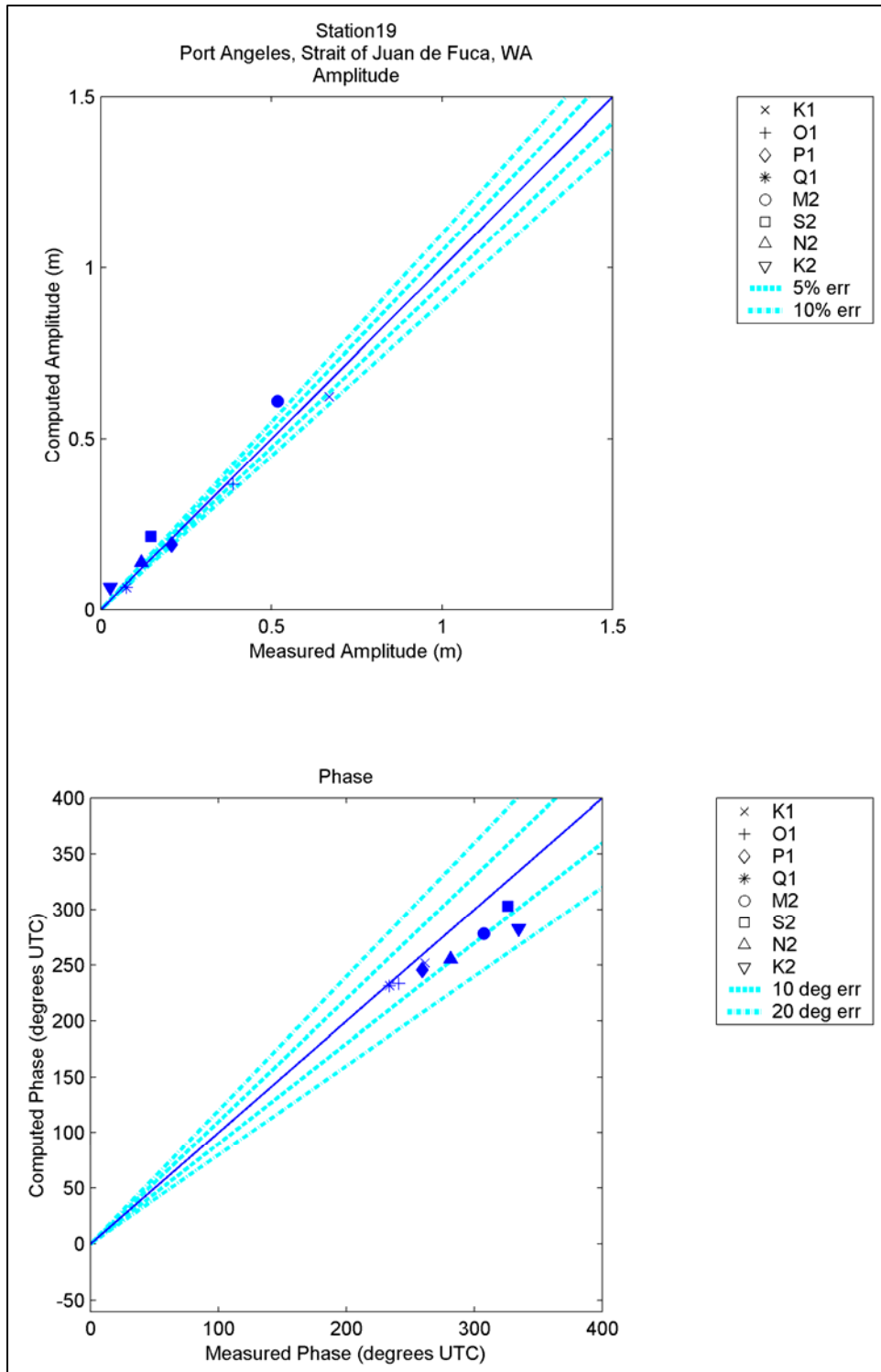


Figure 99. Computed vs. measured harmonic constituents at sta 19

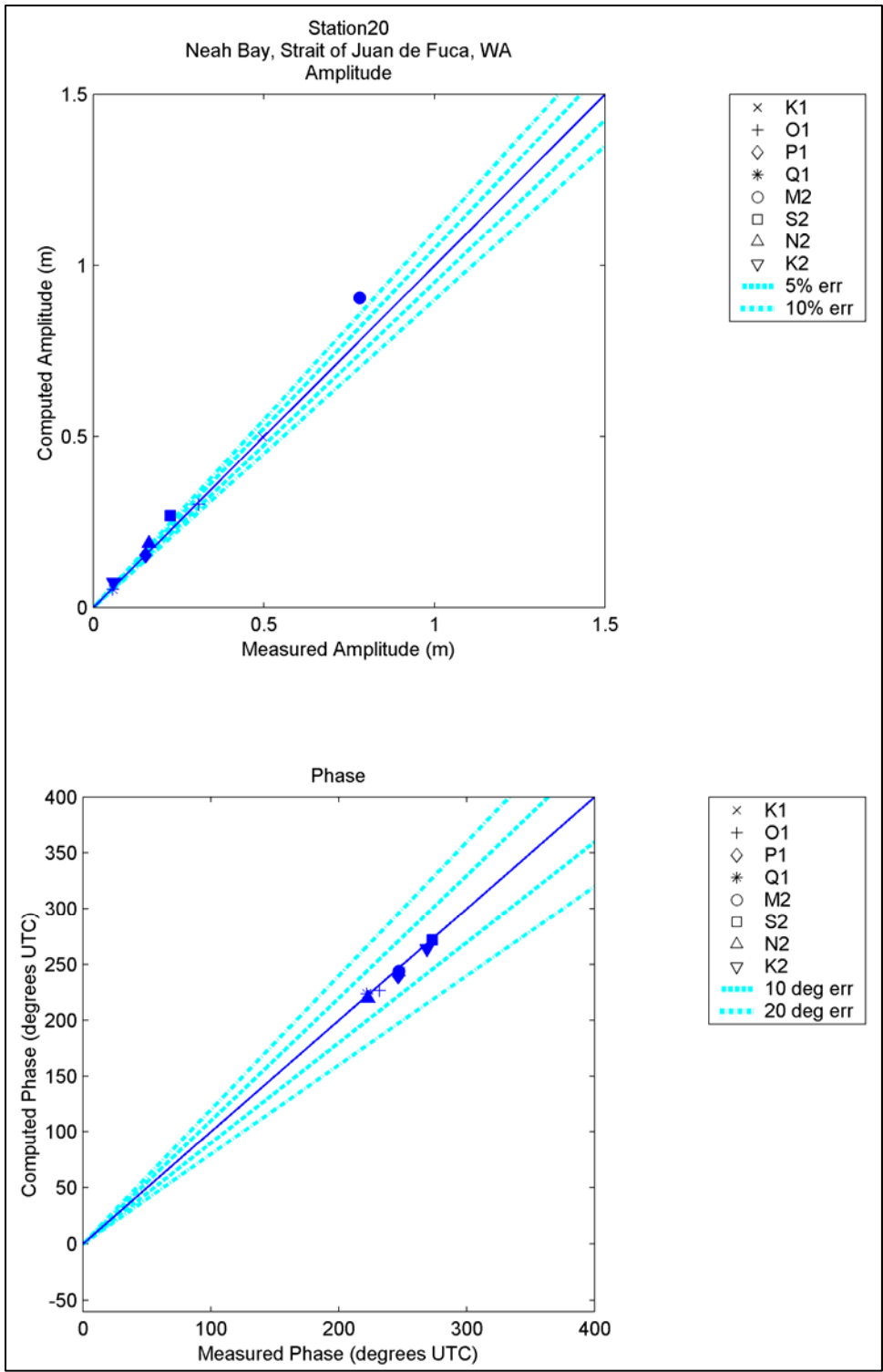


Figure 100. Computed vs. measured harmonic constituents at sta 20

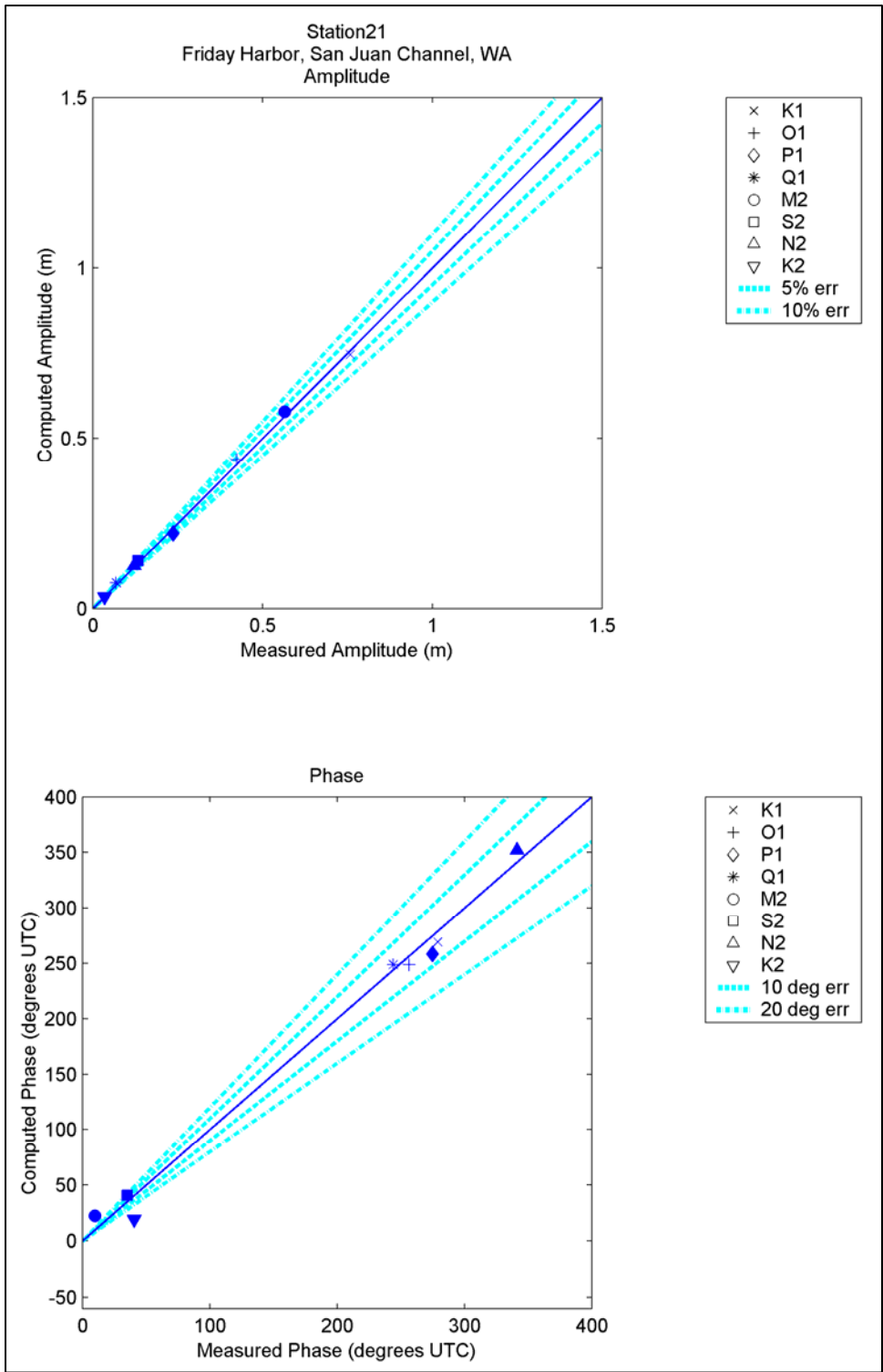


Figure 101. Computed vs. measured harmonic constituents at sta 21

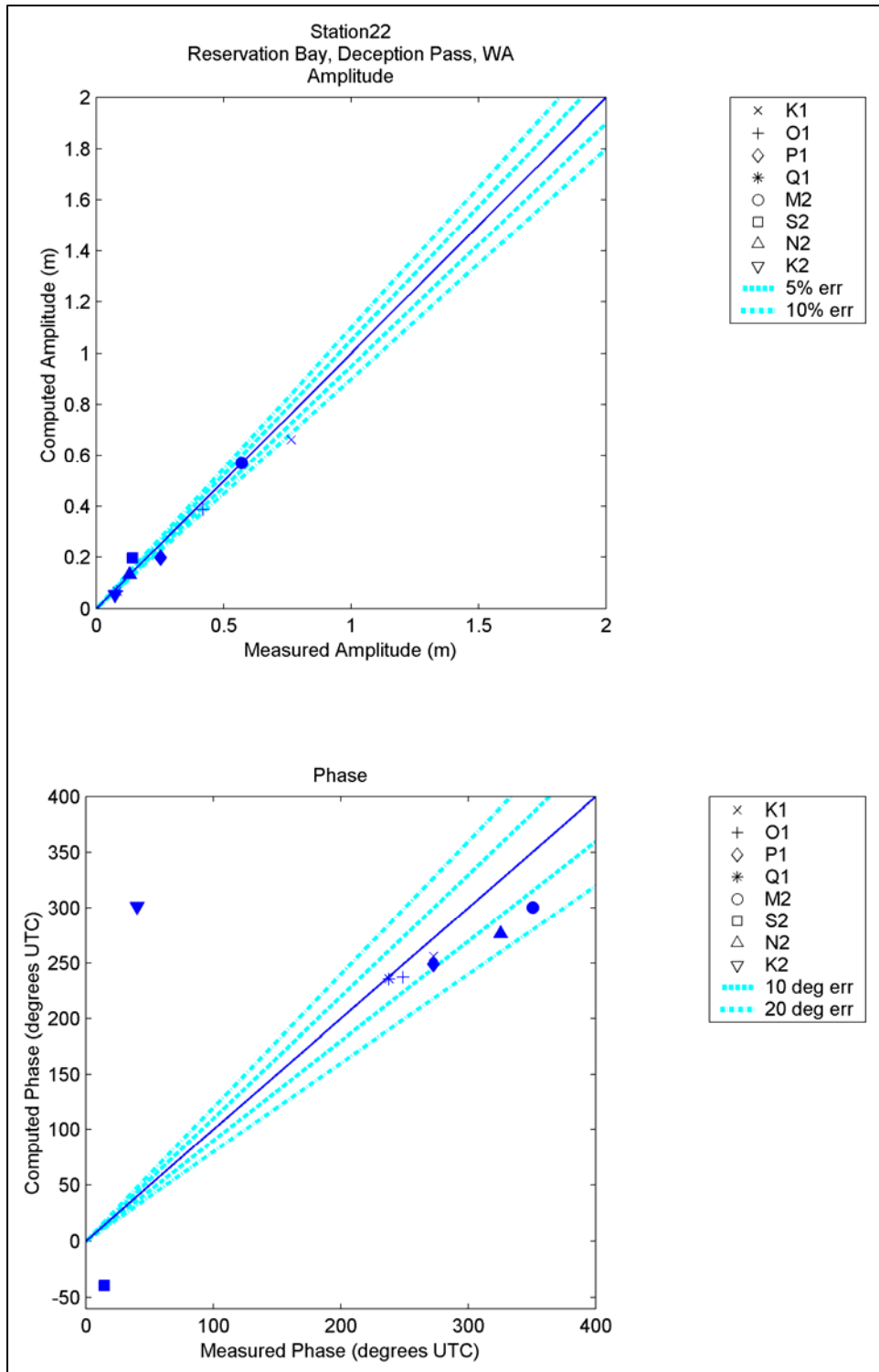


Figure 102. Computed vs. measured harmonic constituents at sta 22

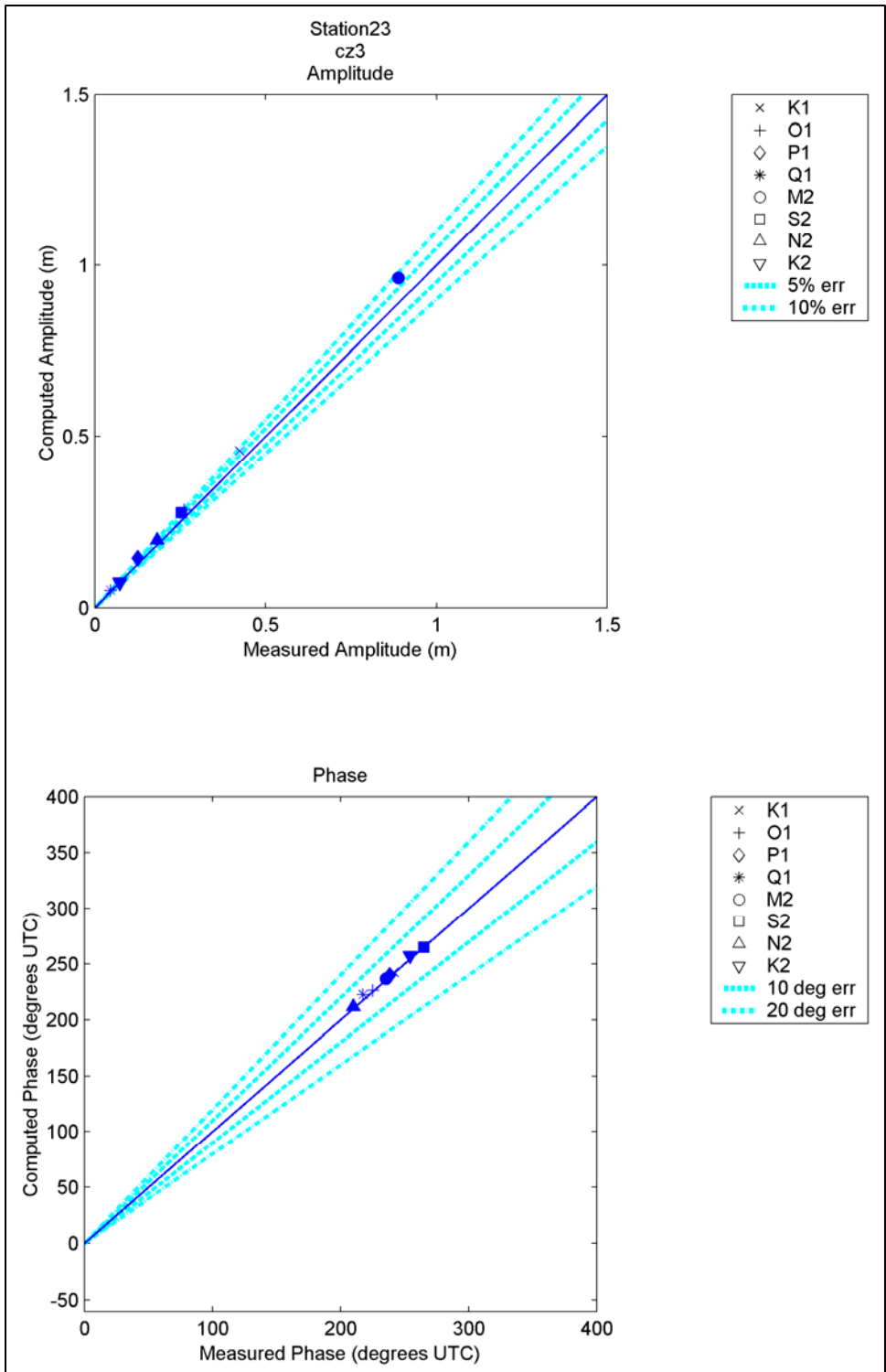


Figure 103. Computed vs. measured harmonic constituents at sta 23

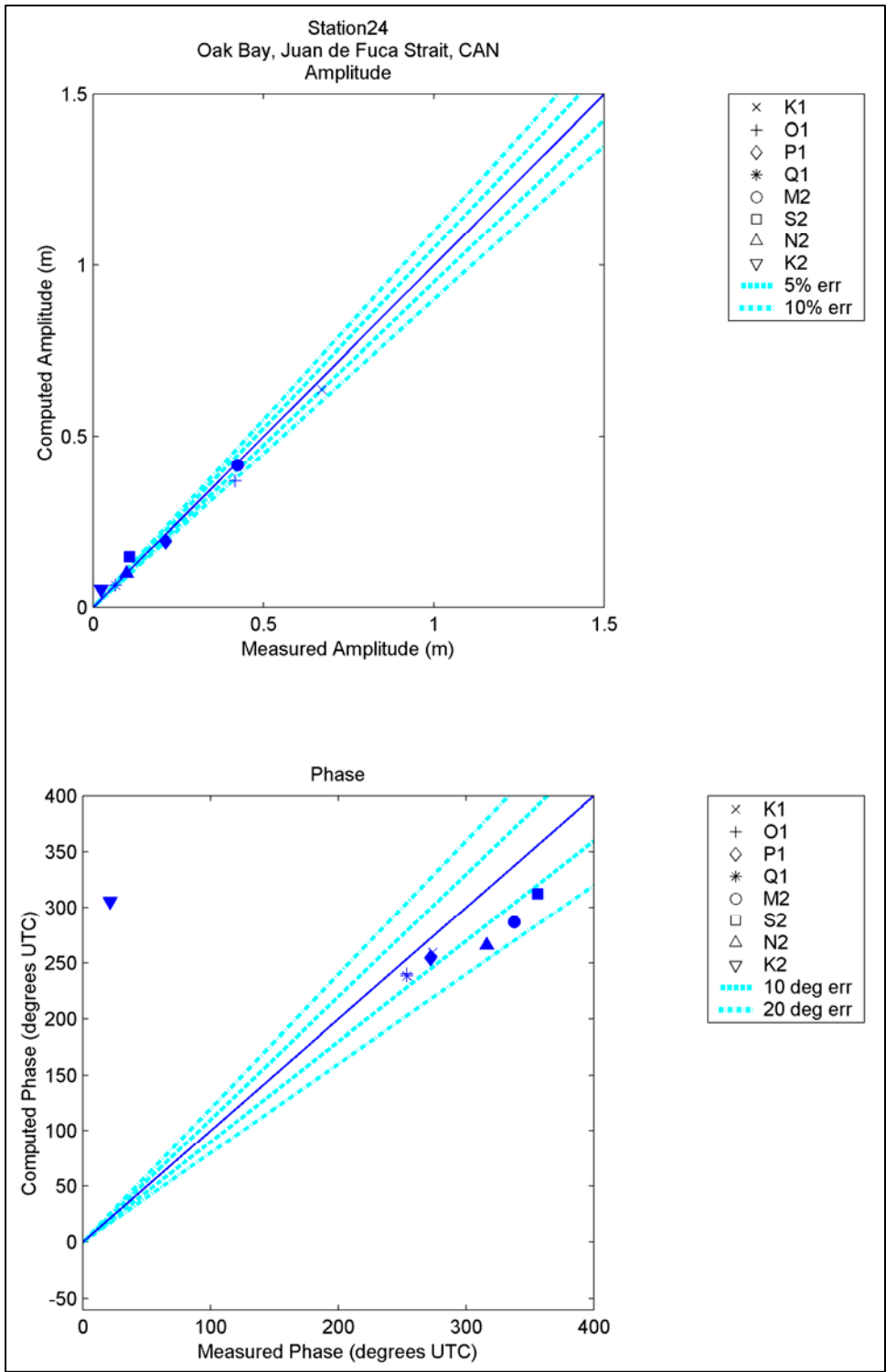


Figure 104. Computed vs. measured harmonic constituents at sta 24

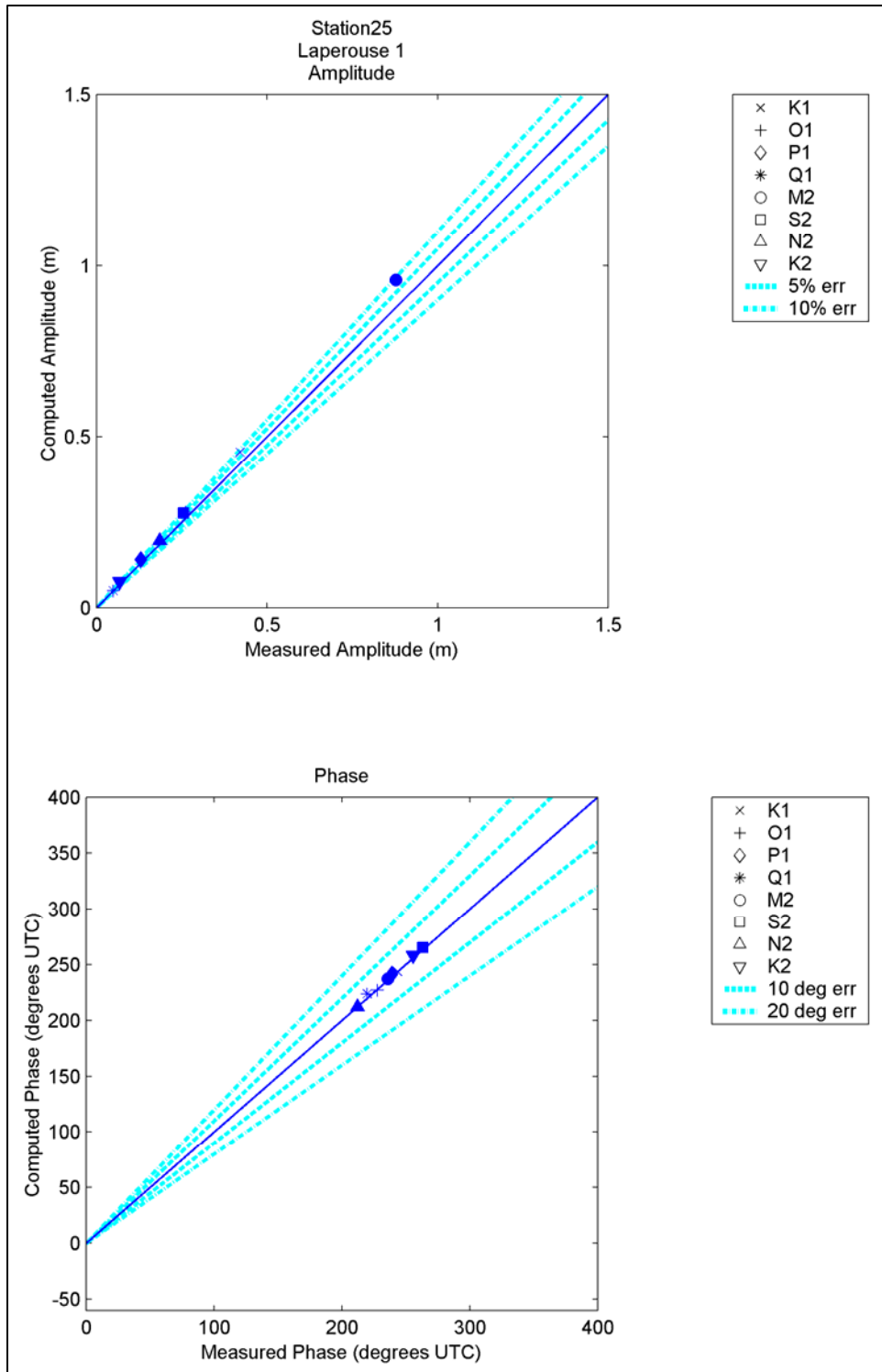


Figure 105. Computed vs. measured harmonic constituents at sta 25

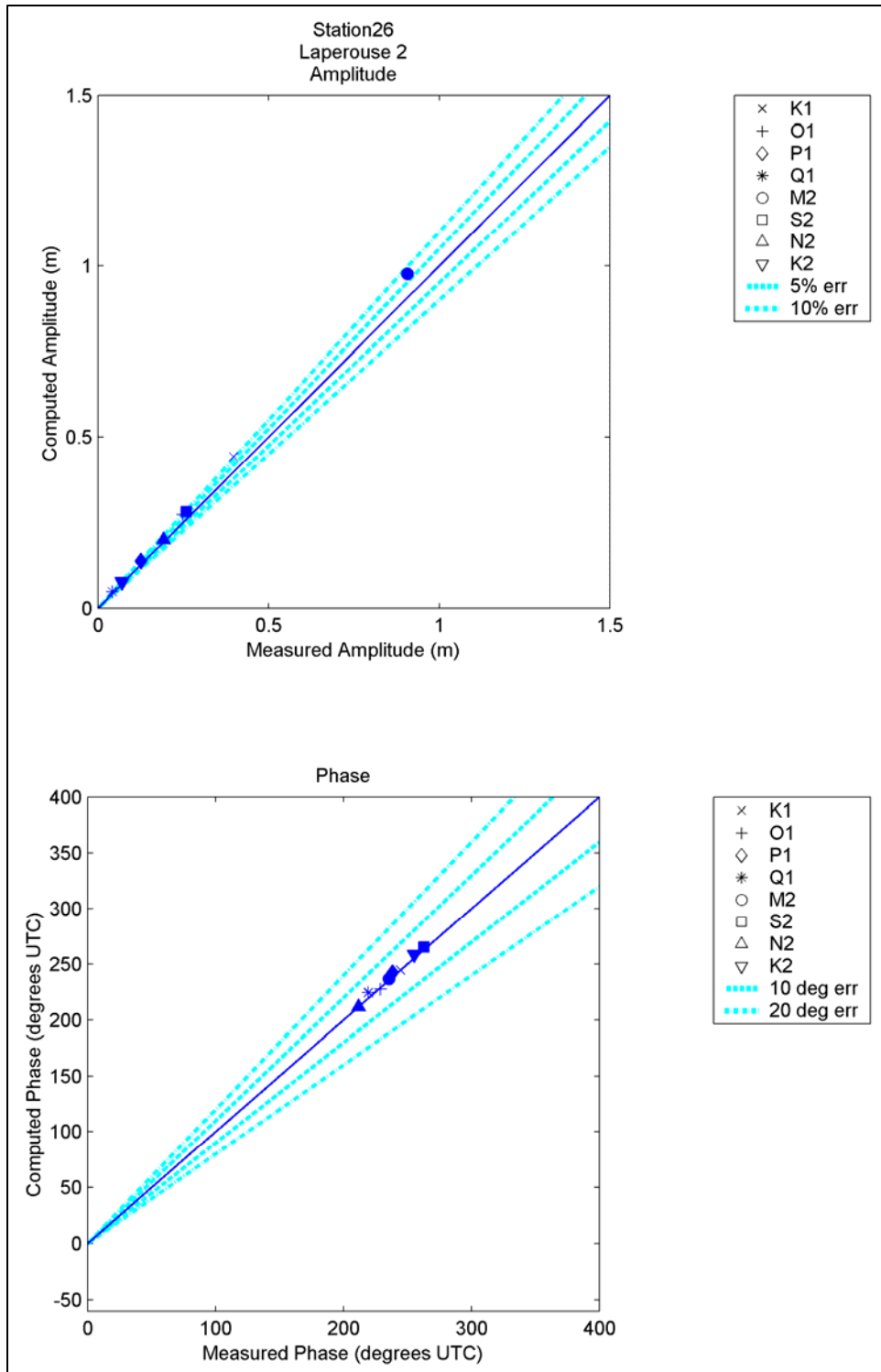


Figure 106. Computed vs. measured harmonic constituents at sta 26

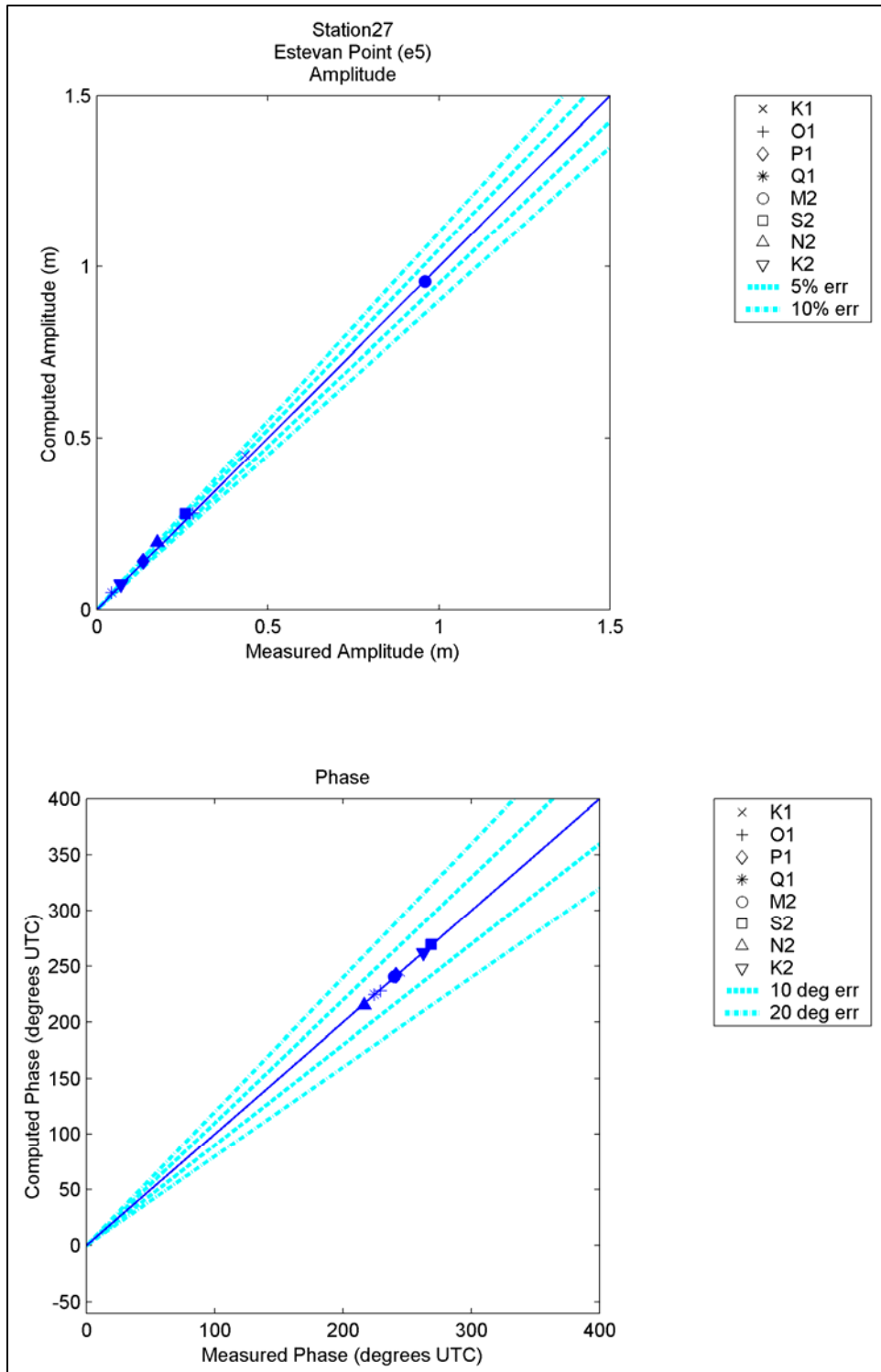


Figure 107. Computed vs. measured harmonic constituents at sta 27

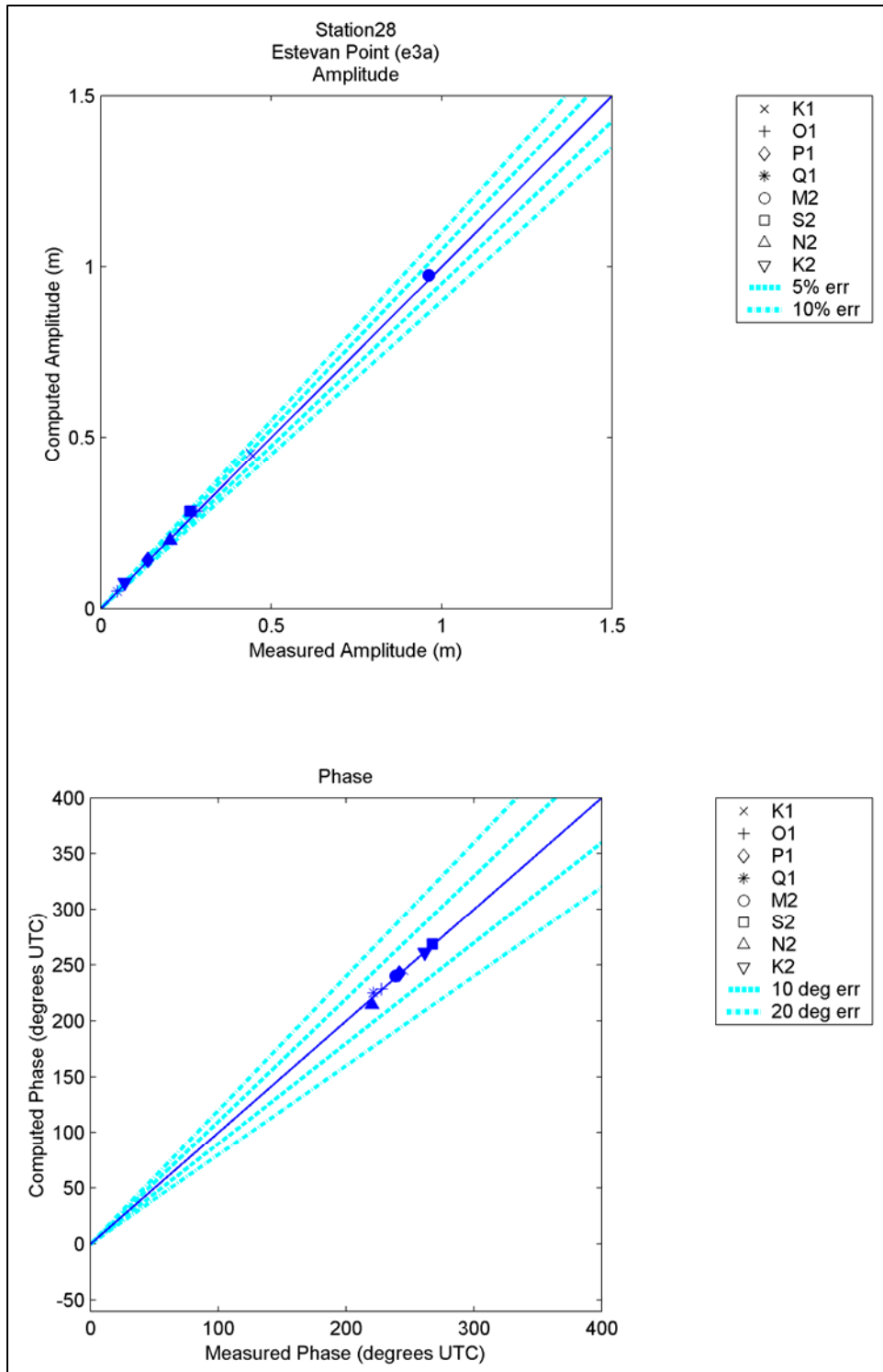


Figure 108. Computed vs. measured harmonic constituents at sta 28

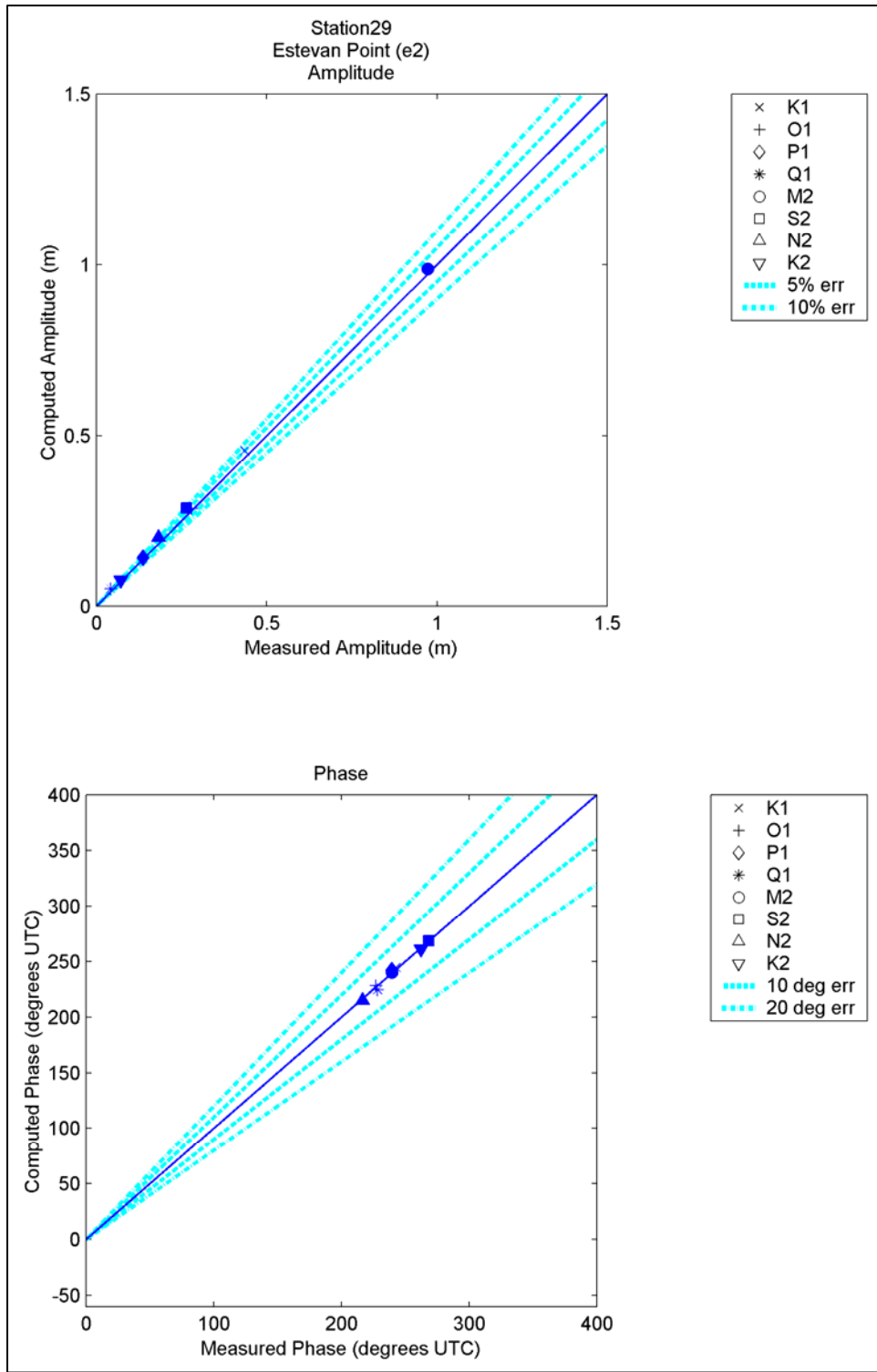


Figure 109. Computed vs. measured harmonic constituents at sta 29

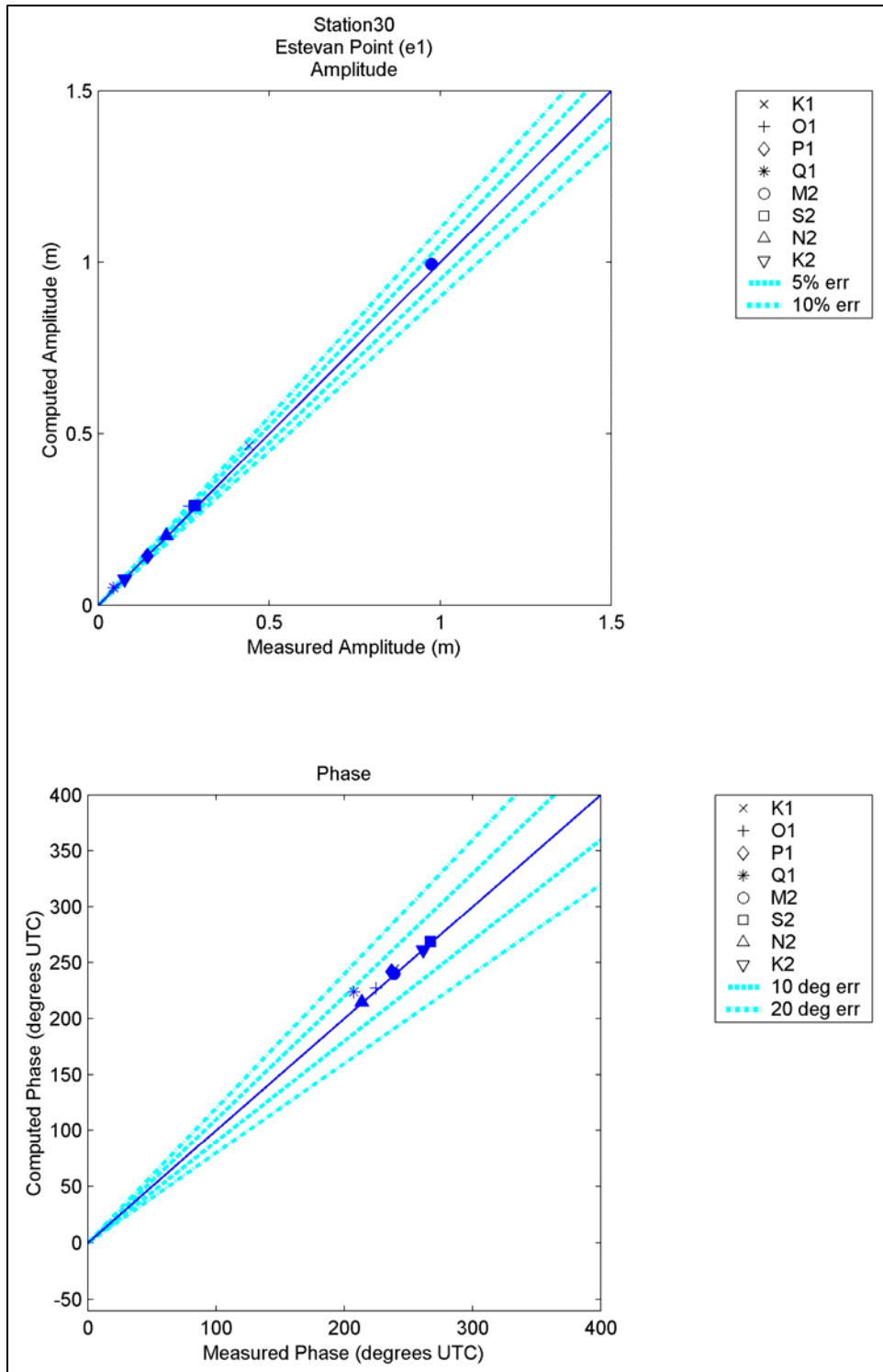


Figure 110. Computed vs. measured harmonic constituents at sta 30

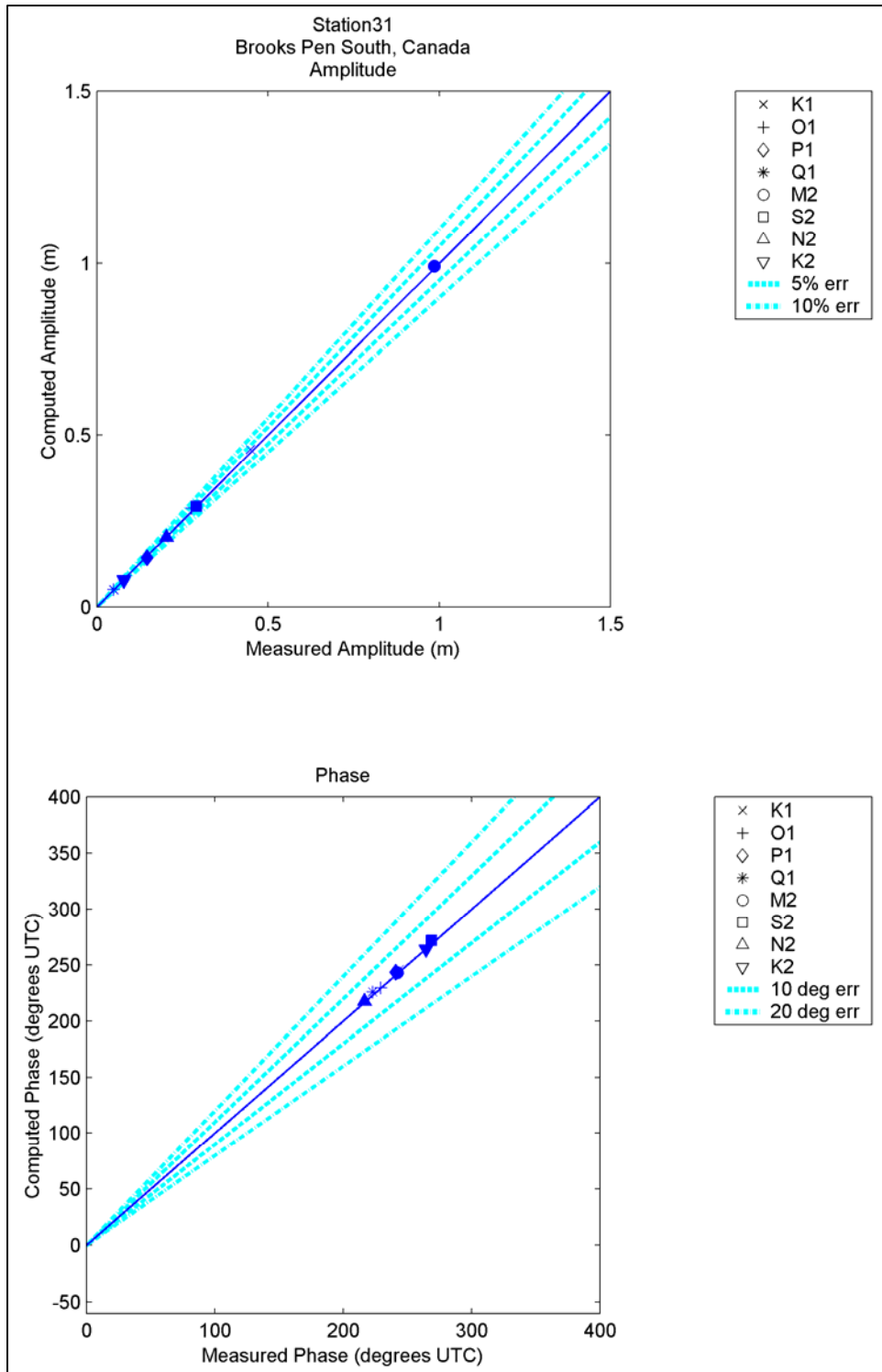


Figure 111. Computed vs. measured harmonic constituents at sta 31

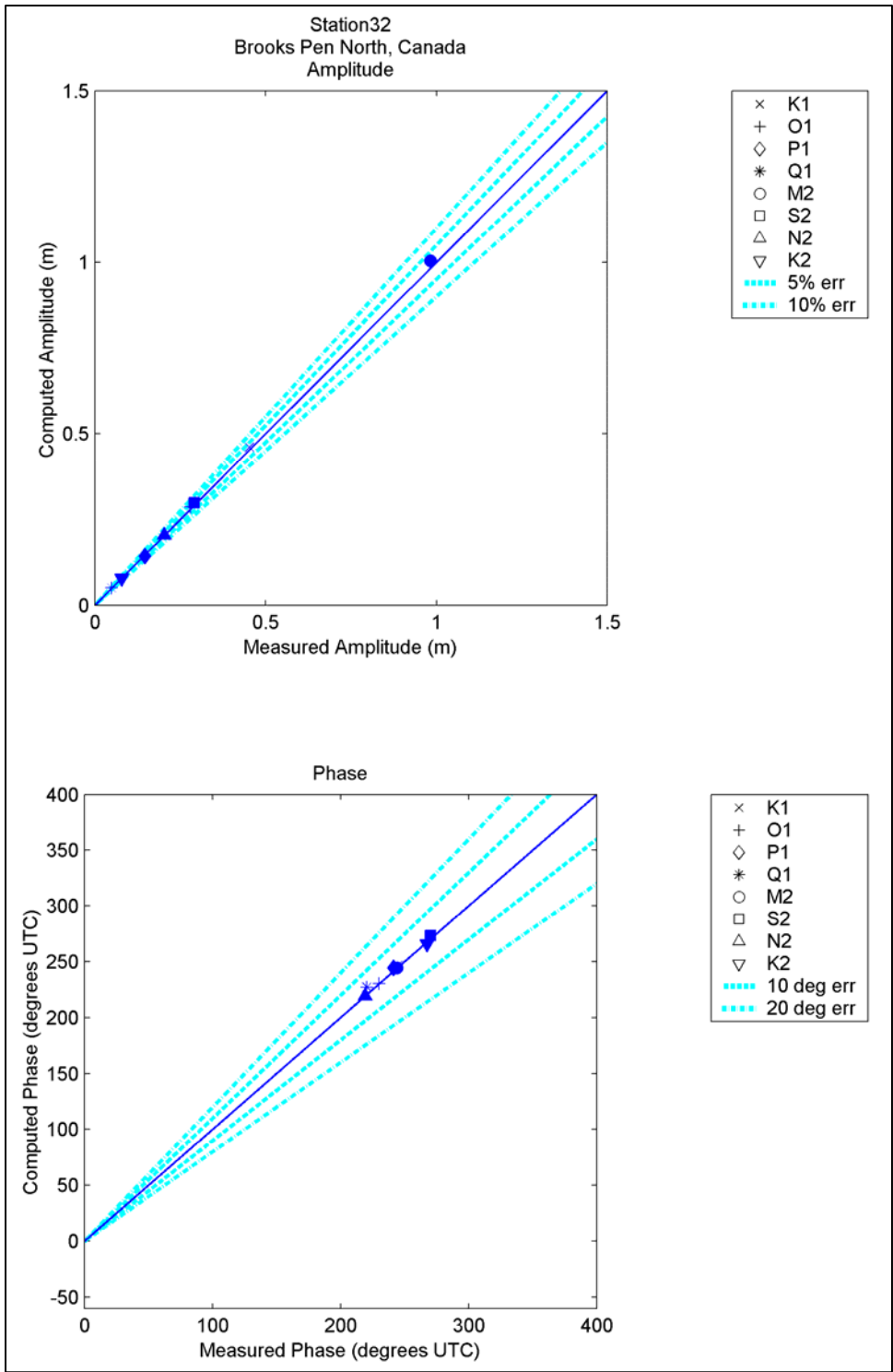


Figure 112. Computed vs. measured harmonic constituents at sta 32

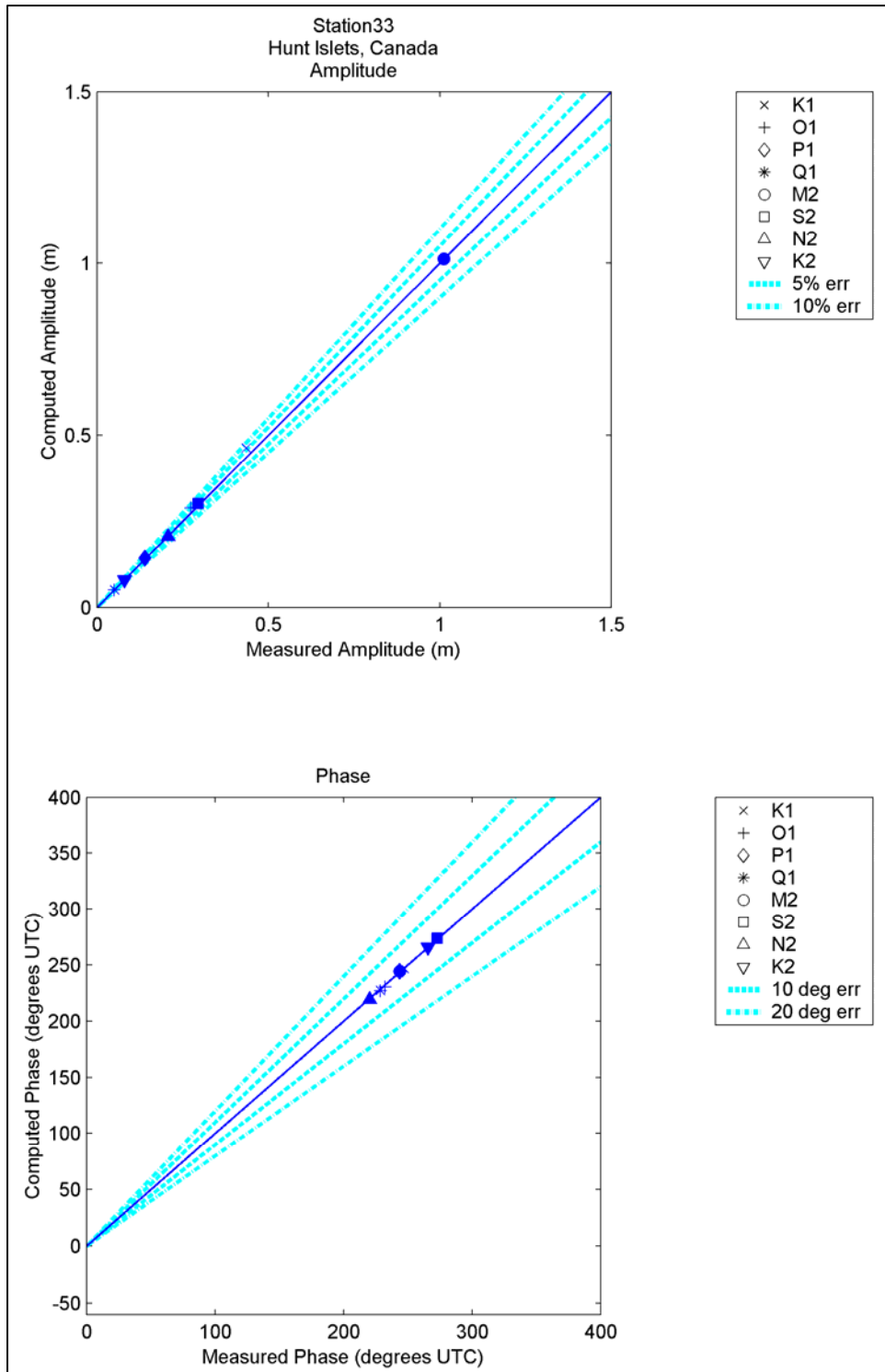


Figure 113. Computed vs. measured harmonic constituents at sta 33

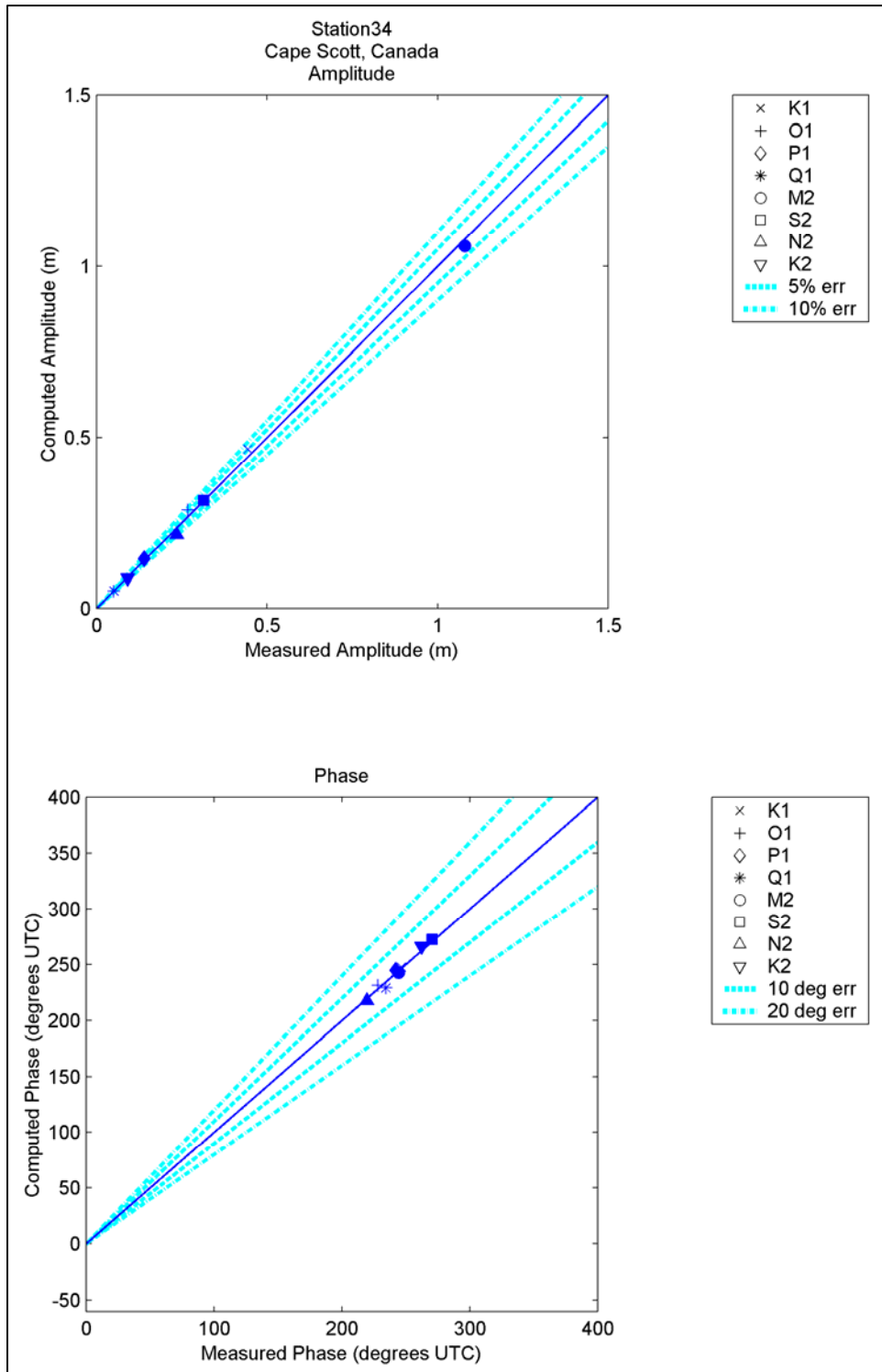


Figure 114. Computed vs. measured harmonic constituents at sta 34

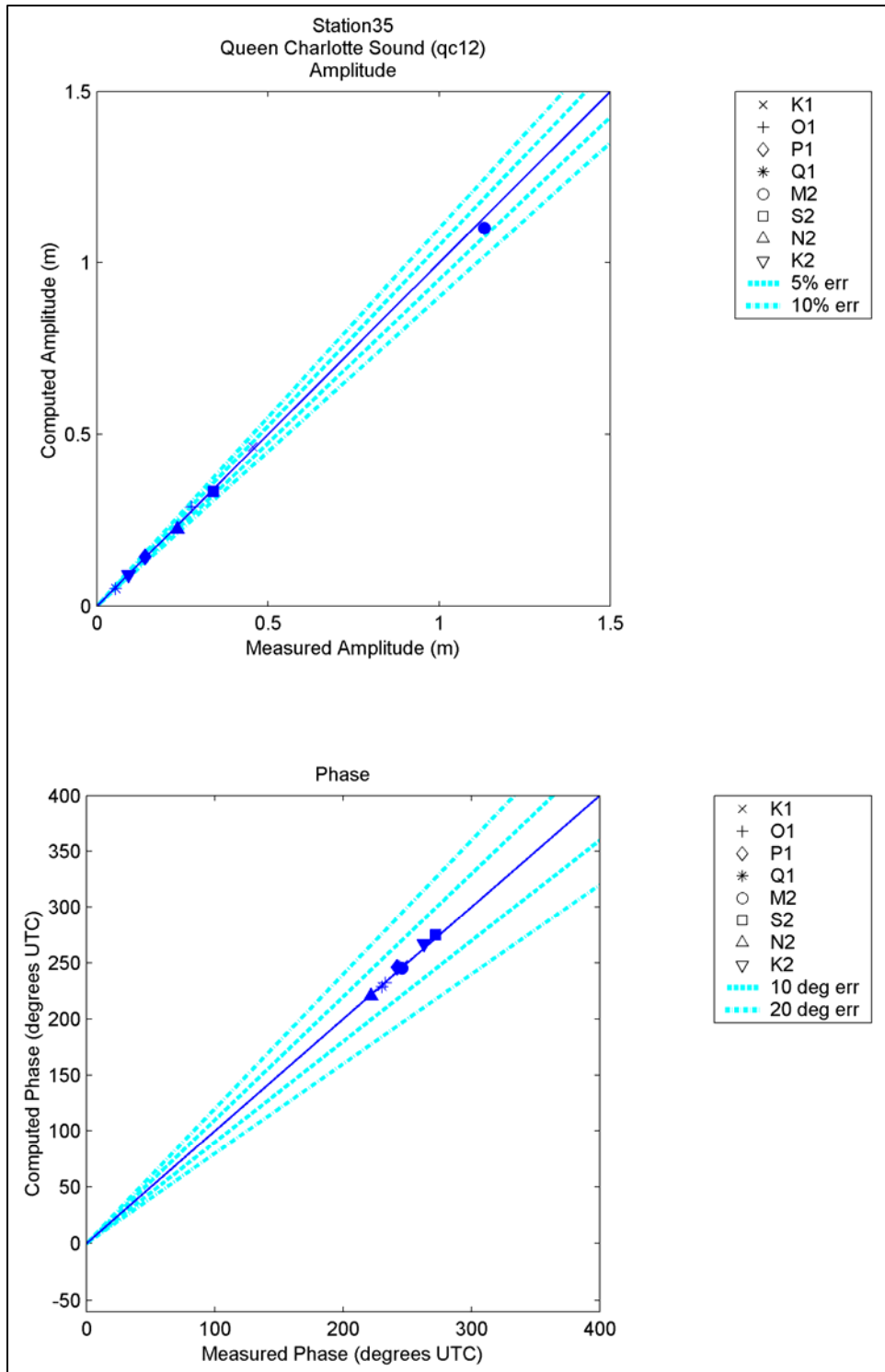


Figure 115. Computed vs. measured harmonic constituents at sta 35

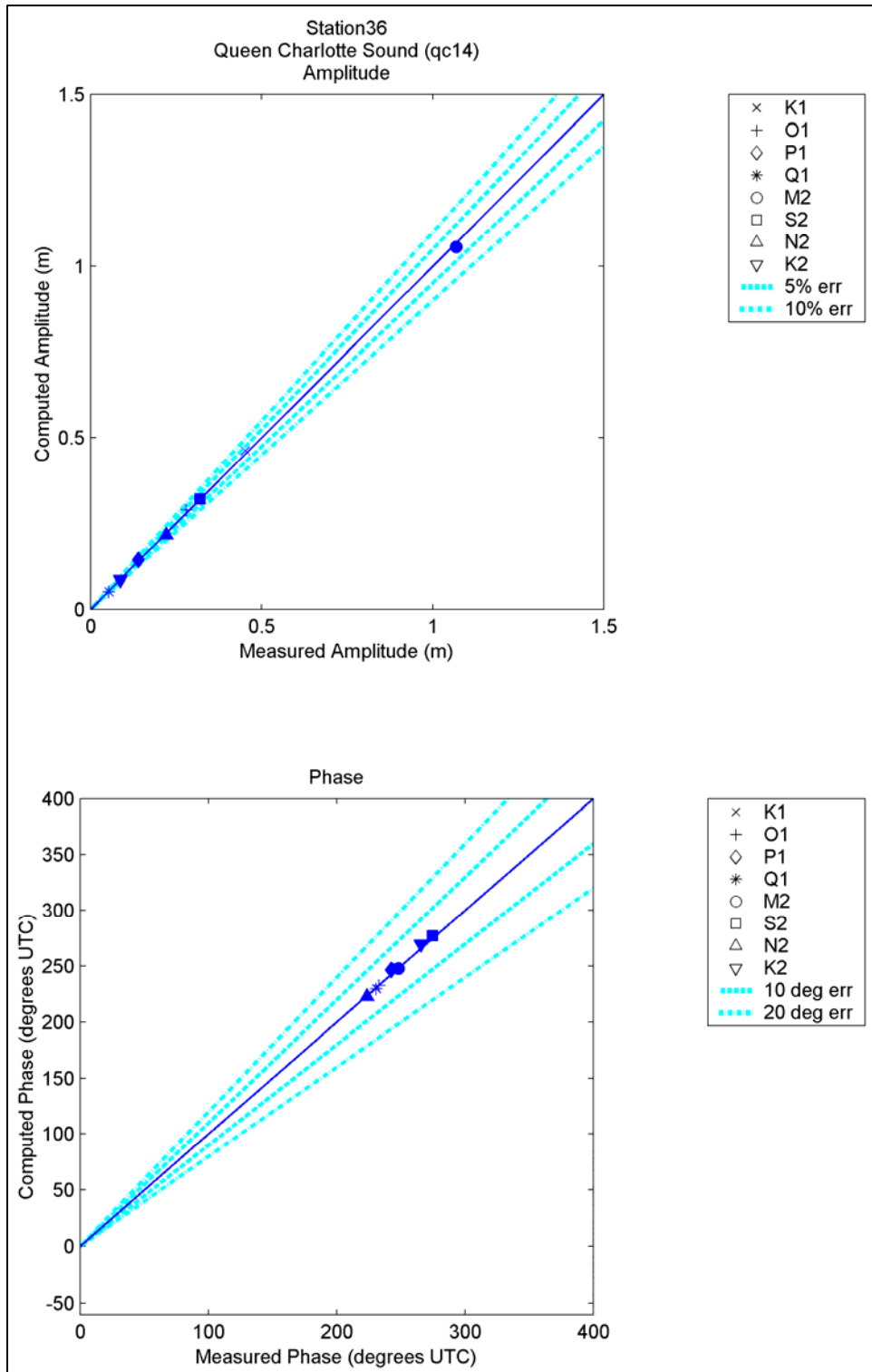


Figure 116. Computed vs. measured harmonic constituents at sta 36

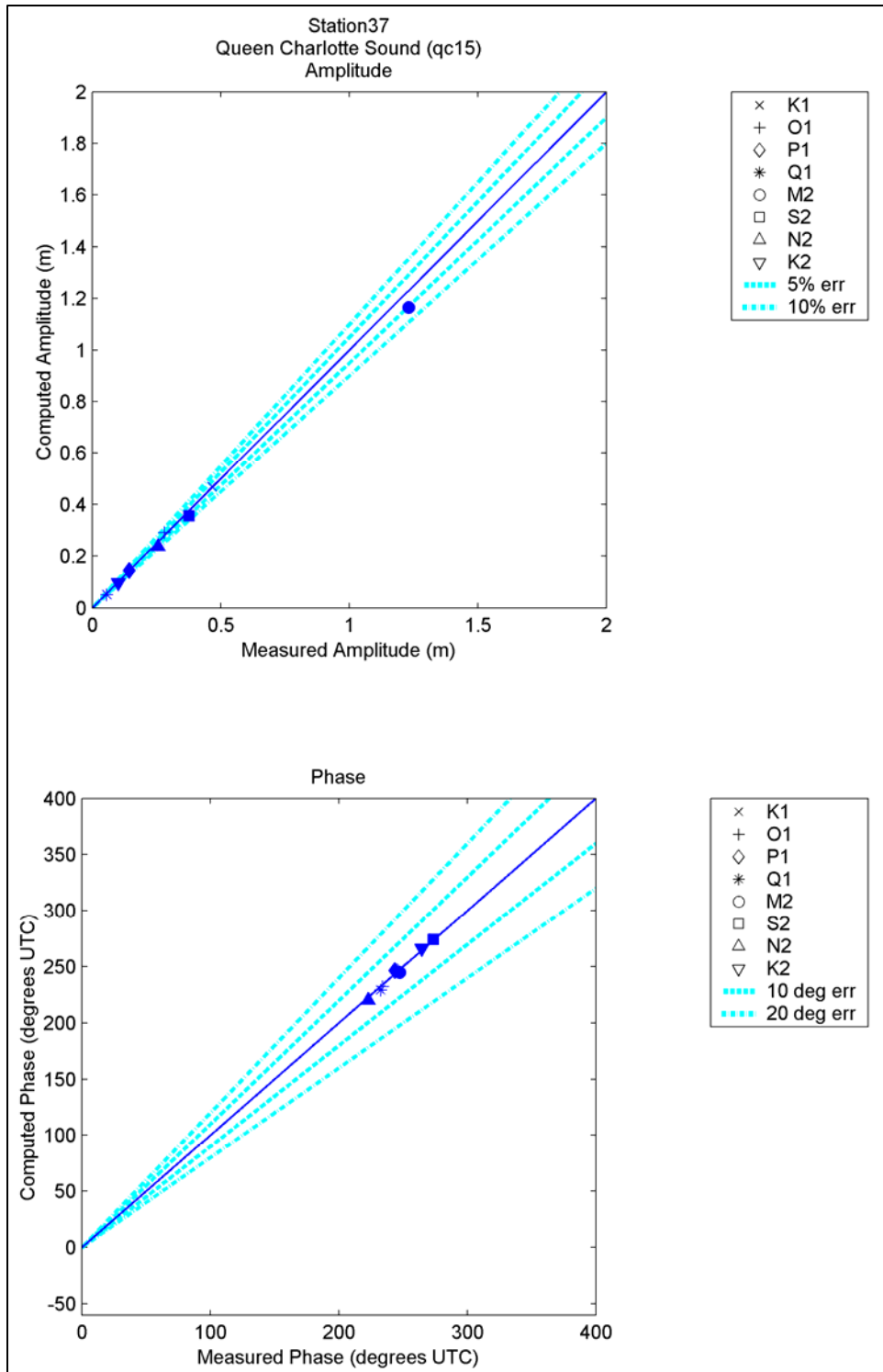


Figure 117. Computed vs. measured harmonic constituents at sta 37

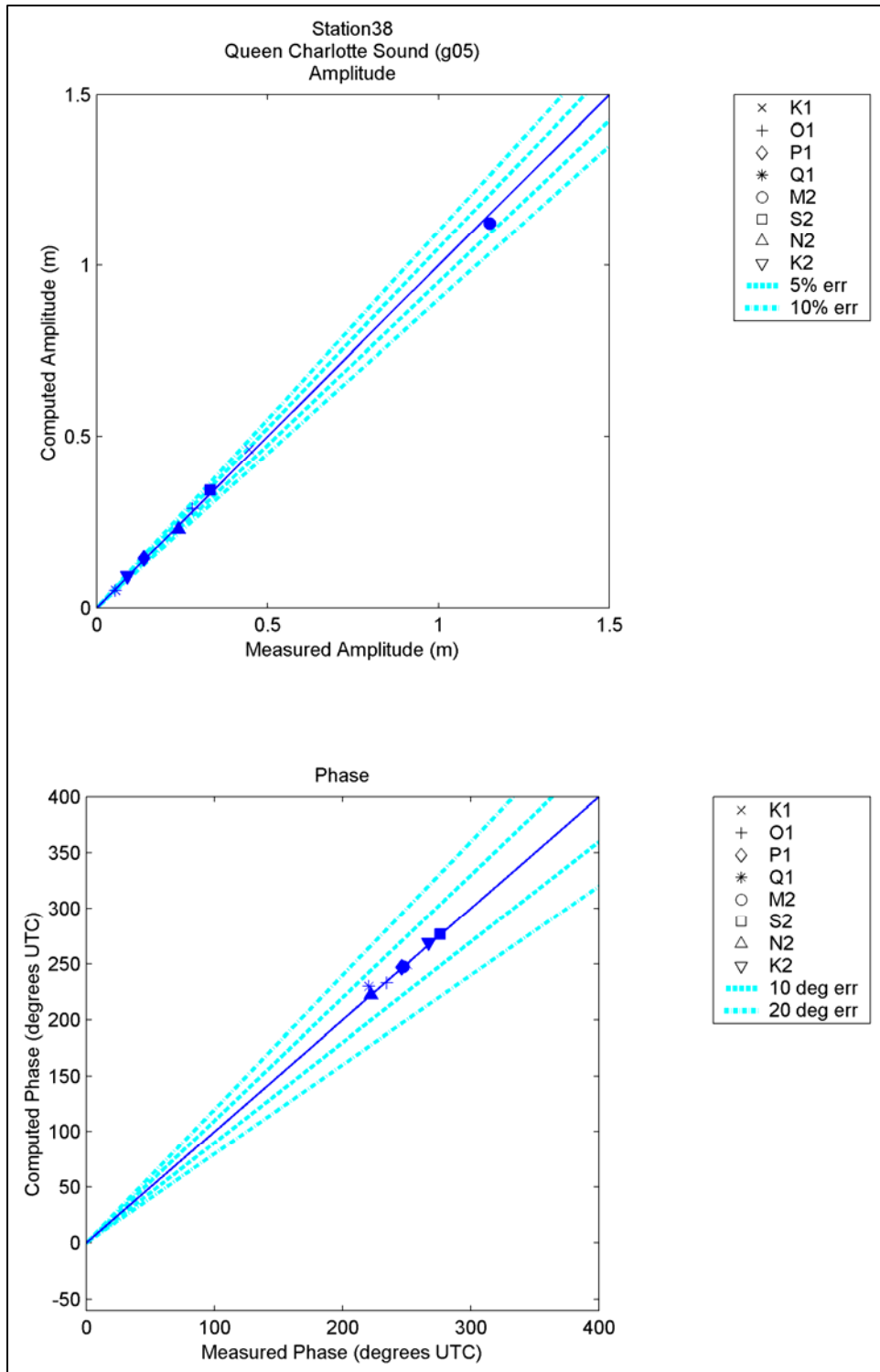


Figure 118. Computed vs. measured harmonic constituents at sta 38

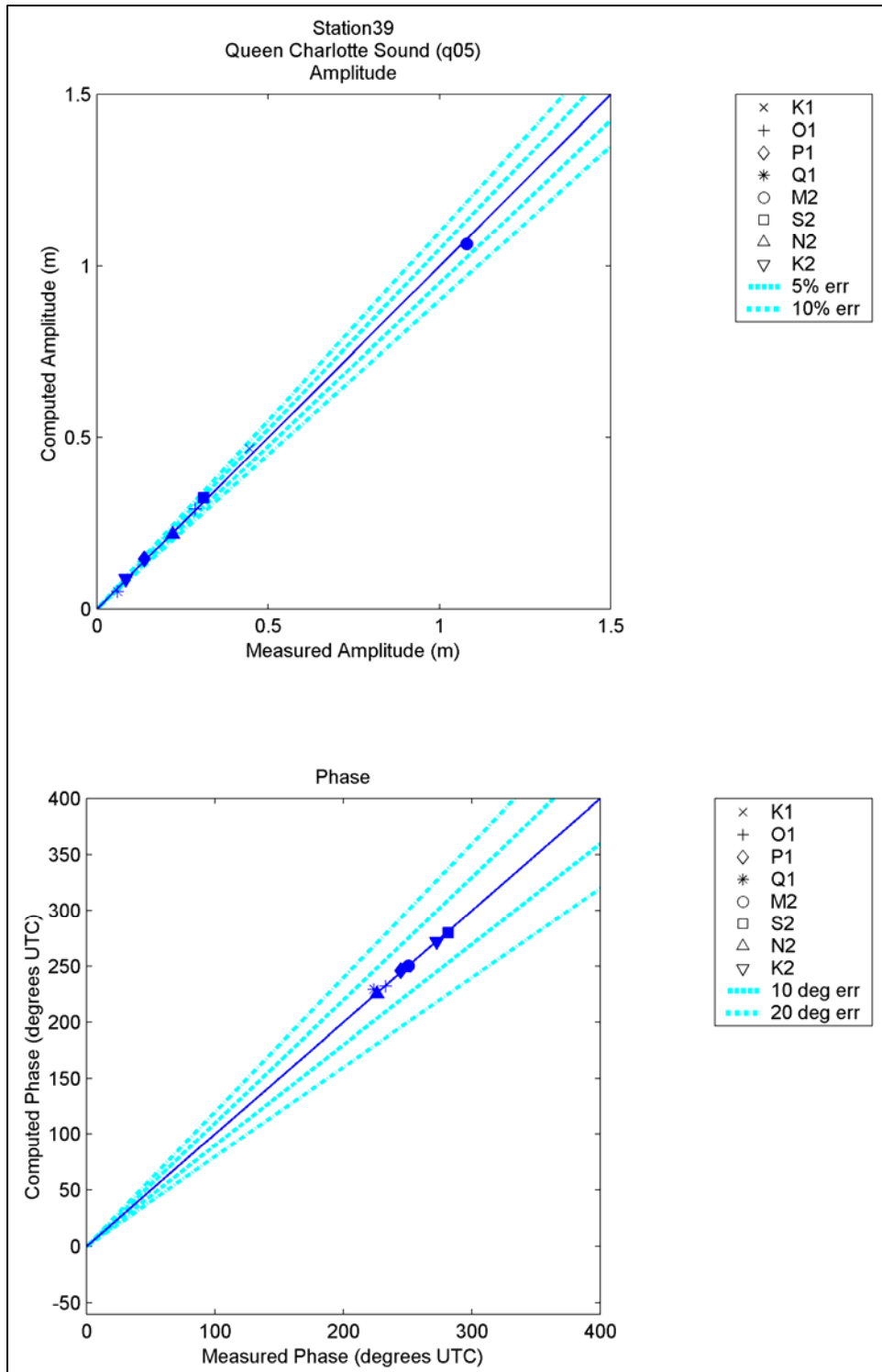


Figure 119. Computed vs. measured harmonic constituents at sta 39

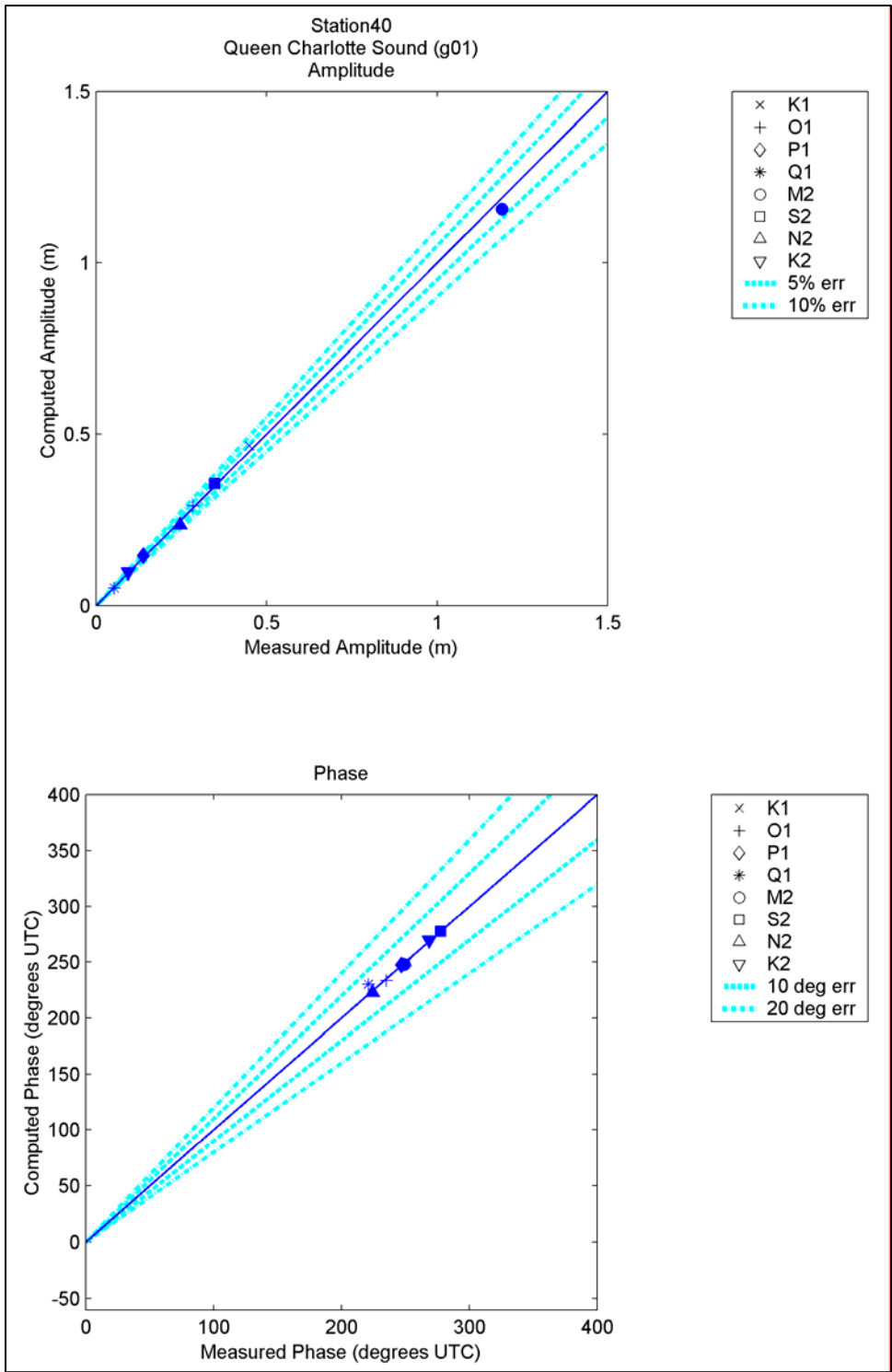


Figure 120. Computed vs. measured harmonic constituents at sta 40

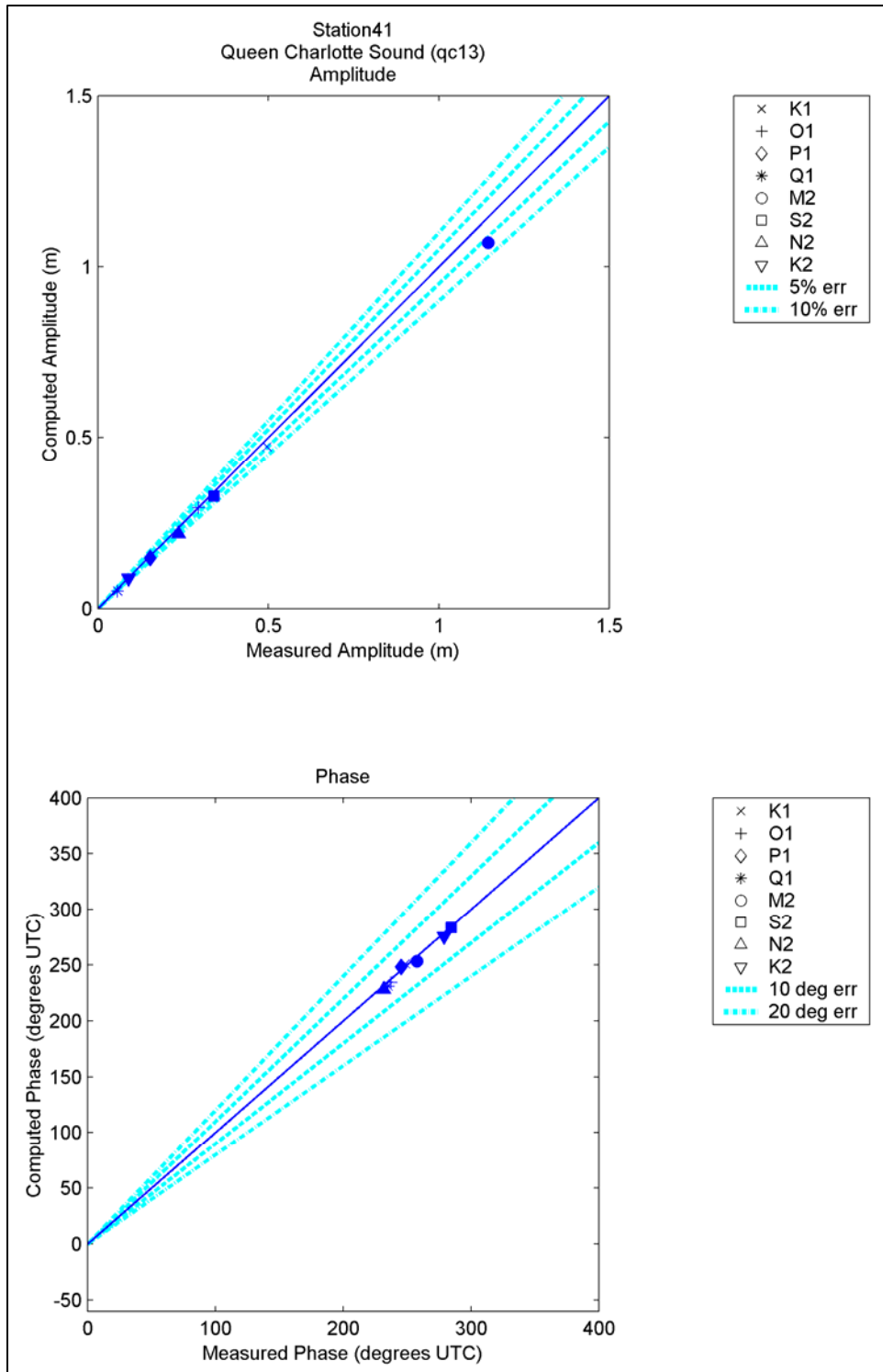


Figure 121. Computed vs. measured harmonic constituents at sta 41

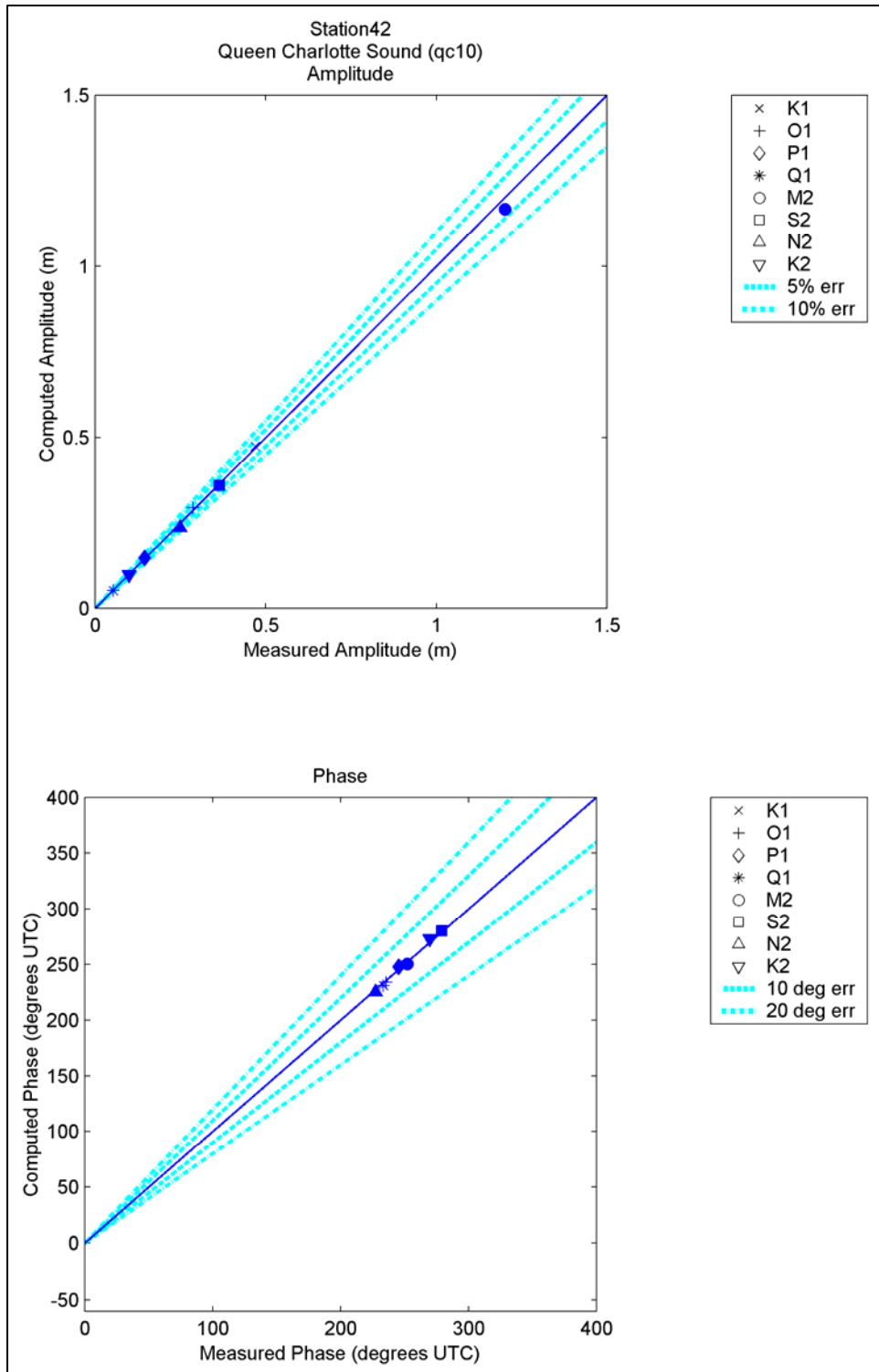


Figure 122. Computed vs. measured harmonic constituents at sta 42

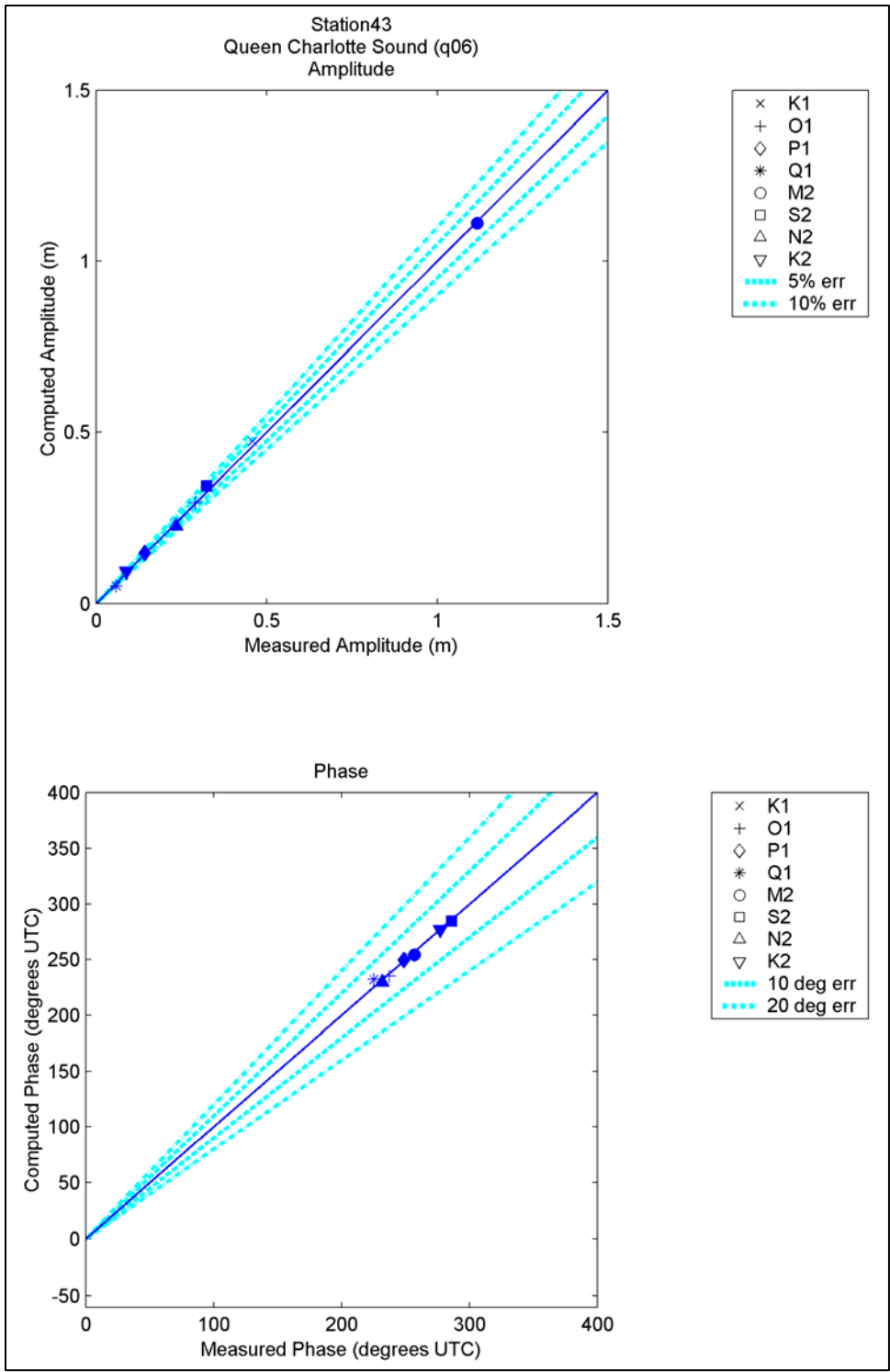


Figure 123. Computed vs. measured harmonic constituents at sta 43

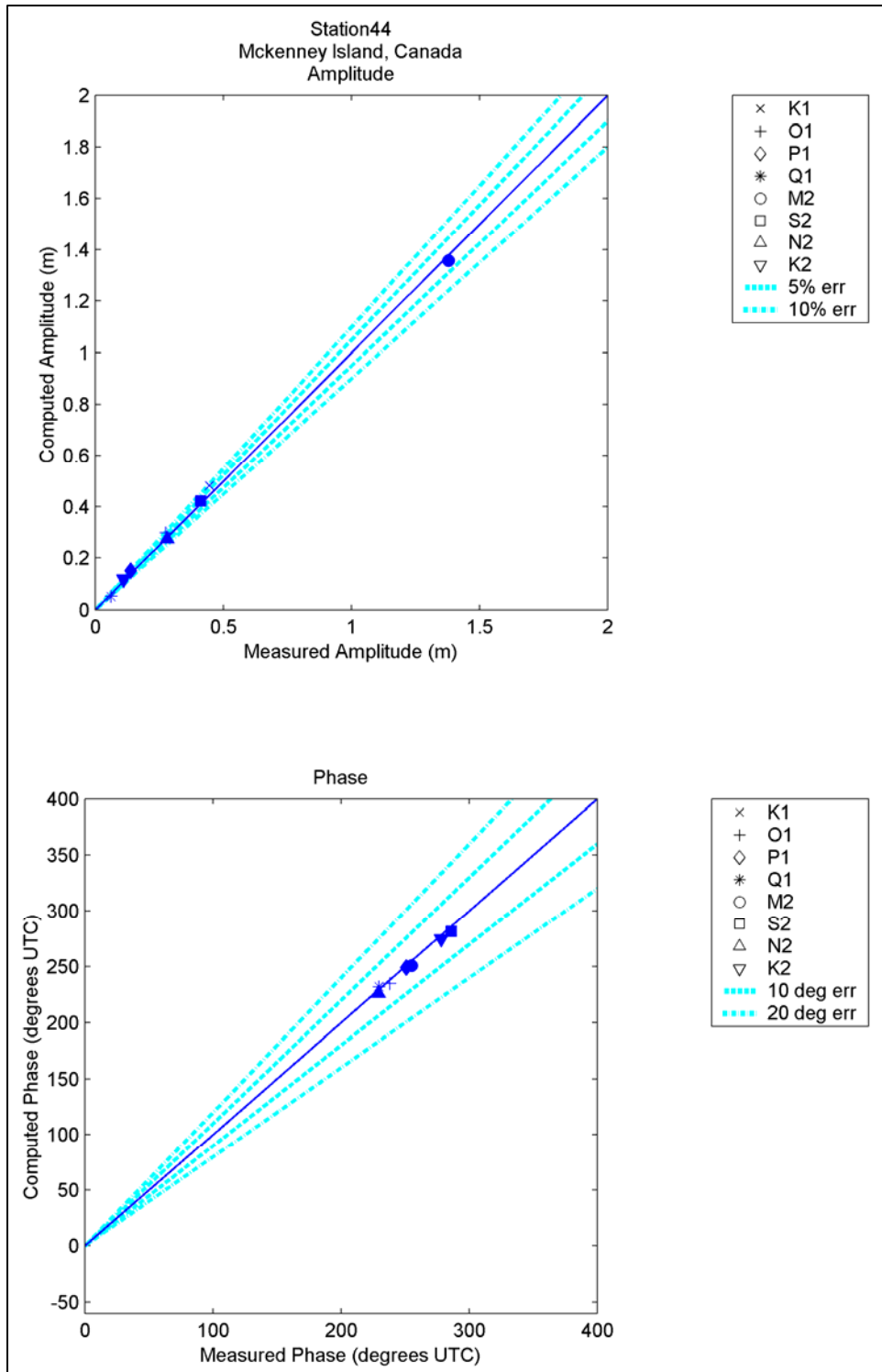


Figure 124. Computed vs. measured harmonic constituents at sta 44

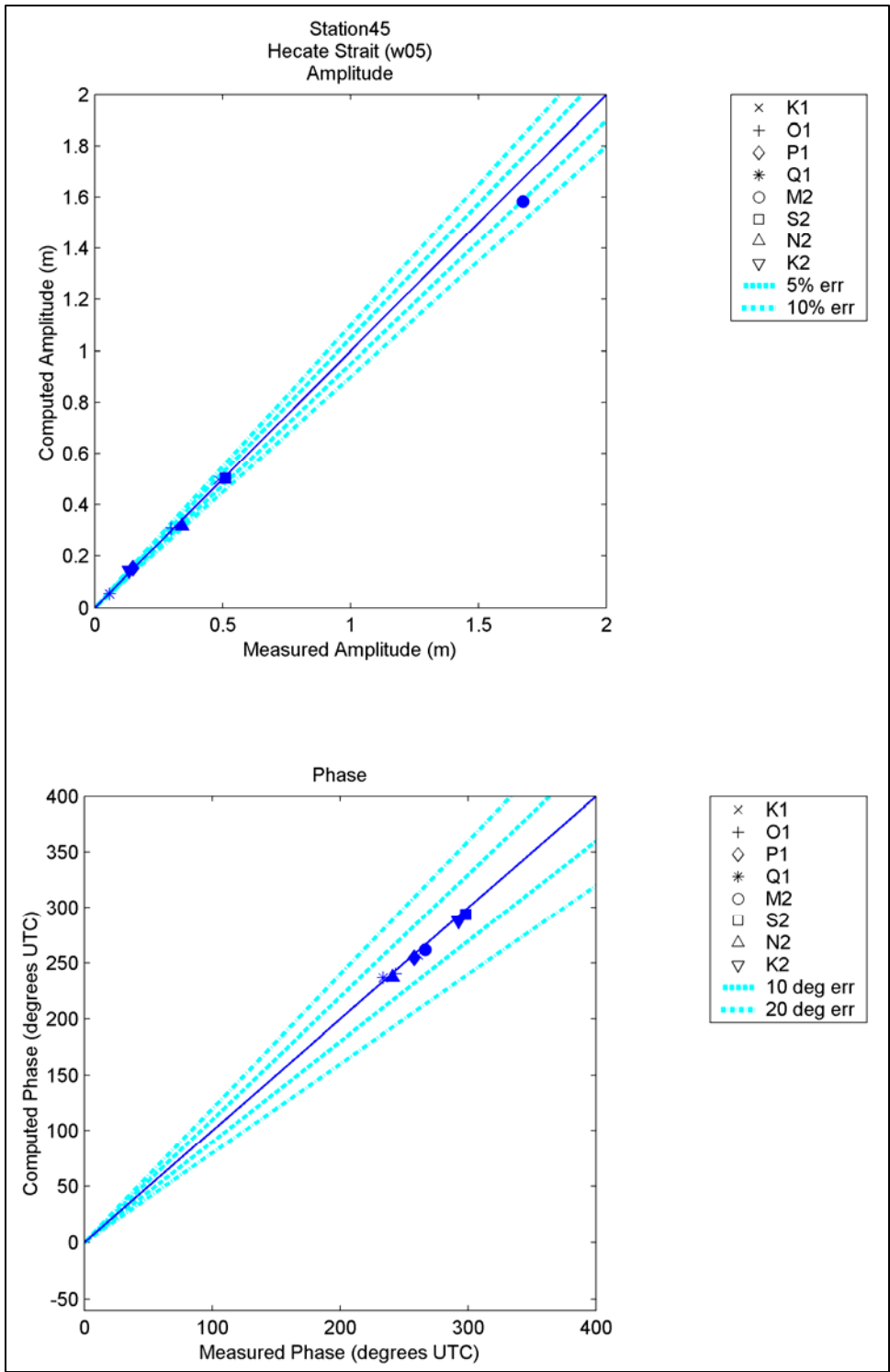


Figure 125. Computed vs. measured harmonic constituents at sta 45

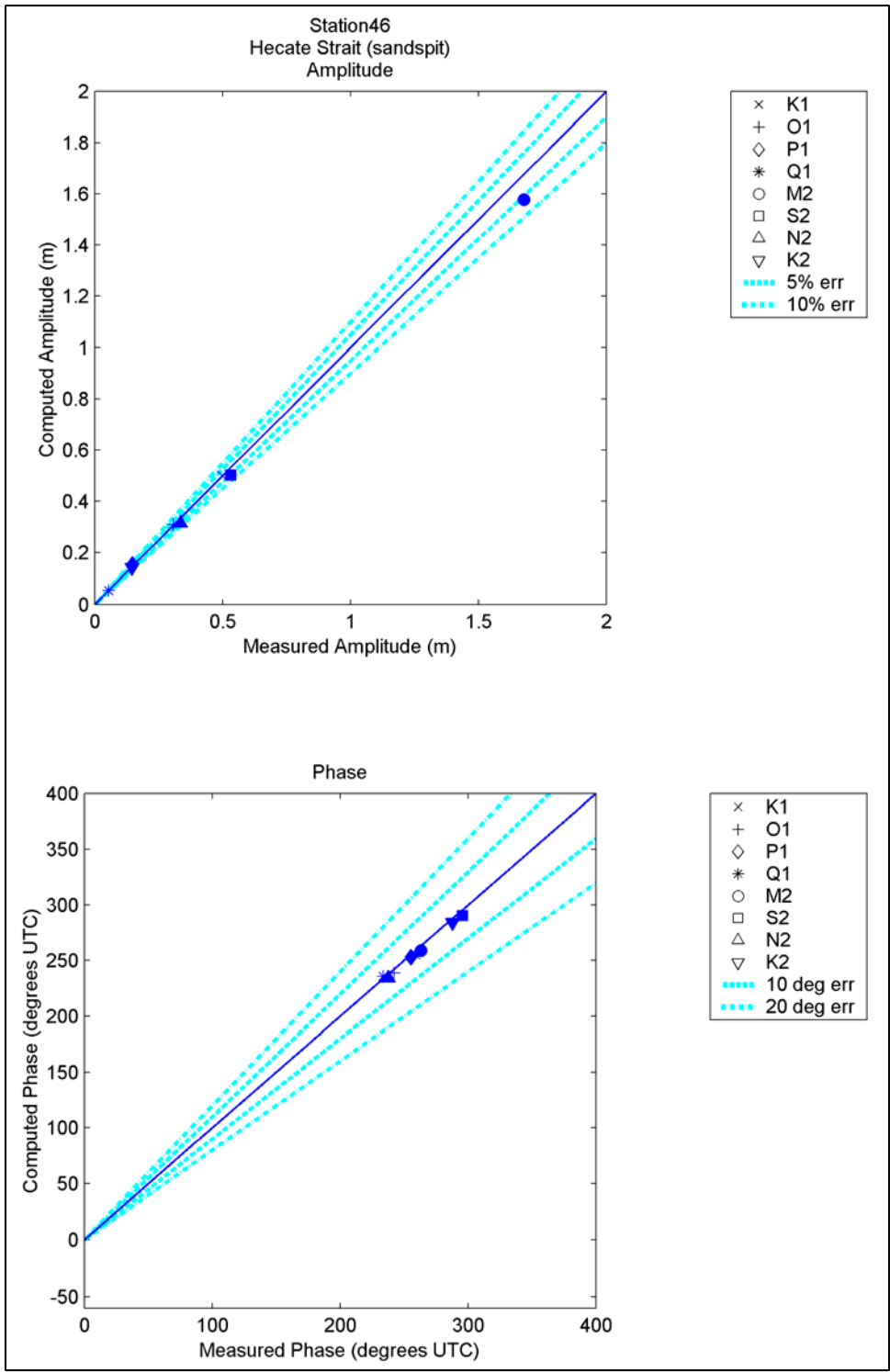


Figure 126. Computed vs. measured harmonic constituents at sta 46

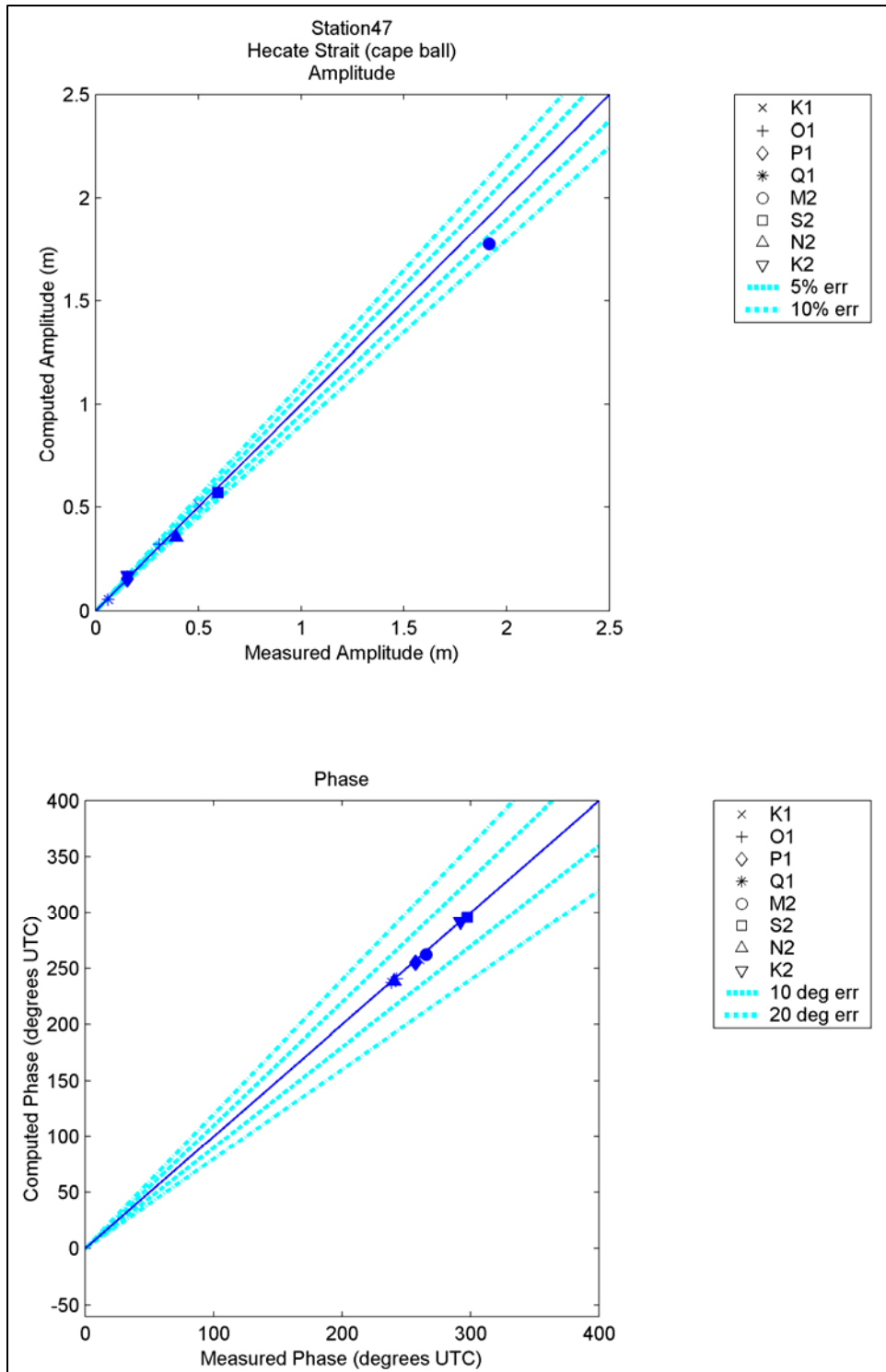


Figure 127. Computed vs. measured harmonic constituents at sta 47

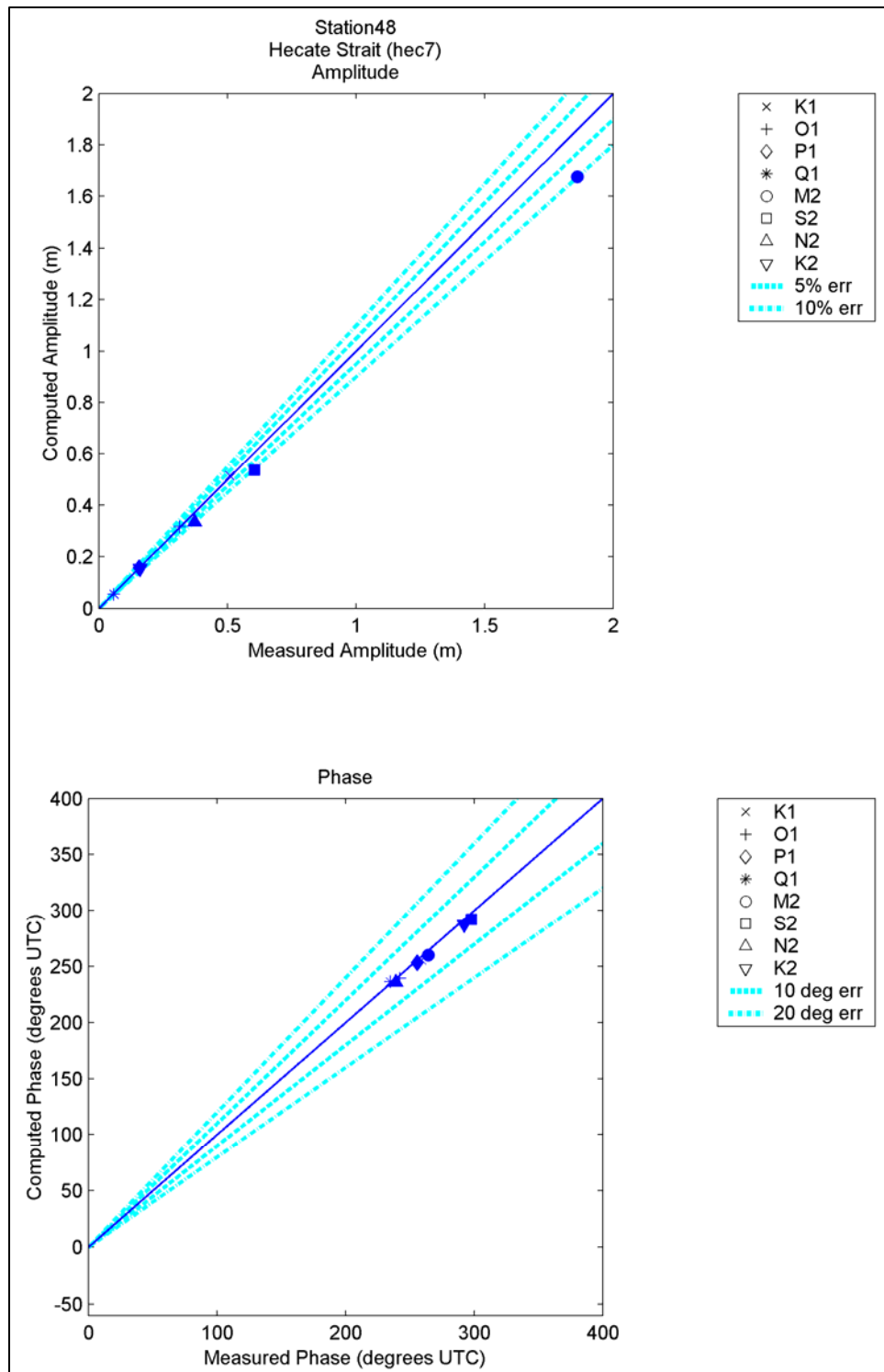


Figure 128. Computed vs. measured harmonic constituents at sta 48

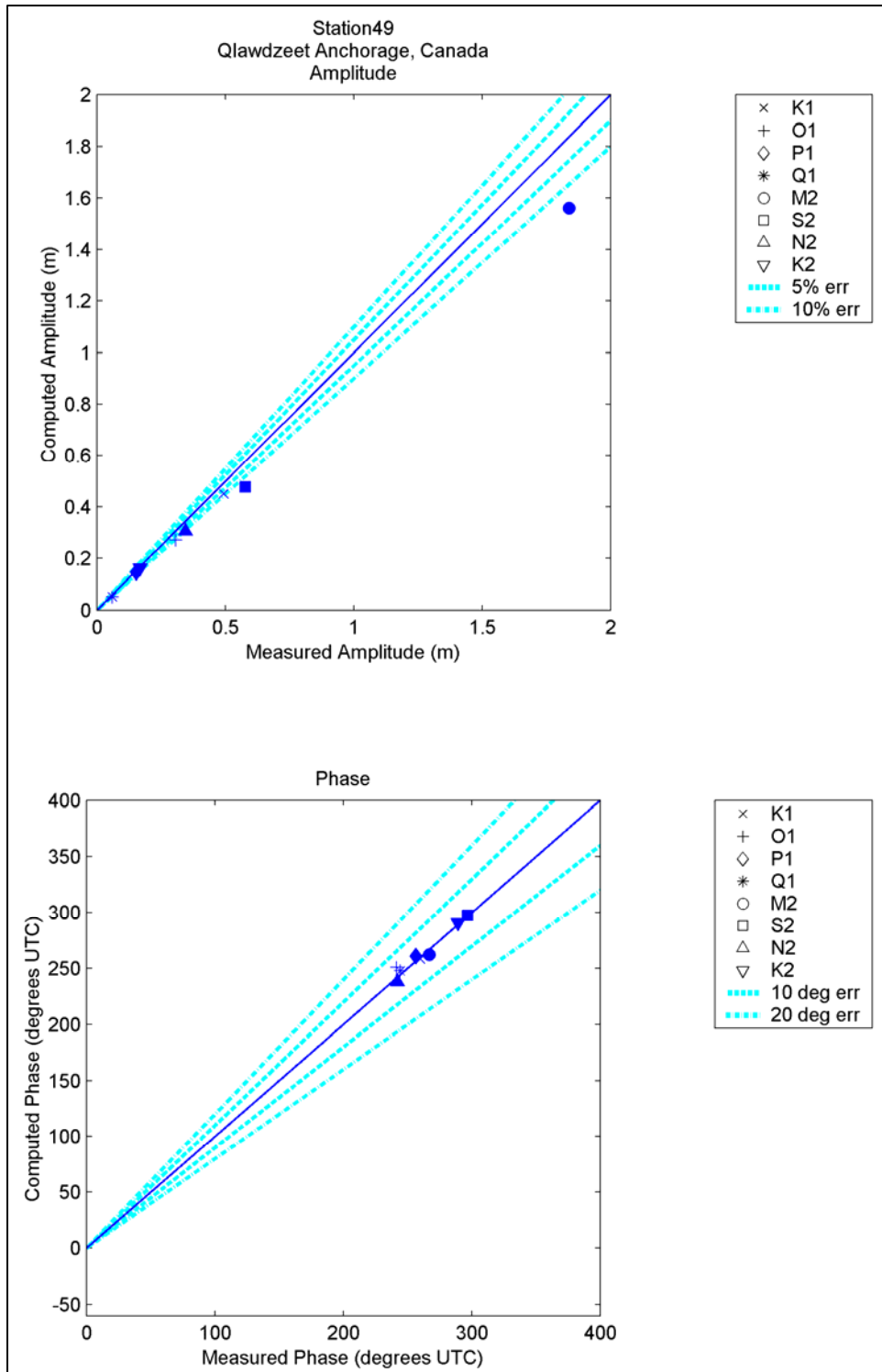


Figure 129. Computed vs. measured harmonic constituents at sta 49

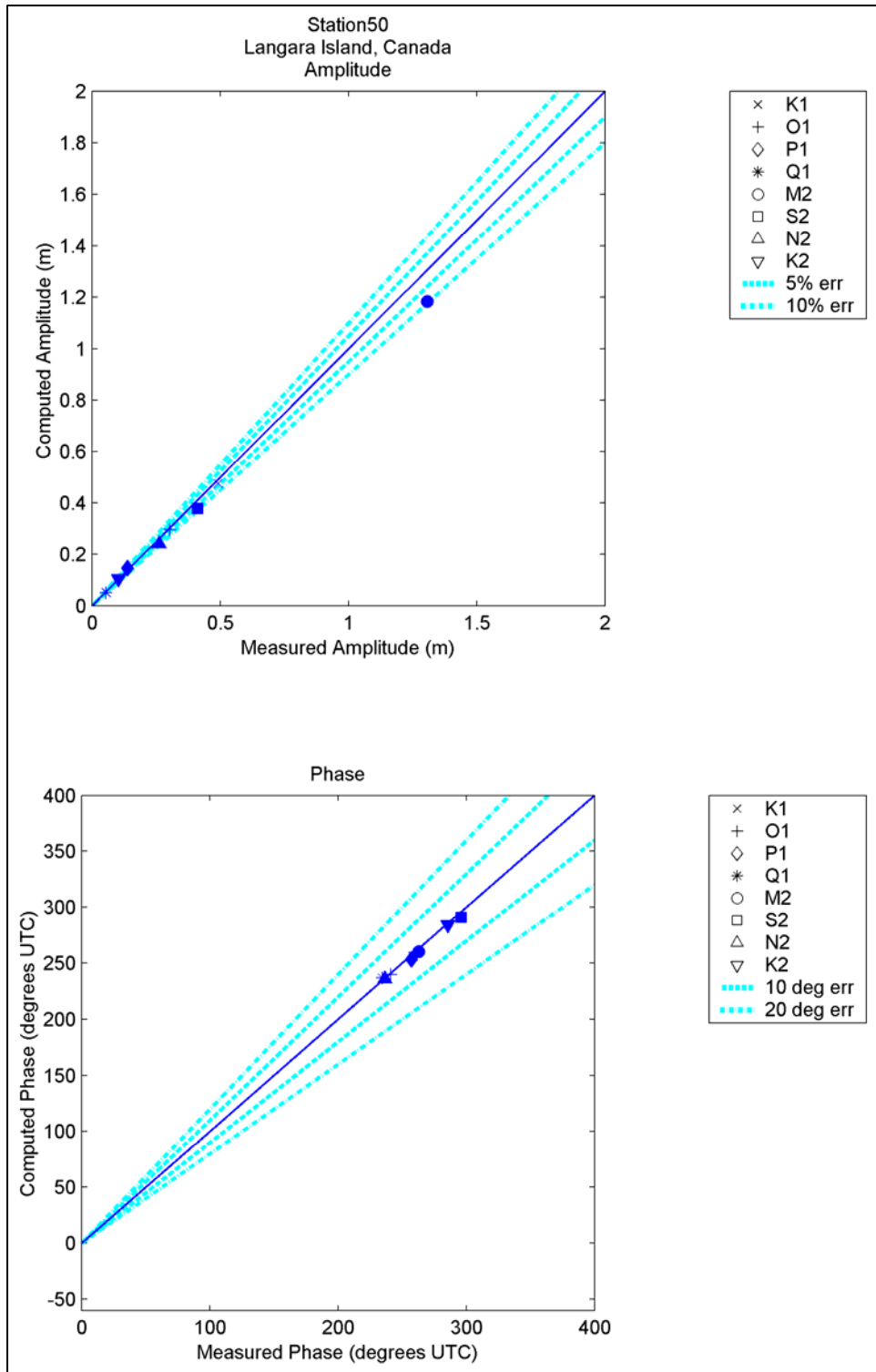


Figure 130. Computed vs. measured harmonic constituents at sta 50

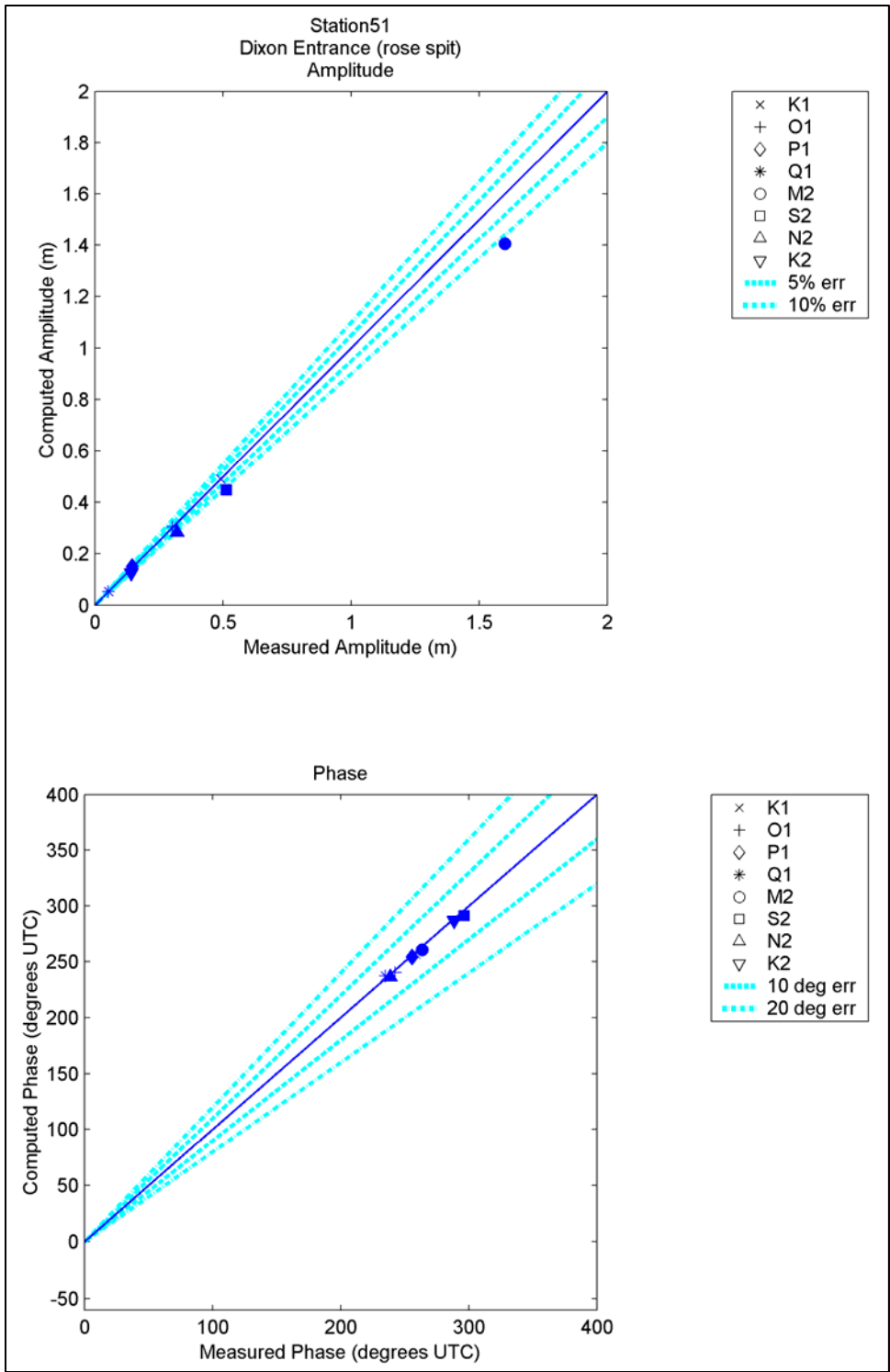


Figure 131. Computed vs. measured harmonic constituents at sta 51

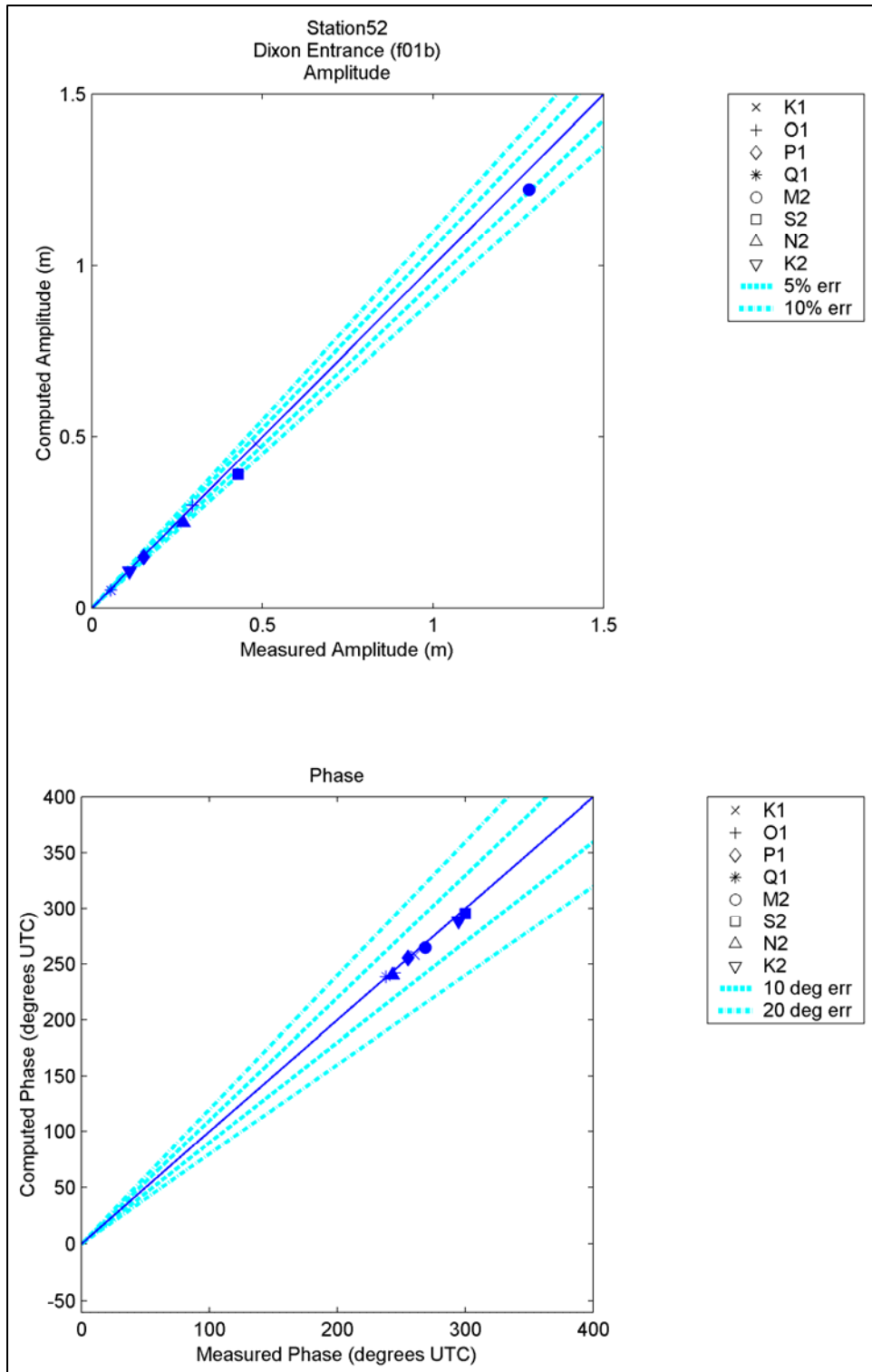


Figure 132. Computed vs. measured harmonic constituents at sta 52

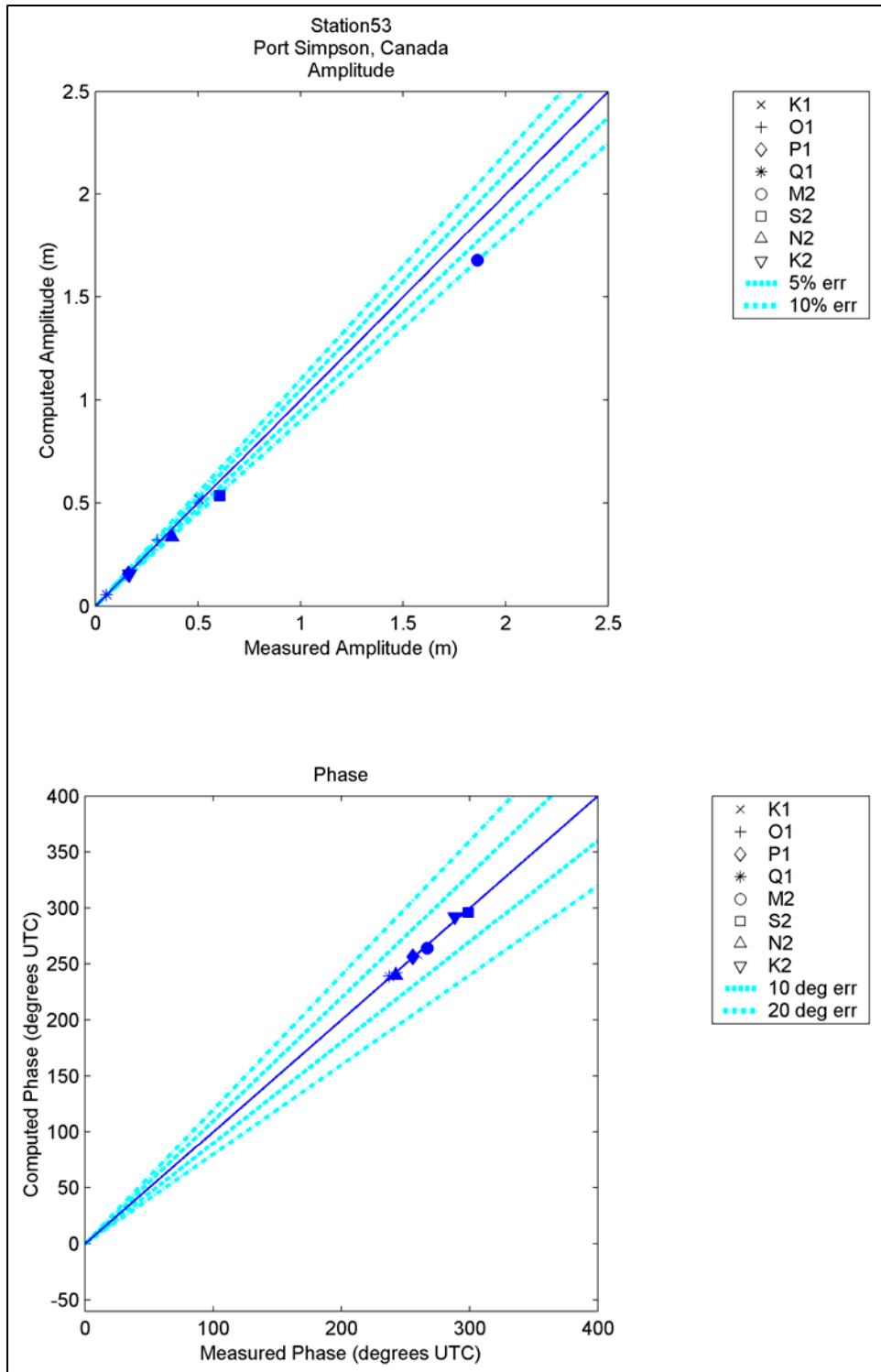


Figure 133. Computed vs. measured harmonic constituents at sta 53

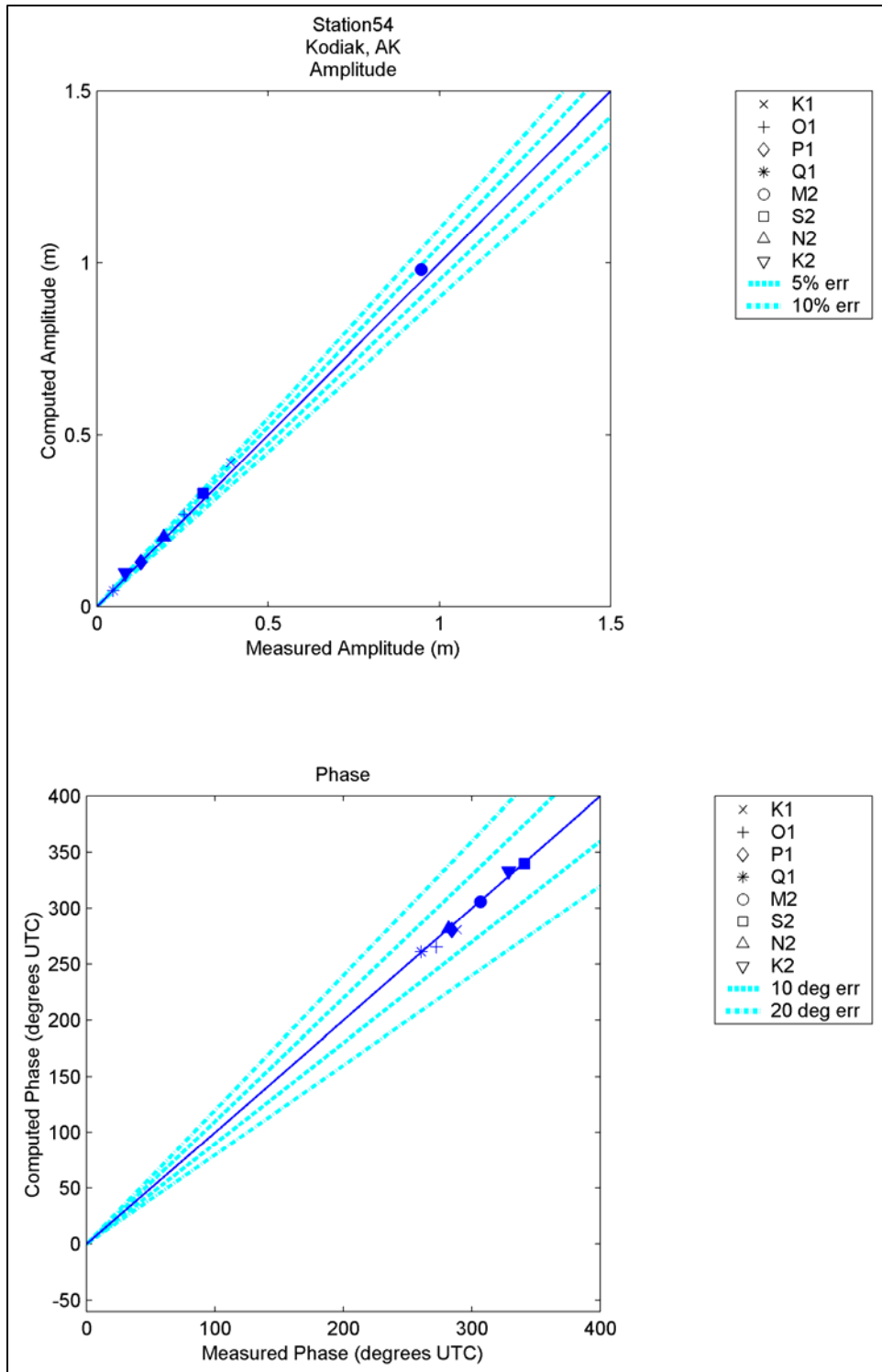


Figure 134. Computed vs. measured harmonic constituents at sta 54

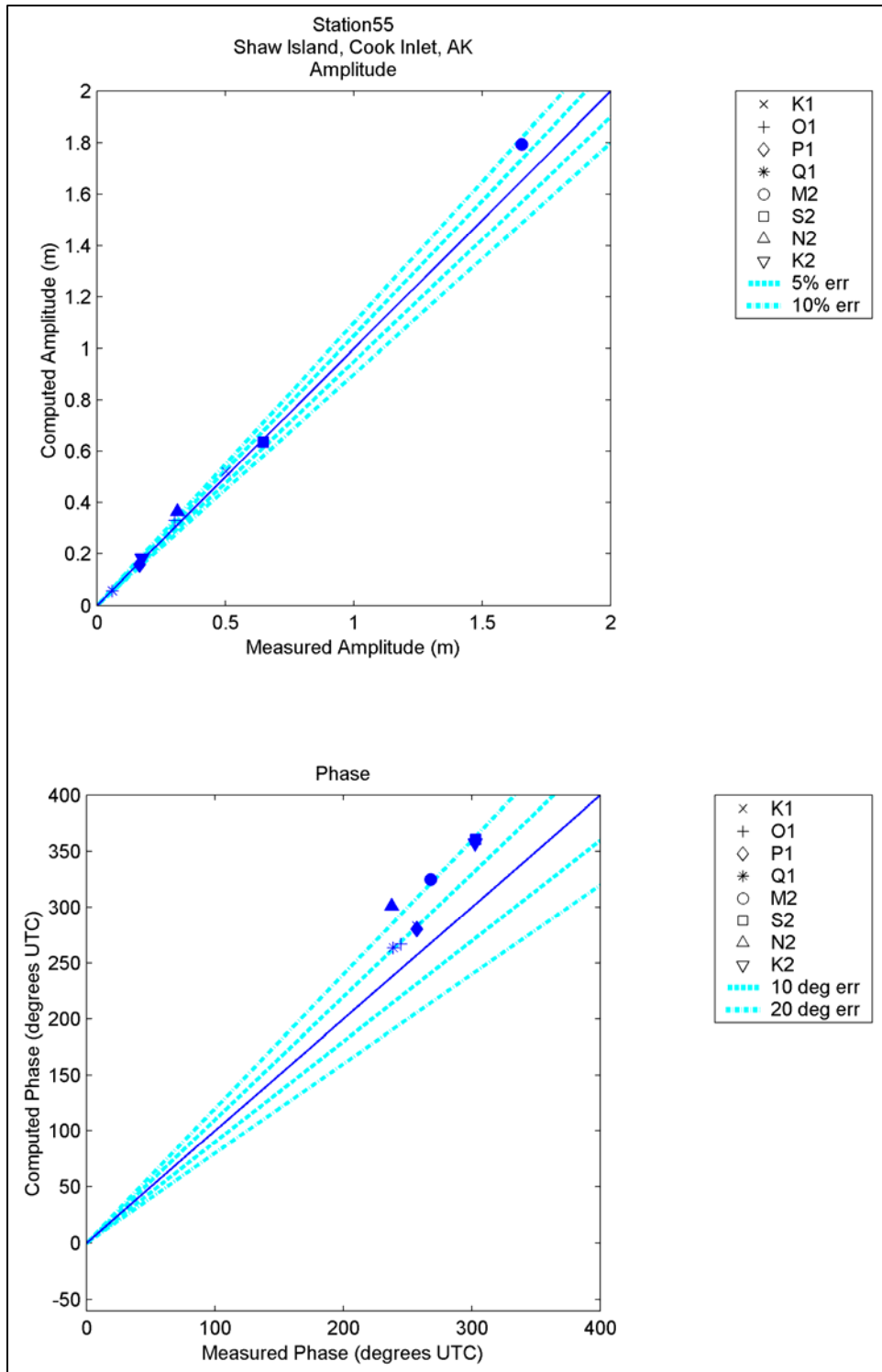


Figure 135. Computed vs. measured harmonic constituents at sta 55

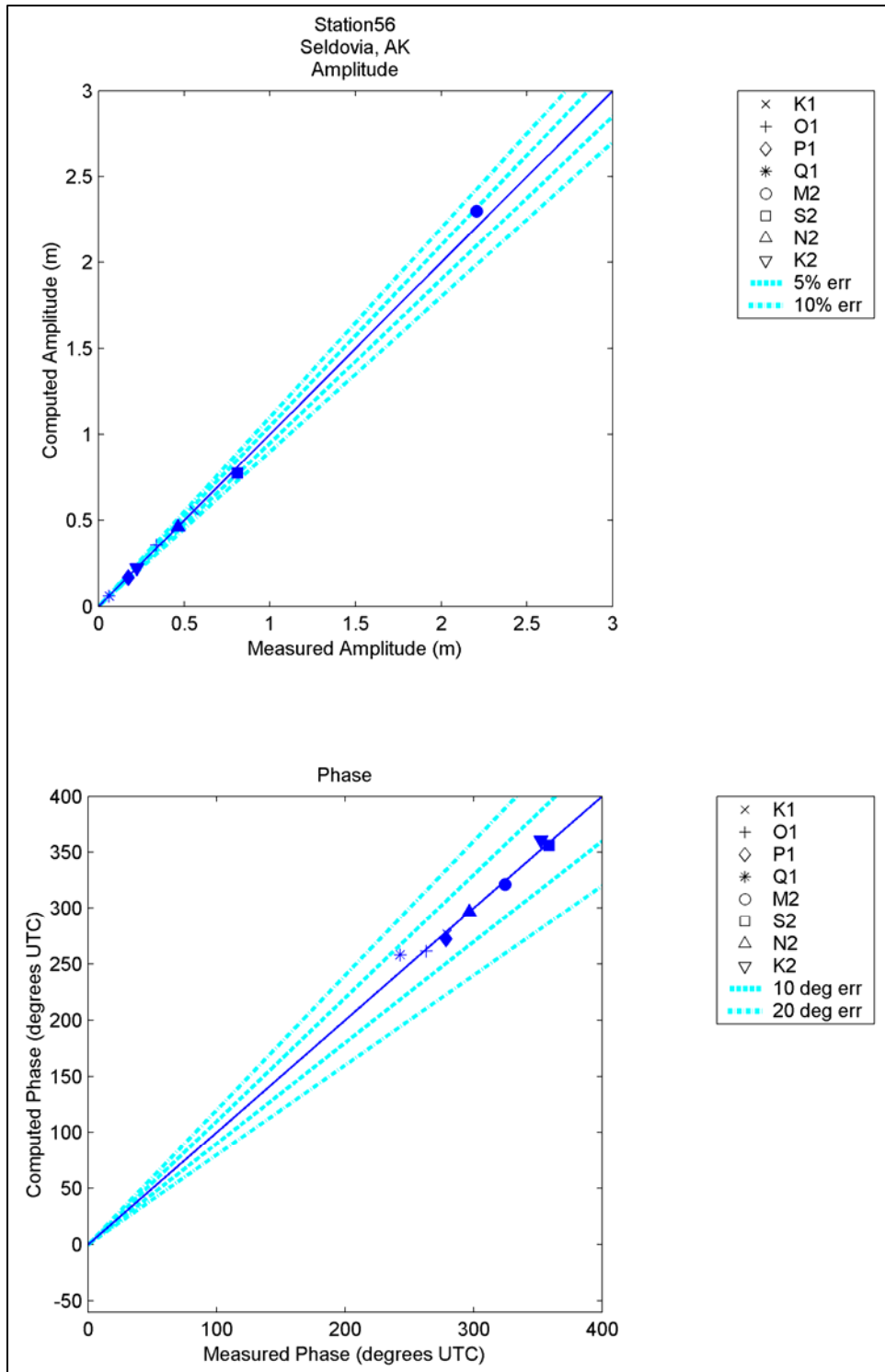


Figure 136. Computed vs. measured harmonic constituents at sta 56

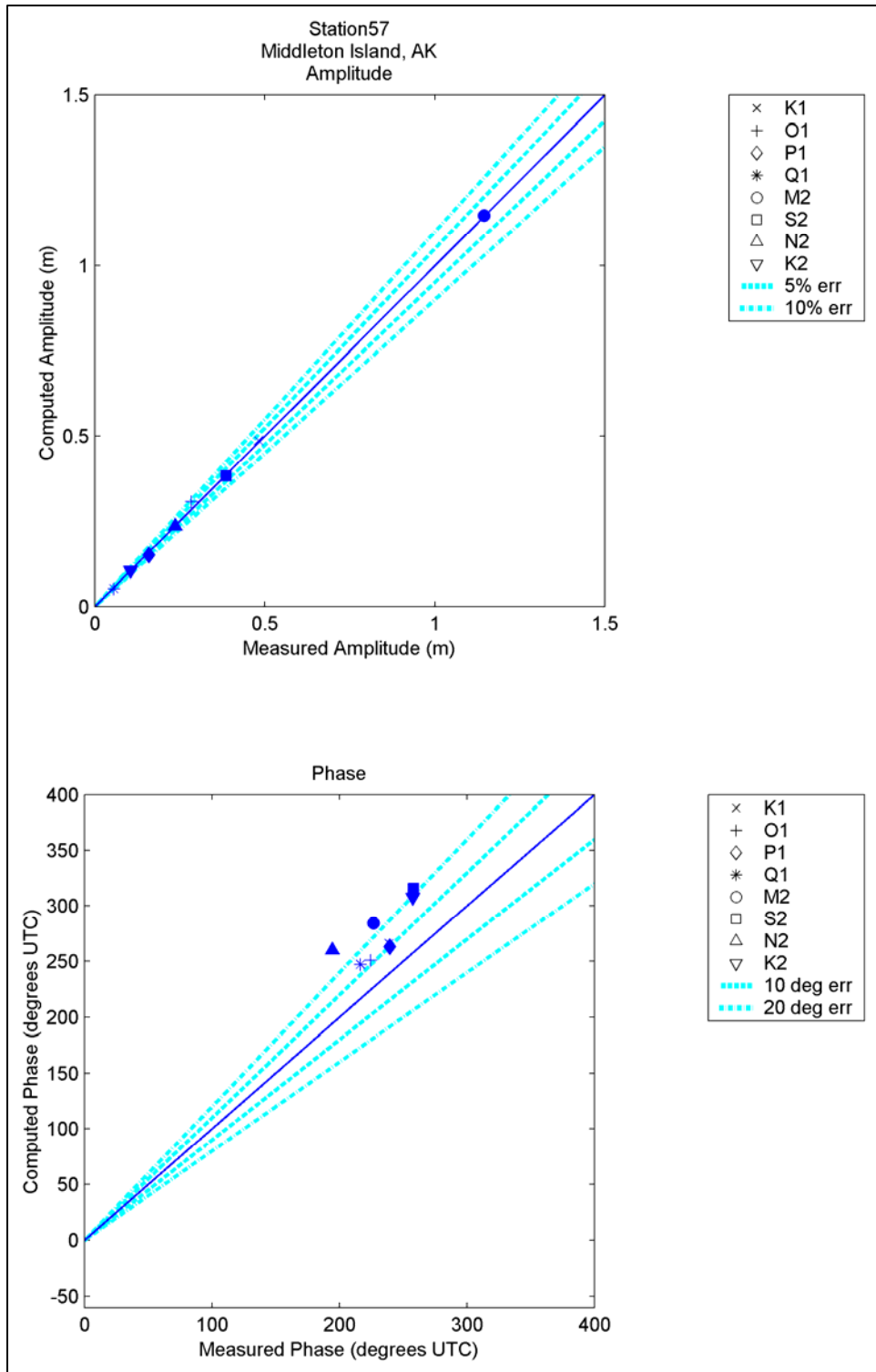


Figure 137. Computed vs. measured harmonic constituents at sta 57

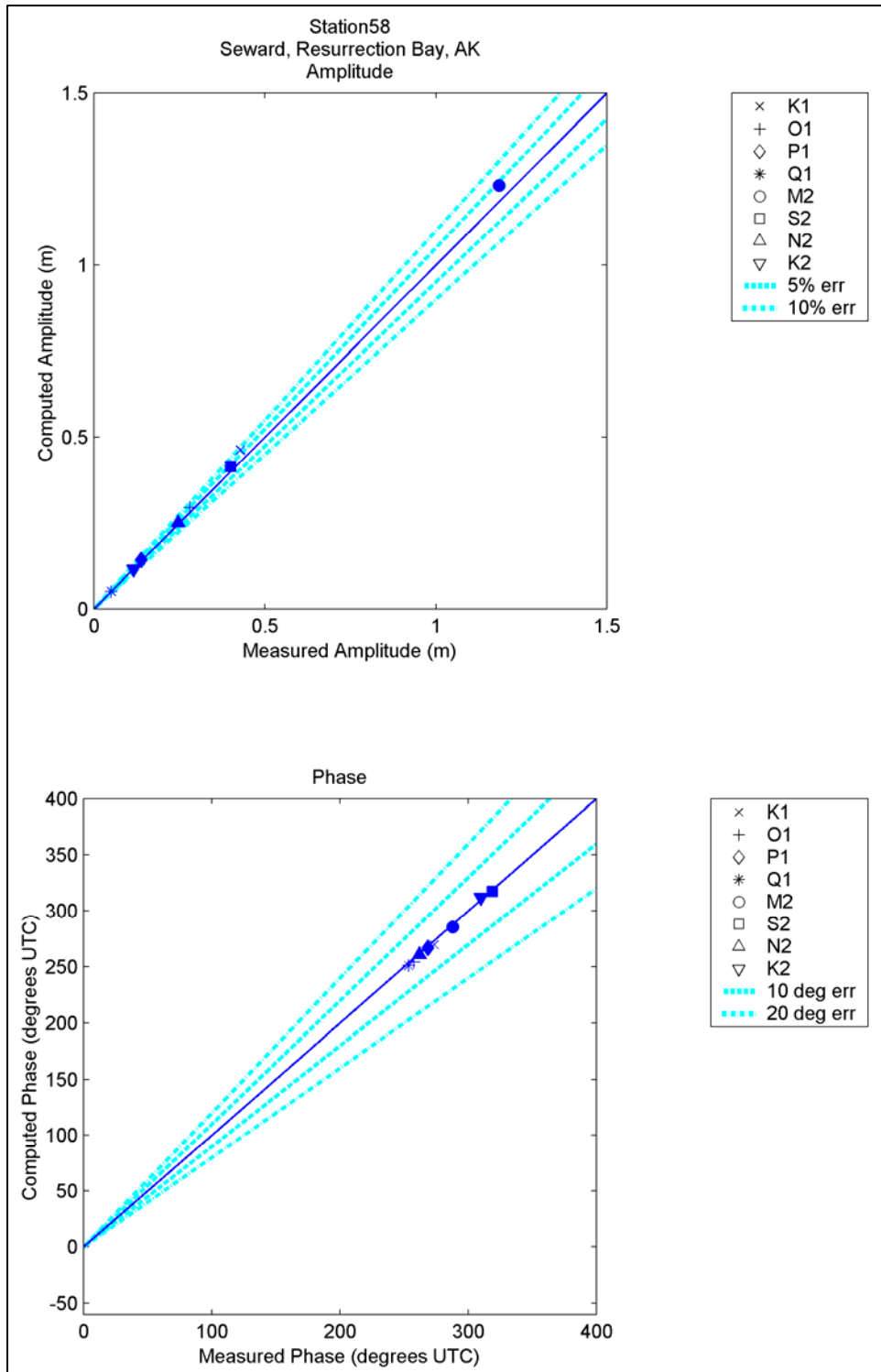


Figure 138. Computed vs. measured harmonic constituents at sta 58

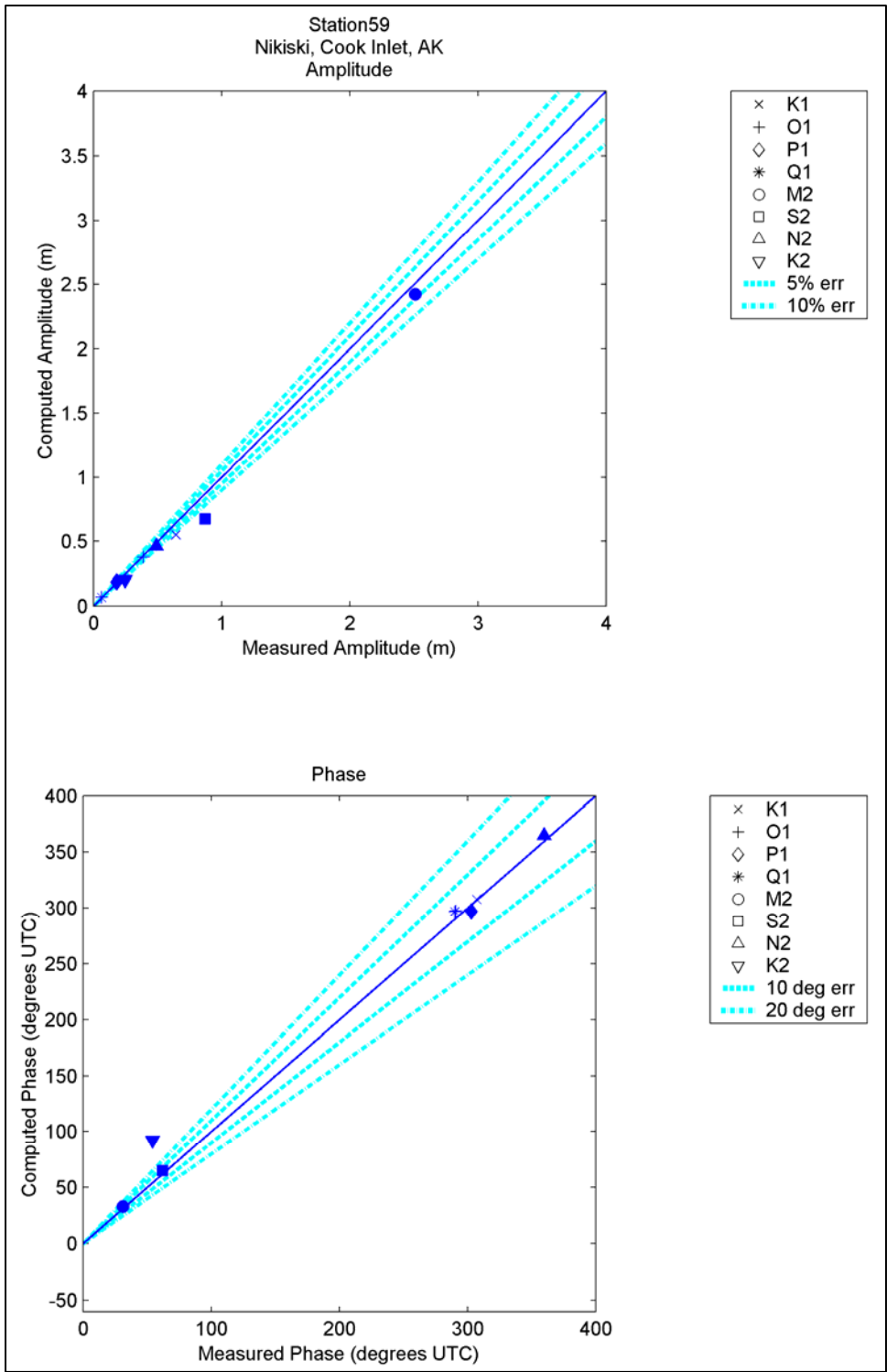


Figure 139. Computed vs. measured harmonic constituents at sta 59

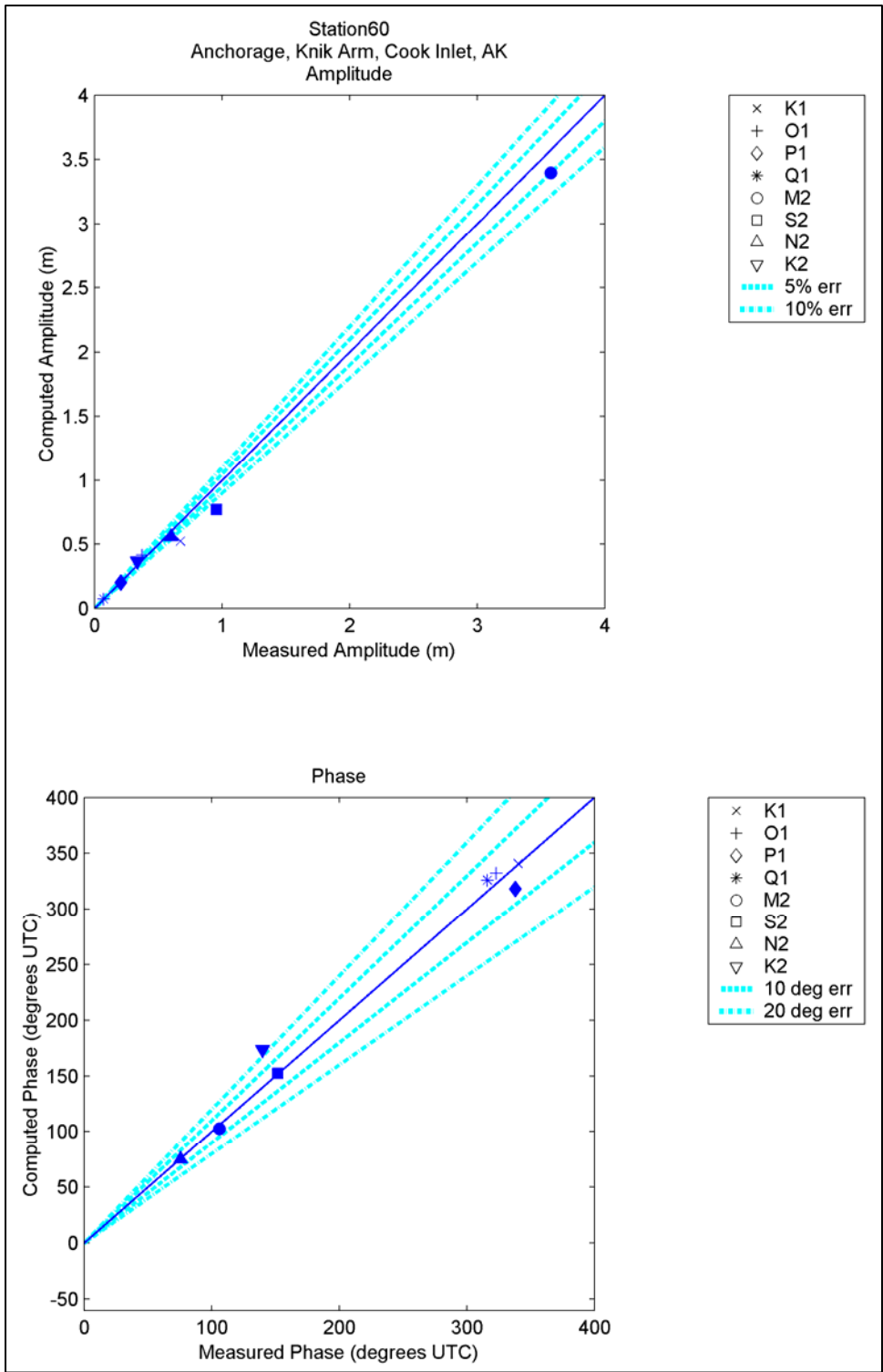


Figure 140. Computed vs. measured harmonic constituents at sta 60

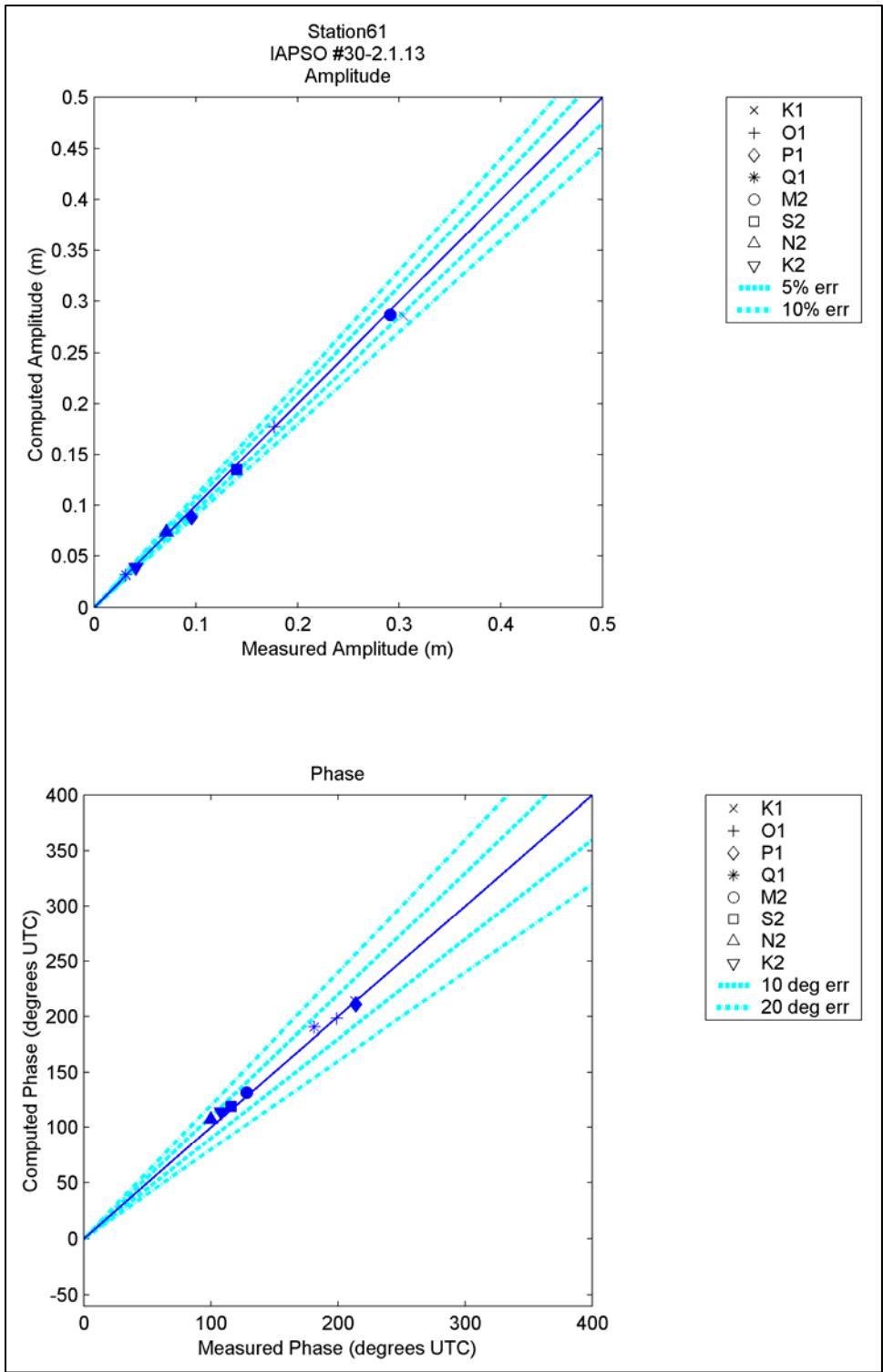


Figure 141. Computed vs. measured harmonic constituents at sta 61

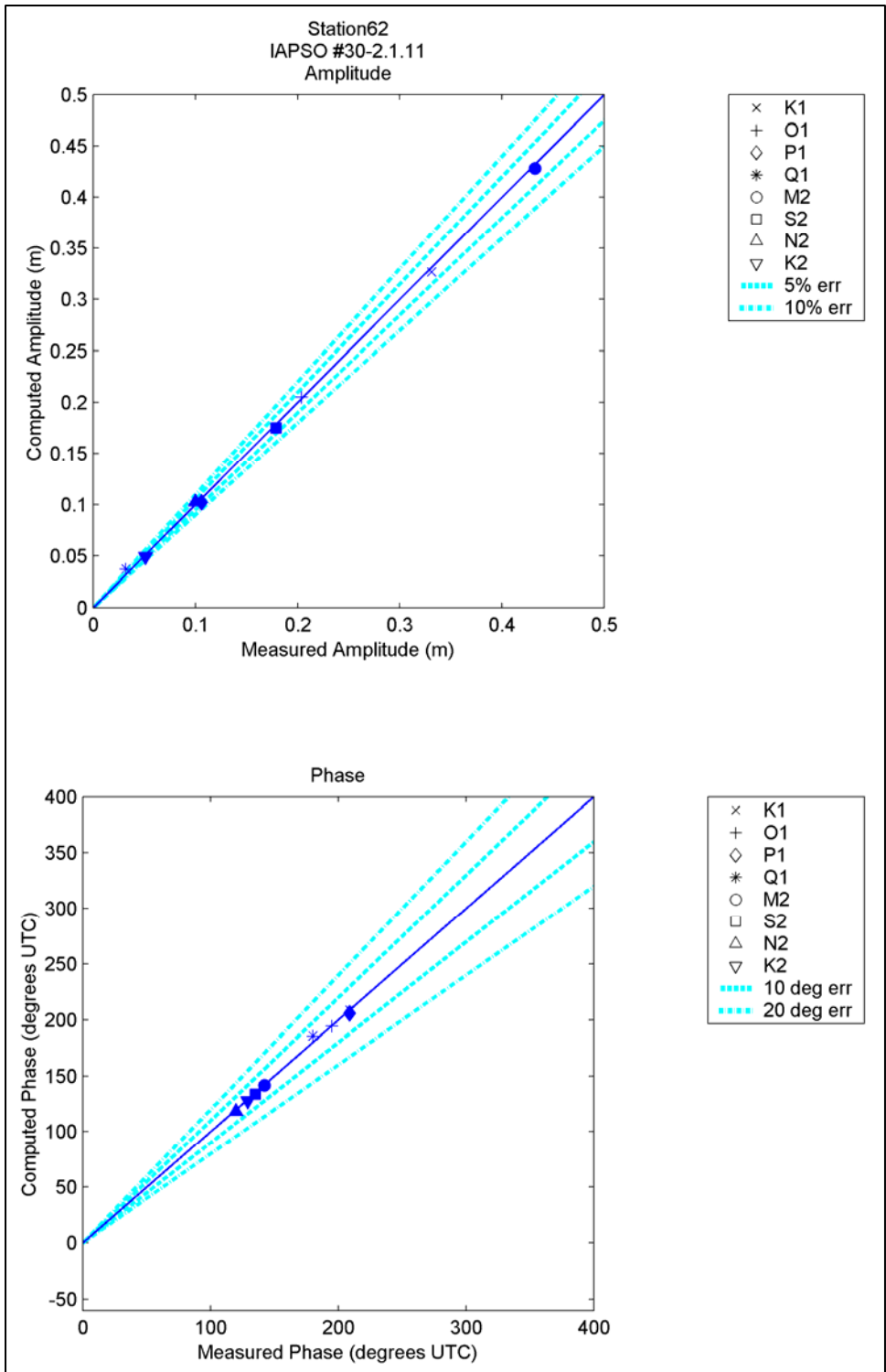


Figure 142. Computed vs. measured harmonic constituents at sta 62

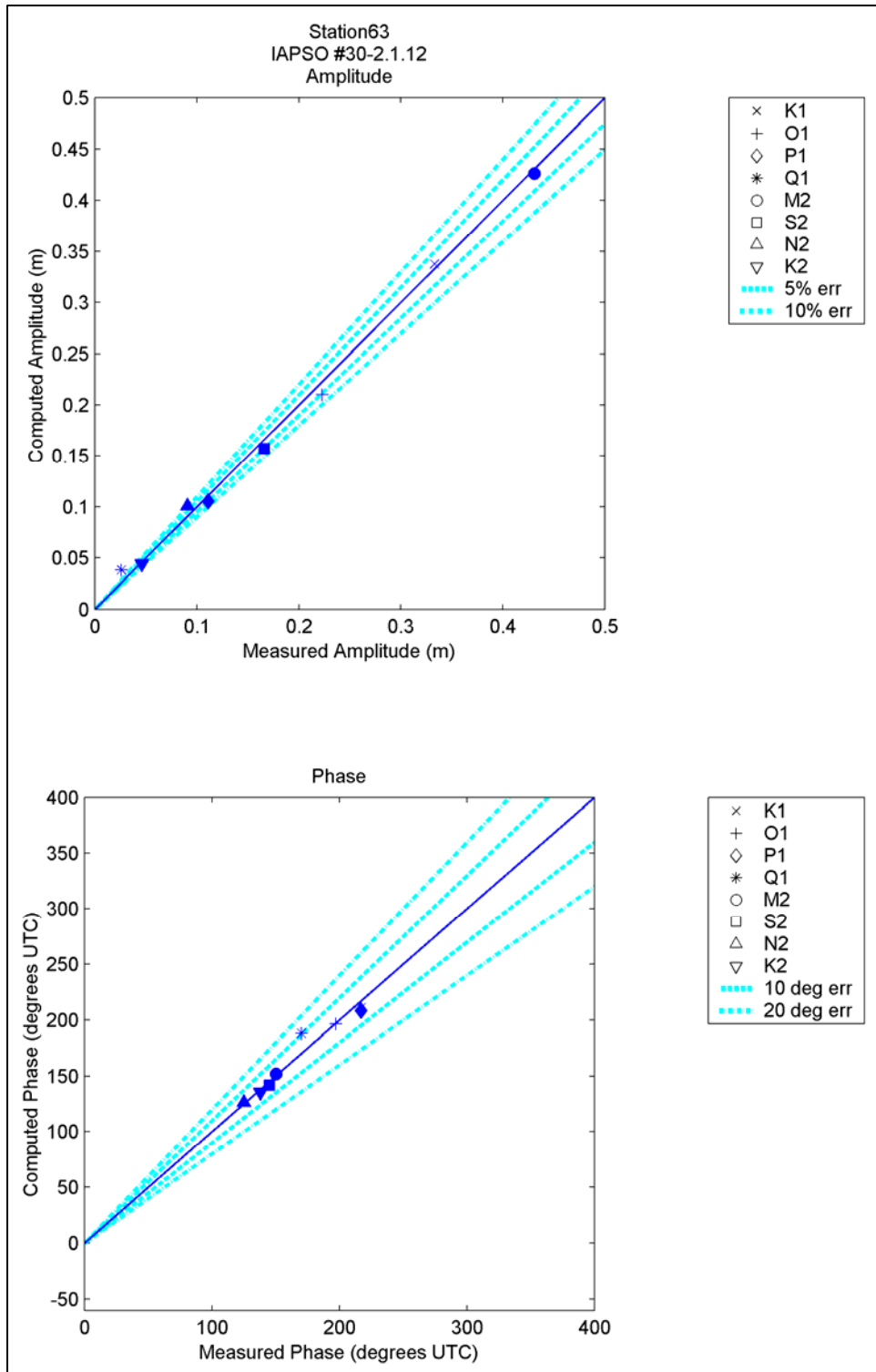


Figure 143. Computed vs. measured harmonic constituents at sta 63

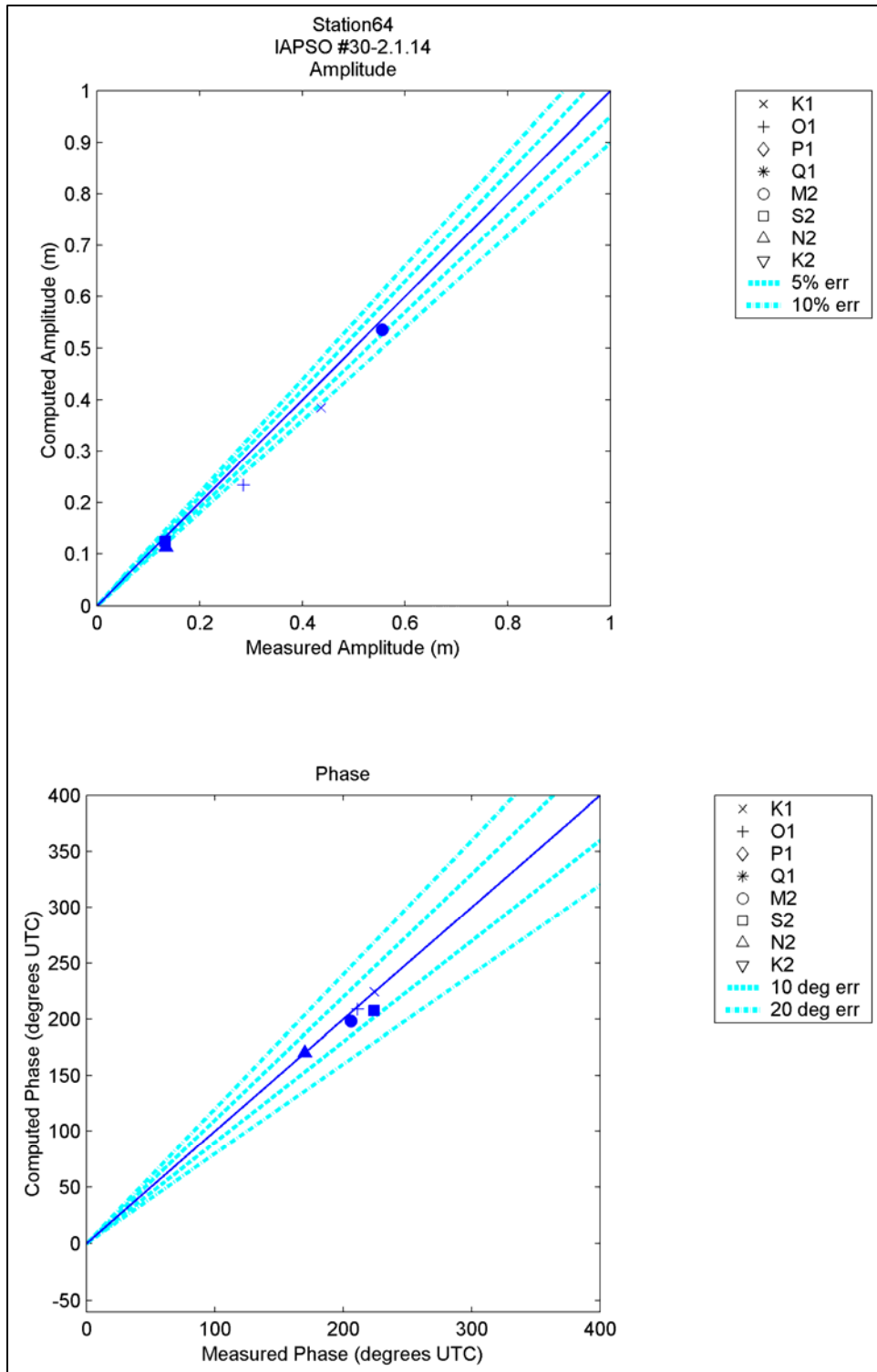


Figure 144. Computed vs. measured harmonic constituents at sta 64

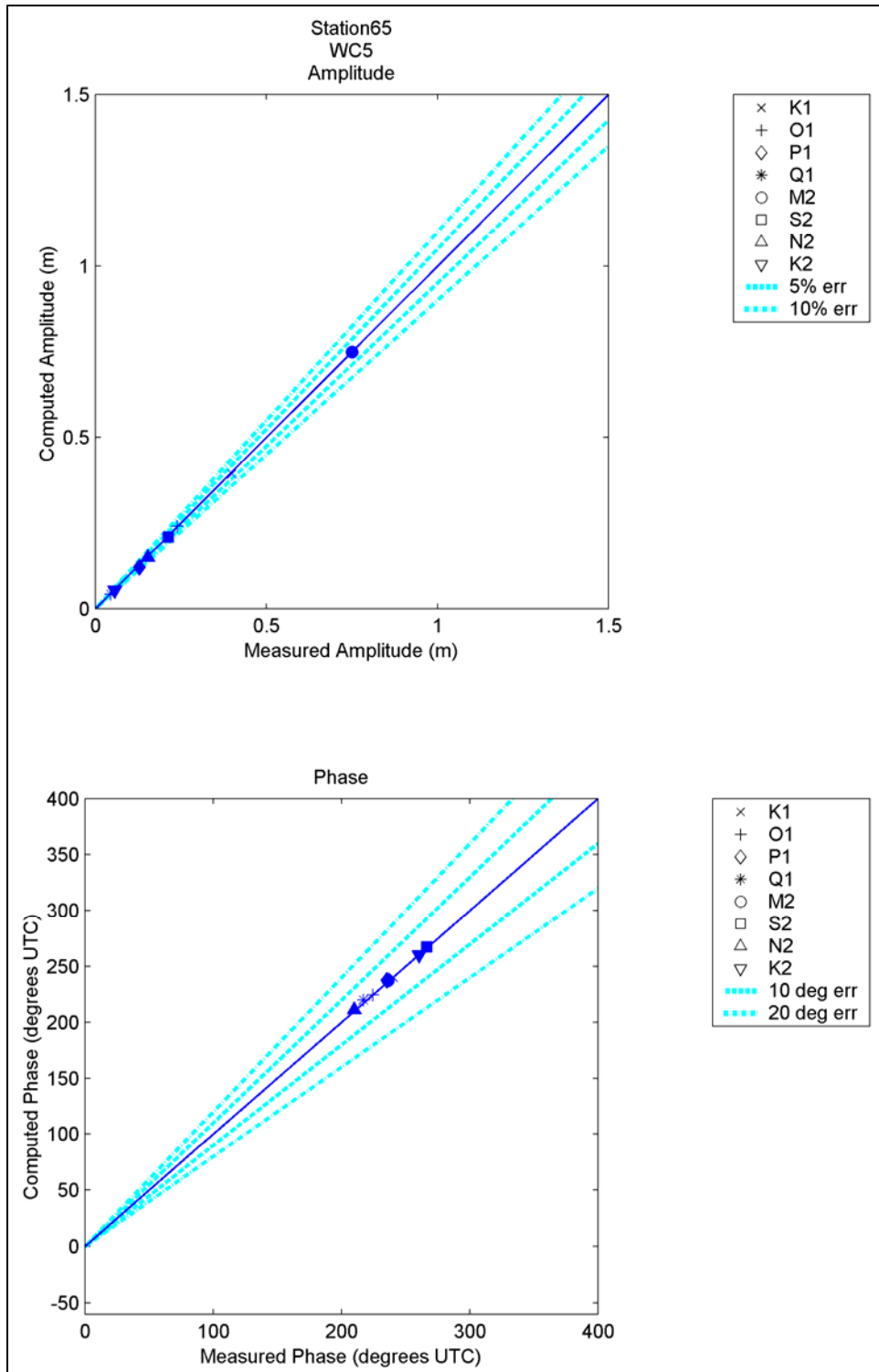


Figure 145. Computed vs. measured harmonic constituents at sta 65

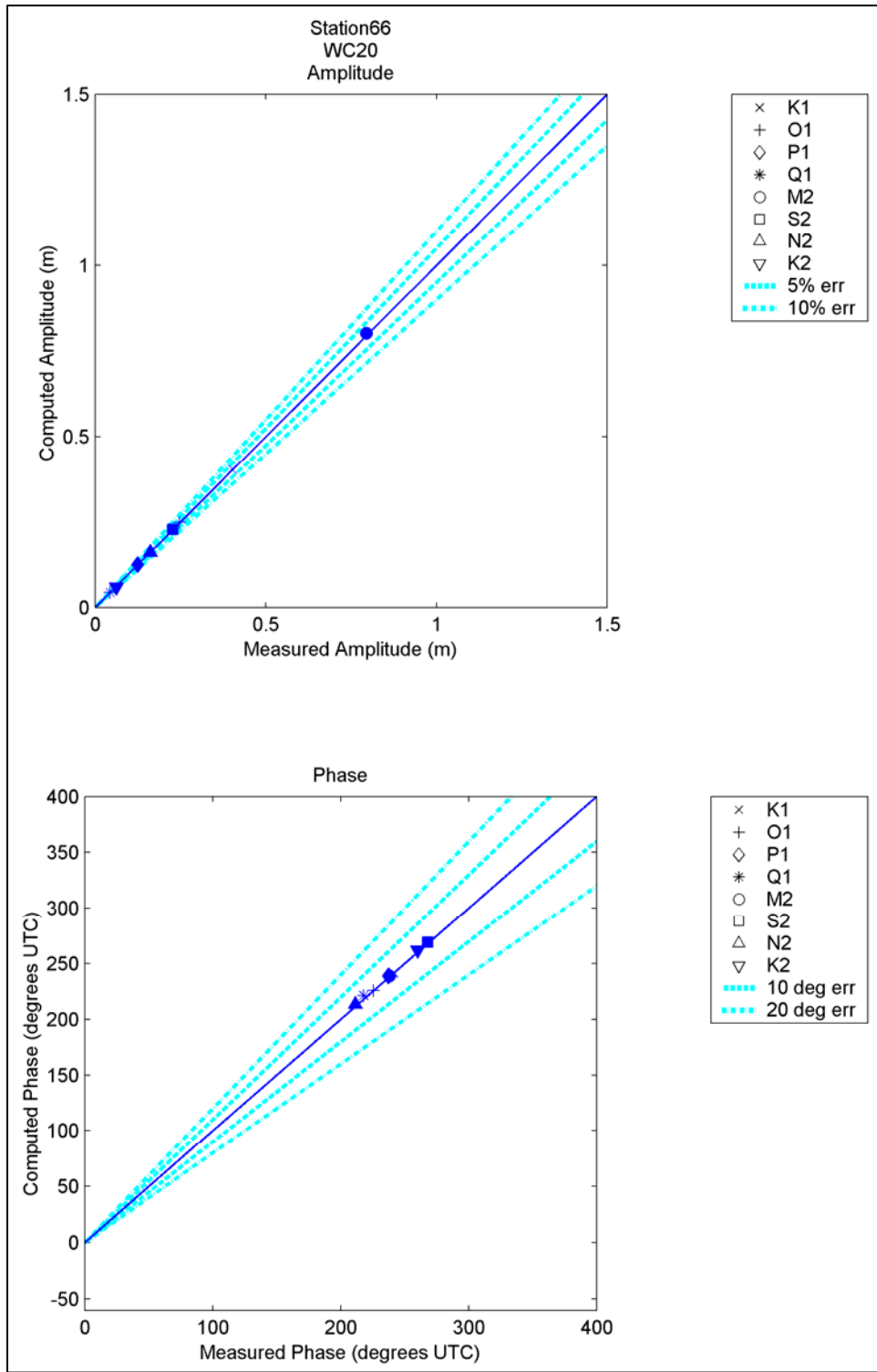


Figure 146. Computed vs. measured harmonic constituents at sta 66

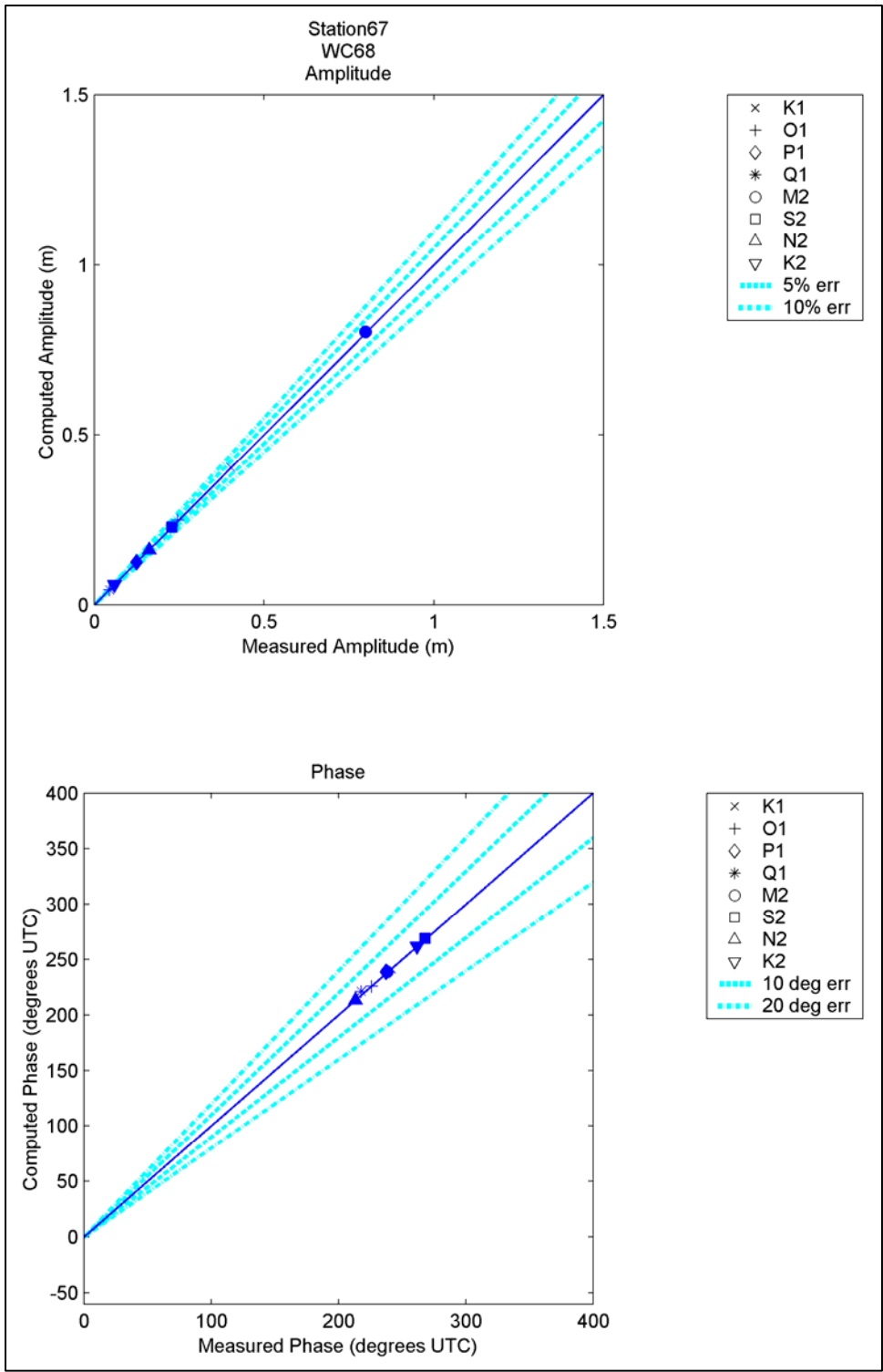


Figure 147. Computed vs. measured harmonic constituents at sta 67

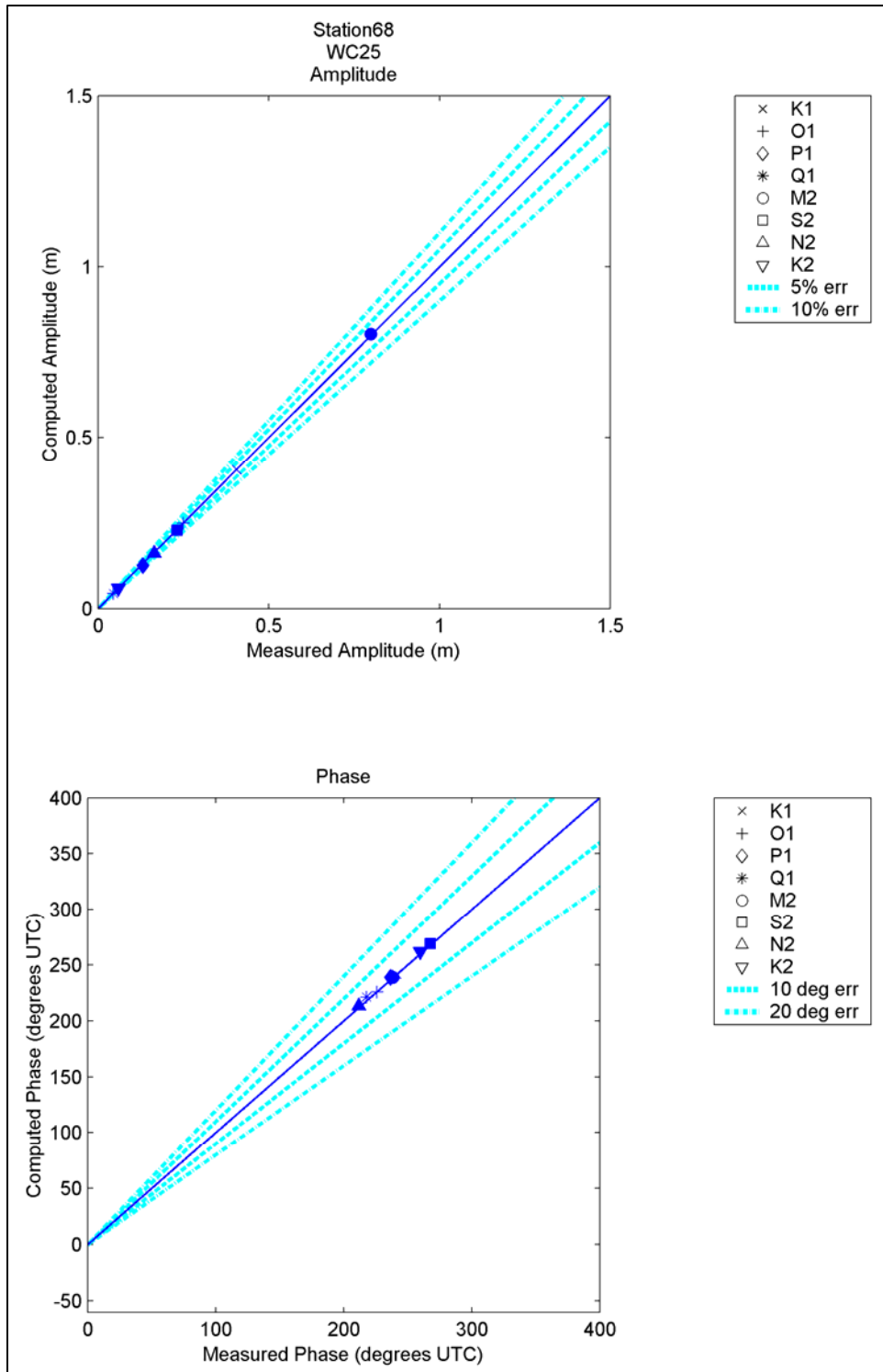


Figure 148. Computed vs. measured harmonic constituents at sta 68

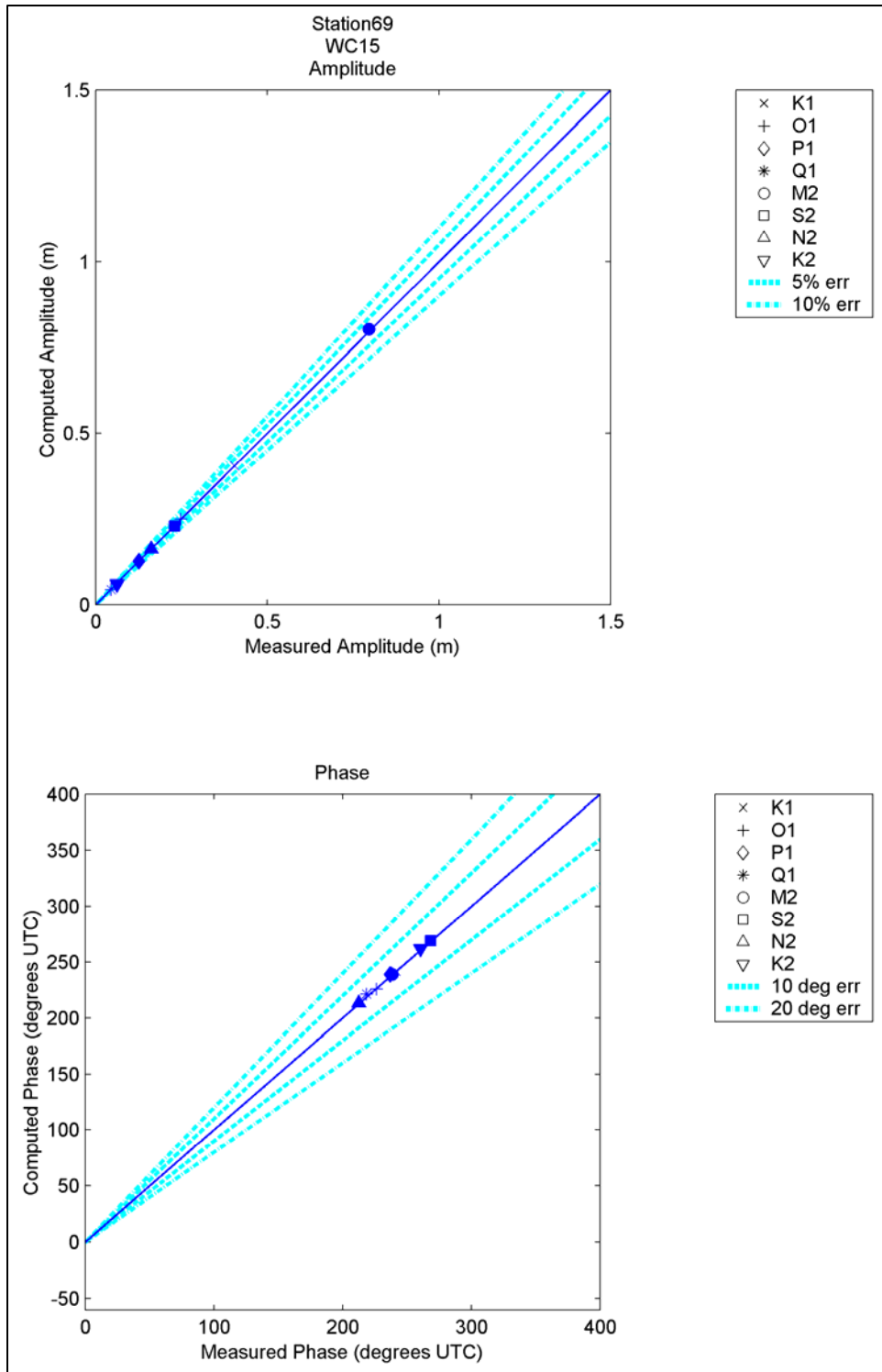


Figure 149. Computed vs. measured harmonic constituents at sta 69

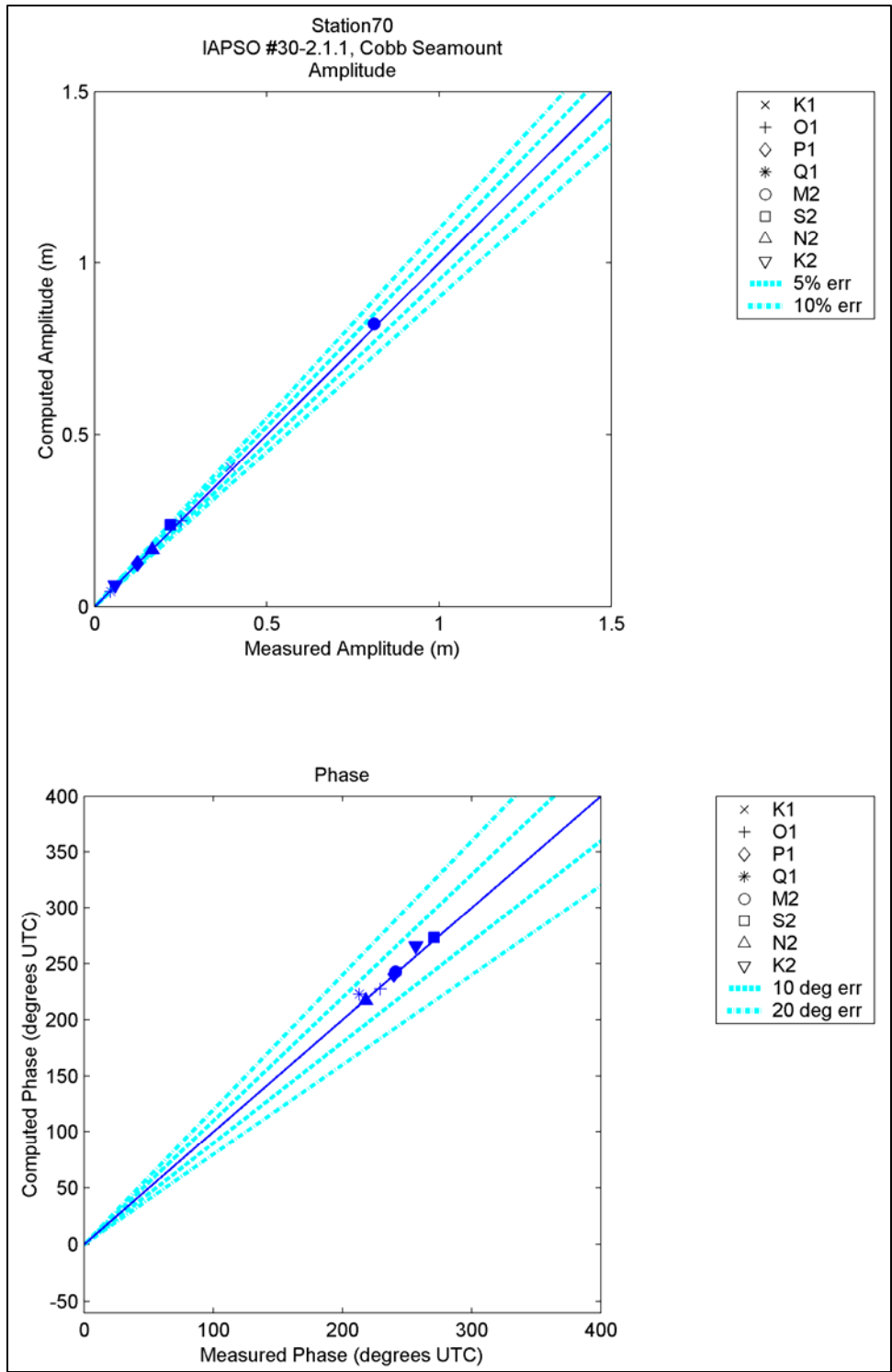


Figure 150. Computed vs. measured harmonic constituents at sta 70

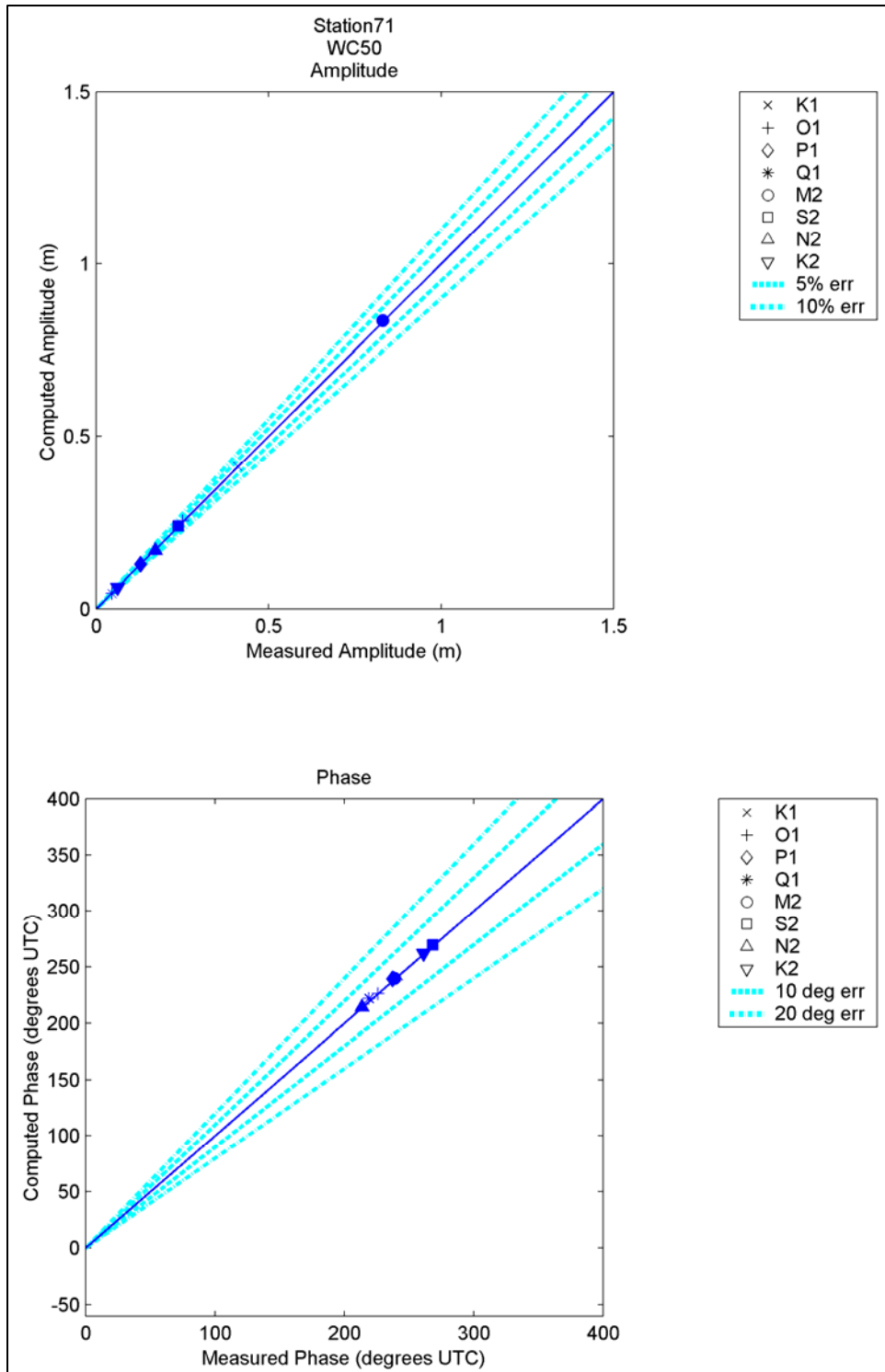


Figure 151. Computed vs. measured harmonic constituents at sta 71

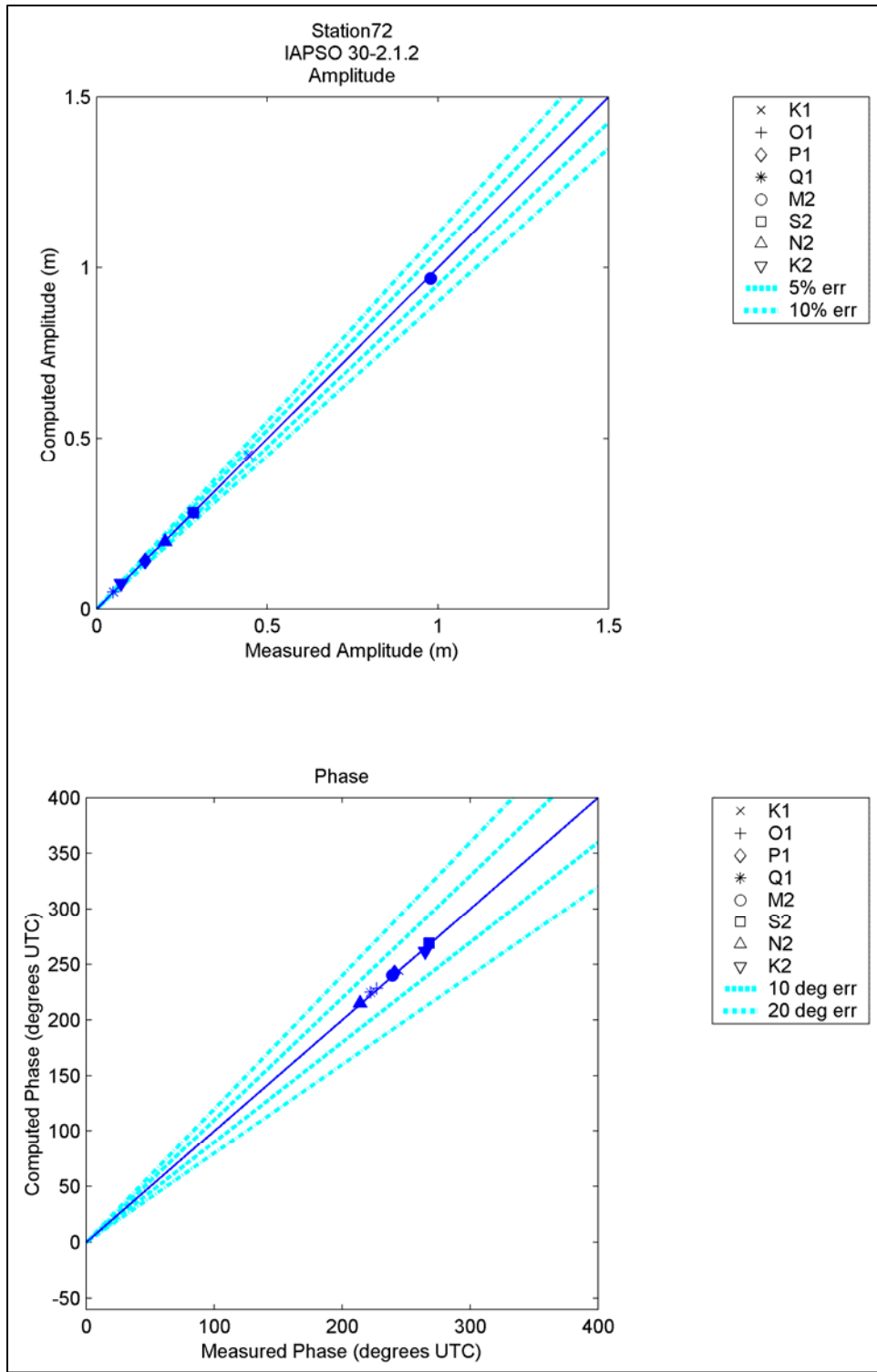


Figure 152. Computed vs. measured harmonic constituents at sta 72

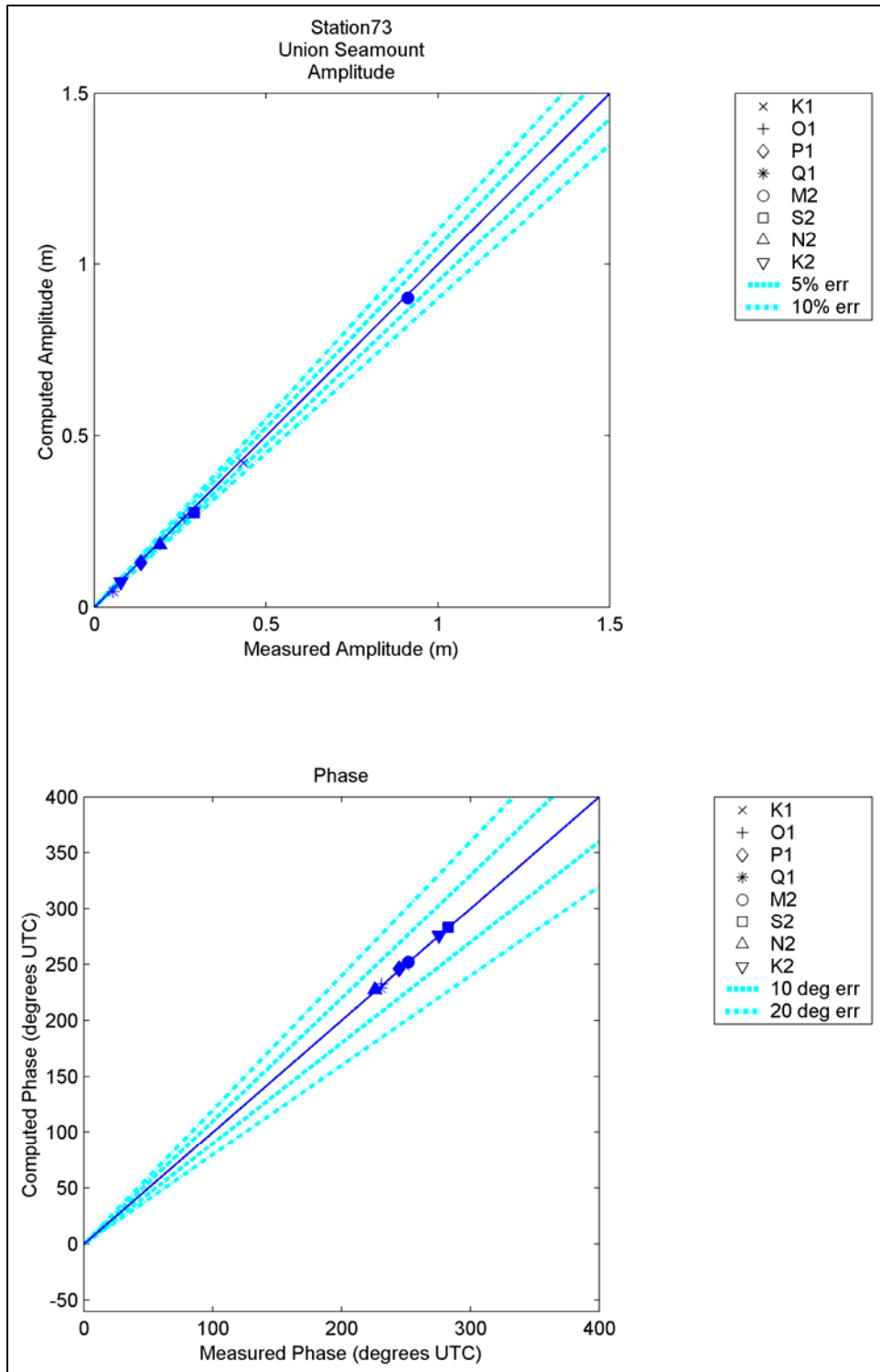


Figure 153. Computed vs. measured harmonic constituents at sta 73

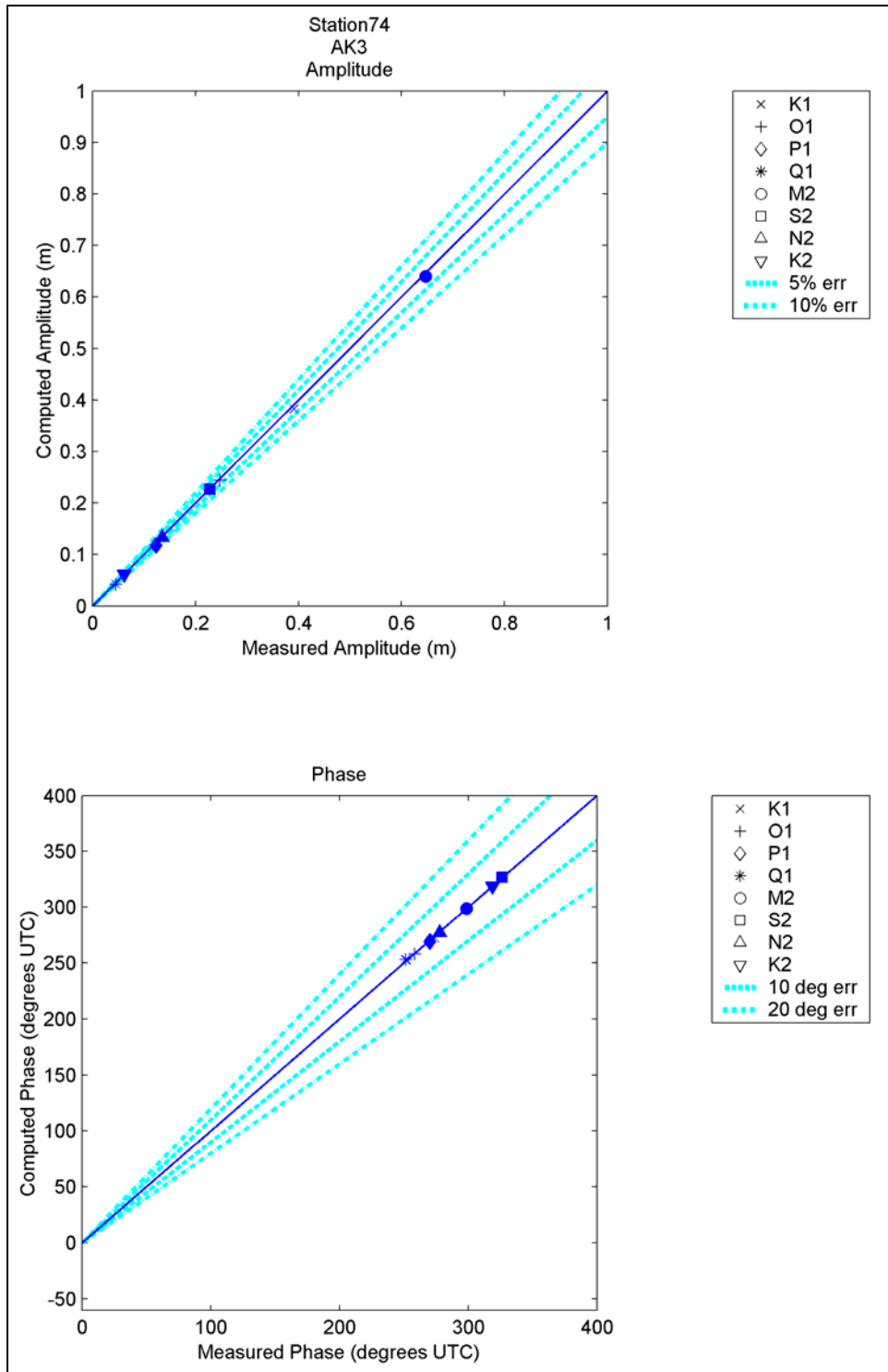


Figure 154. Computed vs. measured harmonic constituents at sta 74

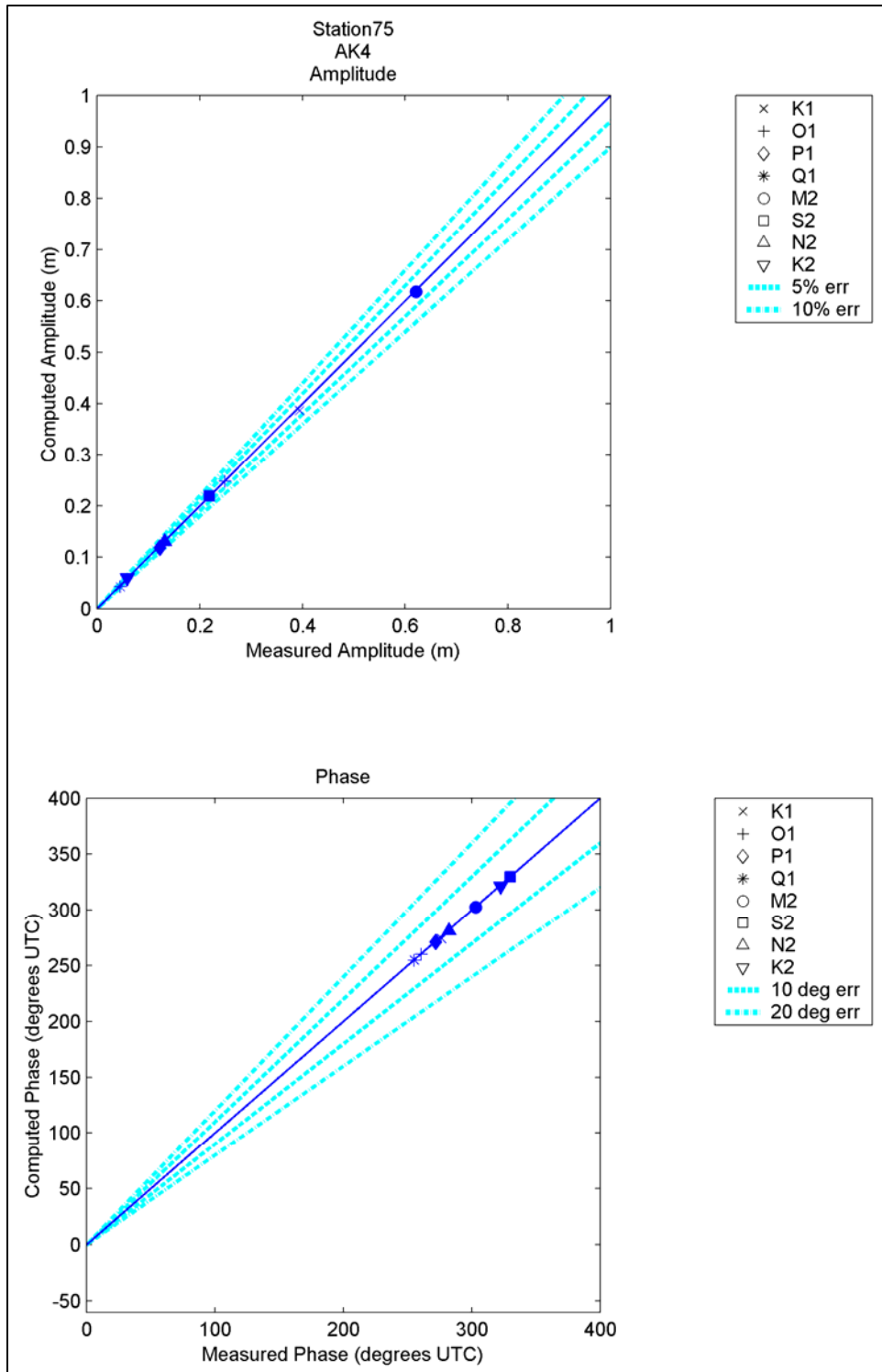


Figure 155. Computed vs. measured harmonic constituents at sta 75

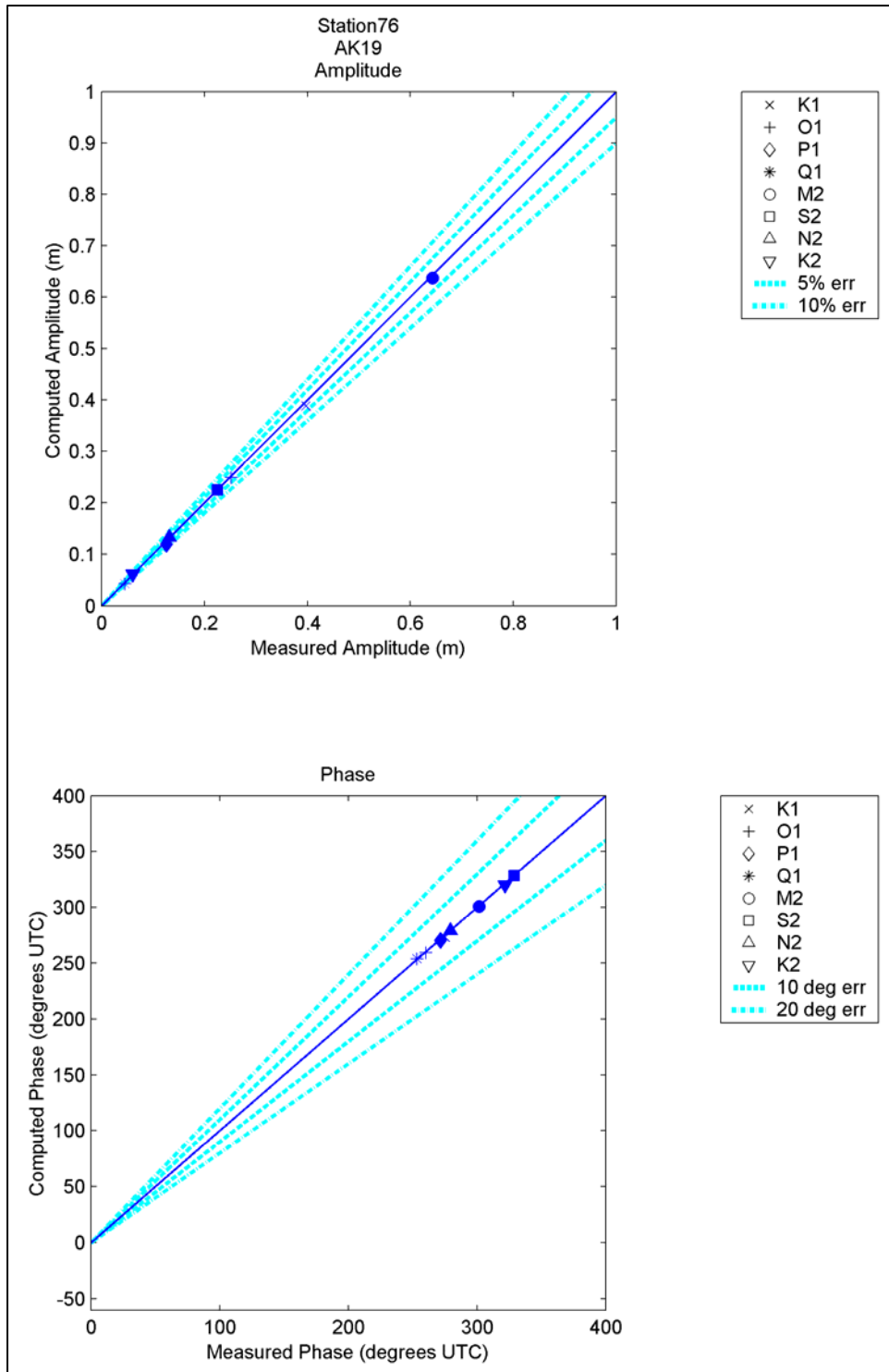


Figure 156. Computed vs. measured harmonic constituents at sta 76

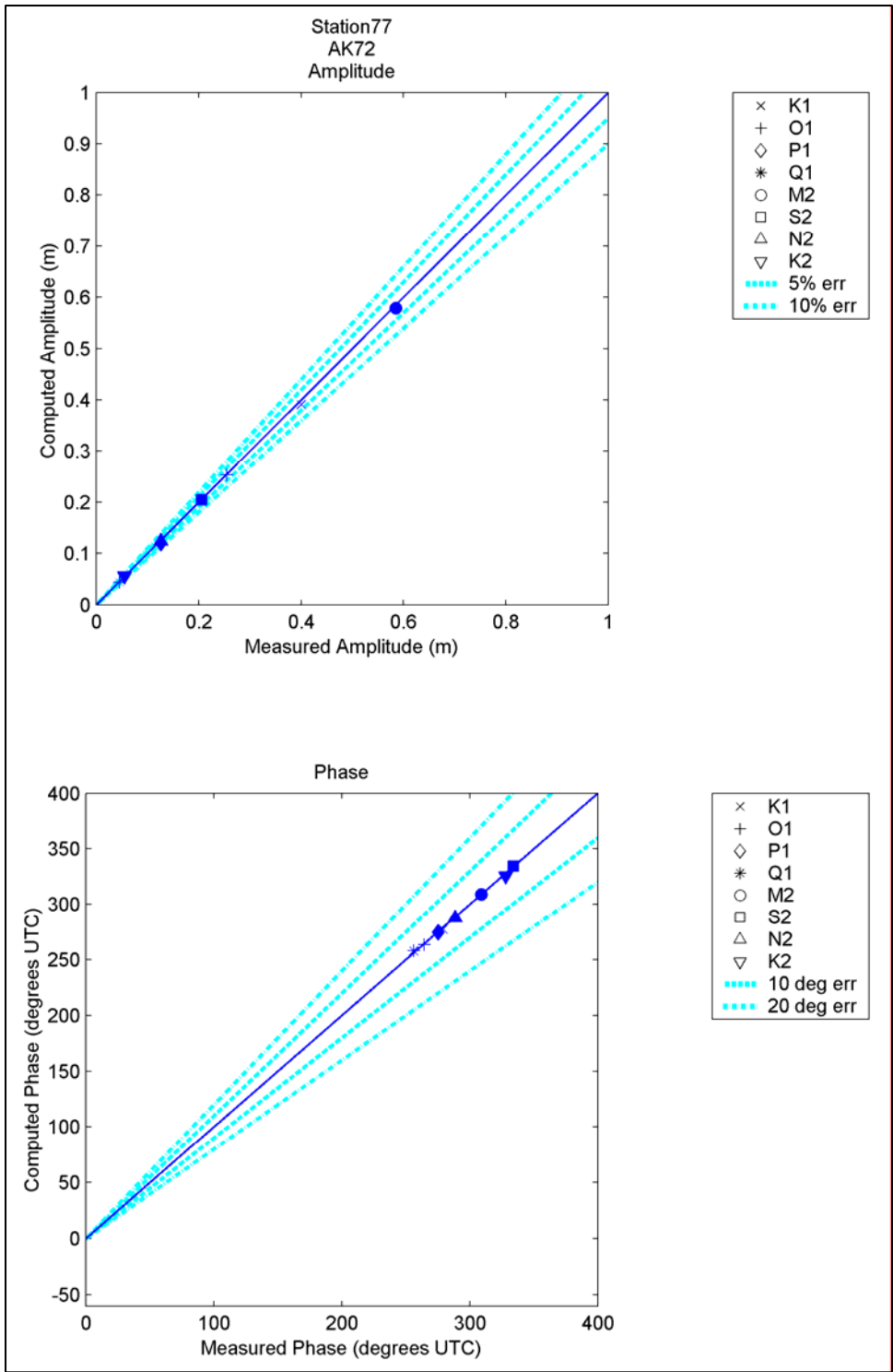


Figure 157. Computed vs. measured harmonic constituents at sta 77

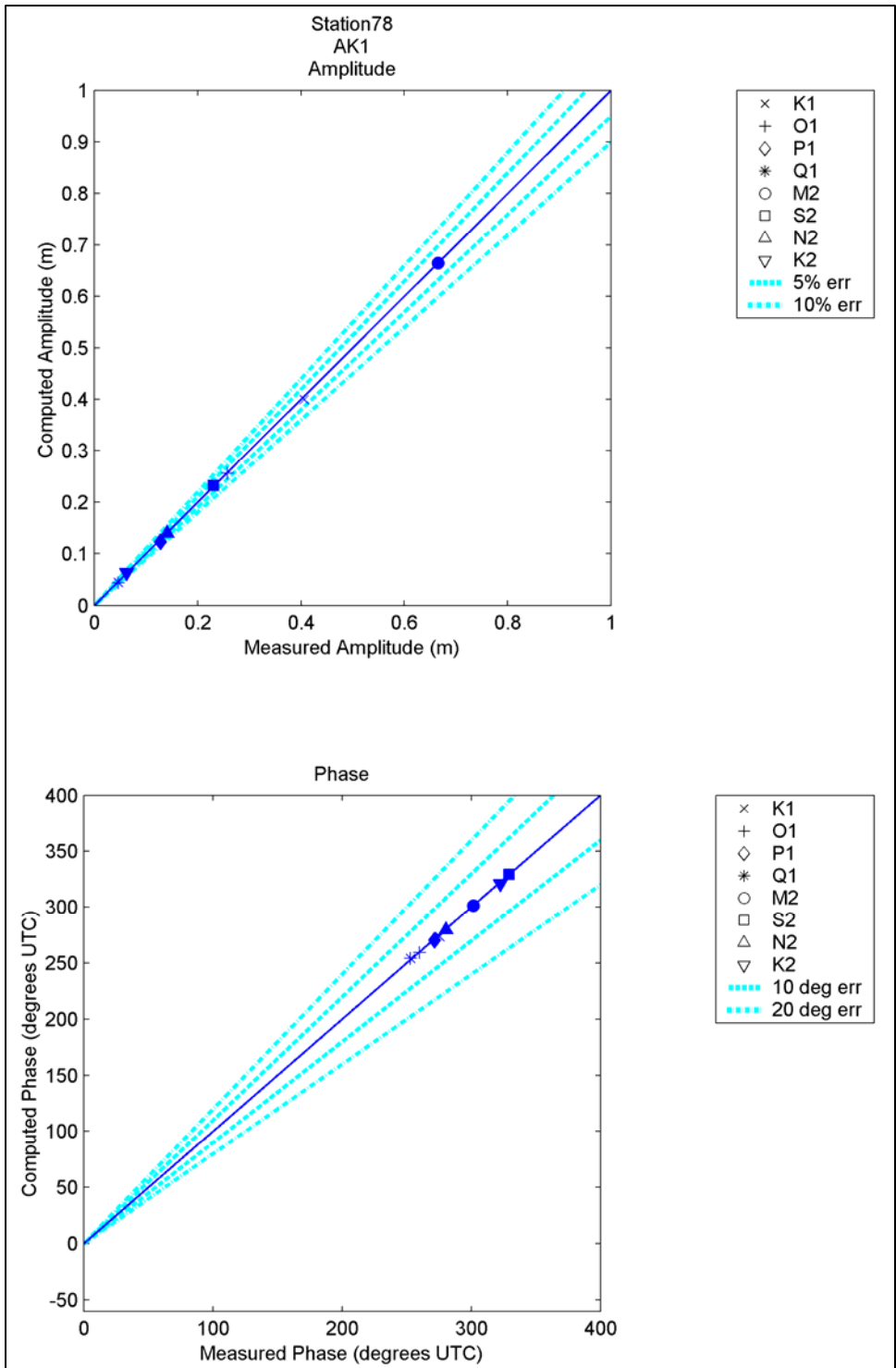


Figure 158. Computed vs. measured harmonic constituents at sta 78

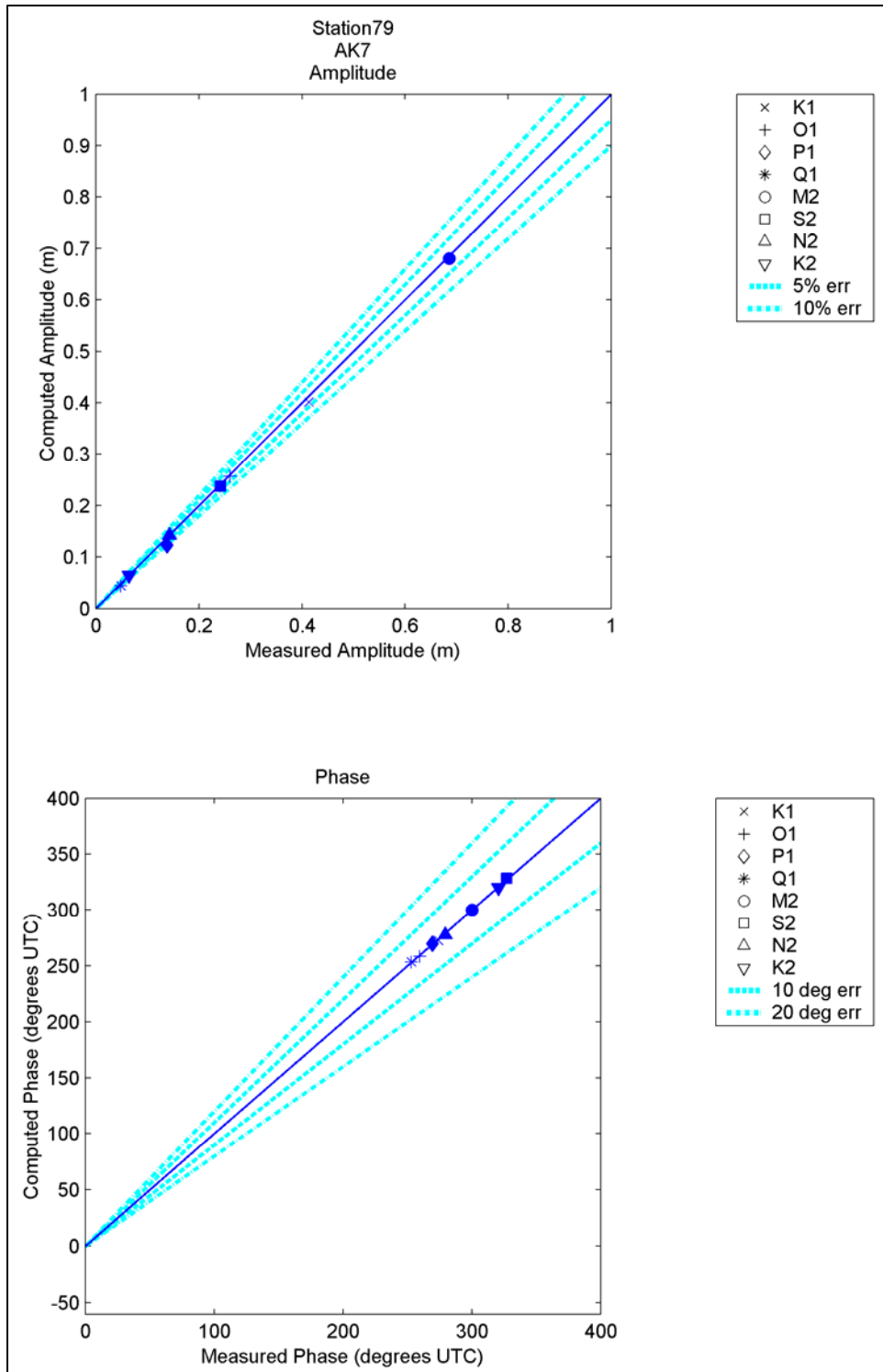


Figure 159. Computed vs. measured harmonic constituents at sta 79

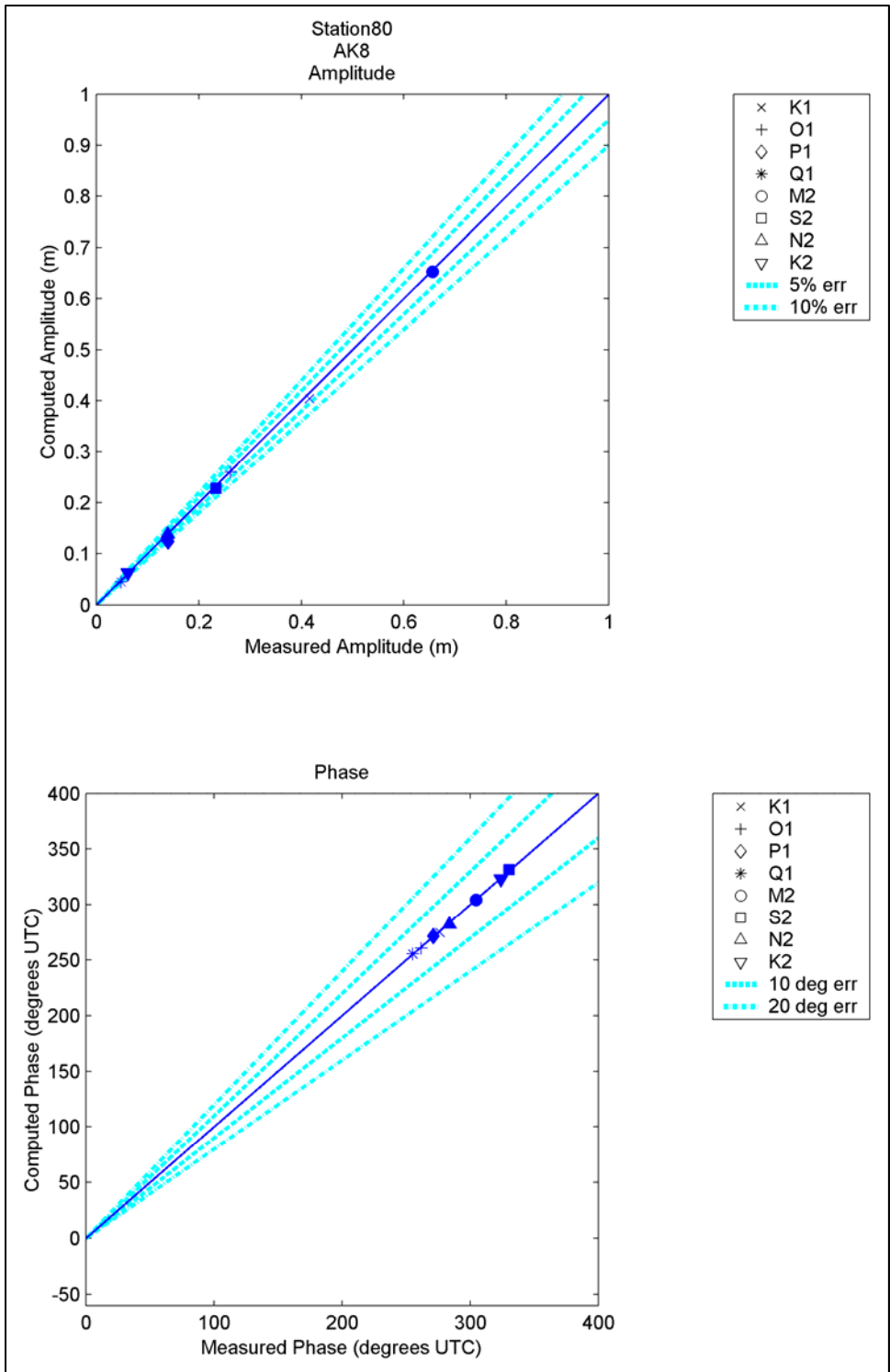


Figure 160. Computed vs. measured harmonic constituents at sta 80

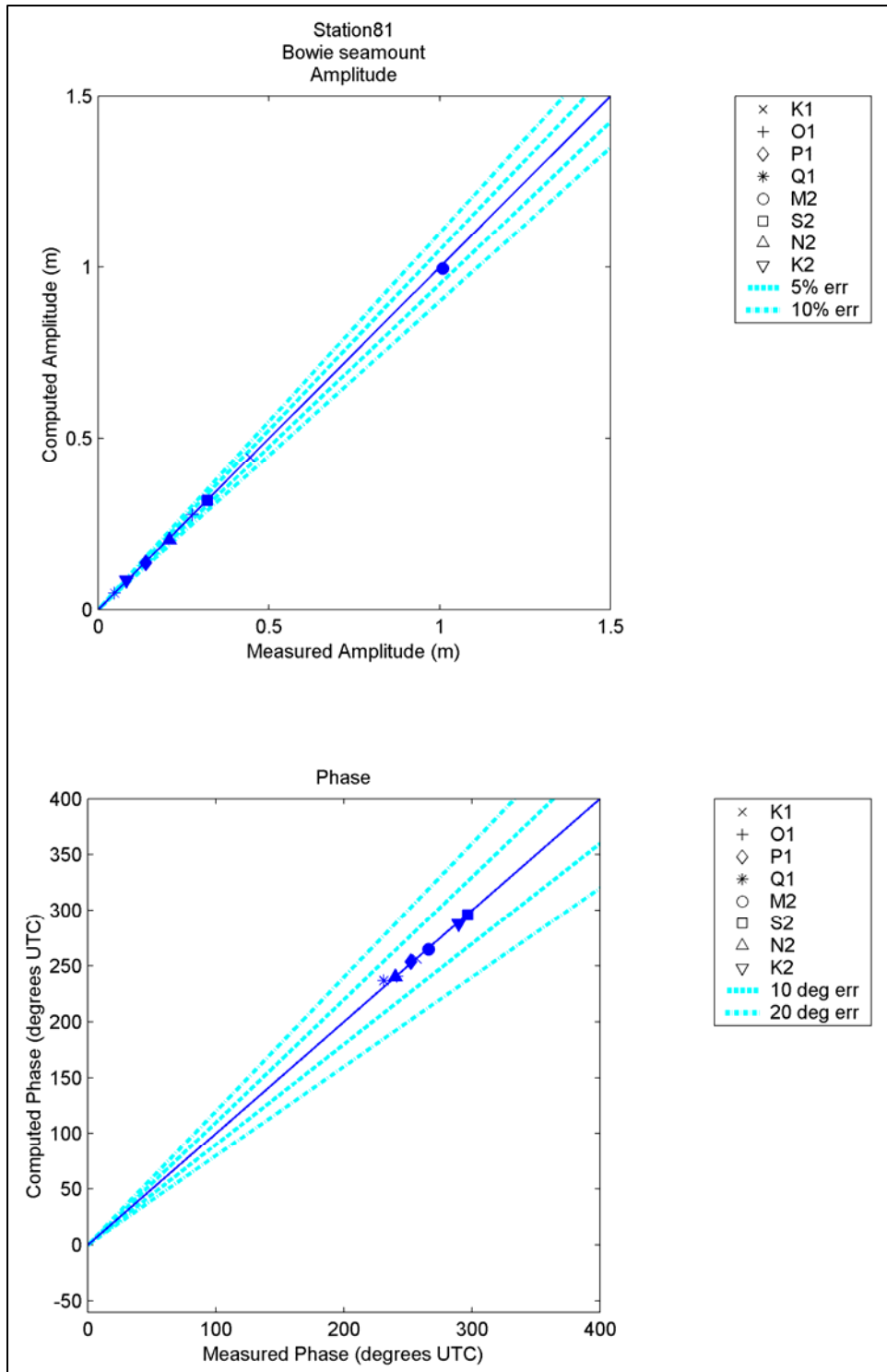


Figure 161. Computed vs. measured harmonic constituents at sta 81

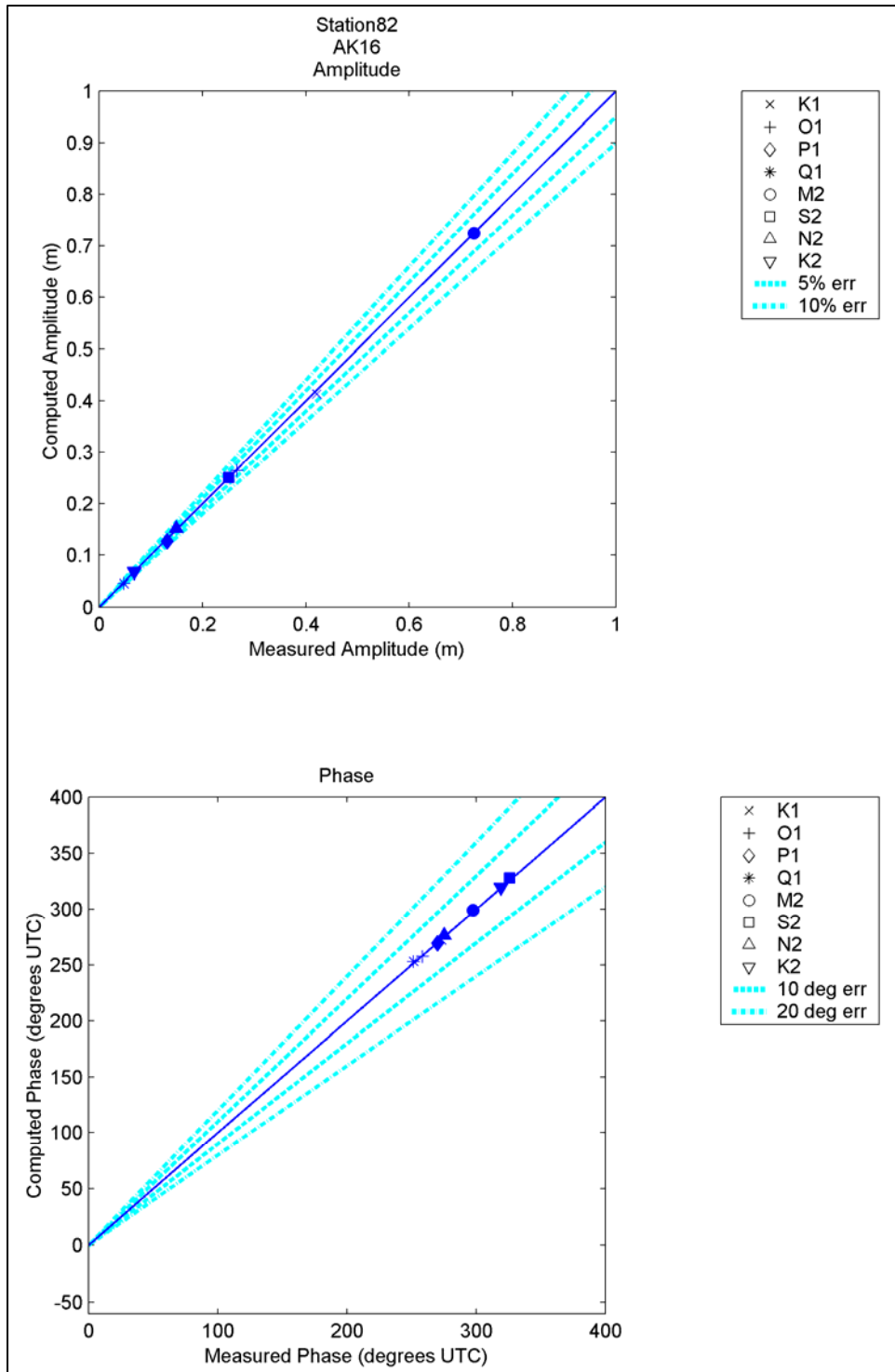


Figure 162. Computed vs. measured harmonic constituents at sta 82

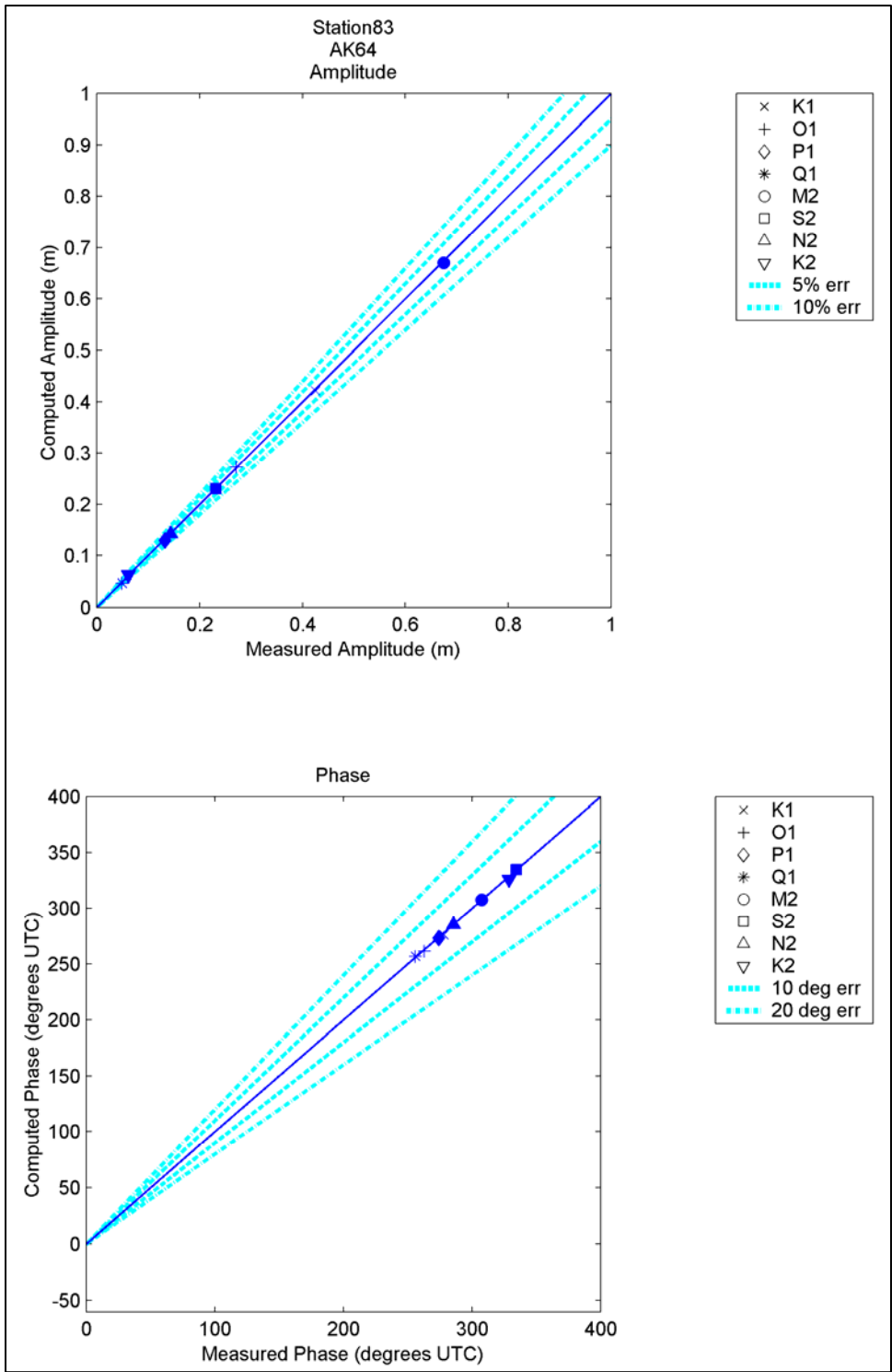


Figure 163. Computed vs. measured harmonic constituents at sta 83

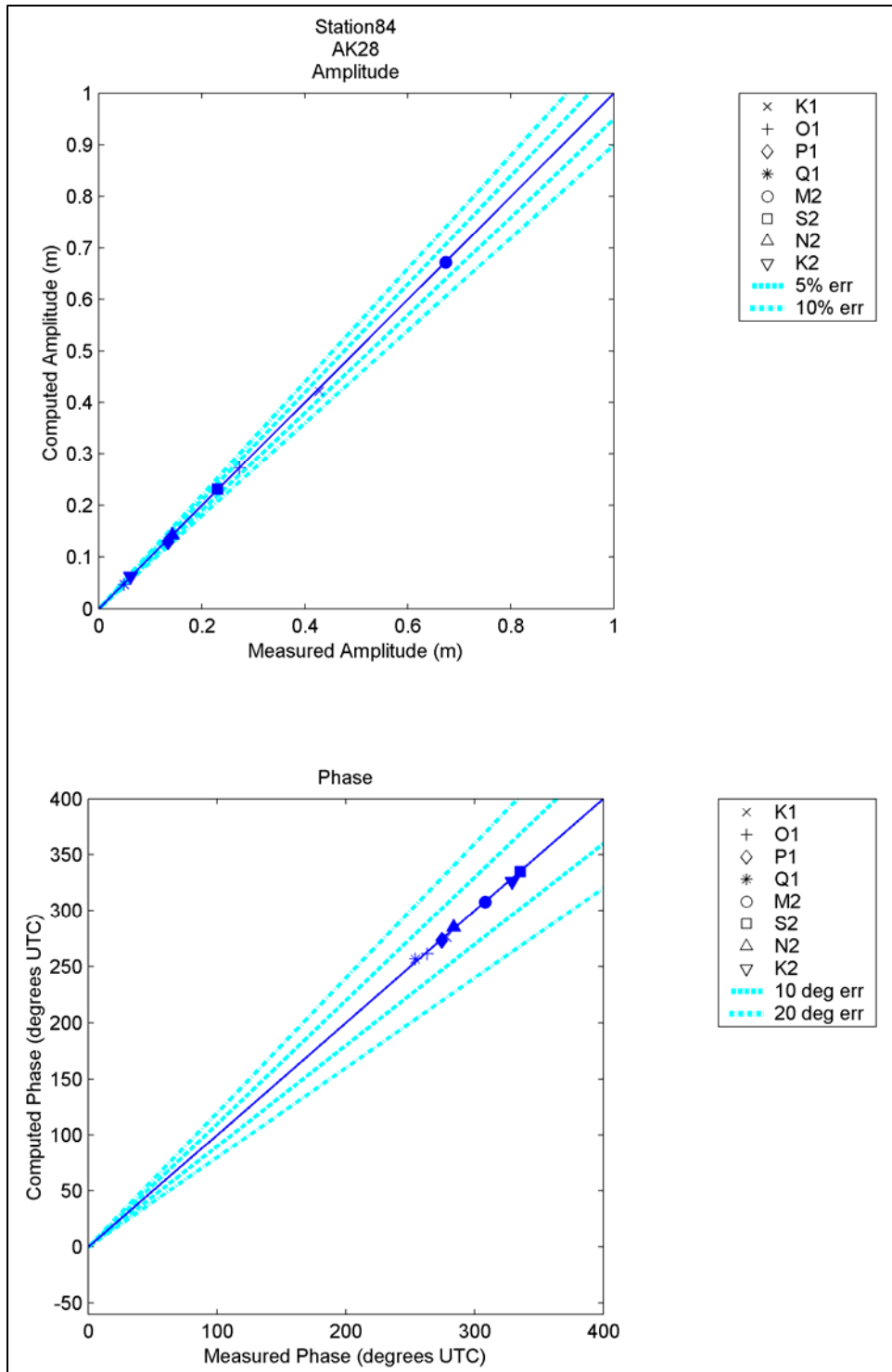


Figure 164. Computed vs. measured harmonic constituents at sta 84

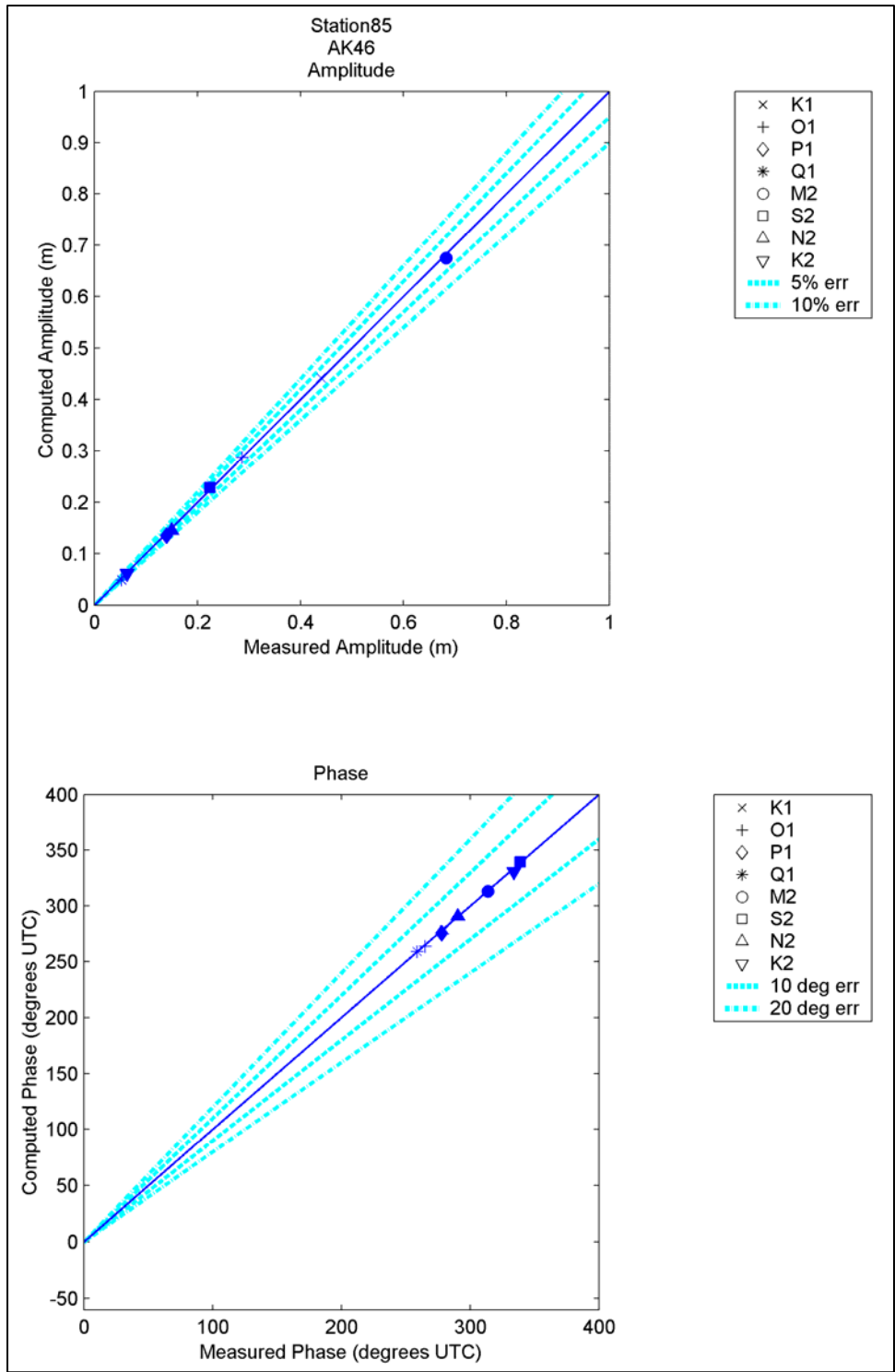


Figure 165. Computed vs. measured harmonic constituents at sta 85

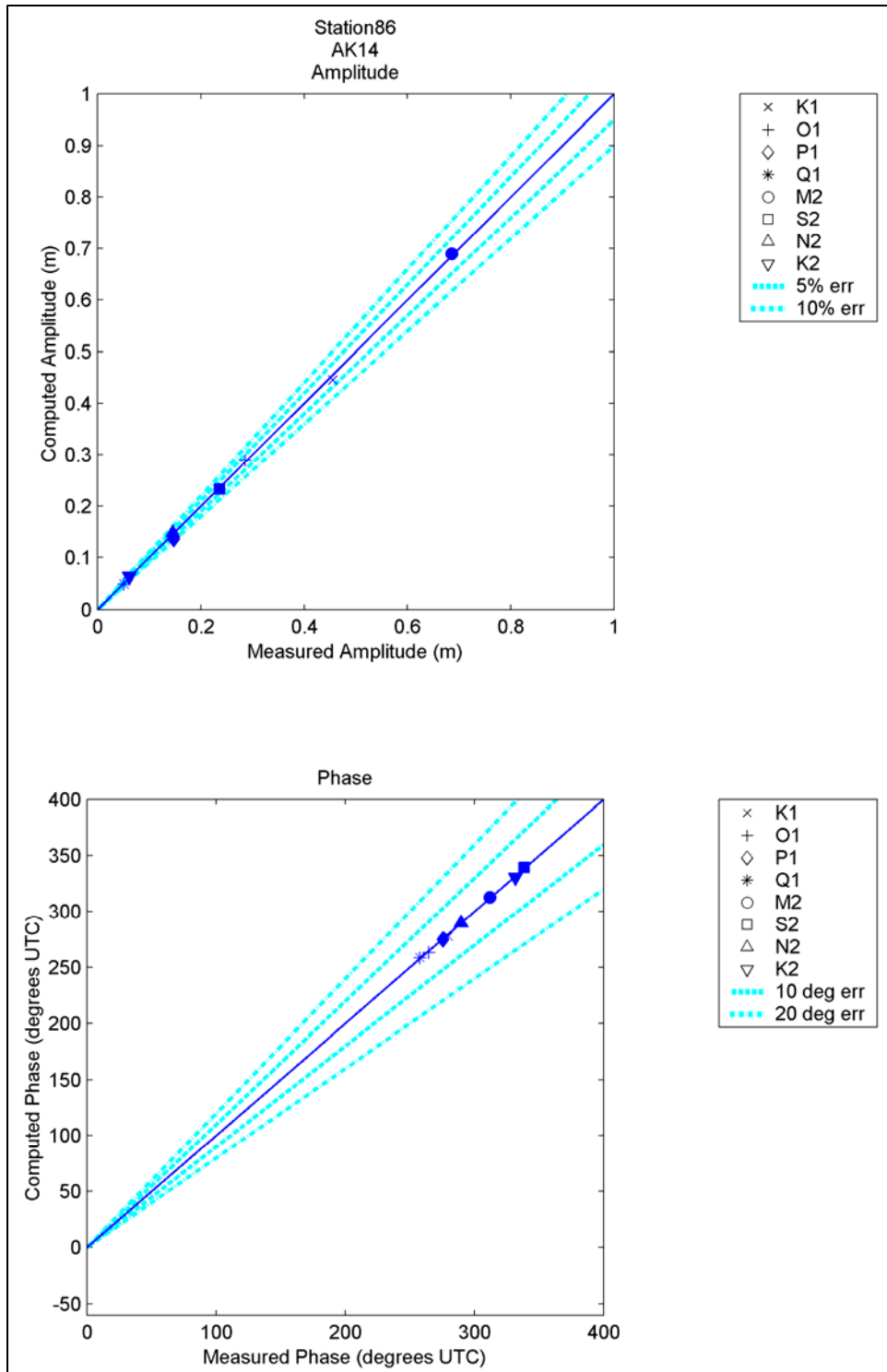


Figure 166. Computed vs. measured harmonic constituents at sta 86

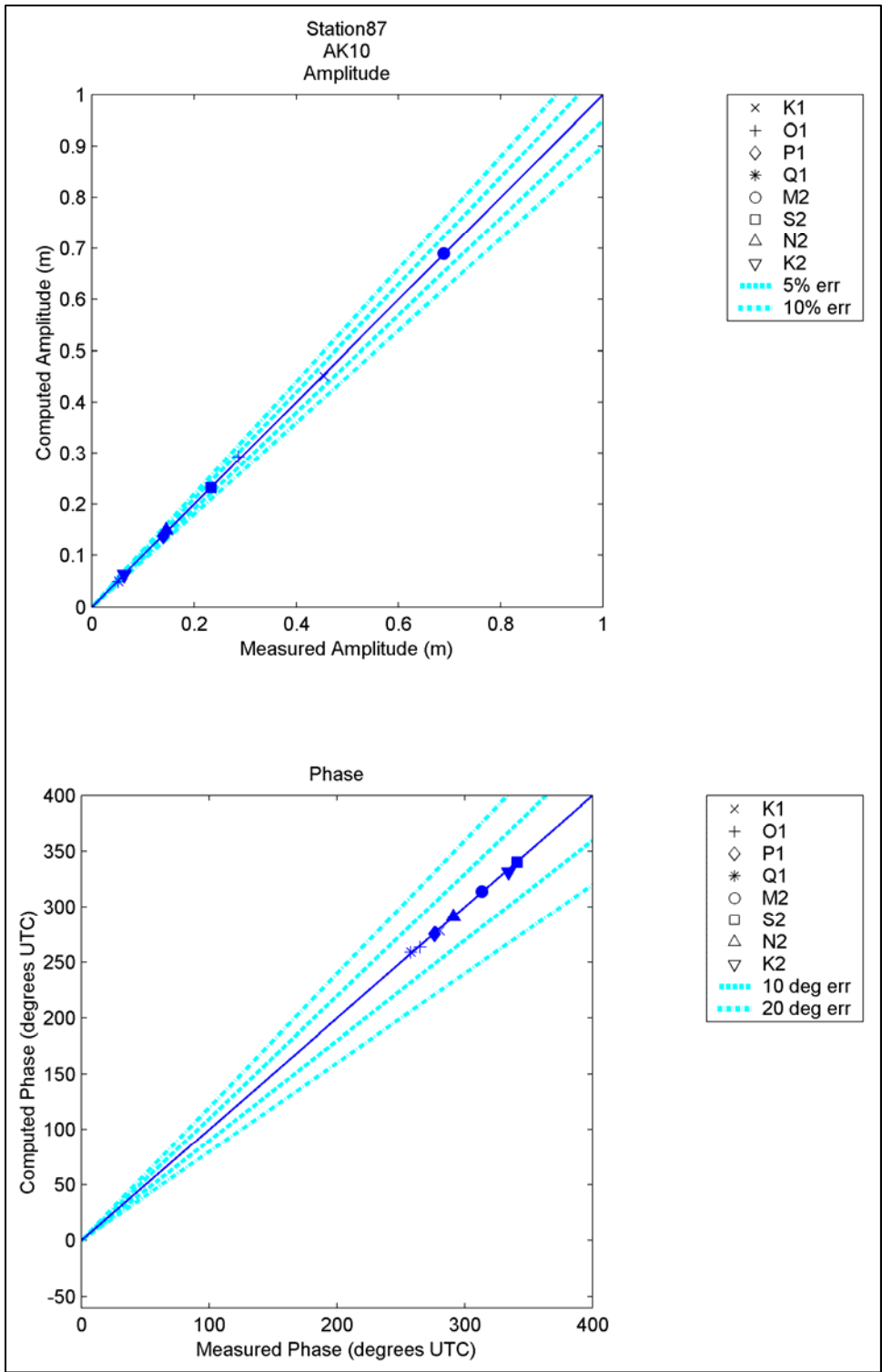


Figure 167. Computed vs. measured harmonic constituents at sta 87

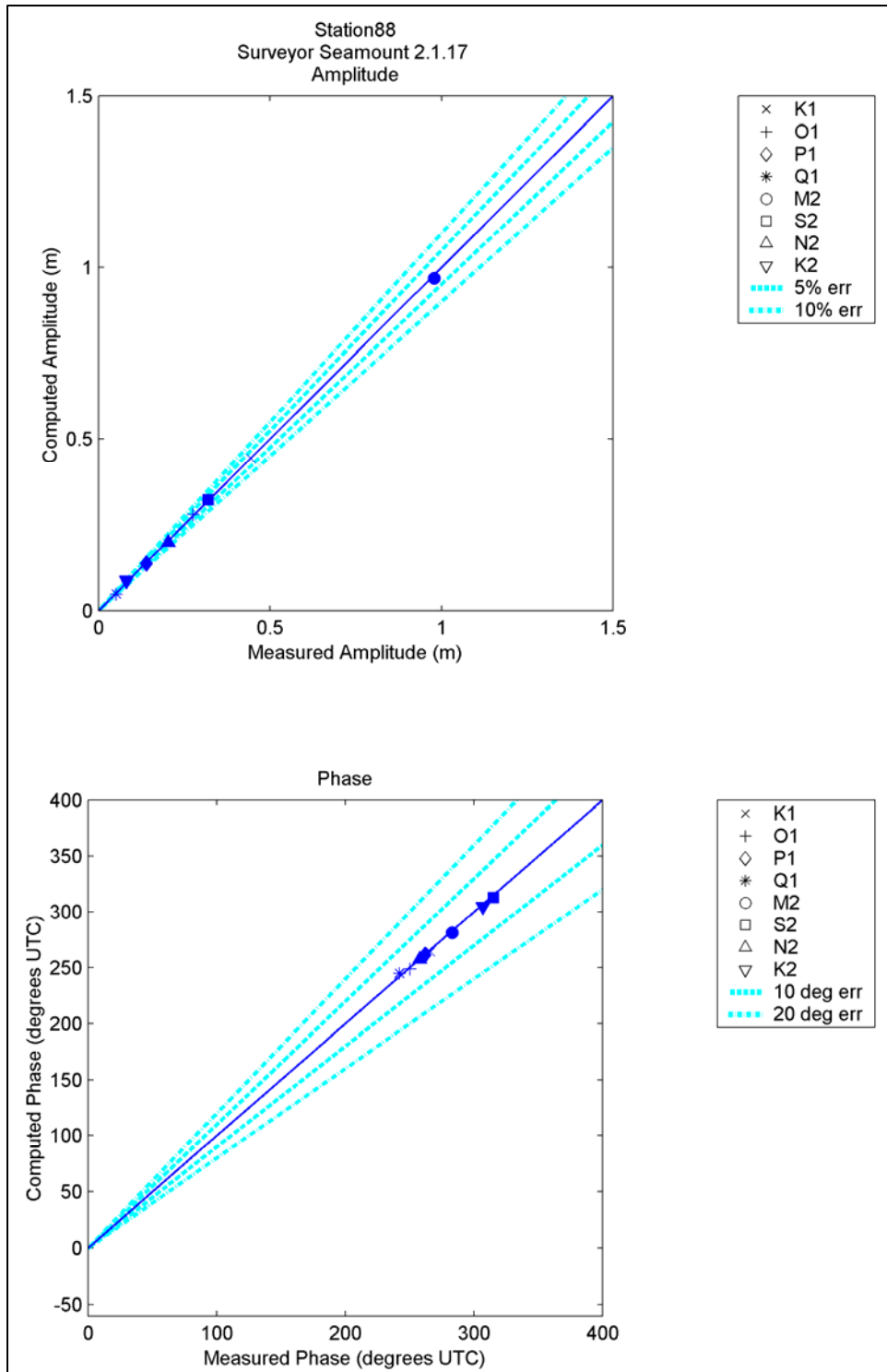


Figure 168. Computed vs. measured harmonic constituents at sta 88

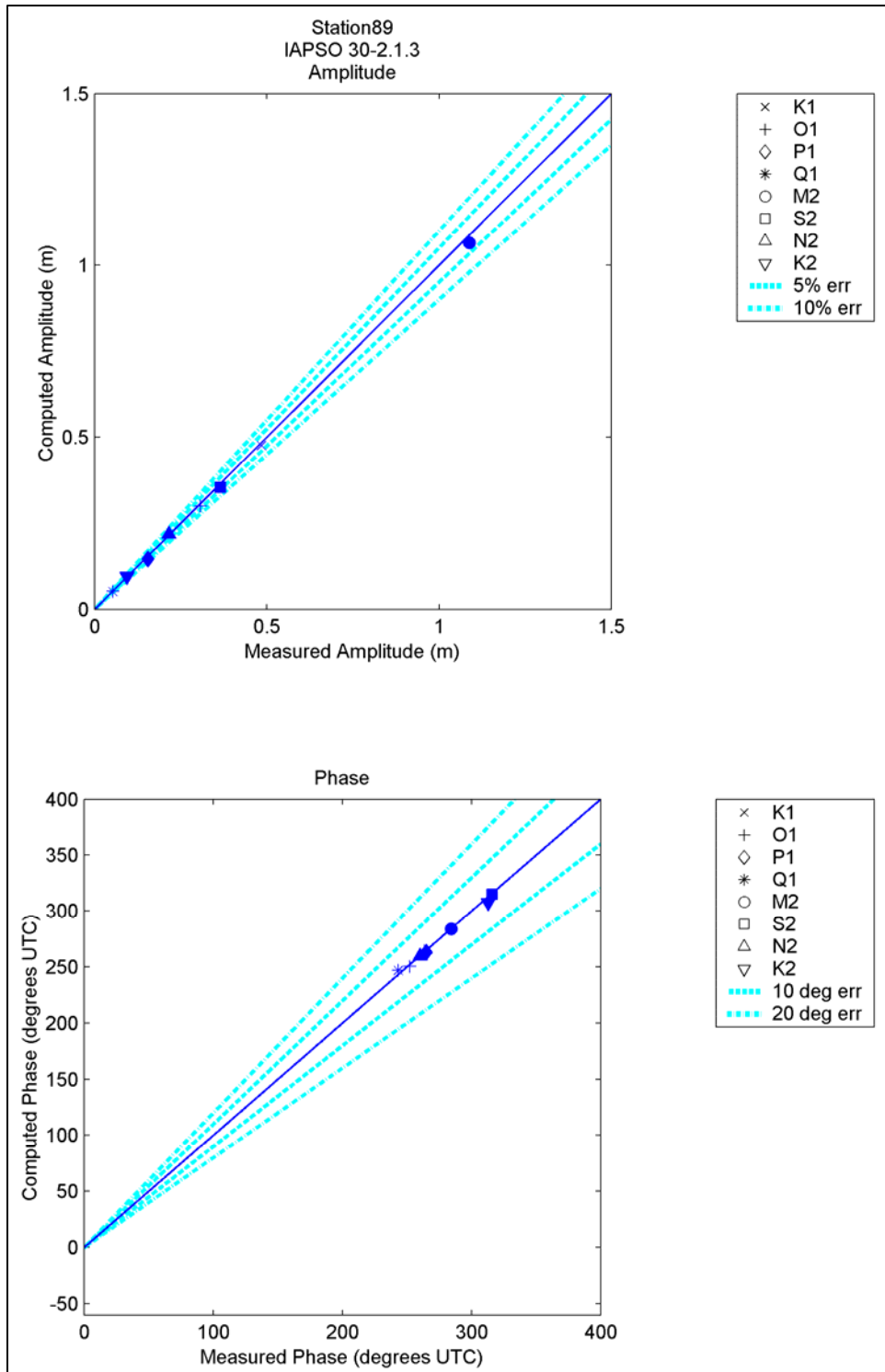


Figure 169. Computed vs. measured harmonic constituents at sta 89

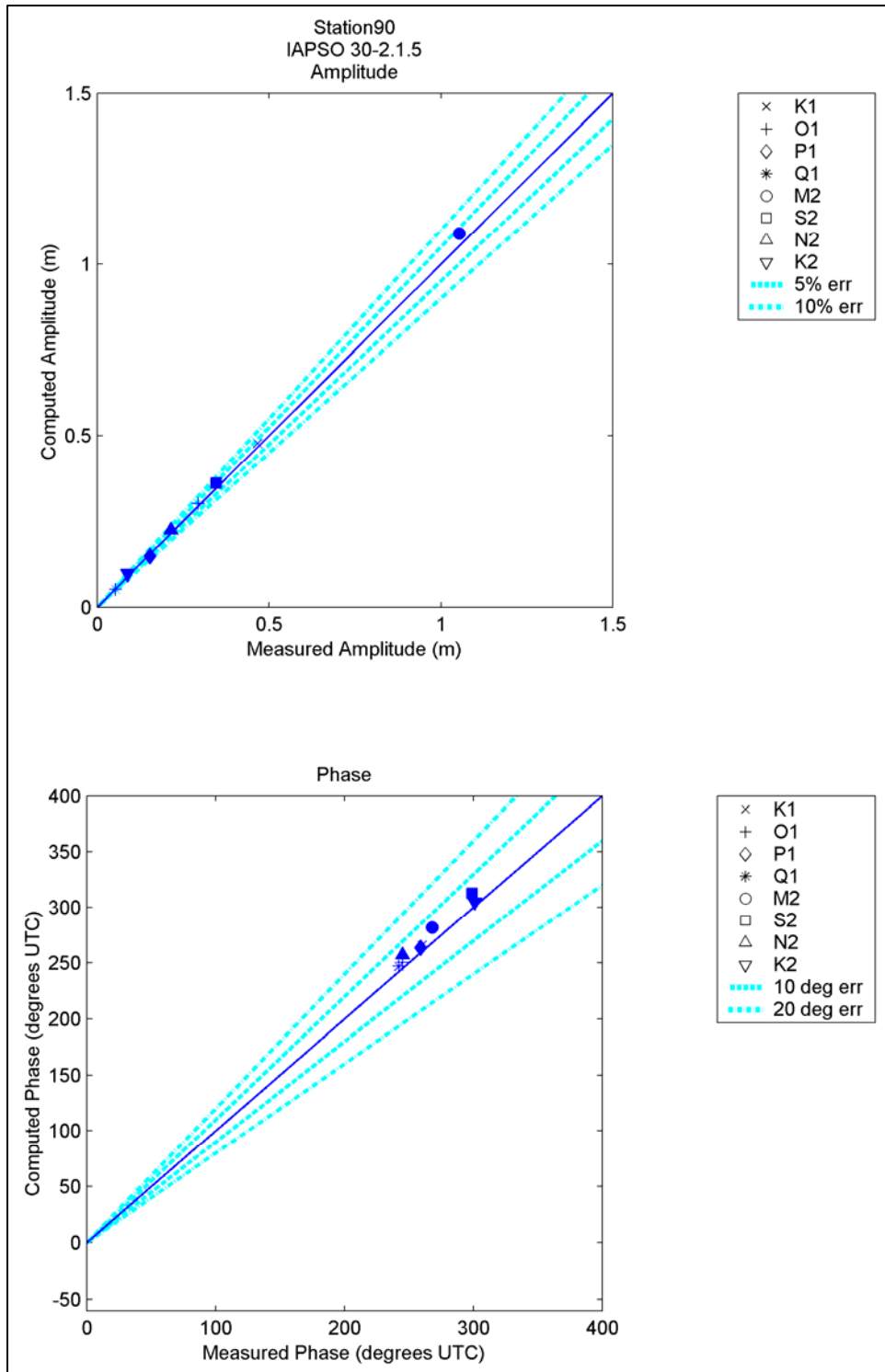


Figure 170. Computed vs. measured harmonic constituents at sta 90

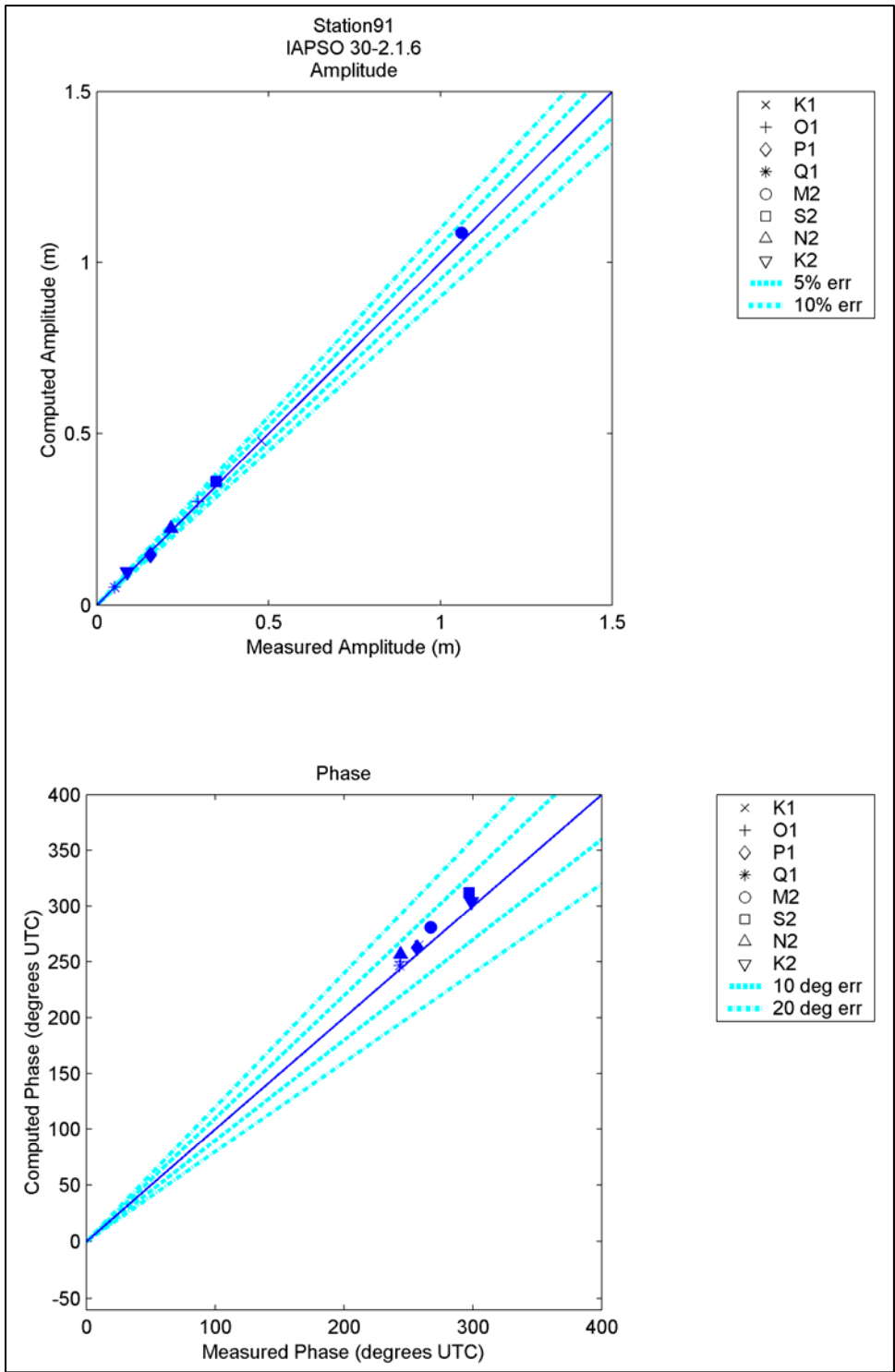


Figure 171. Computed vs. measured harmonic constituents at sta 91

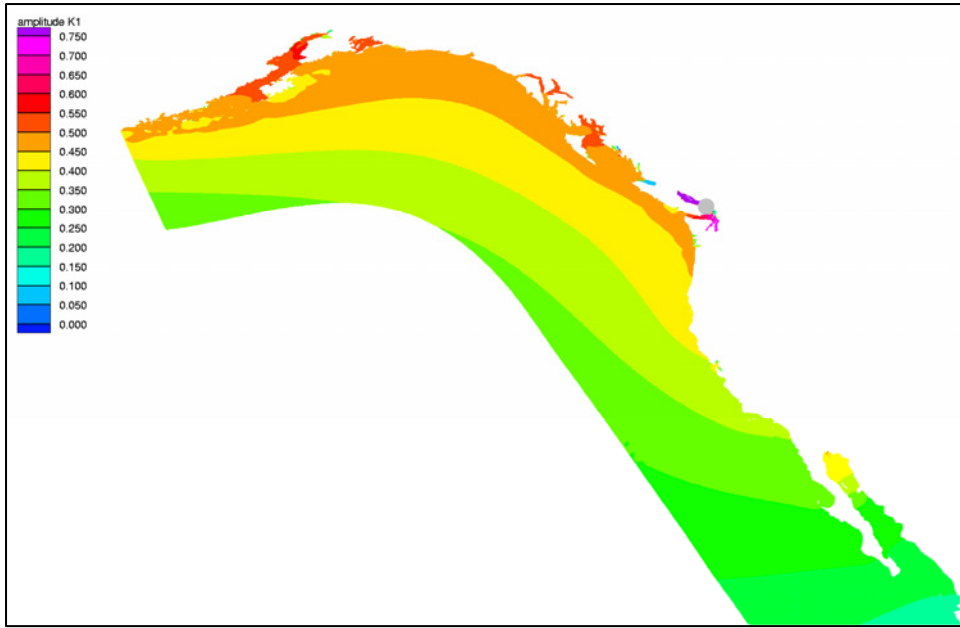


Figure 172. K_1 Amplitude (meters) Cotidal Chart

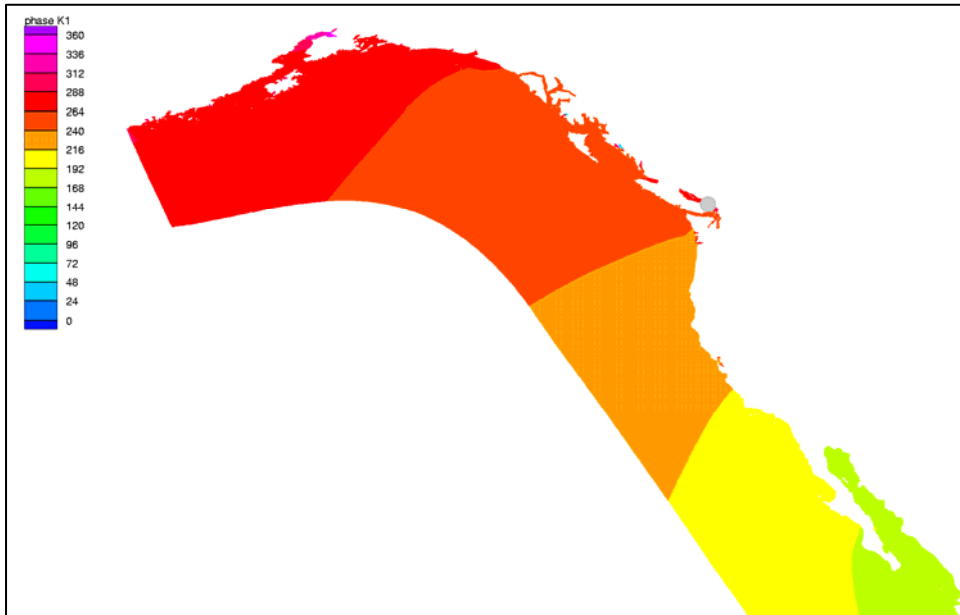


Figure 173. K_1 phase (degrees) cophase chart

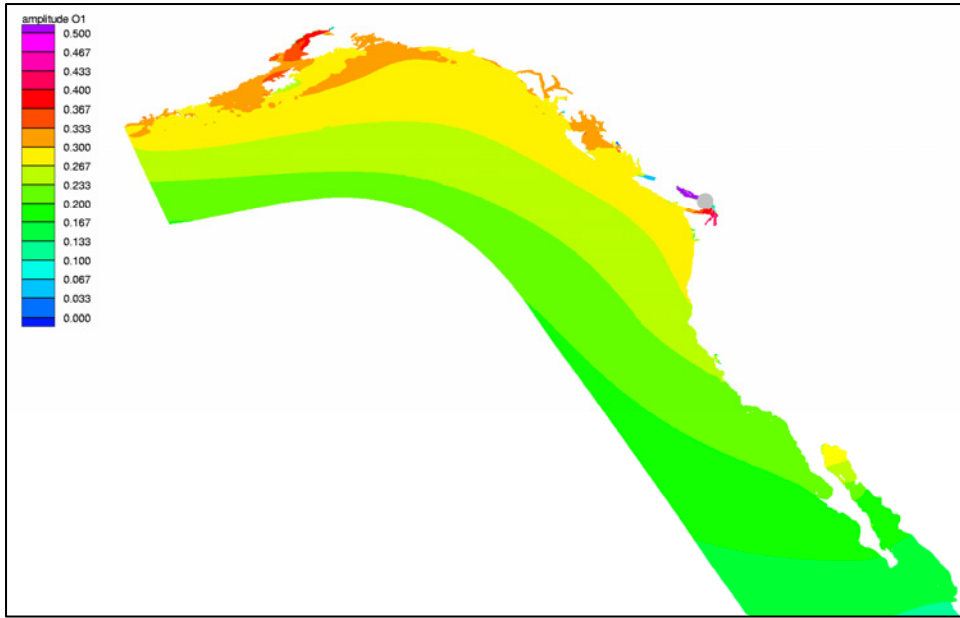


Figure 174. O_1 amplitude (meters) cotidal chart

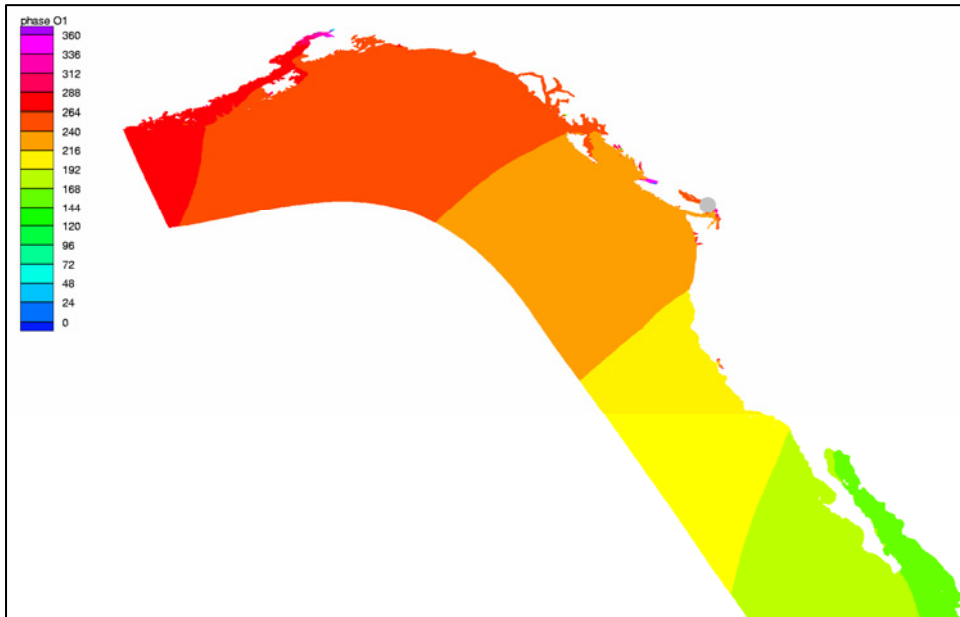


Figure 175. O_1 phase (degrees) cophase chart

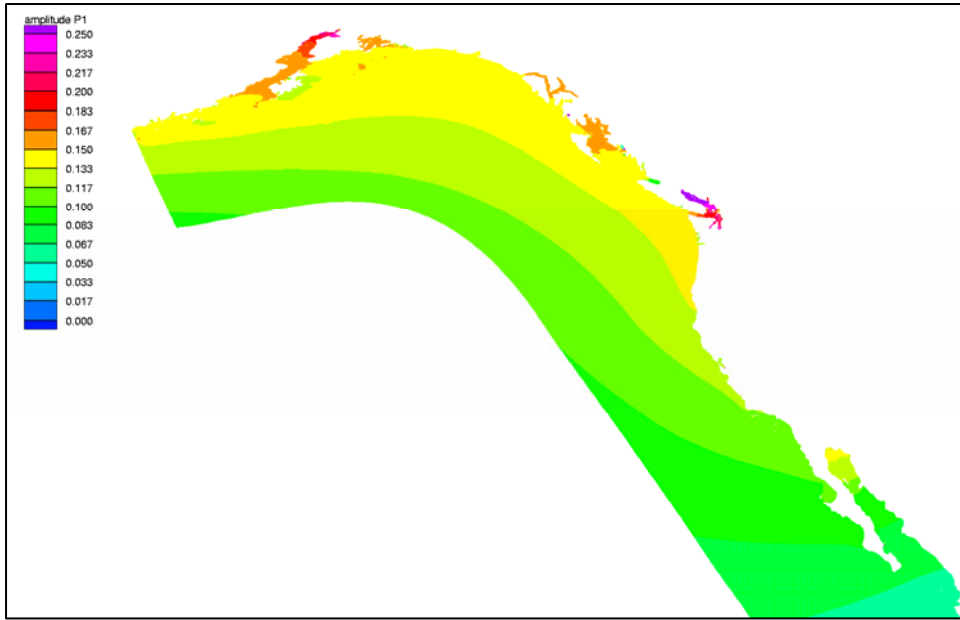


Figure 176. P₁ amplitude (meters) cotidal chart

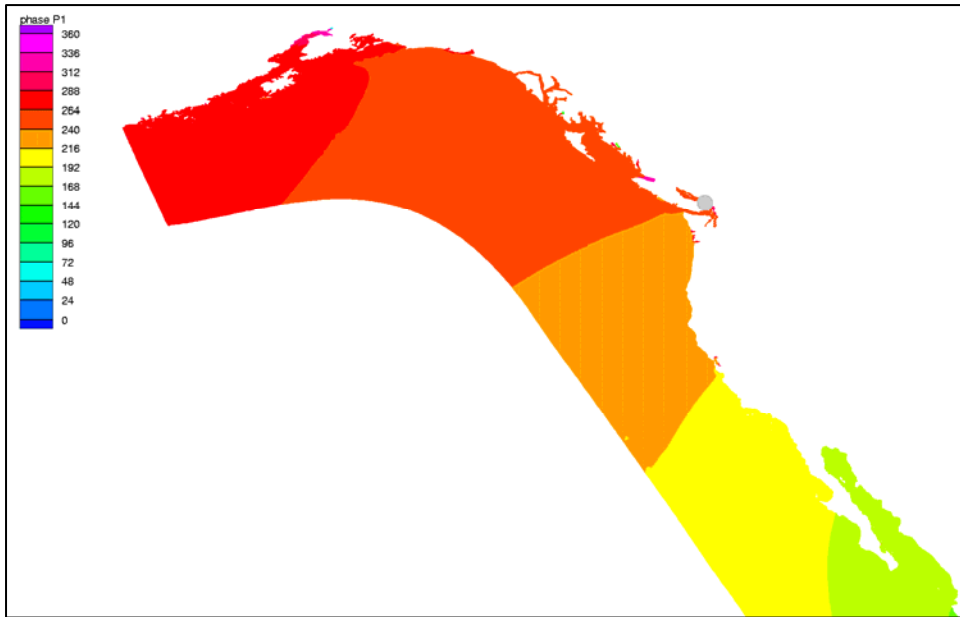


Figure 177. P₁ phase (degrees) cophase chart

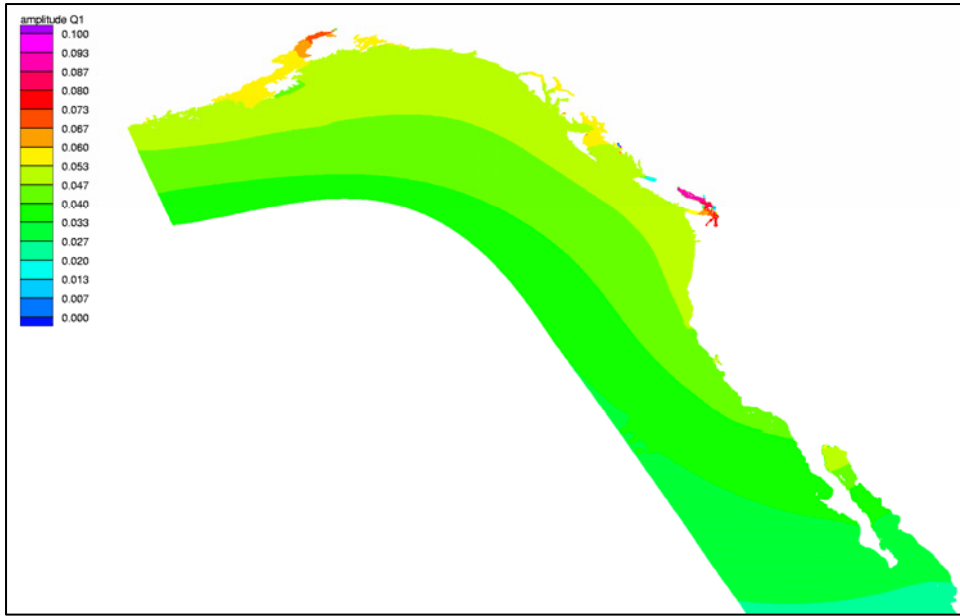


Figure 178. Q_1 amplitude (meters) cotidal chart

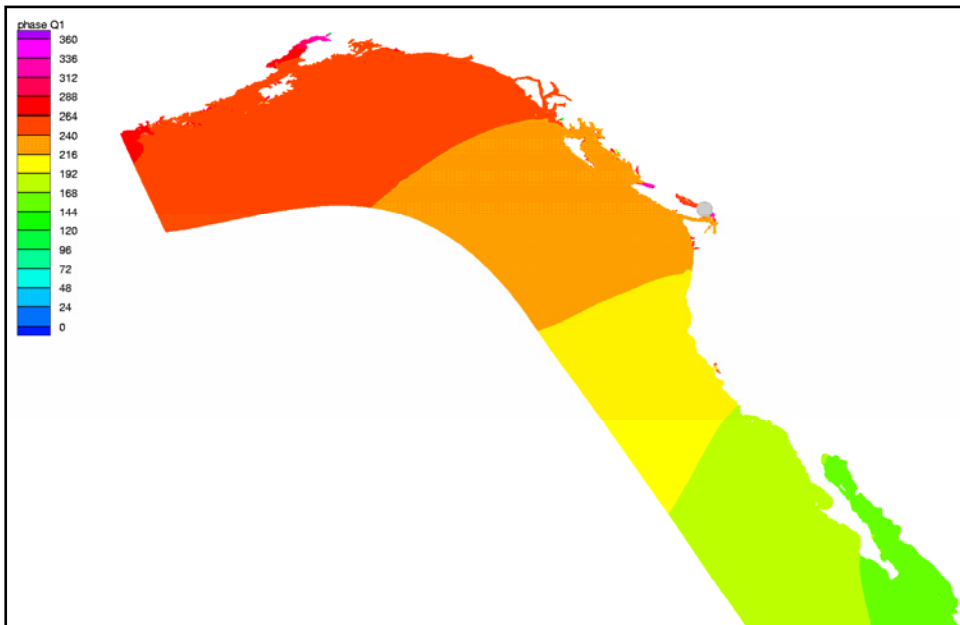


Figure 179. Q_1 phase (degrees) cophase chart

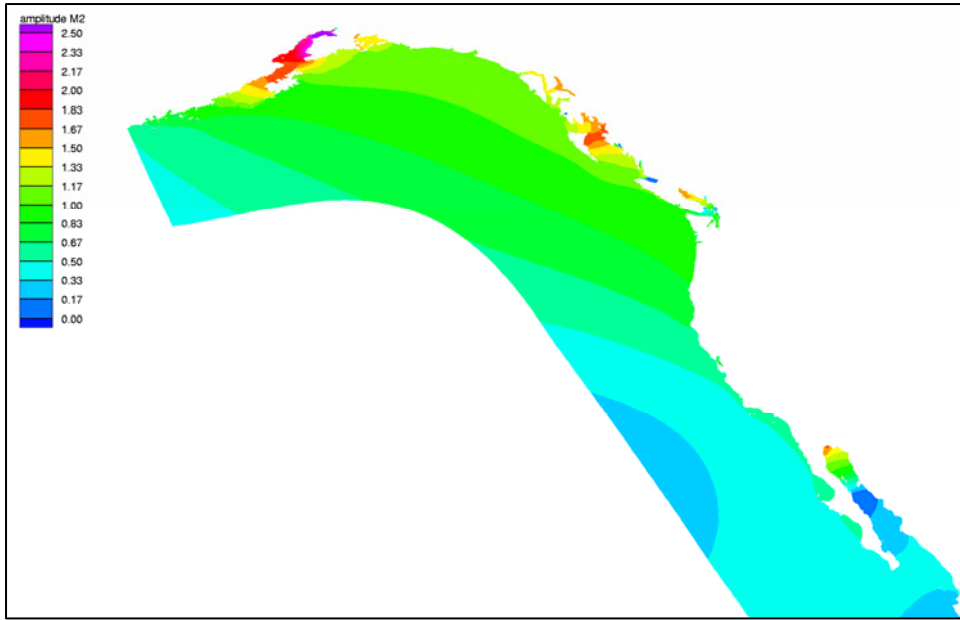


Figure 180. M₂ amplitude (meters) cotidal chart



Figure 181. M₂ phase (degrees) cophase chart

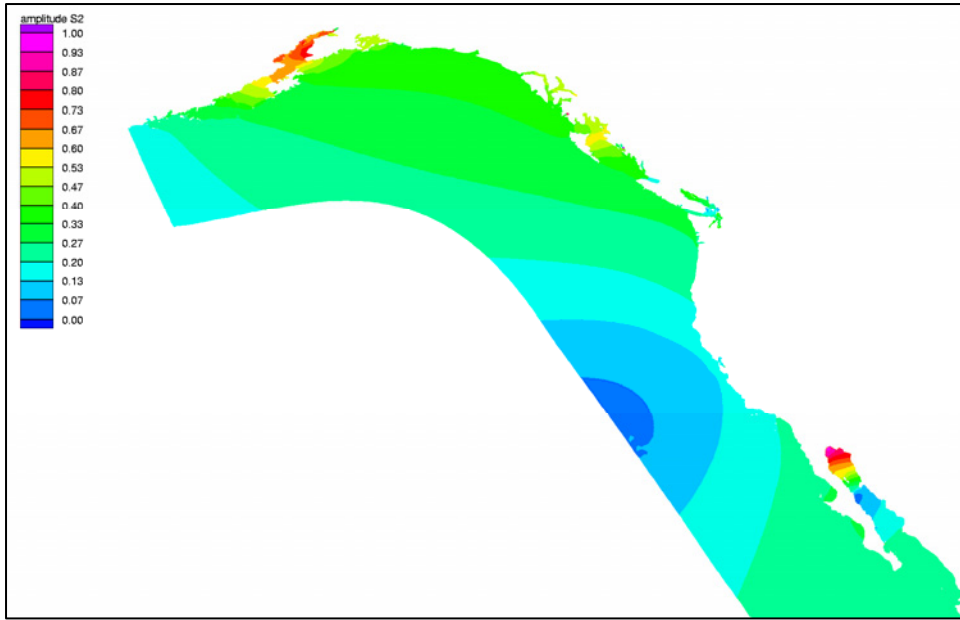


Figure 182. S₂ amplitude (meters) cotidal chart

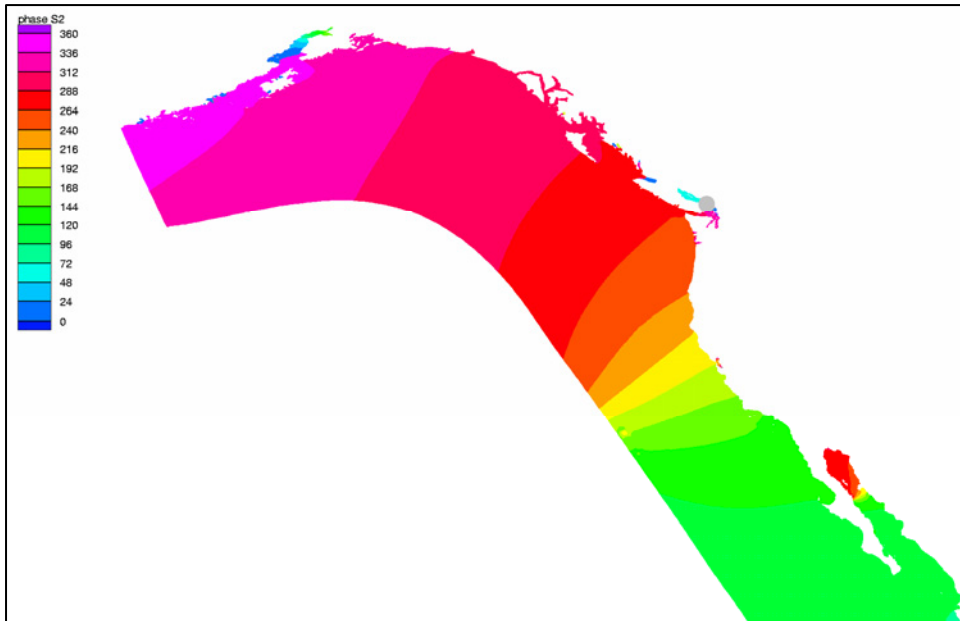


Figure 183. S₂ phase (degrees) cophase chart

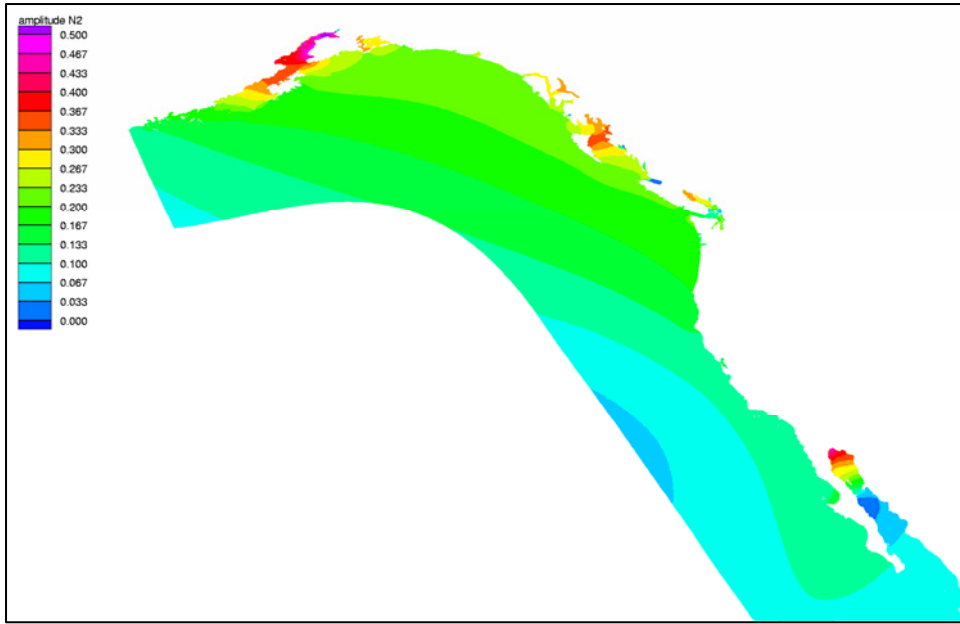


Figure 184. N_2 amplitude (meters) cotidal chart

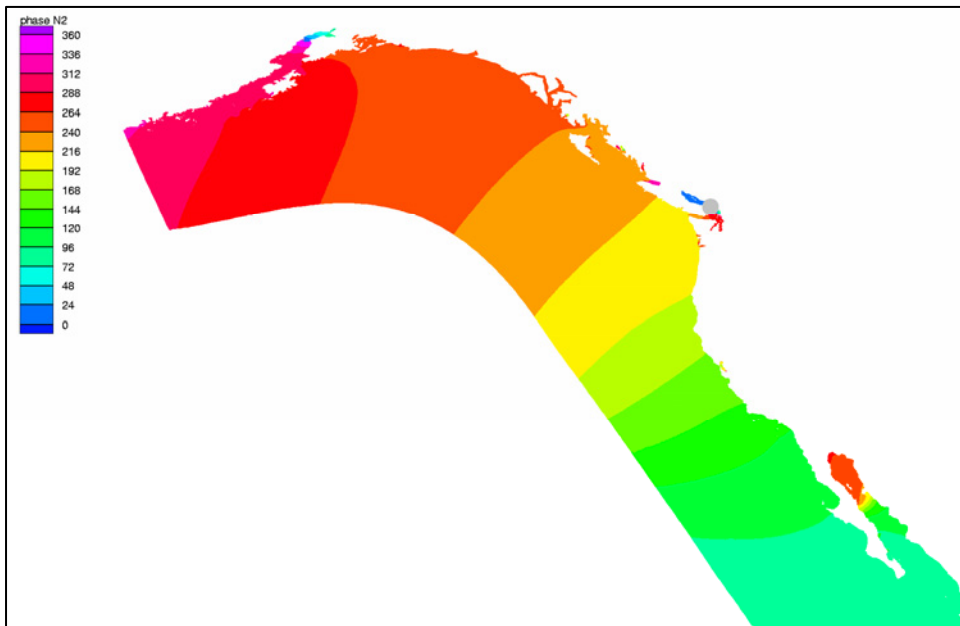


Figure 185. N_2 phase (degrees) cophase chart

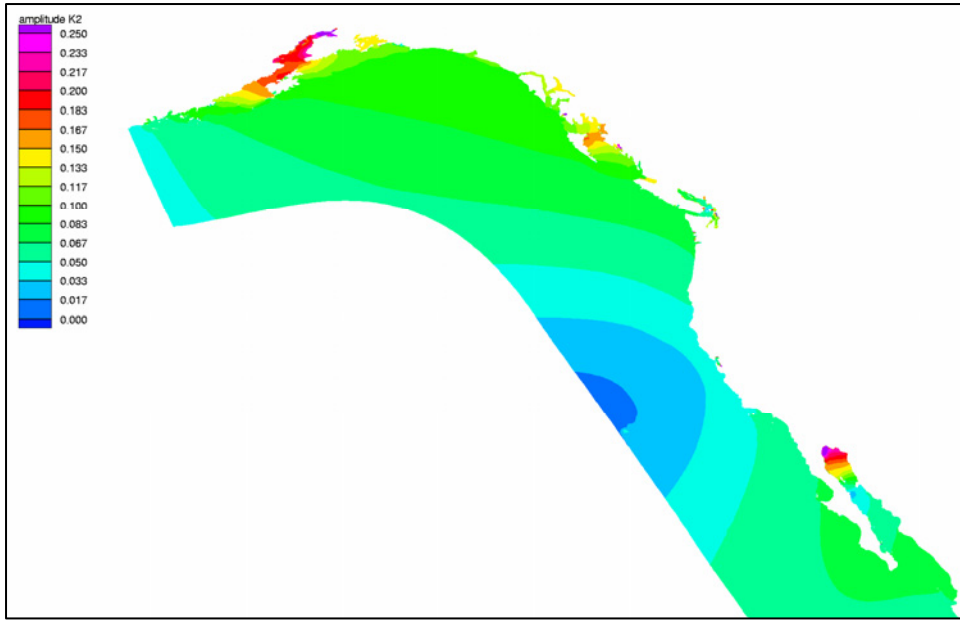


Figure 186. K_2 amplitude (meters) cotidal chart

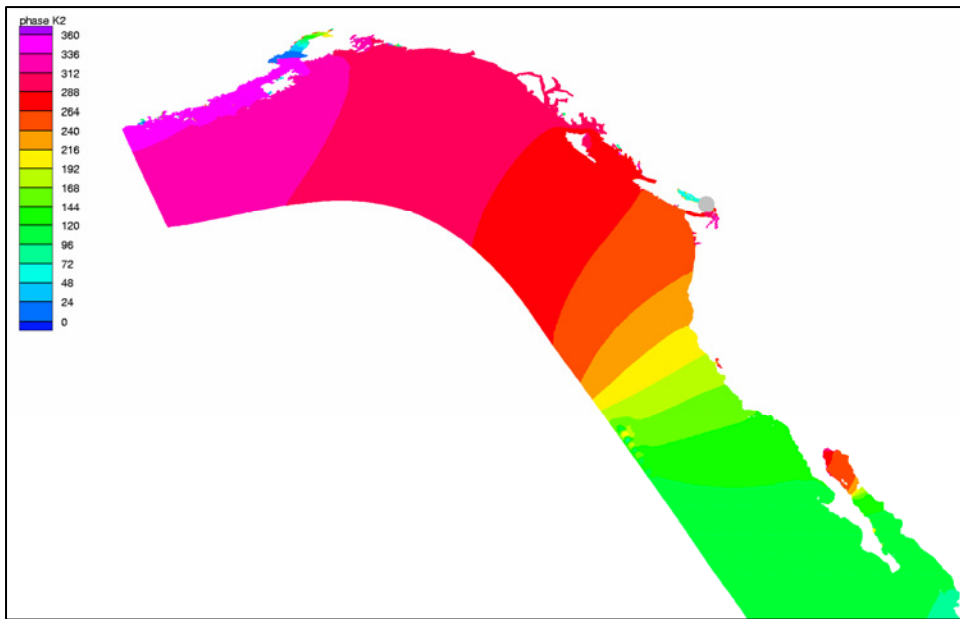


Figure 187. K_2 phase (degrees) cophase chart

Table 1
Tidal Potential Constants for Principle Tidal Constituents and
Associated Effective Earth Elasticity Factor

Species, j	n		Constituent	T_{jn} (h)	C_{nj} (m)	α_{jn}
1	1	K_1	Luni-solar	23.934470	0.141565	0.736
	2	O_1	Principal lunar	25.819342	0.100514	0.695
	3	Q_1	Elliptical lunar	26.868357	0.019256	0.695
2	1	M_2	Principal lunar	12.420601	0.242334	0.693
	2	S_2	Principal solar	12.000000	0.112841	0.693
	3	N_2	Elliptical lunar	12.658348	0.046398	0.693
	4	K_2	Luni-solar	11.967235	0.030704	0.693

Table 2
Station Location and Data Source Information

Station No.	Station Name	Longitude (deg)	Latitude (deg)	Subdomain	Source(s)
1	Puerto Vallarta, Mexico	-105.233330	20.600000	Mexico	IHO
2	Cabo San Lucas, Mexico	-109.900000	22.883330	Mexico	IHO
3	Mazatlan, Mexico	-106.400000	23.183330	Mexico	IHO
4	Isla Guadalupe, Mexico	-116.283330	28.866670	Mexico	IHO
5	Ensenada, Mexico	-116.633330	31.850000	Mexico	IHO
6	Scripps Institute, CA	-117.258330	32.866670	U.S. West Coast	IHO & NOS
7	Avalon, CA	-118.316670	33.350000	U.S. West Coast	IHO
8	Balboa, CA	-117.900000	33.600000	U.S. West Coast	IHO
9	Los Angeles, CA	-118.271670	33.720000	U.S. West Coast	NOS
10	Santa Monica, CA	-118.500000	34.008330	U.S. West Coast	IHO & NOS
11	Santa Barbara, CA	-119.686670	34.408330	U.S. West Coast	NOS
12	Avill, Ca	-120.733330	35.166670	U.S. West Coast	IHO
13	Monterey, CA	-121.883330	36.605000	U.S. West Coast	IHO & NOS
14	Golden Gate Bridge, CA	-122.465000	37.806670	U.S. West Coast	IHO & NOS
15	Crescent City, CA	-124.183330	41.745000	U.S. West Coast	IHO & NOS
16	Brookings, OR	-124.283330	42.050000	U.S. West Coast	IHO
17	Port Orford, OR	-124.496670	42.740000	U.S. West Coast	IHO & NOS
18	Toke Point, Wa	-123.965000	46.708330	U.S. West Coast	IHO & NOS
19	Port Angeles, WA	-123.440000	48.125000	U.S. West Coast	PMEL & NOS
20	Neah Bay, WA	-124.616670	48.368330	U.S. West Coast	PMEL & NOS
21	Friday Harbor, WA	-123.010000	48.546670	U.S. West Coast	NOS
22	Deception Pass, WA	-122.666670	48.416670	U.S. West Coast	IHO
23	Station CZ3, Canada	-125.758000	48.262000	U.S. West Coast	PMEL
24	Oak Bay, Canada	-123.300000	48.433330	Canada	IHO
25	Laperouse #1, Canada	-125.268000	48.480000	Canada	PMEL
26	Laperouse #2, Canada	-125.568000	48.750000	Canada	PMEL
27	Estevan Point (e5), Canada	-127.592000	48.782000	Canada	PMEL
28	Estevan Point (e3a), Canada	-127.070000	49.068000	Canada	PMEL
29	Estevan Point (e2), Canada	-126.878000	49.270000	Canada	PMEL
30	Estevan Point (e1), Canada	-126.757000	49.352000	Canada	PMEL
31	Brooks Pen South, Canada	-127.943000	49.837000	Canada	PMEL
32	Brooks, Pen North, Canada	-128.352000	50.267000	Canada	PMEL
33	Hunt Islet, Canada	-128.317000	50.473999	Canada	IHO
34	Cape Scott, Canada	-128.416670	50.783330	Canada	PMEL
35	Queen Charlotte Sound (qc12), Canada	-128.698000	51.005000	Canada	PMEL

Table 2 (Continued)					
Station No.	Station Name	Longitude (deg)	Latitude (deg)	Subdomain	Source(s)
36	Queen Charlotte Sound (qc14), Canada	-129.438000	51.053000	Canada	PMEL
37	Queen Charlotte Sound (qc15), Canada	-127.945000	51.120000	Canada	PMEL
38	Queen Charlotte Sound (g05), Canada	-128.915000	51.363000	Canada	PMEL
39	Queen Charlotte Sound (q05), Canada	-130.017000	51.367000	Canada	IHO
40	Queen Charlotte Sound (g01), Canada	-128.883000	51.600000	Canada	PMEL
41	Queen Charlotte Sound (qc13), Canada	-130.565000	51.680000	Canada	PMEL
42	Queen Charlotte Sound (qc10), Canada	-129.578000	51.847000	Canada	PMEL
43	Queen Charlotte Sound (q06), Canada	-130483000	51.867000	Canada	PMEL
44	Mckenney Island, Canada	-129.483000	52.650000	Canada	PMEL
45	Hecate Strait (W05), Canada	-131.275000	53.173000	Canada	PMEL
46	Hecate Strait (sandspit), Canada	-130.982000	53.275000	Canada	PMEL
47	Hecate Strait (cape ball), Canada	-131.733000	53.717000	Canada	PMEL
48	Hecate Strait (hec7), Canada	-133.024000	54.122000	Canada	PMEL
49	Qlawdzeet Anchorage, Canada	-130.766670	54.216670	Canada	IHO
50	Langara Island, Canada	-133.050000	54.250000	Canada	IHO
51	Dixon Entrance (rose spit), Canada	-131.950000	54.260000	Canada	PMEL
52	Dixon Entrance (f01b), Canada	-132.937000	54.562000	Canada	PMEL
53	Port Simpson, Canada	-130.433330	54.566670	Canada	IHO
54	Kodiak, AK	-152.511670	57.731670	Alaska	IHO, PMEL & NOS
55	Show Island, AK	-153.383330	59.000000	Alaska	IHO
56	Seldovia, AK	-151.720000	59.440000	Alaska	IHO, PMEL & NOS
57	Middleton Island, AK	-146.316670	59.466670	Alaska	IHO
58	Seward, AK	-149.426670	60.120000	Alaska	PMEL & NOS
59	Nikiski, AK	-151.398330	60.683330	Alaska	NOS
60	Anchorage, AK	-149.890000	61.238330	Alaska	PMEL & NOS
61	IAPSO 30-2.1.13	-124.433330	27.750000	Offshore	IHO

Table 2 (Concluded)					
Station No.	Station Name	Longitude (deg)	Latitude (deg)	Subdomain	Source(s)
62	IAPSO 30-2.1.11	-119.800000	31.033330	Offshore	IHO
63	IAPSO 30-2.1.12	-120.850000	32.233330	Offshore	IHO
64	IAPSO 30-2.1.14	-124.900000	38.150000	Offshore	IHO
65	WC 5	-130.365010	44.863000	Offshore	PMEL
66	WC 20	-130.024000	45.950000	Offshore	PMEL
67	WC 68	-130.000000	45.957000	Offshore	PMEL
68	WC 25	-130.011990	45.957000	Offshore	PMEL
69	WC 15	-130.020000	45.960000	Offshore	PMEL
70	Cobb Seamount	0130.816670	46.766670	Offshore	IHO
71	WC 50	-129.576000	46.533000	Offshore	PMEL
72	IAPSO 30-2.12	-127.28330	48.966670	Offshore	IHO
73	Union Seamount	-132.78330	49.583330	Offshore	IHO & PMEL
74	AK 3	-155.044010	51.785000	Offshore	PMEL
75	AK 4	-156.485000	51.907000	Offshore	PMEL
76	AK 19	-155.727010	52.026000	Offshore	PMEL
77	AK 72	-158.751010	52.039000	Offshore	PMEL
78	AK 19	-155.580990	52.614000	Offshore	PMEL
79	AK 72	-155.003010	52.733000	Offshore	PMEL
80	AK 8	-156.480000	52.733000	Offshore	PMEL
81	Bowie Seamount	-135.633000	53.317000	Offshore	PMEL
82	AK 16	-154.281010	53.422000	Offshore	PMEL
83	AK 64	-157.287000	53.425000	Offshore	PMEL
84	AK 28	-157.216000	53.426000	Offshore	PMEL
85	AK 46	-158.526990	54.028000	Offshore	PMEL
86	AK 14	-158.248990	54.164000	Offshore	PMEL
87	AK 10	-158.520000	54.286000	Offshore	PMEL
88	Surveyor Seamount	-144.367000	56.133000	Offshore	PMEL
89	IAPSO 30-1.1.3	-145.716670	58.766670	Offshore	IHO
90	IAPSO 30-2.1.5	-142.566670	59.716670	Offshore	IHO & PMEL
91	IAPSO 30-2.1.6	-141.983330	59.333330	Offshore	IHO & PMEL

Table 3
Standard Proportional Deviation Amplitude and Absolute Phase Errors for Field Data Records

Amplitude Errors, E_{j-amp}^{c-m}					
Constituent	Entire Domain	U.S. West Coast	Canada	Alaska	Deep Ocean
K ₁	0.0277	0.0246	0.0081	0.0395	0.0038
O ₁	0.0241	0.0291	0.0064	0.0193	0.0061
P ₁	0.0542	0.0295	0.0076	0.0972	0.0000
Q ₁	0.0231	0.0409	0.0082	0.0156	0.0017
M ₂	0.0346	0.0627	0.0029	0.0290	0.0088
S ₂	0.0810	0.1641	0.0196	0.0172	0.0028
N ₂	0.1205	0.1020	0.0054	0.1372	0.0398
K ₂	0.0519	0.0597	0.0330	0.0485	0.0110

Phase Errors, $E_{j-phase}^{c-m}$					
Constituent	Entire Domain	U.S. West Coast	Canada	Alaska	Deep Ocean
K ₁	2.41	0.97	0.30	6.63	0.03
O ₁	2.27	1.12	0.37	5.77	0.13
P ₁	3.19	1.92	1.63	7.13	0.10
Q ₁	4.60	2.19	0.37	12.06	0.03
M ₂	4.41	1.66	0.63	12.33	0.17
S ₂	5.02	2.33	0.60	12.61	2.03
N ₂	6.40	4.95	1.27	12.62	0.43
K ₂	2.95	2.02	1.10	6.27	0.00

Table 4
Standard Proportional Deviation Amplitude and Absolute Phase Errors for ENPAC 1994 Domain

Amplitude Errors, E_{j-amp}^{c-m}						
Constituent	Entire Domain	Mexico	U.S. West Coast	Canada	Alaska	Deep Ocean
K ₁	0.2098	0.0830	0.2709	0.1023	0.4758	0.0367
O ₁	0.2008	0.1017	0.2392	0.1124	0.4762	0.0550
M ₂	0.3841	0.3130	0.5674	0.1874	0.6032	0.1849
S ₂	0.7548	0.6682	1.4770	0.7827	0.5336	0.6860
N ₂	0.3377	0.1454	0.4293	0.1265	0.6017	0.1034

Phase Errors, $E_{j-phase}^{c-m}$						
Constituent	Entire Domain	Mexico	U.S. West Coast	Canada	Alaska	Deep Ocean
K ₁	6.97	12.48	3.04	2.16	57.93	1.53
O ₁	7.18	13.75	3.48	1.98	57.44	2.00
M ₂	30.85	43.70	42.58	20.02	82.80	21.46
S ₂	53.82	72.83	81.07	35.06	119.56	39.73
N ₂	36.86	29.92	40.18	23.31	149.64	24.26

Table 5
Amplitude and Phase Weighted and Straight Average Errors for ENPAC 2002 Model with TPXO.2, TPXO.5, and TPXO.6 Open Boundary Forcing

E_{weighted}			
	TPXO.2 Forcing	TPXO.5 Forcing	TPXO.6 Forcing
Amplitude Error	0.1085	0.0903	0.0944
Phase Error	10.9464	9.9251	10.4617
E_{straight}			
	TPXO.2 Forcing	TPXO.5 Forcing	TPXO.6 Forcing
Amplitude Error	0.1081	0.1064	0.1077
Phase Error	11.0896	9.3882	9.9233

Table 6
Amplitude and Phase Weighted and Straight Average Error for ENPAC 2003 Model with TPXO.2, TPXO.5, and TPXO.6 Open Boundary Forcing

E_{weighted}			
	TPXO.2 Forcing	TPXO.5 Forcing	TPXO.6 Forcing
Amplitude Error	0.0806	0.0722	0.0725
Phase Error	5.4518	5.1562	5.3089
E_{straight}			
	TPXO.2 Forcing	TPXO.5 Forcing	TPXO.6 Forcing
Amplitude Error	0.0873	0.0783	0.0794
Phase Error	5.9312	5.2938	5.5465

